

# Supercontinuum generation in higher order modes of microstructured optical fibre

**Samuel Robert Legge**

B.Sc (Hons)

A thesis submitted for the Degree of

**Doctor of Philosophy**

Discipline of Physics

School of Mathematical and Physical Sciences

The University of Newcastle

April 2016



***Declaration***

This thesis contains no material which has been accepted for the award of any other degree or diploma in any university or other tertiary institution and, to the best of my knowledge and belief, contains no material previously published or written by another person, except where due reference has been made in the text. I give consent to this copy of my thesis, when deposited in the University Library, being made available for loan and photocopying subject to the provisions of the *Copyright Act 1968*.

(Signed)\_\_\_\_\_

Samuel Legge



## *Acknowledgments*

I would like to thank my family for their love and understanding over the past years that I have worked on this project. I would like to give my mum and dad a special thank you for always being there for me and encouraging my curiosity in science.

I would like to thank my supervisors John Holdsworth and Bruce King for their help and guidance. John in particular has been an amazing mentor over the last nine years of my life and I thank him immensely for everything he has helped me achieve.

Thank you to all the undergraduate and honours students I have worked with on this project. Ben Zwan deserves a mention for both his experimental work and input into the scientific process.

Most importantly I would like to thank my wife Kim for all her support and encouragement over these last few years. Your love and kindness has kept me going through this and I look forward to our next big adventure together.



## ***Abstract***

The focus of this thesis is the observation and characterisation of supercontinuum generation within multimode microstructured optical fibre and the development of the techniques required to both create and measure the generated supercontinua. In addition, the nonlinear effects of light in silica are reviewed, and the experimental results from supercontinua generated with a low number of solitons add novel scientific weight to recent theories on dispersive wave and soliton interactions in microstructured optical fibre.

The supercontinua generated in various hexagonal core and elliptical core microstructured optical fibres when pumped with femtosecond pulses sourced from a Ti:Sapphire laser system are observed. The electromagnetic mode excited within the core is selected by an offset to the incident beam position on the fibre end face through a precise coupling system under computer control. A novel experimental measurement technique was developed to simultaneously characterise the electromagnetic mode output of these fibres in spectral and spatial domains.

This technique revealed previously unobserved complexity in the mode structure of the supercontinuum output from microstructured optical fibre. In the generated dispersive wave, it was found that the electromagnetic mode structure was orientated in a hexagonal higher order mode structure with each orientation producing a slightly varied wavelength of light.

From this work, and by selectively coupling into higher order modes, it was discovered that the creation of a “sparse supercontinuum” with a low number of solitons was possible while still maintaining strong nonlinear effects. This work allowed experimental soliton and dispersive wave pairs matched in higher order modes to be compared to the recent theories on dispersive wave trapping and the group index matching between these light pulses.

To aid in the understanding of this data the full vector solutions for the electromagnetic modes in all fibres used were simulated using finite element frequency domain analysis, providing both the mode field structure and the effective mode index and dispersion for all modes in each fibre.

A polarisation study was performed on the output of the higher order electromagnetic modes confirming the expected simulated vector modes and using the rotation direction of the field pattern with polarisation rotation to determine the specific mode generated.

This thesis comprises significant work that expands the scientific knowledge in the fields of supercontinuum generation, nonlinear optics and higher order electromagnetic modes in microstructured optical fibres through both simulation and experimental measurement and analysis.

## *Table of Contents*

Declaration .....	i
Acknowledgments.....	iii
Abstract .....	v
Table of Contents .....	vii
1 Introduction.....	1
1.1 Optical Fibre.....	2
1.1.1 Numerical Aperture.....	2
1.1.2 Attenuation.....	3
1.1.3 Refractive Index of Optical Fibre .....	4
1.1.4 Electromagnetic Modes in Optical Fibre .....	6
1.2 Microstructured Optical Fibre .....	12
1.3 Nonlinear Optics.....	14
1.3.1 Kerr Effect.....	16
1.3.2 Self-Phase Modulation .....	17
1.3.3 Cross-Phase Modulation .....	19
1.3.4 Wave Mixing.....	22
1.3.5 Solitons.....	23
1.3.6 Stimulated Raman Scattering.....	26
1.4 Supercontinuum.....	28
1.4.1 Discovery and History.....	28
1.4.2 The Supercontinuum .....	29
1.4.3 Soliton Formation and Fission .....	30
1.4.4 Soliton Self-Raman Shift .....	30
1.4.5 Dispersive Wave .....	31
1.4.6 Gravity-like Trapping.....	33
1.4.7 Four Wave Mixing .....	36

1.4.8	Numerical Simulation .....	36
1.5	Supercontinuum in Higher Order EM Modes .....	37
1.5.1	Initial Research .....	38
1.5.2	Current Research.....	39
1.5.3	The Scope of this Thesis .....	44
2	Experimental.....	46
2.1	Ultrafast Lasers.....	46
2.1.1	Titanium-Sapphire Laser.....	46
2.1.2	Measurement and Characterisation of Ti:S Laser.....	47
2.2	Microstructured Optical Fibre .....	49
2.3	Optics.....	53
2.3.1	Faraday Isolator.....	53
2.3.2	Beam Steering and Stabilisation .....	54
2.3.3	Fibre Coupling System.....	58
2.3.4	Apparatus Configuration.....	59
2.3.5	Collimator and Mode Scanner .....	59
2.3.6	Polariser and Screen.....	61
2.4	Spectrometers .....	62
2.4.1	HR2000+.....	62
2.4.2	NIRQuest .....	62
2.5	Processing.....	64
2.5.1	Radiometric Calibration.....	64
2.5.2	Data Restructure and Visualisation.....	65
3	Modelling of Optical Modes in Microstructured Optical Fibres .....	67
3.1	Multipole Method.....	67
3.2	Finite Element Frequency Domain Method .....	68
3.3	Curve Fitting.....	68

3.4	Results .....	69
3.4.1	Thorlabs NL-2.8-850-02 .....	69
3.4.2	Thorlabs NL-2.0-745-02 .....	74
3.4.3	Thorlabs NL-3.0-850.....	77
3.4.4	OFTC Spun High Birefringence Fibre.....	79
4	Observation of Supercontinuum Generation in Higher Order Modes of Microstructured Optical Fibre.....	83
4.1	Overview .....	83
4.2	Results and Discussion.....	84
4.3	Conclusions .....	90
5	The Sparse Supercontinuum.....	91
5.1	Overview .....	91
5.2	Method and Reasoning.....	92
5.3	Results and Discussion.....	93
5.4	Conclusions .....	97
6	Polarisation Study.....	98
6.1	Overview .....	98
6.2	Experimental and method.....	98
6.3	Results and discussion.....	102
6.4	Conclusions .....	106
7	Conclusions and Further Work.....	107
8	References.....	109
9	Papers.....	112
9.1	Supercontinuum Generation in Higher Order Modes of Photonic Crystal Fibre .....	113
9.2	Spatio-spectral Identification of Solitons Occupying Higher Order Electromagnetic Modes in Photonic Crystal Fibre.....	119

9.3	Spatio-spectral Analysis of Supercontinuum Generation in Higher Order Electromagnetic Modes of Photonic Crystal Fiber .....	123
9.4	Low Order Solitons in Higher Order Electromagnetic Modes of Photonic Crystal Fibre .....	129
9.5	Higher-Order Electromagnetic Mode Solitons Illuminate Theory.....	132
9.6	Sparse Supercontinuum with Low Order Solitons in Higher Order Electromagnetic Modes .....	135
10	Appendices .....	139
10.1	Taylor Series Expansion of Phase Constant.....	139
10.2	Radiometric Calibration .....	141
10.3	Source Code for Programs .....	142
10.3.1	List of other Programs Witten.....	142
10.3.2	Refraction of Fused Silica.....	143
10.3.3	Self-Phase Modulation Simulation .....	144
10.3.4	Quadrant Detection Simulation.....	145

## ***1 Introduction***

This field of study has seen a large increase in research over the past 15 years ever since the discovery of Microstructured Optical Fibre (MOF) supercontinuum generation by Ranka et al in 2000 [1]. Although, once discovered, the experimental generation of this type of supercontinuum was easily achieved, understanding the physical processes occurring proved more difficult as the broad continuum of light made isolation of the various nonlinear effects difficult [2]. The resulting research has pushed the boundaries of knowledge for fibre structure and novel waveguide manufacturing, as well as the nonlinear optical effects within these waveguides. This thesis adds to this area of knowledge by investigating the nonlinear effects and supercontinuum generation in multiple electromagnetic modes of these waveguides.

This thesis adds the following to the body of knowledge on this subject. A new experimental method of characterising the spatial and spectral output of a MOF supercontinuum has been developed and the first observations of mode dependant wavelengths in the supercontinuum arising from this new approach are reported. The observation of the “sparse supercontinuum” arising from solitons of order  $N \leq 5$  and the analysis of results adds new experimental evidence supporting theories of dispersive wave and soliton interactions directly, where previous measurements only provided indirect support. Finally, a full exploration of the electromagnetic modes in hexagonal core MOF performed in simulation and experimentally validated, provides the definitive measure of low order electromagnetic mode propagation in MOFs.

This chapter introduces the fields of nonlinear and ultra-fast optics and specifically supercontinuum generation in MOF. The topics of fibre waveguides; electromagnetic modes; nonlinear optics; solitons; and supercontinuum generation necessary to discuss the application are reviewed.

At this point, it is also useful to define the following commonly used units and their relation.

$\omega$  is the angular frequency of an electromagnetic field.

$\lambda_0$  is the free space wavelength. The two are related through the speed of light.

$$\omega = \frac{2\pi c}{\lambda_0} \quad (1.1)$$

Quantities are usually referenced with respect to their free space wavelengths but mathematically it is often easier to use angular frequency. The two are interchangeable (with relevant scaling) in all following equations.

## 1.1 Optical Fibre

This section will focus on the relevant effects optical fibres impose on transmitted light, namely attenuation and wavelength dependent linear effects such as dispersion. The nonlinear effects will be discussed in section 1.3. The differences in the structural and therefore optical properties of MOF will also be examined and the changes such unique guides have on the waveguide properties for fundamental and potential higher-order electromagnetic modes in these fibres will be detailed.

### 1.1.1 Numerical Aperture

The simplified explanation for light guiding by an optical fibre is one of total internal reflection, where a higher refractive index core glass is surrounded by a lower refractive index cladding glass, and guidance is achieved for light undergoing total internal reflection at the interface between the two glasses. The structure of the basic step-index optical fibre, shown in Figure 1.1, can be considered as a cylindrical waveguide.

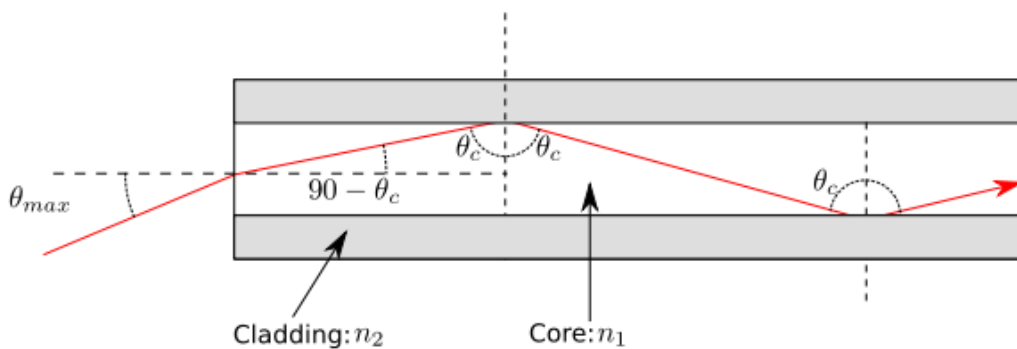


Figure 1.1: Propagation of light by an optical fibre [3]

Light must enter the core of the fibre below a maximum angle to satisfy the condition for total internal refraction at the core/cladding boundary as expressed in equation (1.2).

$$\theta_{max} = \sin^{-1} \left( \frac{\sqrt{n_1^2 - n_2^2}}{n} \right) \quad (1.2)$$

The Numerical Aperture (NA) of a fibre is defined by the refractive indices of the media.

$$NA = n \sin(\theta_{max}) = \sqrt{n_1^2 - n_2^2} \quad (1.3)$$

In these equations,  $n_1$  and  $n_2$  are the core and cladding refractive indices and  $n$  is the refractive index external to the fibre and is usually simplified to 1 as, in most cases, the fibre is held in free space or air.

### 1.1.2 Attenuation

Optical fibre is made from the most pure and transparent materials ever manufactured, however, it still has intrinsic optical loss. This loss is defined by the attenuation, a value that is a specified property of an optical fibre for engineering purposes, given in deciBels/length by;  $a(\lambda_0) \text{ dB/km}$  and varies with wavelength  $\lambda_0$  as shown in Figure 1.2.

$$a(\text{dB/km}) = \frac{P_2(\text{dBm}) - P_1(\text{dBm})}{|L_2(\text{km}) - L_1(\text{km})|} \quad (1.4)$$

The electromagnetic (EM) power transmitted through some distance  $L_2(\text{km})$  of a fibre,  $P_{2z}(\text{dBm})$ , is measured and the fibre “cut-back” to a length,  $L_1(\text{km})$ , resulting in a higher power  $P_1(\text{dBm})$  being measured. The attenuation,  $a$  (dB/km), is calculated from equation 1.4 as the initial launched power,  $P_o$ , is unknown due to coupling losses at the interface. It may be converted to the Beer’s Law absorbance of the fibre if needed.

The mechanisms behind loss in an optical fibre are mostly due to the material properties of the fused silica. This material can have water embedded from initial manufacture, creating OH bond vibrational absorptions, as well as the inherent UV electronic and infrared vibrational absorptions of  $\text{SiO}_2$ , with the Rayleigh scattering properties of the glassy state of silica and waveguide losses as a minor contributor.

The wavelength dependence of loss is shown in Figure 1.2. The minimum loss is where the Rayleigh scattering and residual UV absorption have minimised and is after the

water (OH) peak at 1400 nm, before the NIR vibrational absorption begins. The various loss mechanisms are not critical to the understanding of this thesis apart from the fact that they exist. There is a relatively low loss optical window from 400 nm – 2000 nm in which silica fibre is used and in this thesis, the transmission length is of the order of 1 meter so loss is not a significant factor.

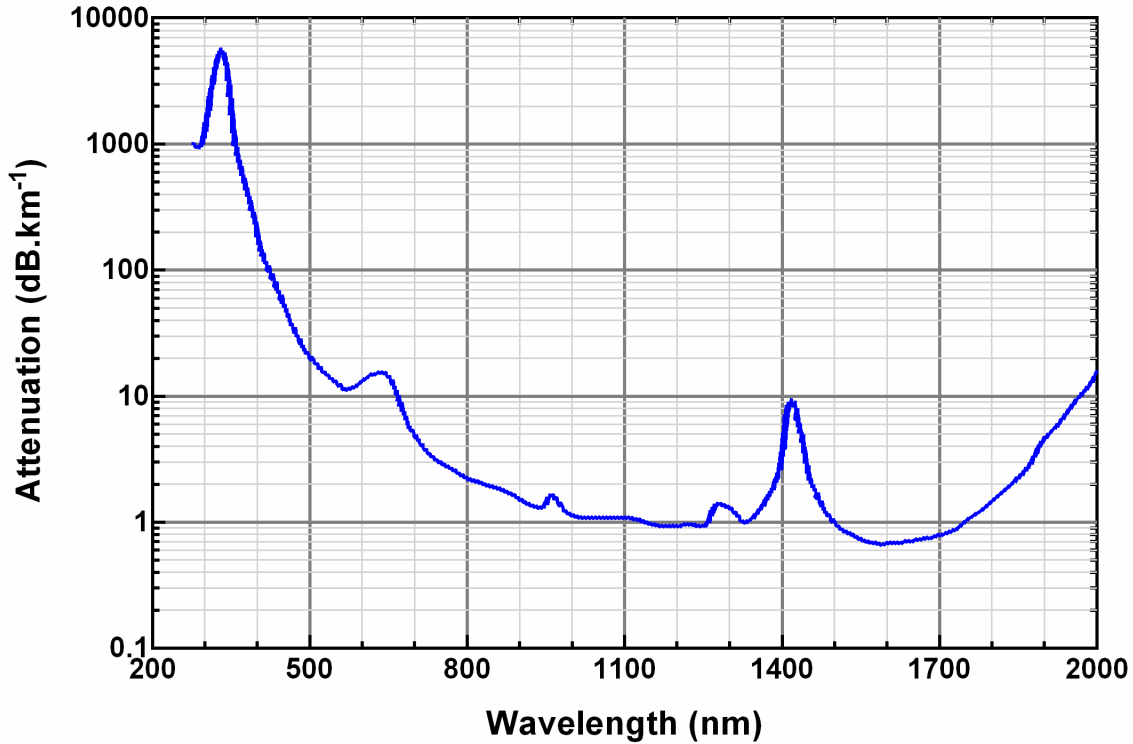


Figure 1.2: Attenuation of fused silica optical fibre [4].

### 1.1.3 Refractive Index of Optical Fibre

The interaction of light propagation within a bulk material is often described primarily by a refractive index. The refractive index  $n$  is a measure of the ratio of the phase velocity of light in that material with respect to the free space velocity of light,  $c \cong 3 \times 10^8 \text{ m s}^{-1}$ . This phase velocity is wavelength dependent and is in this text defined as a function of the free space wavelength ( $\lambda_0$ ). The actual wavelength in the material  $\lambda$  is changed by shift in phase velocity.

$$n(\lambda_0) = \frac{c}{v(\lambda_0)} \quad (1.5)$$

$$\lambda = \frac{\lambda_0}{n(\lambda_0)} \quad (1.6)$$

The material properties are not the only factor that affects refractive index. In waveguides such as optical fibre, the EM mode that conveys the optical energy also has an effect on the phase velocity of light. These EM modes are defined to have an effective index  $n_{eff}$ , that is, the linear combination of the material refractive index and waveguide mode refractive index. This will be discussed further in section 1.1.4 but it is important to note that the mode affects all of the following parameters.

The group index  $n_g$  is similarly a measure of the group velocity of light,  $v_g$ . This is important for pulses and wave packets as the enveloping light amplitude pulse will travel at the group velocity so the group index is directly related to the refractive index derivative.

$$n_g(\lambda_0) = \frac{c}{v_g(\lambda_0)} = n(\lambda_0) - \lambda_0 \frac{dn}{d\lambda_0} \quad (1.7)$$

The group velocity is useful as it is the true indication of the velocity of information through a fibre.

Group Velocity Dispersion (GVD), often referred to as simply dispersion, is the measure of the variation of group velocity with respect to wavelength. This is a critical optical fibre property as it dictates the spread of a finite bandwidth pulse over time as different wavelengths travel at different velocities. It is directly related to the derivative of the group index and is often referred to as  $D$  (in units of ps.nm<sup>-1</sup>.km<sup>-1</sup>) or as  $\beta_2$  (in units of ps<sup>2</sup>.km).

$$D = \frac{1}{c} \frac{dn_g}{d\lambda_0} = -\frac{\lambda_0}{c} \frac{d^2n}{d\lambda_0^2} = -\frac{2\pi c}{\lambda_0^2} \beta_2 \quad (1.8)$$

Dispersion can be both positive and negative (unlike refractive and group index) and is defined as normal when  $D$  is negative (longer wavelengths will travel faster) and anomalous when  $D$  is positive (longer wavelengths will travel slower). As can be seen in Figure 1.3, most materials will change from normal to anomalous dispersion at some point. This is known as the zero GVD point and is located at approximately 1300 nm for bulk silica. A pulse in the linear regime at a zero GVD point wavelength will have

effectively no dispersion, maintaining its temporal shape and spectral characteristics as it propagates.

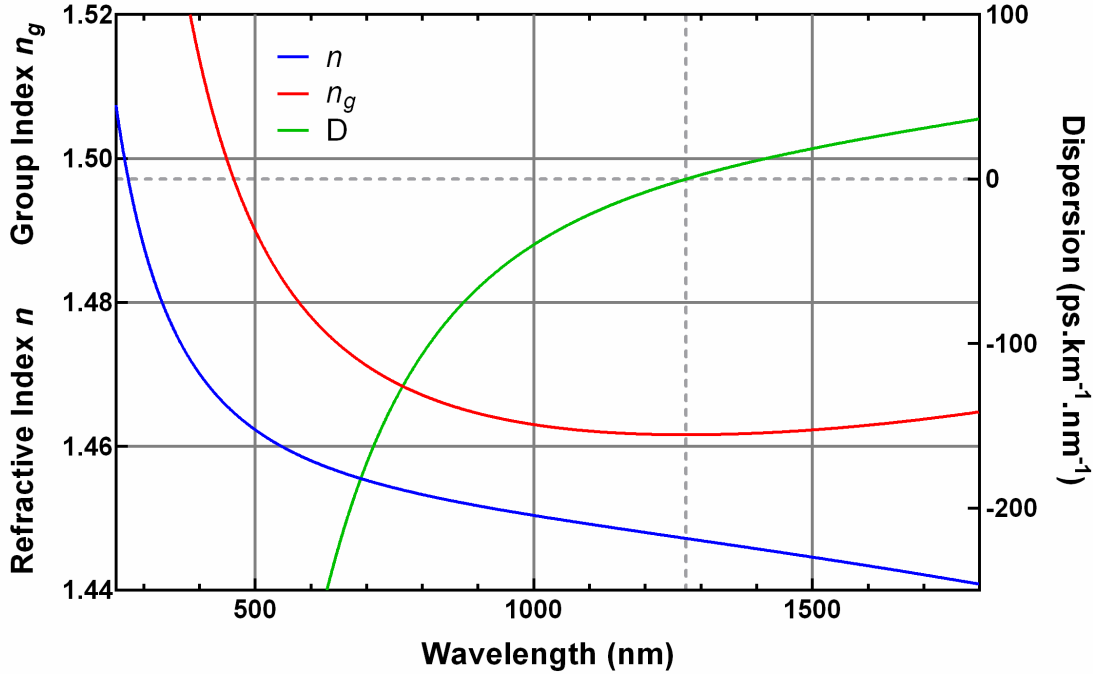


Figure 1.3: Refractive index, group index and dispersion for bulk fused silica. These data are modelled from the Sellmeier equation of fused silica shown in equation (3.1). The code can be found in appendix 10.3.2.

#### 1.1.4 Electromagnetic Modes in Optical Fibre

The most common form of optical fibre is that used in telecommunications, i.e. a step-index optical fibre which can be thought of as a cylindrical waveguide. The propagation of electromagnetic (EM) waves through this structure is determined by the propagation constant  $\gamma$ .

$$\gamma = \alpha + i\beta \quad (1.9)$$

$$\frac{A_z}{A_0} = e^{\gamma z} \quad (1.10)$$

where

$A(x, y, z)$  is the complex spatial amplitude of the EM field in the media, and is confined by the boundary limits when propagating in a waveguide.

$\alpha(\lambda_0)$  is the attenuation constant and is a function of wavelength as shown in 1.1.2.

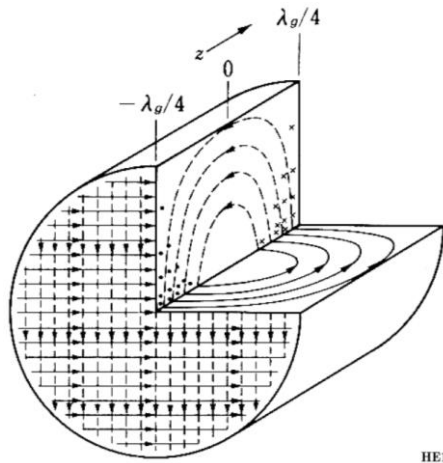
$\beta(\lambda_0)$  is the phase constant and is also a function of wavelength and is directly related to the refractive index  $n_{eff}$ , combining the conventional material refractive index,  $n$ , and the waveguide index mentioned in 1.1.3.

$$\beta(\lambda_0) = n_{eff}(\lambda_0) \frac{2\pi}{\lambda_0} \quad (1.11)$$

The values for  $\alpha$  and  $\beta$  are dependent on the physical size, shape and material of the waveguide, the wavelength of the light, and the EM mode within the particular waveguide in which the light is travelling. Each EM mode is a discrete solution that allows a constructive phase relation of the EM field within the geometry of the waveguide. The principal guided modes have minimal loss, while “leaky” modes lose energy and are therefore, lossy. Analytical solutions exist for perfectly circular waveguides and perfect boundary conditions, while numerical methods may be employed to solve for the lossy modes.

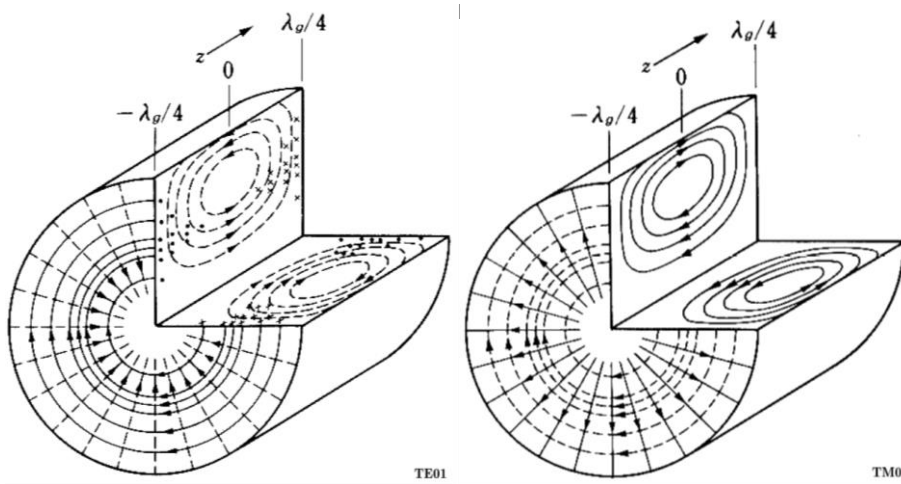
Modes of an electro-magnetic waveguide are designated:

- TEM (Transverse Electromagnetic). Light propagating in free space has this property. These modes can also exist in waveguides with at least two conducting surfaces.
- TM (Transverse Magnetic). The magnetic field is perpendicular to the direction of travel.
- TE (Transverse Electric). The electric field is perpendicular to the direction of travel.
- HE (Hybrid mode TE dominates). These hybrid fields have both electric and magnetic fields in the direction of travel.
- EH (Hybrid mode TM dominates).



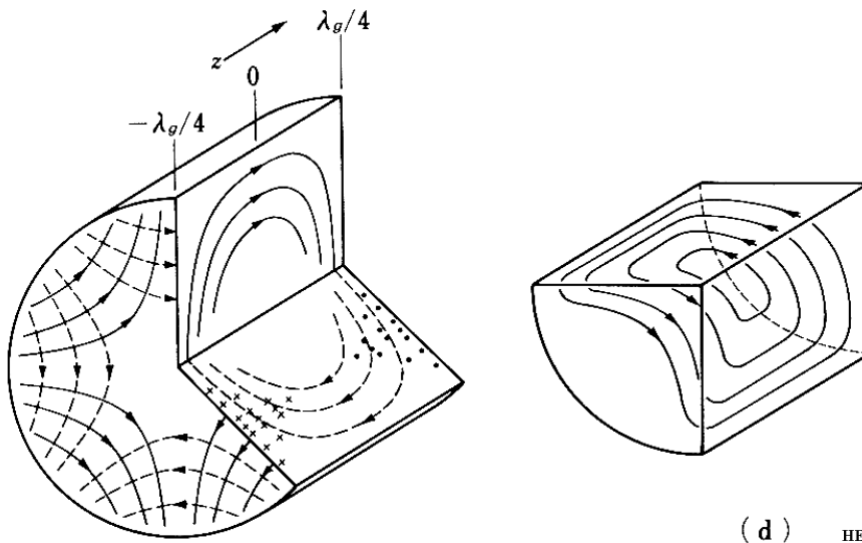
HE11

Figure 1.4: HE<sub>11</sub> mode of an optical fibre. Solid lines represent E field and dashed lines represent H field.  $\lambda_g$  is the waveguide wavelength and  $z$  is the direction of travel. This mode combines with near energetically degenerate modes to form the LP<sub>01</sub> mode [5].



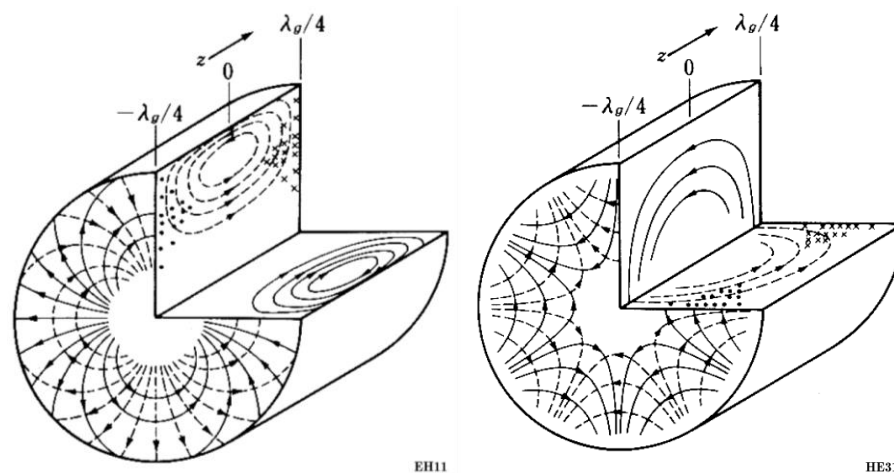
TE01

TM01



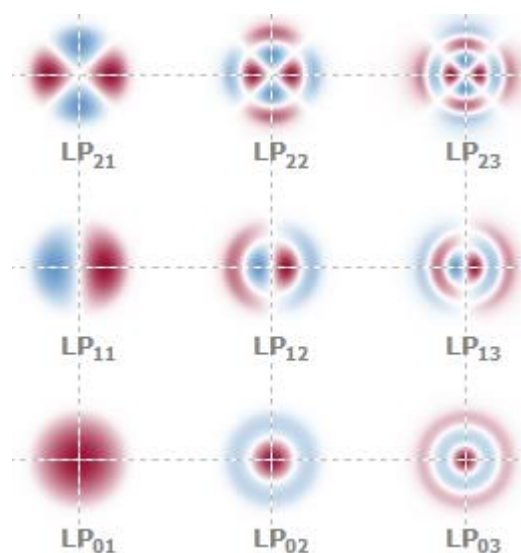
(d) HE21

Figure 1.5: TE<sub>01</sub> TM<sub>01</sub> and HE<sub>21</sub> EM modes in optical fibre. These modes combine with near energetically degenerate modes to form to the LP<sub>11</sub> mode [5].



**Figure 1.6:  $\text{EH}_{11}$  and  $\text{HE}_{31}$  EM mode. These modes combine with near energetically degenerate modes to form the  $\text{LP}_{21}$  mode [5].**

Often these modes are simplified to Linearly Polarised (LP) modes as it is difficult to separate them without reference to a discrete feature of the fibre defining an axis. For example, the linear polarisation of the modes in Figure 1.5 result in the  $\text{LP}_{11}$  EM mode shown in Figure 1.7. In much of the work in this thesis, the LP approximation cannot be used as, indeed, there is a feature of the fibre providing an axis of discrimination and the modes are not energetically degenerate as a result of the fibre structure.



**Figure 1.7: Linearly polarised (LP) modes for step index fibre. The colour designates the sign of the electric field (red +, blue -) in the plane of the page direction while the colour depth represents the intensity [6].**

Each mode will have a different propagation constant, and, as a result, a different effective refractive index. Coupling between modes is usually minimal and will only occur strongly if the propagation constants overlap.

It is enlightening to look at one of the most common fibres in the world, Corning SMF-28. This is a step-index fibre that has single mode propagation at telecommunication wavelengths but can easily support higher order modes at shorter wavelengths. The following diagram shows the effective index of a number of propagating modes in SMF-28.

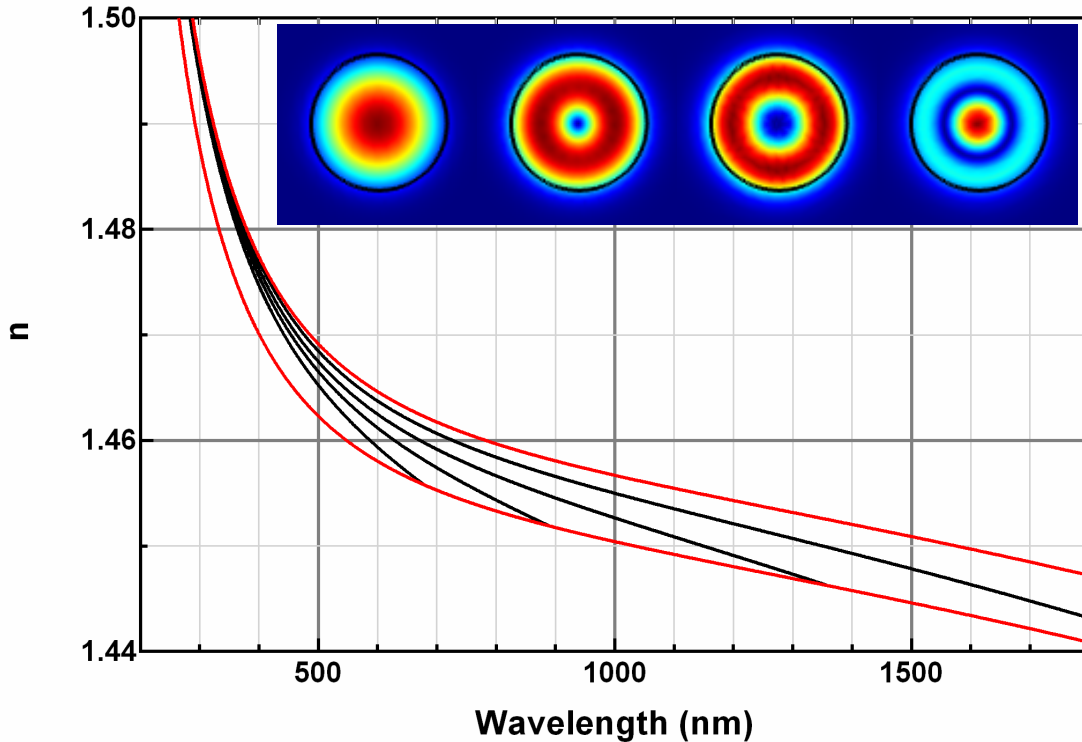


**Figure 1.8: First four effective mode refractive indices (black) for corning SMF-28 with the core and cladding index shown in red. Note this fibre is single moded past 1440 nm. Inserts show normalised E field intensities at 500 nm for the four modes in order of decreasing index from left to right with the 8.2 micron core shown in black.**

Wavelengths that are too long will not strongly propagate within the fibre. This is observed as a cut-off wavelength and is where each of the higher order mode effective indices visible in Figure 1.8 fall to equal the cladding index so that the mode will no longer propagate as a guided mode at any longer wavelength.

The four modes displayed in Figure 1.8 are all combinations of the modes shown in the previous figures (Figures 1.4 - 1.6). Many of those modes are degenerate, meaning that while the structure of the E and H field is different, the effective mode index is the same. The following diagrams show the modes comprising the mode structure for each of the four intensity profiles shown in Figure 1.8 and their E fields in the x-y plane. These match the diagrams shown previously in Figures 1.4 - 1.6.

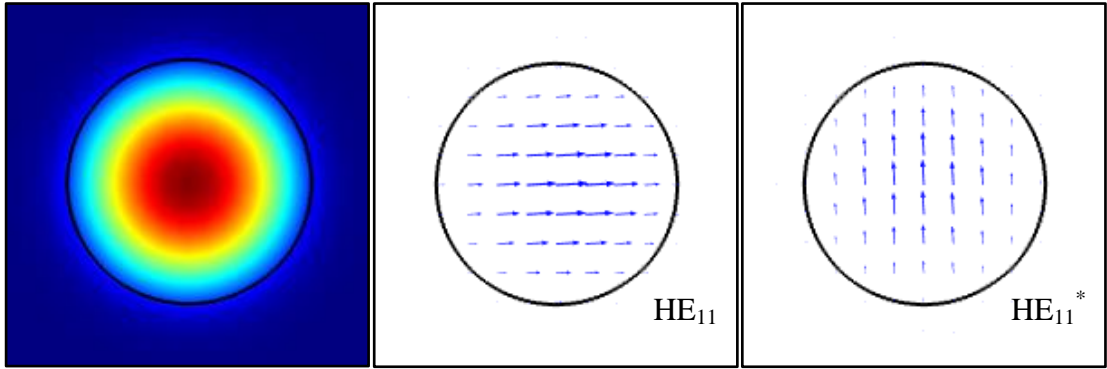


Figure 1.9: First (fundamental,  $LP_{01}$ ) mode of SMF-28. This is a  $HE_{11}$  mode as shown in Figure 1.4. This mode has a degeneracy of 2 as can be seen by the two E field orientations.

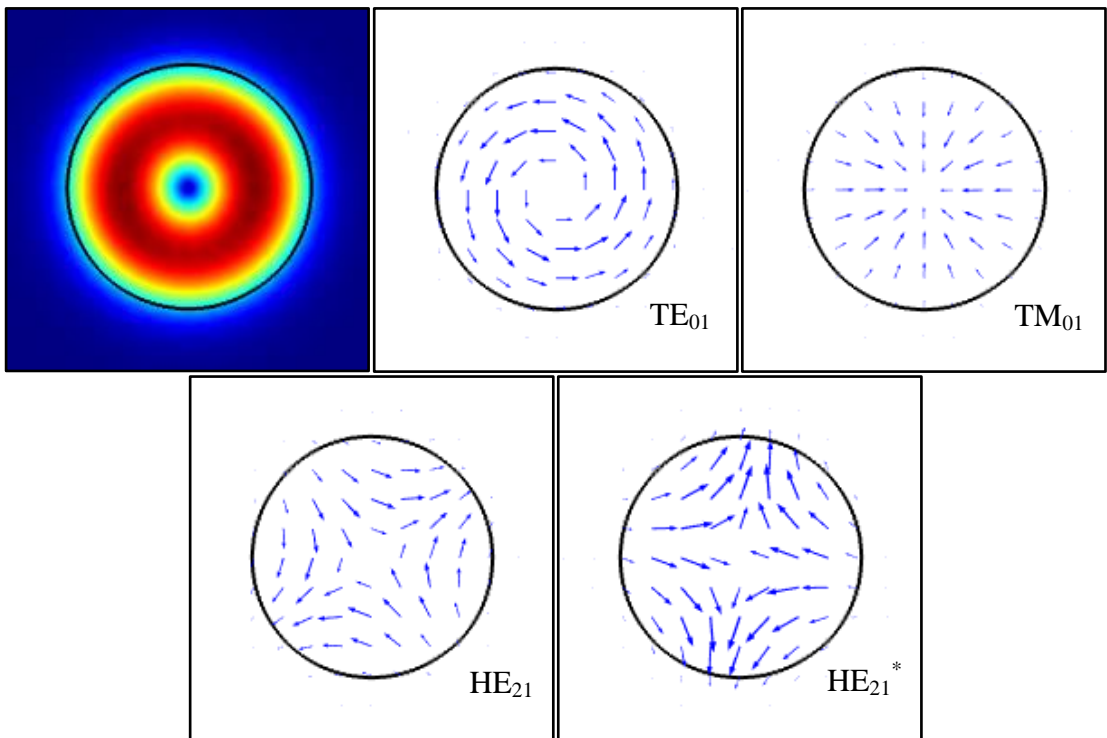


Figure 1.10: Second ( $LP_{11}$ ) mode of SMF-28. This is a  $TE_{01}$  mode,  $TM_{01}$  mode and a  $HE_{21}$  mode with a degeneracy of 2 resulting in a total of four degenerate modes. Full diagrams of these modes can be found in Figure 1.5.

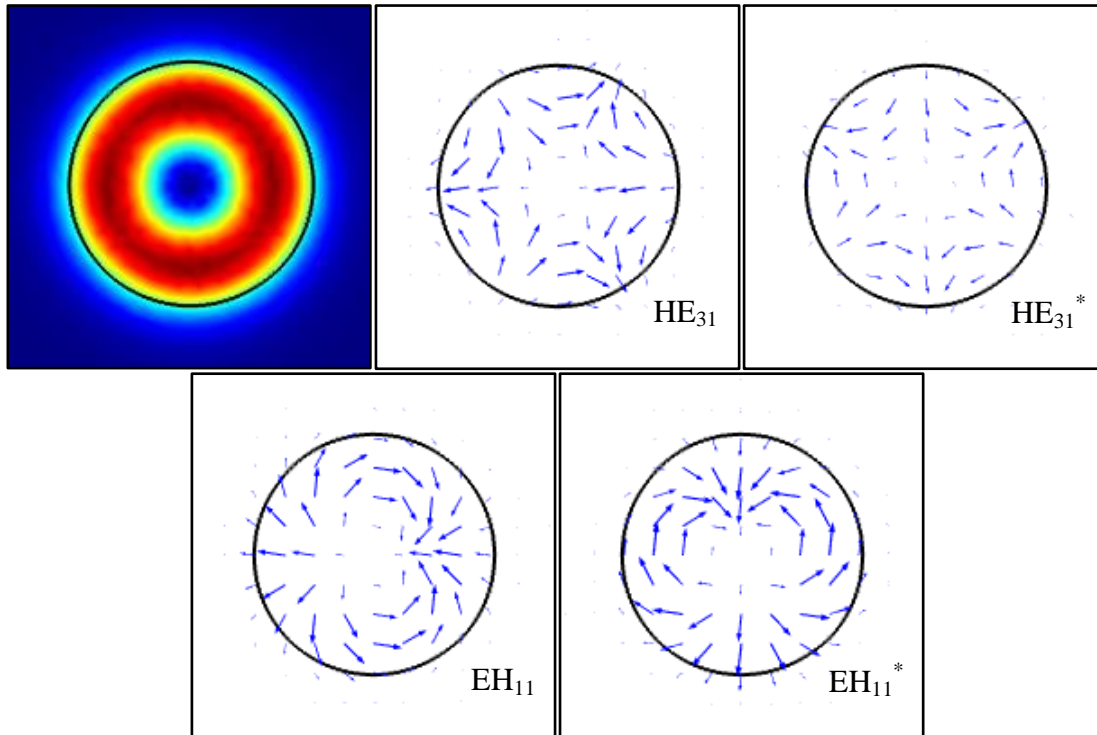


Figure 1.11: Third ( $LP_{21}$ ) mode of SMF-28. This a pair of two degeneracy  $HE_{31}$  and  $EH_{11}$  modes resulting in four mode degeneracy. Full diagrams of these modes can be found in Figure 1.6

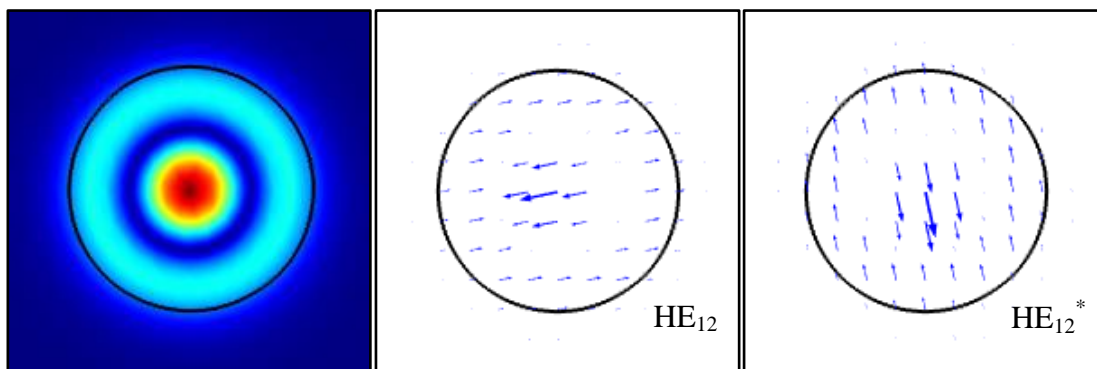


Figure 1.12: Fourth ( $LP_{02}$ ) mode of SMF-28. This is a doubly degenerate  $HE_{12}$  mode.

## 1.2 Microstructured Optical Fibre

While most optical fibres are made of silica doped with a small concentration of impurities to give the required variation in refractive index, there are other ways to achieve this guiding property. In the 1990s, people began manufacturing fibre that was not a solid cylinder, but was instead a cylinder of pure silica, providing the solid structure, with arrangements of voids or holes running the length of the fibre that were simply filled with air. These complicated fibres are generally referred to as Microstructured Optical Fibre (MOF), although they are sometimes referred to as photonic crystal fibre due to the ability for certain designs to make use of a Bragg reflection based photonic band gap effect to contain the light. This effect is not

prevalent in the fibres used within this thesis, however, and the guiding property of the fibre is still that of total internal reflection where a solid core has a higher effective refractive index than the array of air holes which surrounds it.

Early examples of this type of fibre were not particularly uniform, as the manufacturing and, principally, drawing techniques were not yet developed. However, the technology still allowed for the development of endlessly single moded fibre [7,8] and novel sensing and optical control when the voids were filled with liquids and gases other than atmosphere.

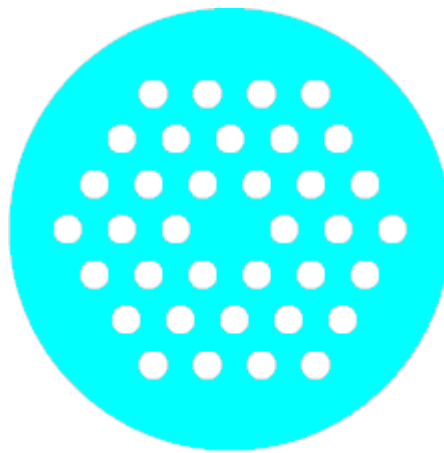


**Figure 1.13: A simple example of a MOF. Blue areas indicate pure fused silica and white spaces indicate voids. The design geometry is not limited, however, a hexagonal base pattern is often used as it allows equal spacing between elements and is a consequence of the hexagonal close packing of rods and tubes in the fibre preform assembly. Further real examples can be seen in Section 2.2.**

A potential design of a MOF is shown in Figure 1.13. The guiding mechanism for this fibre uses the average refractive index of the area surrounding the core. While the core section of the fibre itself has a refractive index of pure fused silica, the surrounding area is a combination of silica and air and has a lowered averaged refractive index. With the correct ratio of air to silica and the size of the microstructured elements, these MOFs will act as a waveguide quite similar to standard optical fibre, however, the large refractive index difference between the core and the cladding allows for a much smaller core and hence a much smaller effective mode area, increasing the intensity of the light within the waveguide.

As well as significant changes to the waveguide index, modifying  $n_{eff}$  significantly changes the overall dispersion of the waveguide and greatly lowers the zero GVD point as shown in Figure 1.14

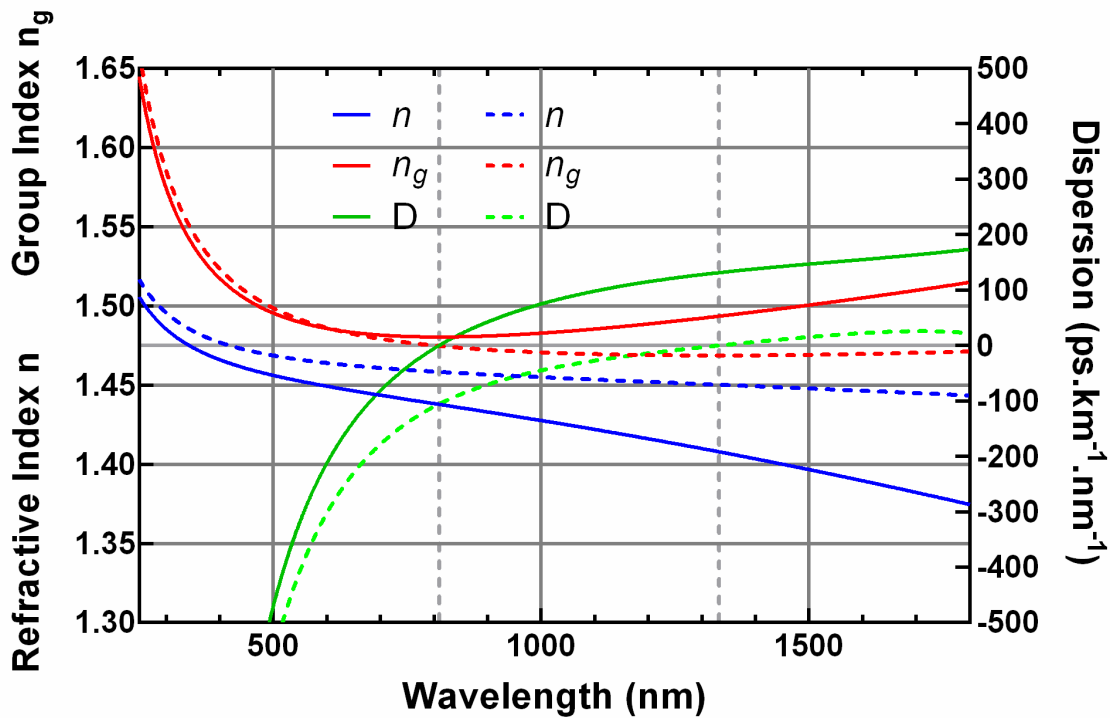


Figure 1.14: Refractive index, group index and dispersion for Thorlabs NL-2.8-850-02 fibre (solid) and Corning SMF28 fibre (dashed), showing the significant difference in the group index and dispersion of MOF in comparison to regular step index fibre where only small changes from the index of bulk silica cause guiding. The data shown is from Chapter 3.

Unless specifically designed to be single moded, most MOF will allow the propagation of multiple EM modes within the visible and near infrared wavelengths. These modes, while similar to the ideal cylindrical case discussed in section 1.1.4, will not follow the same pattern exactly, and while the fundamental mode is usually a Gaussian shape or similar, the higher order modes will often have much more complicated structure [9]. In addition to this, the degeneracy of the modes found in the SMF-28 fibre can be split by the large refractive index changes in the microstructure. Full modelling of the supported EM modes can be seen in Chapter 3.

### 1.3 Nonlinear Optics

Nonlinear optics arises from the response of material to extreme optical intensity. In linear optics, the electromagnetic radiation is considered (and defined) to have a directly linear effect on the medium. Most optically transparent materials can be considered to be a rigid lattice of positive charges, each with a tightly bound negative charge of equal magnitude. The application of an external electric field to this lattice causes the electric

charges to separate slightly into a dipole. This is measured as an electric dipole moment  $\mathbf{p}$  defined by

$$\mathbf{p} = q\mathbf{d} \quad (1.12)$$

where  $q$  is the charge magnitude and  $\mathbf{d}$  is the displacement vector from the negative to the positive charge.

While this value is useful for defining a single dipole, the effects in bulk material occur over a large number of atoms. A more useful form of this is the polarisation density  $\mathbf{P}$ , often simply referred to as polarisation, and defined as the density of induced electric dipole moment  $\mathbf{p}$  within a volume.

$$\mathbf{P} = \frac{d\mathbf{p}}{dV} \quad (1.13)$$

As most materials are not ferroelectric they have no base polarisation, so the direction of the dipole moment and hence the polarisation is defined entirely by the electric field  $\mathbf{E}$ . The degree of this polarisation is controlled by the electrical susceptibility of the material  $\chi$ .

$$\mathbf{P} = \epsilon_0\chi\mathbf{E} \quad (1.14)$$

Here,  $\chi$  defines the degree to which the charges in the atomic structure of the dielectric will separate into dipoles under the effect of an external electric field. For all the materials in use, the permeability is assumed equal to that of free space and hence  $\chi$  can be directly related to the refractive index for all homogenous and isotropic mediums.

$$\mu_r = 1 \quad (1.15)$$

$$n_{eff}^2 = \chi + 1 \quad (1.16)$$

Equation (1.14), however, is an approximation, as it assumes a fixed uniform simple lattice of charges that can undergo a polarisation due to an external electric field with no interaction between individual charge pairs. While this is a very good approximation of the atomic lattice of highly rigid materials such as silica, under very high intensity electric fields the complexity of the lattice structure with unequal negative and positive charge distributions in each Cartesian coordinate direction, and the interactions of near

neighbouring charges, means that the resultant polarisation density for an electrical field is expanded as a Taylor series.

$$\mathbf{P} = \varepsilon_0[\chi^1\mathbf{E} + \chi^2\mathbf{E}^2 + \chi^3\mathbf{E}^3 + \dots + \chi^n\mathbf{E}^n] \quad (1.17)$$

This is the general expression of (1.14) that can accommodate all nonlinear effects. Here  $\chi^n$  are the  $n^{\text{th}}$  order electric susceptibilities of the medium. In the general form,  $\chi^n$  is an  $n+1$  order tensor representing the nonlinear interaction in all directions. Higher order susceptibilities become increasingly smaller and, as such, historically, effects past those of  $\chi^3$  were rarely considered. The advent of extreme ultra-short pulsed laser intensities does, however, require higher orders than  $\chi^3$  to be included in any analysis.

$\chi^1$  is identical to the linear susceptibility in equation (1.14).

$\chi^2$  is nonzero only for compounds that lack an inversion symmetry on a molecular or crystalline level. Silica is symmetric and therefore  $\chi^2$  is zero and any of the nonlinear phenomena dependent on it are not observed in silica optical fibre.

$\chi^3$  is nonzero for all materials and relatively small, however, when factored with  $\mathbf{E}^3$  has a significant effect on the polarisation density at high optical intensities.

Thus it is possible to split the overall polarisation density into linear and nonlinear components when considering  $\chi^1$  and  $\chi^3$  effects as shown below. This can help to simplify proofs, as the total polarisation density is the linear combination of the two.

$$\mathbf{P}_L = \varepsilon_0\chi^1\mathbf{E} \quad (1.18)$$

$$\mathbf{P}_{NL} = \varepsilon_0\chi^3\mathbf{E}^3 \quad (1.19)$$

$$\mathbf{P} = \mathbf{P}_L + \mathbf{P}_{NL} \quad (1.20)$$

### 1.3.1 Kerr Effect

The Kerr effect is the most basic material response of a nonlinear medium. This response is observed as a change in the medium refractive index proportional to the optical intensity within that medium. As such, the refractive index can be written as a combination of the material or waveguide refractive index and the nonlinear response.

The full derivation of this is not shown, as it is an inherent part of the Cross-Phase Modulation (XPM) derivation that is shown in 1.3.3.

$$\tilde{n}(\lambda_0, |E|^2) = n_{eff}(\lambda_0) + n_2 |E|^2 \quad (1.21)$$

$$n_2 = \frac{3}{8n_{eff}(\lambda_0)} \text{Re}(\chi_{rrrr}^3) \quad (1.22)$$

Here  $|E|^2$  is the optical intensity of the  $\mathbf{E}$  field and  $n_2$  is affected by the real component of the  $\chi^3$  tensor in the linear plane of polarisation of the  $\mathbf{E}$  field as denoted by the  $r$  subscript.  $\hat{\mathbf{r}}$  is used as the direction of polarisation in equation (1.24) and throughout this chapter.

This seemingly basic material response results in numerous effects that are discussed in the following sections. Effects resulting from equation (1.21) are known collectively as Kerr effects.

It is useful to define the following parameter, the nonlinear coefficient

$$\gamma = \frac{\omega_0 n_2(\omega_0)}{c A_{eff}(\omega_0)} \quad (1.23)$$

where  $A_{eff}$  is the effective mode area,  $\omega_0$  is the angular frequency,  $n_2$  is defined in equation (1.22) and  $c$  is the speed of light. The nonlinear coefficient is commonly used to represent the magnitude of the nonlinear optical response to incident light.

### 1.3.2 Self-Phase Modulation

Self-Phase Modulation (SPM) is a direct result of the Kerr effect. The SPM experienced by a single optical pulse is investigated.

$$\mathbf{E}(\mathbf{r}, t) = \hat{\mathbf{r}} \frac{1}{2} E(t) [e^{-i\omega_0 t} + e^{i\omega_0 t}] \quad (1.24)$$

Equation (1.24) represents an electrical field propagating at an angular frequency of  $\omega_0$  and with an intensity profile defined by  $E(t)$  that is a slowly varying function of time compared with an optical period. To solve for the nonlinear polarisation density of the pulse in a medium, it must be substituted into (1.19).

For any time-varying light intensity propagating in a fibre, such as an optical pulse, the intensity of the light will generate a time varying refractive index change around the pulse. The front of the pulse will experience an increasing refractive index while the back of the pulse will experience a decreasing refractive index. This process creates a phase shift within the pulse.

$$\phi = \beta_0 \tilde{n}x - \omega_0 t = \frac{2\pi}{\lambda_0} x [n_{eff}(\lambda_0) + n_2 |E|^2] - \omega_0 t \quad (1.25)$$

where  $x$  is the distance the pulse has propagated and  $\beta_0$  is the free space wavenumber. This can be rewritten as a function of time for a varying optical intensity, using  $\omega_0$  as the centre angular frequency of the pulse.

$$\phi(t) = \frac{2\pi}{\lambda_0} x n_{eff}(\lambda_0) + \frac{2\pi}{\lambda_0} x n_2 |E(t)|^2 - \omega_0 t \quad (1.26)$$

This phase shift results in an instantaneous frequency change given by

$$\tilde{\omega}(t) = -\frac{d\phi(t)}{dt} = \omega_0 - \frac{2\pi}{\lambda_0} x n_2 \frac{d|E(t)|^2}{dt} \quad (1.27)$$

This phase shift is entirely dependent on the intensity of the pulse and can be calculated for various pulse profiles. This effect is shown in Figure 1.15 where the leading and trailing edges of the pulse generate a lower and higher instantaneous frequency. As a result of this, the pulse will develop a “chirp” where the pulse angular frequency will shift to a lower frequency at the leading edge, moving back to  $\omega_0$  at the centre and generating a higher frequency as the intensity decreases past the temporal maximum.

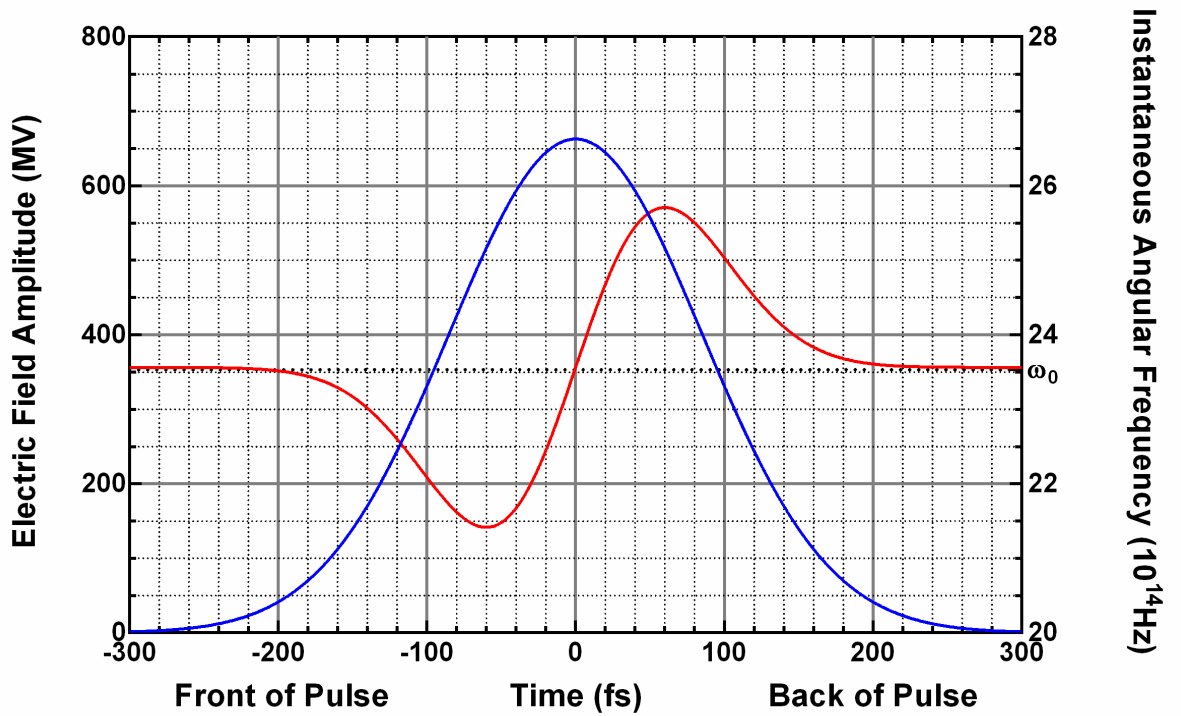


Figure 1.15: The instantaneous frequency (red) of a Gaussian light pulse (blue) with a 200 fs FWHM and 10 nJ energy at 800 nm wavelength contained evenly in a silica fibre with a core radius of 5  $\mu\text{m}$  and a length of 0.1 m. The code can be found in appendix 10.3.3.

### 1.3.3 Cross-Phase Modulation

Cross-Phase Modulation (XPM) occurs with co-propagating beams and is another Kerr effect. In XPM the refractive index seen by the propagating light depends not only on the intensity of the beam itself but any other light also propagating in the same medium at the same time.

$$\mathbf{E}(\mathbf{r}, t) = \mathbf{E}_1(\mathbf{r}, t) + \mathbf{E}_2(\mathbf{r}, t) \quad (1.28)$$

$$\mathbf{E}(\mathbf{r}, t) = \hat{\mathbf{r}} \frac{1}{2} E_1(t) [e^{-i\omega_1 t} + e^{i\omega_1 t}] + \hat{\mathbf{r}} \frac{1}{2} E_2(t) [e^{-i\omega_2 t} + e^{i\omega_2 t}] \quad (1.29)$$

Here the electric field  $\mathbf{E}$  is a combination of two fields polarised in the same direction similar to equation (1.24). By substituting equation (1.29) into (1.19) the nonlinear effects of these two beams can be observed. As the result is quite large,  $E_1(t)$  and  $E_2(t)$  have been written as  $E_1$  and  $E_2$  to neaten the result, however, they are still functions of time.

$$\begin{aligned}
\mathbf{P}_{NL} = \hat{\mathbf{r}} \frac{1}{2^3} \varepsilon_0 \chi^3 & \left[ \{3E_1^3 + 6E_1E_2^2\} \{e^{(-i\omega_1 t)} + e^{(i\omega_1 t)}\} \right. \\
& + \{3E_2^3 + 6E_1^2E_2\} \{e^{(-i\omega_2 t)} + e^{(i\omega_2 t)}\} \\
& + \{E_1^3\} \{e^{(-i3\omega_1 t)} + e^{(i3\omega_1 t)}\} \\
& + \{E_2^3\} \{e^{(-i3\omega_2 t)} + e^{(i3\omega_2 t)}\} \\
& + \{3E_1^2E_2\} \{e^{(-i(2\omega_1+\omega_2)t)} + e^{(i(2\omega_1+\omega_2)t)}\} \\
& + \{3E_1E_2^2\} \{e^{(-i(2\omega_1-\omega_2)t)} + e^{(i(2\omega_1-\omega_2)t)}\} \\
& + \{3E_1E_2^2\} \{e^{(-i(2\omega_2+\omega_1)t)} + e^{(i(2\omega_2+\omega_1)t)}\} \\
& \left. + \{3E_1E_2^2\} \{e^{(-i(2\omega_2-\omega_1)t)} + e^{(i(2\omega_2-\omega_1)t)}\} \right]
\end{aligned} \tag{1.30}$$

The first two lines of this equation show the nonlinear response at the two input frequencies. The remaining lines show responses at altered frequencies with lines three and four indicating third harmonic generation, an effect that requires phase matching and is rarely seen in silica. Lines five and onwards show the effects of four wave mixing and will be discussed further in section 1.3.4. For now the SPM and XPM parts of this equation are:

$$\mathbf{P}_{NL \omega_1}(\hat{\mathbf{r}}, t) = \frac{3}{4} \varepsilon_0 \chi^3 [|E_1|^2 + 2|E_2|^2] \hat{\mathbf{r}} \frac{1}{2} E_1 [e^{(-i\omega_1 t)} + e^{(i\omega_1 t)}] \tag{1.31}$$

or

$$\mathbf{P}_{NL \omega_1}(\hat{\mathbf{r}}, t) = \frac{3}{4} \varepsilon_0 \chi^3 [|E_1|^2 + 2|E_2|^2] \mathbf{E}_1(\hat{\mathbf{r}}, t) \tag{1.32}$$

where (1.31) is taken from line one of (1.30). The same proof can be used for  $\omega_2$  as well as all following equations in this section. The full polarisation density at this frequency can hence be written as

$$\mathbf{P}_{\omega_1}(\hat{\mathbf{r}}, t) = \varepsilon_0 \chi^1 \mathbf{E}_1 + \varepsilon_0 \frac{3}{4} \chi^3 [|E_1|^2 + 2|E_2|^2] \mathbf{E}_1 \tag{1.33}$$

or

$$\mathbf{P}_{\omega_1}(\hat{\mathbf{r}}, t) = \varepsilon_0 \left[ \chi^1 + \frac{3}{4} \chi^3 [|E_1|^2 + 2|E_2|^2] \right] \mathbf{E}_1 \tag{1.34}$$

This is of the same form as (1.14) and as such the term in the brackets can be taken as the perturbed  $\chi$  due to nonlinearities. This can be directly related to the refractive index through (1.16).

$$\tilde{n}^2 = 1 + \chi^1 + \frac{3}{4}\chi^3[|E_1|^2 + 2|E_2|^2] \quad (1.35)$$

so

$$\tilde{n}^2 = n_{eff}^2 \left[ 1 + \frac{3}{4n_{eff}^2}\chi^3[|E_1|^2 + 2|E_2|^2] \right] \quad (1.36)$$

or

$$\tilde{n}(\lambda_0, |E_1|^2, |E_2|^2) \approx n_{eff}(\lambda_0) + n_2[|E_1|^2 + 2|E_2|^2] \quad (1.37)$$

where

$$n_2 = \frac{3}{8n_{eff}(\lambda_0)} Re(\chi_{rrrr}^3) \quad (1.38)$$

Equation (1.37) has been derived knowing that  $1 + \chi^1 = n_{eff}^2$  and the approximation  $\sqrt{1+x} \approx 1 + \frac{x}{2}$  when  $x$  is small. This is valid as the nonlinear refractive index  $n_2$  is generally very small.

$\chi^3$  has been simplified to its real component in the direction of polarisation and again  $n_2$  has been used to simplify the equation as in equation (1.21). Equation (1.37) should appear similar to equation (1.21) but it now defines both SPM and XPM. The SPM comes from the first term in the brackets and is the intensity of the original field itself. The XPM comes from the second term in the brackets and is dependent on the intensity of the second field. For equally intense optical fields of different wavelengths the contribution from XPM is twice as strong as the contribution from SPM. The total phase modulation can now be written as

$$\phi_1(t) = \frac{2\pi}{\lambda_1} xn_{eff}(\lambda_1) + \frac{2\pi}{\lambda_1} xn_2|E_1(t)|^2 + \frac{4\pi}{\lambda_1} xn_2|E_2(t)|^2 - \omega_1 t \quad (1.39)$$

Equation (1.39), which gives the phase modulation in the first electric field, is the same as that in (1.26), however, it now includes the effects of the second electric field. As can be imagined, the resulting instantaneous frequency shift due to XPM can become quite complicated depending on the intensity profiles of the two propagating fields.

$$\tilde{\omega}(t) = -\frac{d\phi(t)}{dt} = \omega_1 + \frac{2\pi}{\lambda_1} xn_2 \frac{d|E_1(t)|^2}{dt} + \frac{4\pi}{\lambda_1} xn_2 \frac{d|E_2(t)|^2}{dt} \quad (1.40)$$

### 1.3.4 Wave Mixing

As noted previously, the expansion for the polarisation density of two co-propagating waves has numerous components as shown in (1.30). The final four lines of this equation show the generation of new frequencies. These have been included below

$$\begin{aligned}
\mathbf{P}_{NL} = \hat{\mathbf{r}} \frac{1}{2^3} \varepsilon_0 \chi^3 & \left[ \{3E_1^2 E_2\} \{e^{(-i(2\omega_1+\omega_2)t)} + e^{i(2\omega_1+\omega_2)t}\} \right. \\
& + \{3E_1^2 E_2\} \{e^{(-i(2\omega_1-\omega_2)t)} + e^{i(2\omega_1-\omega_2)t}\} \\
& + \{3E_1 E_2^2\} \{e^{(-i(2\omega_2+\omega_1)t)} + e^{i(2\omega_2+\omega_1)t}\} \\
& \left. + \{3E_1 E_2^2\} \{e^{(-i(2\omega_2-\omega_1)t)} + e^{i(2\omega_2-\omega_1)t}\} \right] \quad (1.41)
\end{aligned}$$

Clearly these terms show oscillations at four new frequencies,  $2\omega_1 \pm \omega_2$  and  $2\omega_2 \pm \omega_1$ . This is known as four wave mixing. The full four wave mixing requires an expansion of three E field terms and associated frequencies into equation (1.19) and gives rise to the following 16 new generated frequencies  $\omega_g$  excluding third harmonic generation.

$$\omega_g = \omega_1 \pm \omega_2 \pm \omega_3 \quad (1.42)$$

$$\begin{aligned}
\omega_g &= 2\omega_1 \pm \omega_2 \\
&= 2\omega_1 \pm \omega_3 \\
&= 2\omega_2 \pm \omega_1 \\
&= 2\omega_2 \pm \omega_3 \\
&= 2\omega_3 \pm \omega_1 \\
&= 2\omega_3 \pm \omega_2
\end{aligned} \quad (1.43)$$

While these many new frequencies are excited by the nonlinear interaction of the medium, very rarely are such combinations of light generated. The reason for this is that for any of these frequencies to become significantly intense, they must be phase matched with the original frequencies for efficient energy transfer. When the phase of these frequencies is matched, then the generated polarisation oscillations will constructively interfere and produce the new frequency of light. To phase match, the phase constant,  $\beta(\lambda_0)$ , defined in equation (1.11), must be matched with the original and generated frequencies by the mixing equations defined above in (1.42) and (1.43). As the refractive index of silica varies significantly over a large frequency range, as is evident in Figure 1.3, it is usually rare that this occurs, i.e  $\beta_g \neq 2\beta_2 + \beta_3$ .

The cases where phase matching does occur can usually be narrowed down to situations where the system has been engineered to give efficient generation for some wave mixing component, as well as when the original frequencies are close together. For example  $\omega_g = 2\omega_1 - \omega_2 \approx \omega_1$  as long as  $\omega_1 \approx \omega_2$ . In this case the phases are matched as the refractive index is similar for frequencies that are close together.

For systems with intense wavelengths that are close together, four wave mixing may generate the wavelengths in between, smoothing over the gaps in the spectrum.

### 1.3.5 Solitons

Solitons exist for a material such as silica with a positive  $n_2$  within regions of anomalous dispersion (see section 1.1.3) and are specific temporal intensity profiles such that the dispersion from the material and waveguide is equal and opposite to the dispersion from SPM. While it is possible for spatial solitons to exist in fibre, it is temporal solitons that have a significant effect on supercontinuum generation and as such only they will be discussed here.

The solution comes about from solving the Helmholtz equation

$$\nabla^2 E + \tilde{n}(\omega, |E|^2) k_0^2 E = 0 \quad (1.44)$$

where  $\tilde{n}(\omega)$  is the full nonlinear index as described in equation (1.21) written in terms of angular frequency instead of free space wavelength.  $k_0$  is the wavenumber and  $E$  is the electric field similar to equation (1.24) but  $E$  is also dependent on the propagation distance through the fibre  $z$  as shown below.  $\beta_0$  is the phase constant that was first used in (1.11).

$$\mathbf{E}(\mathbf{r}, t) = \hat{\mathbf{r}} \frac{1}{2} E(t, z) [e^{-i(\omega_0 t - \beta_0 z)} + e^{i(\omega_0 t - \beta_0 z)}] \quad (1.45)$$

The full mathematical proof of solitons in optical fibre can be found in other texts [10] and will not be derived here as only the result is important. It is helpful, however, to consider a number of mathematical tricks to simplify the result. As the soliton is travelling at some group velocity  $v_g = c/n_g(\omega_0)$  and only the relative changes, not the full propagation, are important, a time  $T$  can be normalised as a reference moving with the field at the same velocity.

$$T = t - \frac{c}{n_g(\omega_0)} z \quad (1.46)$$

In addition, the following useful relations can be made, creating dimensionless measurements of time and distance  $\tau$  and  $\zeta$ .

$$L_d = \frac{T_0^2}{|\beta_2|} \quad (1.47)$$

$$\tau = \frac{T}{T_0} \quad (1.48)$$

$$\zeta = \frac{z}{L_d} \quad (1.49)$$

$$N^2 = \frac{\gamma P_0 T_0^2}{|\beta_2|} \quad (1.50)$$

Here  $\beta_2$  is the dispersion defined in (1.8),  $\gamma$  is the nonlinearity of the medium (as opposed to the propagation constant in section 1.1.4),  $P_0$  is the peak pulse power and is dependent on the maximum value of  $E(t, z)$  and  $T_0$  is the temporal width.  $N$  is the corresponding order of the soliton and is an integer, giving rise to multiple solutions as shown in equation (1.51).

The Helmholtz equation (1.44) then becomes the normalised Nonlinear Schrödinger Equation (NSE).

$$\frac{1}{2} \frac{\partial^2 E}{\partial \tau^2} + i \frac{\partial E}{\partial \zeta} + N^2 |E|^2 E = 0 \quad (1.51)$$

This equation dictates the balance between dispersion and nonlinearity.

The fundamental soliton when  $N = 1$  is given by

$$E(\tau, \zeta) = \text{sech}(\tau) e^{\frac{i\zeta}{2}} \quad (1.52)$$

This means that for a light pulse with a hyperbolic secant temporal profile and sufficient intensity, the temporal and spectral profile of the pulse will be constant as it travels along the fibre. There are higher order solutions to Equation 1.51, corresponding to

solitons exhibiting a repeating dynamic inverse frequency bandwidth and temporal compression interchange over characteristic spatial lengths. Figure 1.16 shows propagation in units of this characteristic length  $z_{\text{sol}}$  for  $N = 3$ . For positive integer values of  $N$ , the solutions increase in complexity as  $N$  increases as seen in equations 1.53 and 1.54, the solutions for  $N = 2$  and 3 [2,10,11].

$$E(\tau, \zeta) = 4e^{\frac{i\zeta}{2}} \times \frac{\cosh(3\tau) + 3\cosh(\tau)e^{4i\zeta}}{\cosh(4\tau) + 4\cosh(2\tau) + 3\cos(4\zeta)} \quad (1.53)$$

$$E(\tau, \zeta) = 6e^{\frac{i\zeta}{2}} \times \frac{\left[ \cosh(8\tau) + 8\cosh(6\tau)e^{i4\zeta} + (18e^{i4\zeta} + 10e^{i12\zeta})\cosh(4\tau) \right] + (16 + 40e^{i12\zeta})\cosh(2\tau) + 16e^{i12\zeta} + 22.5e^{i8\zeta} + 2.5e^{-i8\zeta}}{\left[ \cosh(9\tau) + 9\cosh(7\tau) + 36\cos(4\zeta)\cosh(5\tau) \right] + (64 + 20\cos(12\zeta))\cosh(3\tau) + (36 + 90\cos(8\zeta))\cosh(\tau)} \quad (1.54)$$

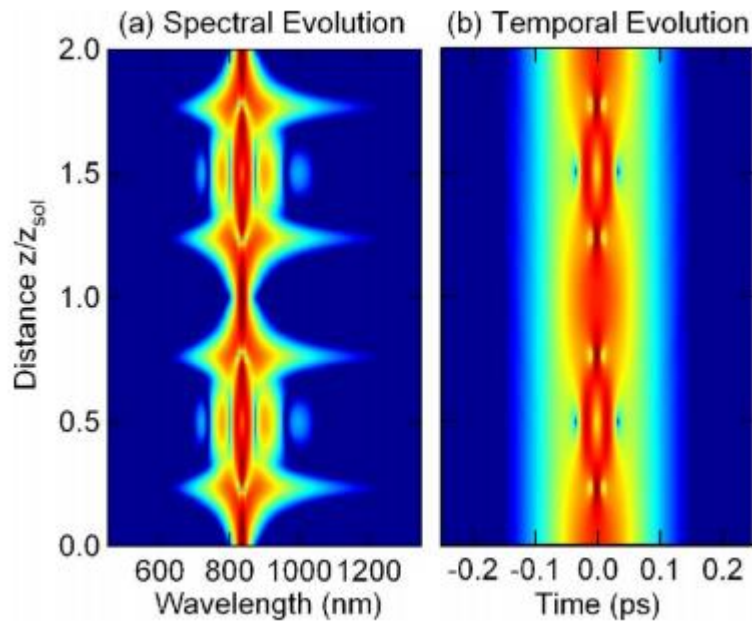


**Figure 1.16: Spectral and temporal evolution of an  $N=3$  or 3<sup>rd</sup> order soliton. [2]**

Solitons are surprisingly robust within optical fibre. As long as the light is propagating in the anomalous dispersion region, any sufficiently intense optical pulse with a temporal and spectral width of the right magnitude will self-phase modulate until it matches the profile of the corresponding  $N^{\text{th}}$  order soliton. The ability of solitons to recover from perturbations decreases as the order is increased. A soliton with order  $N \geq 2$  will often eventually split into  $N$  first order solitons as dispersion and other nonlinear

effects perturb it. First order,  $N = 1$ , solitons are extremely robust and can recover from most perturbations and propagate until their optical power reduces to the point that SPM can no longer efficiently occur.

### 1.3.6 Stimulated Raman Scattering

Within the silica medium, molecular vibrational modes exist with resonant absorption frequencies much lower than that of the light traveling through. A nonlinear scattering process involving the vibrational energy levels of the medium will result in the generation of new frequencies. This effect, known as Raman scattering, is most prominent at higher intensities where more photons can excite an electron to a short lived quantum virtual state. The relaxation of this electron can emit a photon with a different frequency depending on the energy state it relaxes to as shown in Figure 1.17.

The process can be described as a photon with energy  $\hbar\omega_p$  scattering from a molecule at a lower energy  $\hbar\omega_s$  while the molecule makes the transition into a vibrational state with energy  $\hbar\omega_v$ .

$$\hbar\omega_p = \hbar\omega_s + \hbar\omega_v \quad (1.55)$$

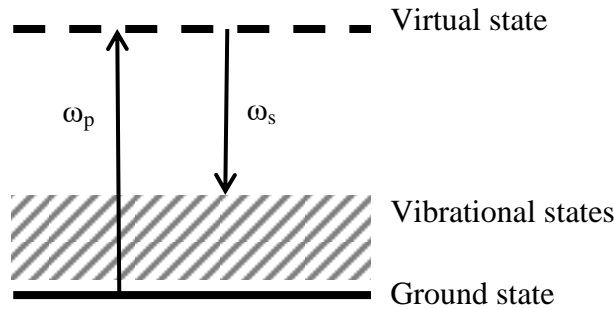


**Figure 1.17: Raman scattering showing electron transfer to a short lived virtual state and back to a molecular vibrational state.**

The above process generates a photon with lower frequency – a so-called Stokes shift. However it is possible for the opposite to occur, where an electron from a vibrational state is excited and relaxes back to the ground state, resulting in an increase in frequency known as an anti-Stokes shift. Generally, the anti-Stokes scattering is less efficient as most electrons are not in higher vibrational states.

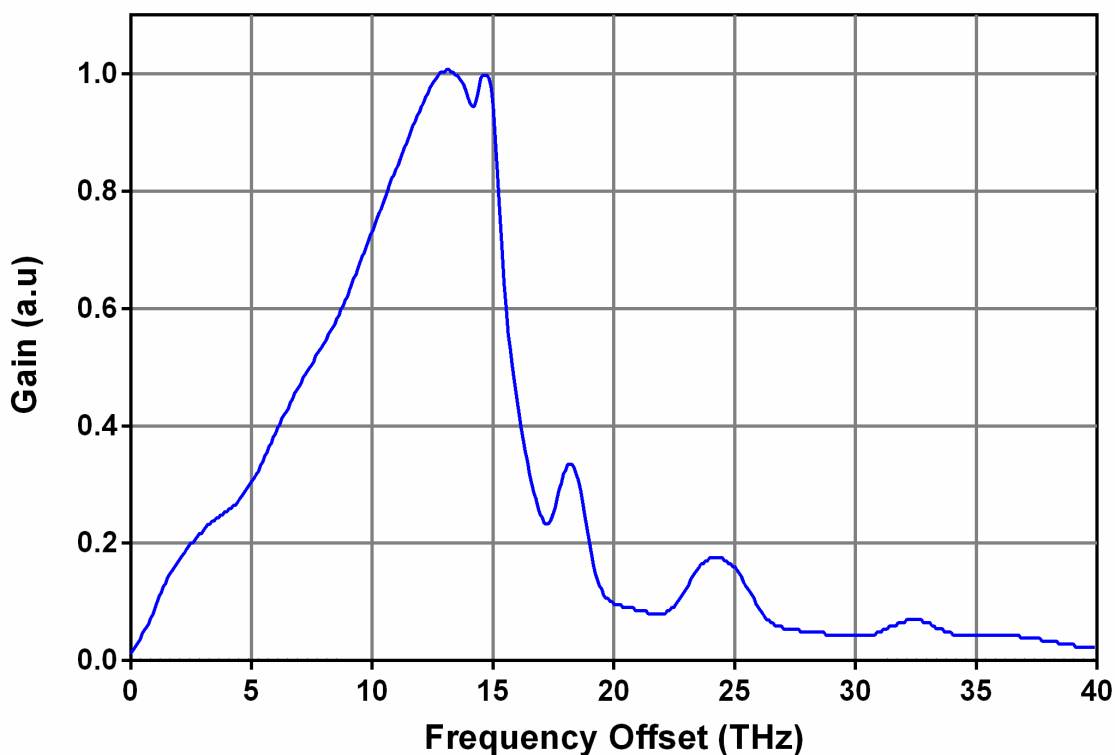


**Figure 1.18: Raman gain for fused silica [12]. This curve is related to the density of vibrational states of the molecule within the glass host.**

The Raman scattering of high intensity radiation in fused silica can generate coherent gain via stimulated emission from the virtual state. This effect is used at telecommunication wavelengths in optical fibres where energy pumped into the fibre at a frequency 13 THz higher, or  $\sim 90$  nm lower in wavelength, than the 1550 nm signal wavelength, provides amplification by stimulated emission of the Raman scatter. The Raman gain profile for the glassy silica relative to the propagating frequency is shown in Figure 1.18.

This coherent Raman gain is important when observing solitons. Due to the intensity of optical solitons and their broad frequency width, an interesting effect is observed where the higher frequency light in the soliton itself creates a Raman gain that the lower frequencies extract as increased power. This effect does not destroy the soliton, as they are remarkably stable against small perturbations, however, the whole soliton effectively moves to a lower frequency [13,14]. This is known as soliton self-frequency shift or Raman shifting, as the “blue” end light is absorbed and the gain enhances the “red” end. The speed of the shift to lower frequencies is dependent on the intensity of the soliton, where higher intensity solitons have an increased Raman gain and therefore

a faster shift. In silica, as the soliton loses power due to attenuation, the shift will slow and will become negligible before the pulse loses enough power to maintain its solitonic nature.

## 1.4 Supercontinuum

This section forms a literature review on supercontinuum generation discussing the articles relevant to this thesis as well as a general overview of the area.

### 1.4.1 Discovery and History

The invention of the laser and subsequent mode locking and pulse generation techniques in the 1960s expanded the world of optics to include the nonlinear effects described in section 1.3. These nonlinear effects were first observed in bulk materials and liquids, however, with the improvements to optical fibres that followed, these effects were soon observed within these waveguides. It was by using these effects that the first nonlinear broadband light sources were generated, first in bulk and then in fibre [15,16]. These results, while interesting, pale in comparison to the spectral broadening that was to be discovered.

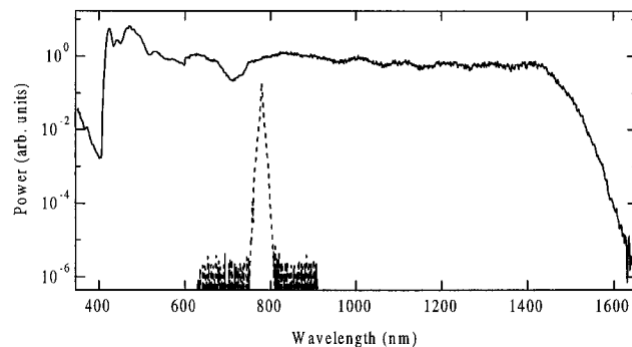


**Figure 1.19: First recorded supercontinuum in MOF. Input bandwidth is shown dashed [1].**

In 1999, Ranka et al. generated what was coined the first supercontinuum using a titanium sapphire laser and a length of MOF [1]. At this time, MOFs were a new field of study with endlessly single mode fibres and photonic band gap guiding [7,8] only being created in 1996.

The customisability of MOF allowed for enhanced modal confinement of light resulting in higher nonlinearity as well as control of the fibre dispersion, allowing anomalous dispersion and solitons from a wide range of sources not possible in bulk materials or

standard waveguides. The ability for these strongly nonlinear fibres to generate octaves of light was novel and impressive and this was the beginning of a new field of study in what became known as supercontinuum generation.

### ***1.4.2 The Supercontinuum***

The supercontinuum quickly became a principal field of study in nonlinear optics. One half of the Nobel prize in physics, 2005, was given to Hall and Hänsch for their contributions to the development of laser-based precision spectroscopy, including the optical frequency comb technique that primarily uses a supercontinuum [17–19]. This is an indication of the popularity of this field and especially the speed at which it expanded.

As easy as it was for supercontinua to be generated once discovered, it was much harder to understand the underlying physical processes that generated such broad sources of light. It is difficult to isolate the individual processes that contribute to the spectrum, as the wide range of inputs and outputs lead to complex structures and therefore difficulty isolating the relative contributions of the relevant nonlinear processes [2].

The key component to understanding these supercontinua has been the utilisation of numerical modelling. The most common situation of femtosecond regime pumping in the anomalous dispersion regime of the waveguide, generating the widest and most interesting continua, is examined here.

When an input pulse of light, with a high peak power, short temporal duration, and a wavelength within the anomalous dispersion regime enters a MOF it will generate a supercontinuum. Initially the pulse will compress temporally, due to self-phase modulation, and will quickly generate a soliton. The strong intensity of light will also generate corresponding Stokes and anti-Stokes Raman peaks on either side of the input pulse.

To fully understand the generation of this light it is important to have a good understanding of all the physics previously discussed in this chapter. Additionally, it is very helpful to make use of numerical simulation to highlight the effects under discussion.

### ***1.4.3 Soliton Formation and Fission***

Figure 1.20 shows that the initial stage of pulse injection and propagation within the first few millimetres results in extreme spectral broadening that is relatively symmetrical around the input, and is coupled with a temporal compression. However, this simple broadening quickly becomes asymmetric with unique spectral peaks appearing. This early asymmetrical broadening is attributed to a process known as soliton fission. This was alluded to in section 1.3.4 but will be explained in more detail here.

The soliton with an order of  $N$  above 1 will form, assuming sufficient input power, however, this soliton will rarely get to complete a full cycle due to the external perturbations such as Raman scattering and fibre imperfections. As such, the soliton will begin to shed fundamental order ( $N=1$ ) solitons that are much more stable with their less complex evolution. It is usually assumed that by the end of the initial broadening process a  $N^{\text{th}}$  order soliton will have split into  $N$  fundamental solitons with varying power.

### ***1.4.4 Soliton Self-Raman Shift***

Fundamental solitons undergo self-Raman scattering and shift to longer wavelengths via Raman gain as outlined in 1.3.6. The first  $N=1$  soliton to fission off has sufficient intensity and spectral width so that the “blue” higher frequency component provides coherent Raman gain to, and thus increases the intensity of, the lower frequency “red” end of the spectrum. As this process is dependent on both intensity and spectral width, the stronger solitons will self-shift to the “red” end spectrally at a greater rate, as evident in Figure 1.20 below. With the shift to longer wavelengths, the solitons’ propagation constants decrease, due to a lower group velocity, and hence the solitons begin to lag behind the rest of the continuum pulse that is propagating along the fibre.

A typical laser pump wavelength in the anomalous dispersion regime of a MOF is 800 nm and the resultant supercontinuum may extend to 1600 nm with this extreme broadening of the supercontinuum spectrum attributed to this Raman shift of soliton light.

### 1.4.5 Dispersive Wave

It should be apparent at this point that a significant amount of light is generated on the short wavelength side of the pump, often in the normal dispersion regime. The creation of this light is due to perturbation of solitons by third and higher orders of dispersion [10]. This radiation had been called Cherenkov radiation [20], nonsolitonic radiation, or dispersive wave generation. This light is emitted at a frequency where the propagation constant matches that of the soliton.

Similar to equation (1.25) the phase shift of the soliton radiation and the dispersive wave may be expressed in terms of propagation factors. The two phases at distance  $x$  after delay  $t = x/v_g$  are given by

$$\phi_D = \beta(\omega_D)x - \omega_D \frac{x}{v_g} \quad (1.56)$$

$$\phi_S = \beta(\omega_S)x - \omega_S \frac{x}{v_g} + \frac{1}{2}\gamma P_S x \quad (1.57)$$

where  $\omega_D$  and  $\omega_S$  are the dispersive wave and soliton frequencies and  $v_g$  is the group velocity of the soliton [10]. The last term in equation (1.57) is due to the nonlinear refraction of the soliton after the fission process (this is not easily measured experimentally).

The dispersive wave is generated at  $\omega_D$  such that  $\phi_D = \phi_S$ . By taking a Taylor series expansion of  $\beta$  around  $\omega_S$  (as discussed in appendix 10.1) this can be simplified as

$$\phi_S = \beta_0 x + \beta_1 x(\omega_D - \omega_S) + \frac{\beta_2}{2} x(\omega_D - \omega_S)^2 + \dots - \omega_D \frac{x}{v_g} \quad (1.58)$$

so

$$\begin{aligned} & \beta(\omega_S) - \frac{\omega_S}{v_g} + \frac{1}{2}\gamma P_S \\ &= \beta(\omega_S) + \frac{1}{v_g}(\omega_D - \omega_S) + \frac{\beta_2}{2}(\omega_D - \omega_S)^2 + \dots - \frac{\omega_D}{v_g} \end{aligned} \quad (1.59)$$

Rearranging

$$\beta(\omega_D) - \beta(\omega_S) + \frac{\omega_D}{v_g} - \frac{\omega_S}{v_g} - \frac{1}{v_g}(\omega_D - \omega_S) + \frac{1}{2}\gamma P_S \quad (1.60)$$

$$= \frac{\beta_2}{2}x(\omega_D - \omega_S)^2 + \dots$$

Cancelling terms

$$\frac{1}{2}\gamma P_S = \frac{\beta_2}{2}x(\omega_D - \omega_S)^2 + \dots \quad (1.61)$$

Finally

$$\sum_{m \geq 2}^{\infty} \frac{\beta_m(\omega_S)}{m!}(\omega_D - \omega_S)^m = \frac{1}{2}\gamma P_S \quad (1.62)$$

This general form accounts for infinite orders of perturbation. As a simple example, equation (1.63) shows the simple solution where  $\beta_2 > 0$  and only the second order is considered

$$\omega_D = \sqrt{\frac{\gamma P_S}{\beta_2}} + \omega_S \quad (1.63)$$

It should be noted that, as the soliton undergoes self-Raman shift,  $\omega_S$  changes and hence the Taylor series is expanded around a different point, changing all  $\beta_m$  coefficients.

Figure 1.20 shows an example of a dispersive wave generated in MOF using a simplified simulation to exaggerate the effect without interference from other nonlinear phenomena.

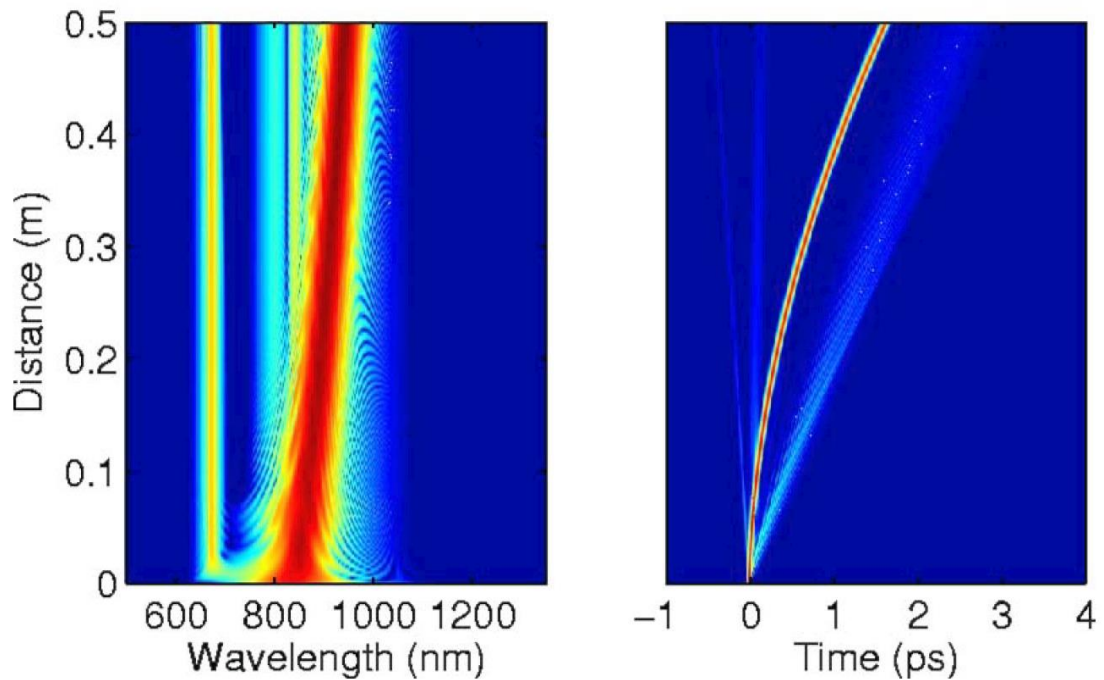


**Figure 1.20: Numerical simulation of dispersive wave generated from a soliton undergoing self-Raman shift [2].**

This process generates light of different wavelengths and accounts for the shift to longer “red” wavelengths. The generation of “blue” shifted light is discussed in the next section.

#### **1.4.6 Gravity-like Trapping**

How is the dispersive wave affected by the NIR solitons after it is generated? The light generated on the normal side of the MOF dispersion curve, while having been affected by standard nonlinear effects, cannot form a soliton as the normal dispersion is unable to be balanced by self-phase modulation. *The light, however, still appears to shift to shorter wavelengths.* This is due to a kind of cross phase modulation and has been the subject of significant debate in the past few years. Solitons in the anomalous dispersion regime create a wall that decreases in speed as the soliton shifts to longer wavelengths through self-Raman shift and the group index of the guiding mode increases. Any blue light that was travelling behind the soliton at a similar group index will be scattered from the interface and will be continually pushed to shorter wavelengths as the blue light cannot overcome the barrier potential created by the soliton [21–23].

As a result, the spread of the continuum light can be seen to be symmetrical around the group index of the EM mode in which the continuum is generated.

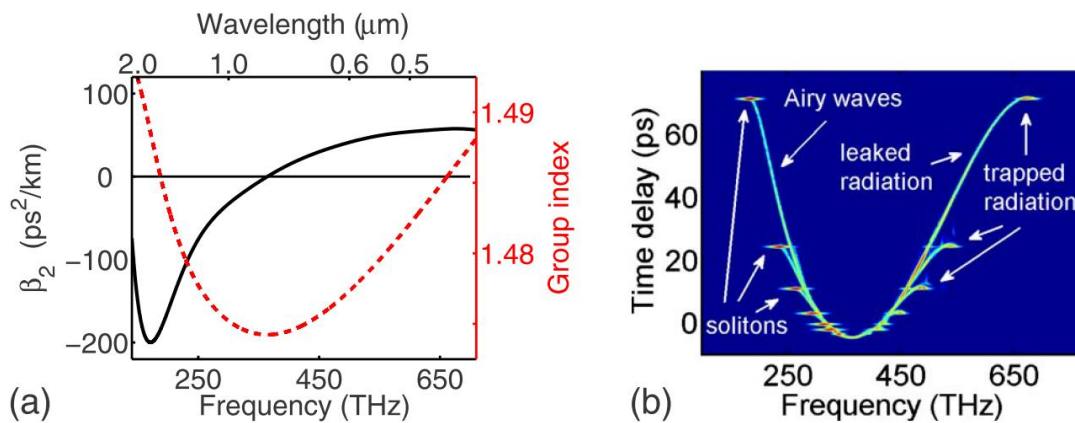


**Figure 1.21: Numerical simulation (b) showing the effects between the dispersive wave and solitons in a typical MOF(a) after 1.5m of propagation with a 850 nm input pump [23].**

Figure 1.21 shows this effect clearly in simulation. On the low frequency side, solitons have formed and are shifting to lower frequencies. At higher frequencies but matched in time are corresponding wave packets that have been shifted to increasing frequencies. As these interactions are dictated by the speed that the soliton is travelling, both the NIR and blue light must have matched group velocities.

Such effects have been reported as early as 1987, particularly in some amazing work by Beaud et al [24] using standard telecommunications fibre of the period. Figure 1.22 and Figure 1.23 reproduce figures from that paper where there is a clear observation of the group velocity matching between red and blue light, where Beaud had ascribed the source of the blue to anti-Stokes scattering. The extent of this shift depends on both the distance travelled through the fibre and the initial input power. This arises from the rate of the soliton self-frequency shift since higher intensity solitons will have a greater Raman gain and shift in frequency more in the same spatial distance along the fibre compared to lower intensity solitons. In addition, the greater the interaction time, the further the soliton will shift, until the power is attenuated to a point where the Raman gain becomes insignificant.

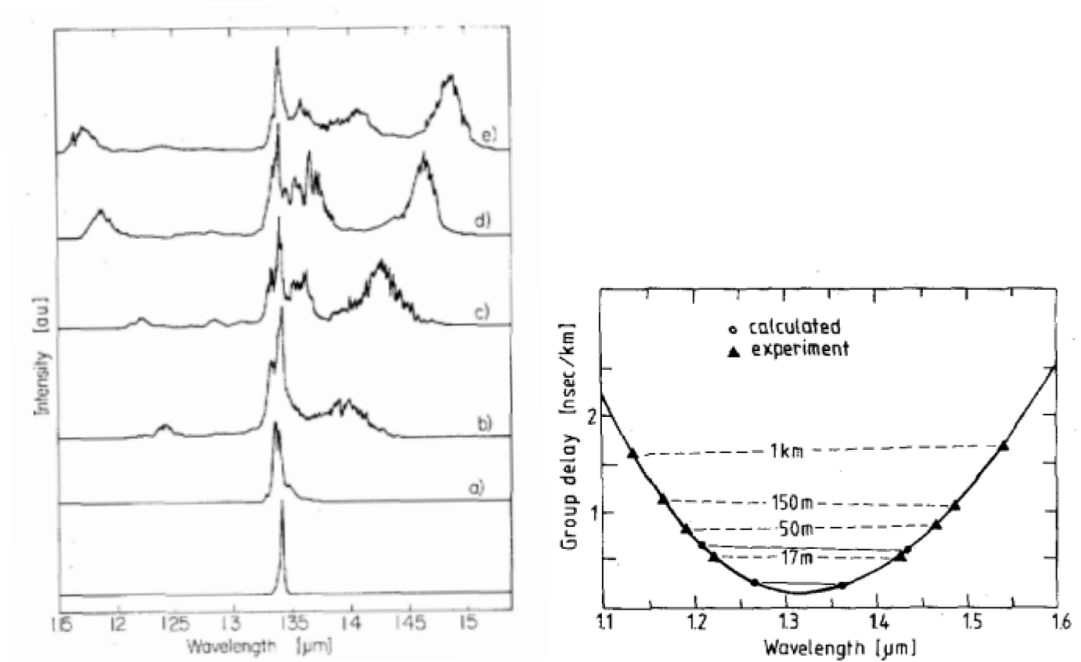


Figure 1.22: Early reports of group index matching between Stokes and anti-Stokes pulses at varying lengths in fibre, (a) 6 m, (b) 12 m, (c) 17 m, (d) 50 m and (e) 150 m [24].

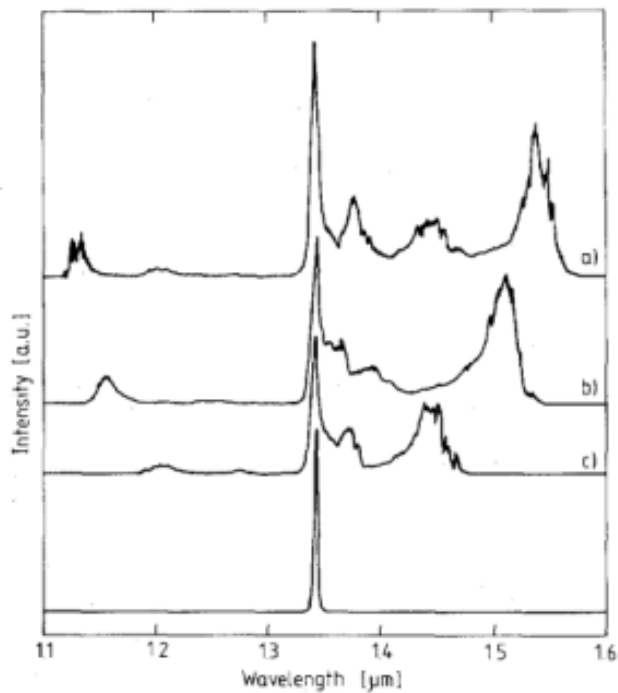
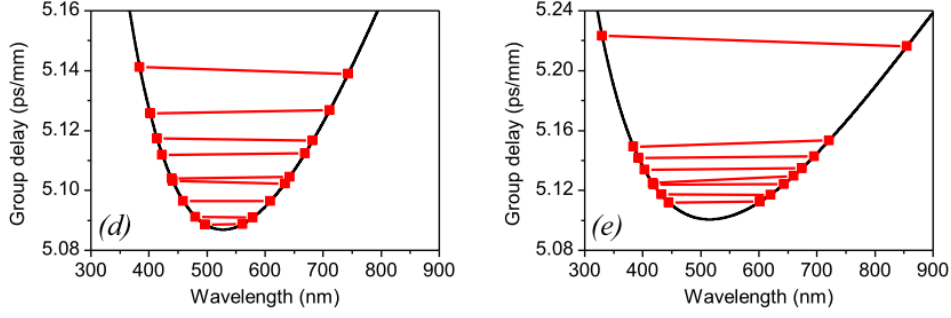


Figure 1.23: Frequency spectra of light propagating through 1km of fibre with input powers of (a) 530 W, (b) 350 W, and (c) 175 W.

Chen et al [25] was one of the first groups to start applying this work to the gravity-like trapping of dispersive waves and solitons discussed shown in Figure 1.24. This work looked at the edges of the generated supercontinuum and matched the limits to the group delay.



**Figure 1.24: Group delay matching of continuum edges [25].**

### 1.4.7 Four Wave Mixing

As discussed in section 1.3.4, four wave mixing will only occur between closely spaced waves, as there is no phase matching between distant wavelengths in the waveguide. Relevant to the continuum generation, light frequencies generated are of high intensity and spectrally close so that phase is closely matched and wave mixing can occur. This has the effect of smoothing out the continuum of generated peaks, yielding a continuous spectrum with no gaps. That said, most reported supercontinua are plotted on a log intensity axis and give the impression of a uniform flat intensity, which is certainly not true.

### 1.4.8 Numerical Simulation

The scale of supercontinuum generation does not lend itself well to standard finite difference simulations. The size of the fibre and the small pixels needed to meet the Nyquist frequency condition for the short wavelengths of light mean that simulations of MOF take large amounts of memory and computation time.

The propagation of light can be modelled with the following equation that is a time domain generalised nonlinear Schrödinger equation

$$\begin{aligned}
 \frac{\partial A}{\partial z} + \frac{\alpha}{2}A - \sum_{k>1} \frac{i^{k+1}}{k!} \beta_k \frac{\partial^k A}{\partial T^k} & \quad (1.64) \\
 & = i\gamma \left( 1 + i\tau_{shock} \frac{\partial}{\partial T} \right) \\
 & \times \left( A(z, t) \int_{-\infty}^{+\infty} R(T') |A(z, T - T')|^2 dT' \right)
 \end{aligned}$$

An input pulse is defined by a complex temporal profile  $A(z, t)$  such that the Fourier transform gives the spectral profile  $\tilde{A}(z, \omega - \omega_0)$ . The full derivation and variable list for equation (1.64) is available in Chapter 3 of Dudley and Taylor (2010) [26].

$A(z, t)$  is determined as a function of position in the fibre by evaluating spectral effects over a small length step, then performing an inverse Fourier transform and then applying spectral effects over a small time step. When solving this, useful plots similar to the spectrogram in Figure 1.25 may be generated, where the wavelength intensity and the time offset are shown as a function of the propagation distance through the fibre. The split step Fourier method has become the de facto simulation method in supercontinuum generation as it allows a quasi one dimensional approach to the pulse propagation simulation.

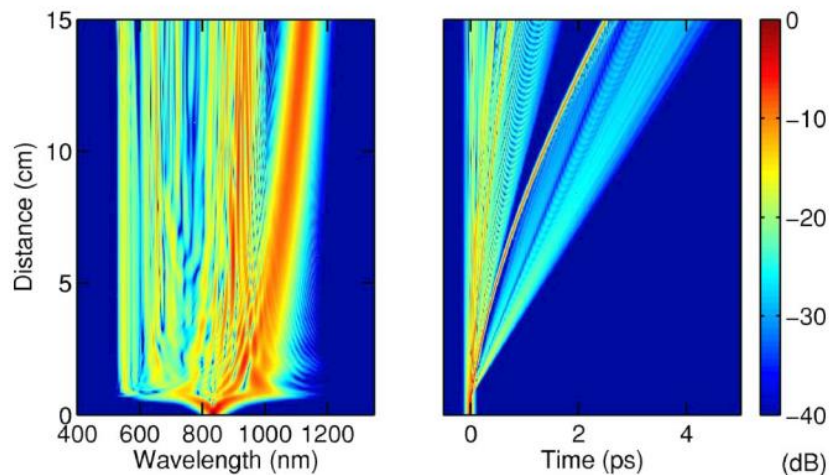


**Figure 1.25: Numerical simulation of supercontinuum generation in MOF. The scale is log normalised to the peak power [2].**

These simulations are very useful as they allow measurements of the temporal and spectral evolution of the pulse within the MOF to be compared to the theory. It is from these results that many of the ideas already discussed were created.

### ***1.5 Supercontinuum in Higher Order EM Modes***

While there is a large body of literature for supercontinuum generation as discussed in 1.4.2, these papers will usually only consider the supercontinuum propagating in the fundamental EM mode of the MOF. This thesis is part of an investigation into the effects of generating supercontinuum within the Higher Order EM Modes (HOM) of optical fibre. This section will detail the current literature on this subject.

A significantly important paper in this field by Guobin et al [9] actually has no mention of supercontinuum generation but instead details the EM modes of microstructured optical fibre. The full details and examples of this can be seen in sections 1.2 and 3.

### 1.5.1 Initial Research

One of the earliest investigations into the higher order EM modes was the work published by Duck et al [27] that showed interesting effects of the mode field output of MOF and how it affected the output wavelengths by varying the coupling into the MOF and changing the mode. In addition, they showed that, once higher order modes are excited, different wavelengths will appear to have varying orientations, as shown in Figure 1.26

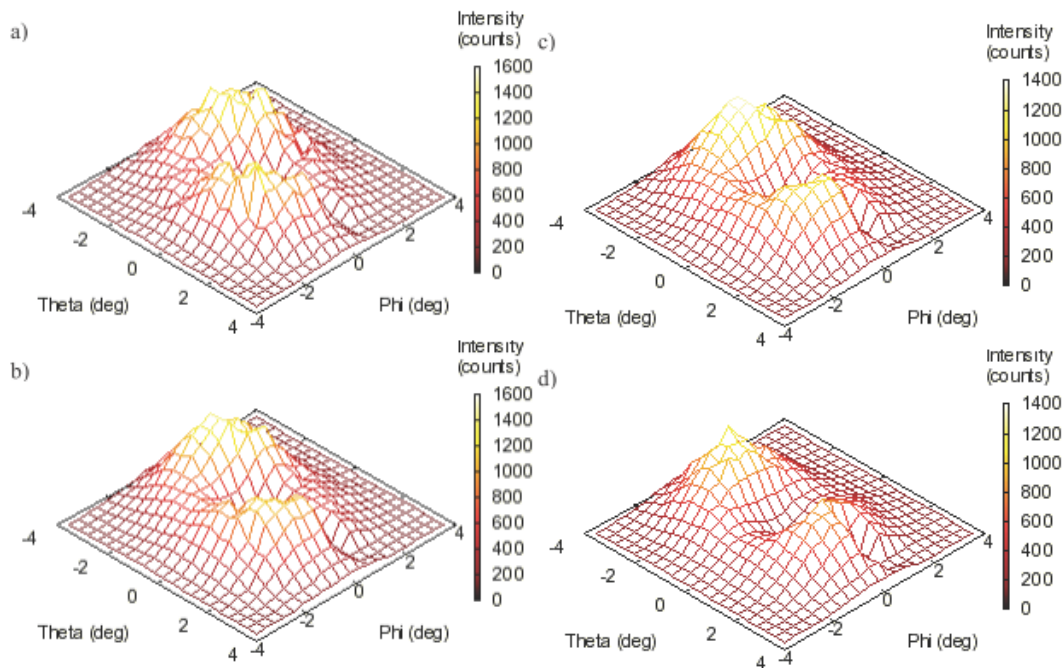


**Figure 1.26: Figure 4 taken from Duck et al [27] showing spatial intensity data at a) 512 nm, b) 515 nm, c) 517 nm, and d) 520 nm.**

While the experimental work in higher order mode excitation was only just beginning, simulations of the waveguide properties of MOF had been well researched [9] showing that for the most part MOF was an index guiding fibre where the modes resembled the traditional circular fibre modes shown in section 1.1.4, only with a slight energetic separation between degenerate modes. These early papers are notable for some of their initial findings showing extended UV generation [28] and the ability to manipulate the waveguide parameters by utilising the varying dispersion in higher order modes [29].



**Figure 1.27: Far field image of MOF supercontinuum generated UV light, clearly in a high order mode [28].**

### ***1.5.2 Current Research***

In the following years, a small number of groups investigated the effect of higher order modes in MOF with relation to supercontinuum generation.

Cherif et al [30,31] performed a number of experiments and simulations investigating the dispersion properties of various modes and the ability of such modes to modify the supercontinuum wavelength range.

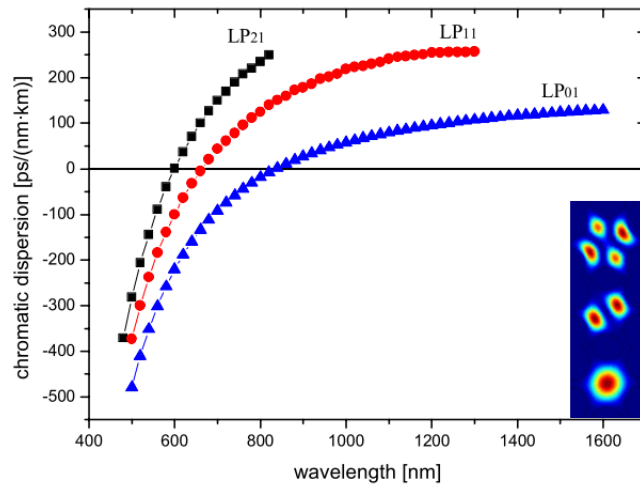


Figure 1.28: Numerically calculated dispersion curves for numerous MOF modes [31].

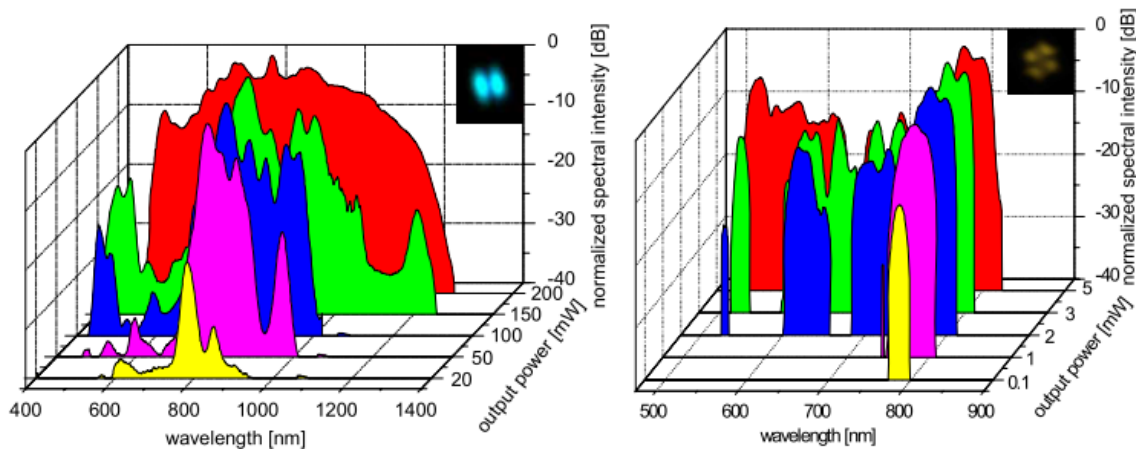
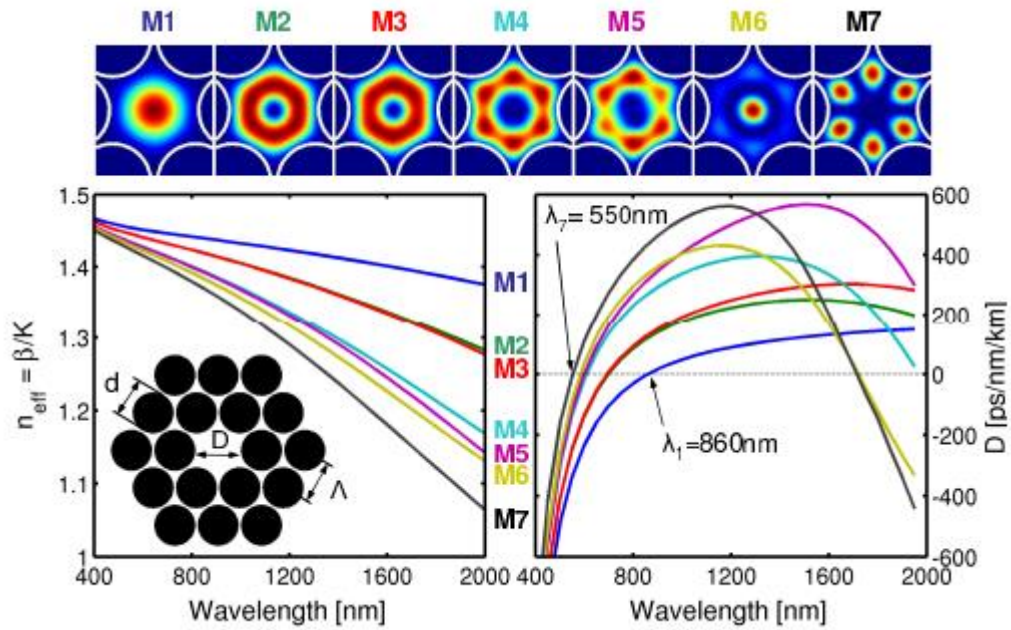


Figure 1.29: Experimental supercontinuum generated in various fibre modes shown in Figure 1.28 [31].

The variations in dispersion shown in Figure 1.28 appear to significantly modify the spectral content of the supercontinuum shown in Figure 1.29. Clearly the propagating mode of the continuum was having significant effects on the spectral generation and, as with most other supercontinuum generation research, numerical simulation serves as one of the easiest ways to understand the effects within the MOF.

Poletti and Horak [32] also performed such numerical simulations of pulse propagation in the first seven modes of MOF as shown below.



**Figure 1.30: Mode fields with effective index and dispersion calculated for a pitch of  $2.7 \mu\text{m}$  and a hole diameter of  $2.5 \mu\text{m}$  [32].**

It should be noted that this paper calculates different infrared cut-off points than Cherif et al [31], but is consistent with the findings of this thesis in stating that the EM modes of MOF will continue to propagate well into the infrared, as the strong index step in the MOF means that the effective index needs to fall to approximately one before the mode is no longer guided. In essence, the mode will not be guided when the mode field is sufficiently large that the critical irradiance for soliton propagation is not met. This limit is not well defined for microstructured optical fibres in comparison to circular cross section step-index optical fibres, which have hard, and easily experimentally measurable, cut-off frequencies for the propagating modes.

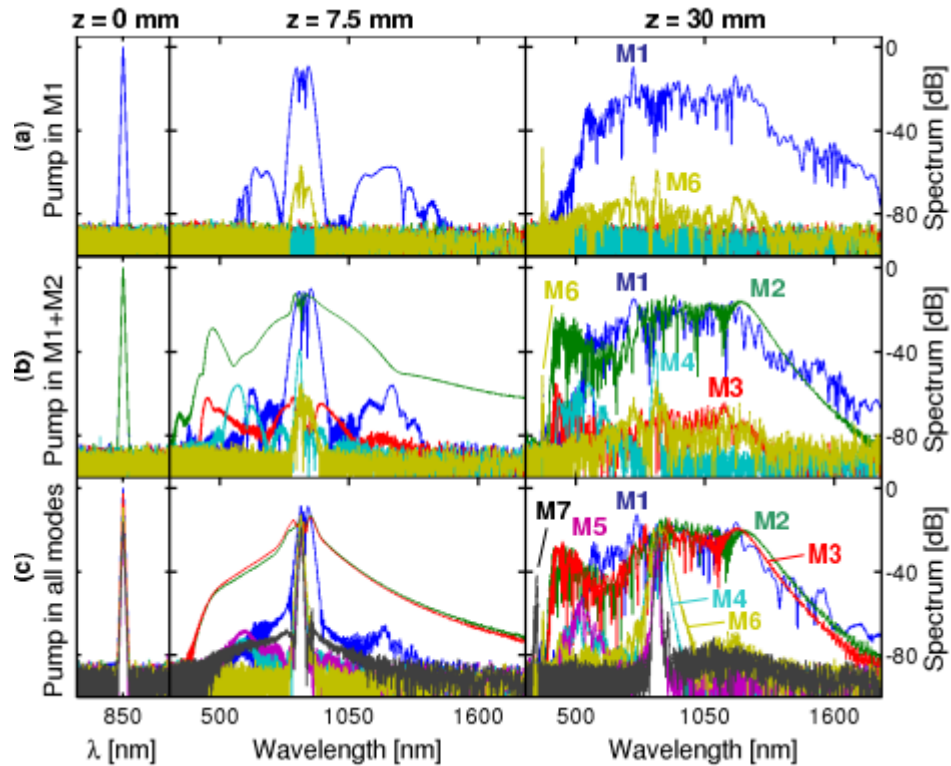


**Figure 1.31:** Numerical simulations of light traveling through the fibre shown in Figure 1.30. Here the input pulse has been injected into various EM modes and the resulting output of each mode shown overlaid [32].

The numerical simulations shown in Figure 1.31 for various inputs into the fibre shown in Figure 1.30 predict the results of intermodal wave mixing through four wave mixing and intermodal cross phase modulation. Of specific interest is the top right panel of Figure 1.31, where the shortest wavelengths appear to be generated from what appears to be a dispersive wave in the M6 mode even when the pump is coupled entirely into the M1 mode. This result indicates that, in many cases where the experimentalist has assumed only the fundamental mode is contributing to the continuum, the shorter wavelengths may have been generated in higher order EM modes where the dispersion parameters are more conducive to making shorter wavelengths of light.

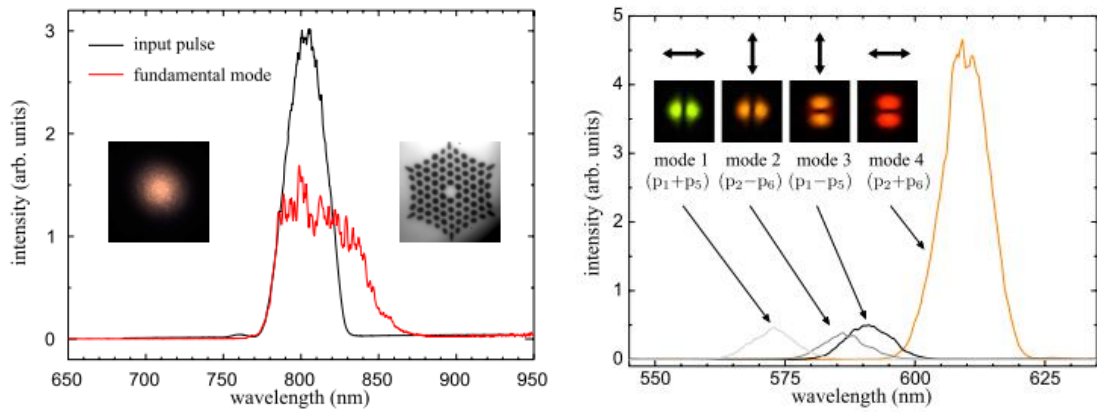


**Figure 1.32: Left shows the input pulse of 50 fs and the resulting spectrum spread generated from propagating through the fundamental mode of the MOF. Right shows the dispersive waves generated in numerous higher order EM modes. Here the variations in wavelength due to mode are clearly seen [33].**

This was further investigated experimentally by Karasawa and Tada [33] who looked at dispersive wave wavelengths of various modes shown in Figure 1.32 and showed that different modes generate different wavelengths.

### 1.5.3 The Scope of this Thesis

It is clear that a number of factors contribute to changing the output of the continuum, all of which are primarily related to the change in guiding index due to higher order EM modes. The need to correlate more information about the supercontinuum, particularly the spectral emission with the spatial structure of the modes in order to definitively explain the physics behind the spectral features was discerned.

The research effort was then directed to developing a new controllable spatio-spectral mapping technique, subsequently published by Legge et al [34,35]. An example of the output spatio-spectral map is shown in Figure 1.33, where spectral features have the spatial mode at that wavelength correlated.

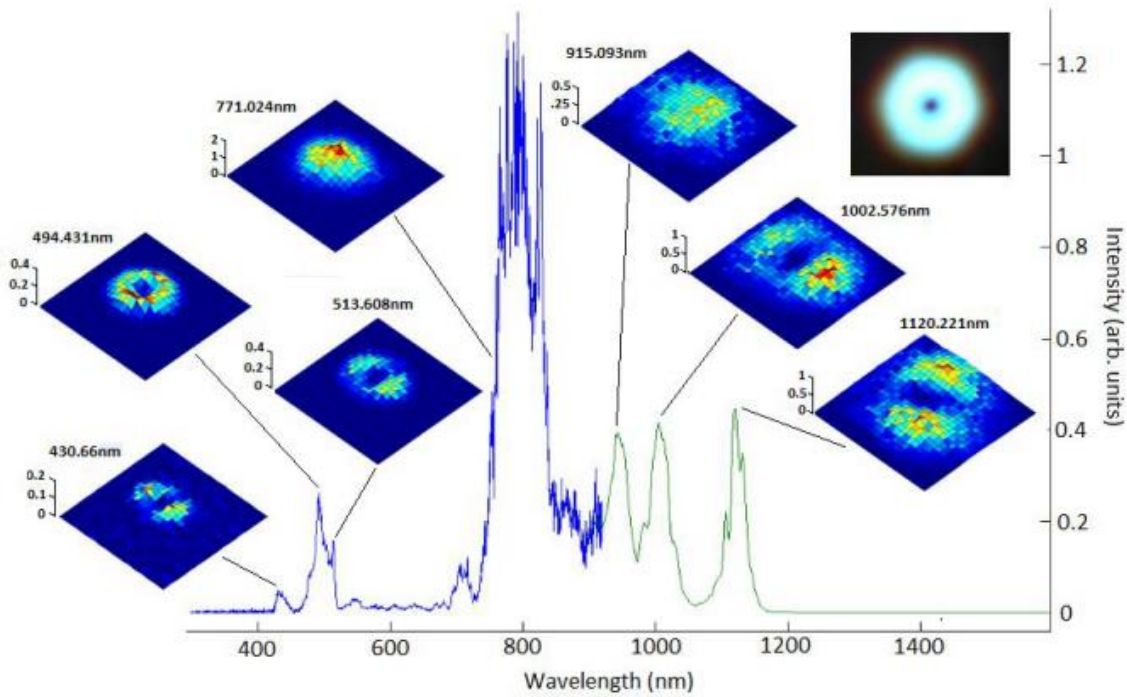


**Figure 1.33: Spectral mode scan of a supercontinuum. Visible image of fibre output shown top right [35].**

The investigation of dispersive wave trapping is especially evident in the higher order modes of MOF where the varying guiding index creates significant changes in the group index. This leads to the seemingly contradictory term of a sparse supercontinuum where the lower power coupling into HOMs can efficiently generate dispersive waves and solitons without creating the broad spectrum spread that usually hides these individual features as shown in Figure 1.34 [36–38].

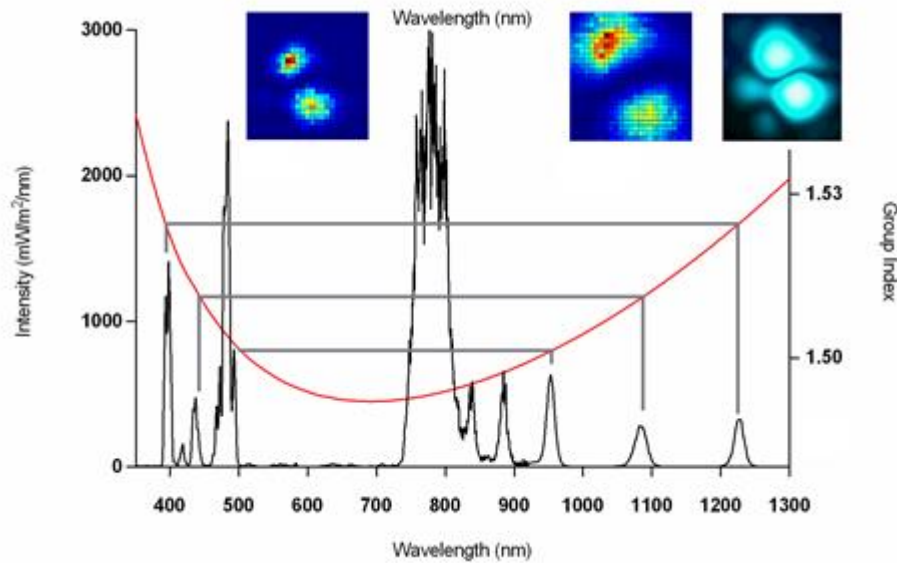


**Figure 1.34: Sparse continuum generated in MOF [37].**

This thesis explores all the discussed concepts of supercontinuum generation in multimode MOF. Chapter 2 details the experimental setup and the initial calibrations and measurements required to begin this work. Knowing that the dispersion of each mode is critical to the generation of supercontinua, Chapter 3 fully characterises the guiding index and vector solutions to EM modes propagating in the MOF through numerical simulation.

Chapter 4 takes the initial observations of this experimental data and explores the results. Before this work, the exact spatial and spectral output of the supercontinuum had only been either qualitatively observed or measured using limited apparatus that distorted the results as shown in section 1.5.2. The resulting clarity of the data lends to the theory of splitting of degenerate EM modes into the six fold symmetry of the hexagonal MOF and the associated energy with each mode.

Chapter 5 illuminates the recent theories on gravity like trapping of dispersive waves in MOF as discussed in section 1.4.6. Previously no direct measurement of this effect is observed in a supercontinuum as the spectral broadening occludes the individual effects. Through the generation of a sparse supercontinuum using higher order EM modes, this effect can be observed directly in the MOF from a standard Ti:S laser source.

Chapter 6 further explores the mode field output of the MOF by analysing the polarisation of the generated supercontinuum. It was found that by using a linear polariser, all modes simulated in Chapter 3 could be identified.

## ***2 Experimental***

This chapter details the general procedure and common equipment used throughout this thesis. It gives a solid overview of all experimental processes. This information is expanded upon for specific cases in later chapters.

The following equipment is used to selectively couple the pump laser into HOMs of MOF for long periods of time, generate nonlinear effects within the MOF, and measure the spectral and spatial structure of the far field output of the MOF.

### ***2.1 Ultrafast Lasers***

High intensity light is required to study nonlinear effects and supercontinuum generation. Ultra-fast pulsed lasers meet this requirement by compressing their output into a short pulse of the order of 100 femtoseconds. The titanium sapphire laser is one of the most common and most versatile ways to generate this light.

#### ***2.1.1 Titanium-Sapphire Laser***

The laser used in this thesis is a Spectra Physics Tsunami Titanium Sapphire (Ti:S) laser with a  $\text{Ti}^{3+}:\text{Al}_2\text{O}_3$  gain crystal. This is pumped by a Spectra Physics Millennium system consisting of a 808 nm diode array pumping a neodymium-doped yttrium vanadate ( $\text{Nd}:\text{YVO}_4$ ) glass host substrate contained in a cavity with a KTP intracavity frequency doubler. This system provides up to 10 W of 532 nm continuous wave (CW) light to excite the Ti:S crystal.

The main Ti:S cavity is a system of 10 mirrors, 4 prisms and an Acousto-Optic Modulator (AOM) mounted on a central Invar bar. The optical layout for this cavity can be seen in Figure 2.1. The prisms create a chirp free cavity by compensating for the dispersion of the prisms themselves and the Ti:S crystal and also allow tuning of the laser wavelength across the gain bandwidth of the crystal by using a physical tuning slit between the prism pairs where the light is dispersed spatially in the vertical plane.

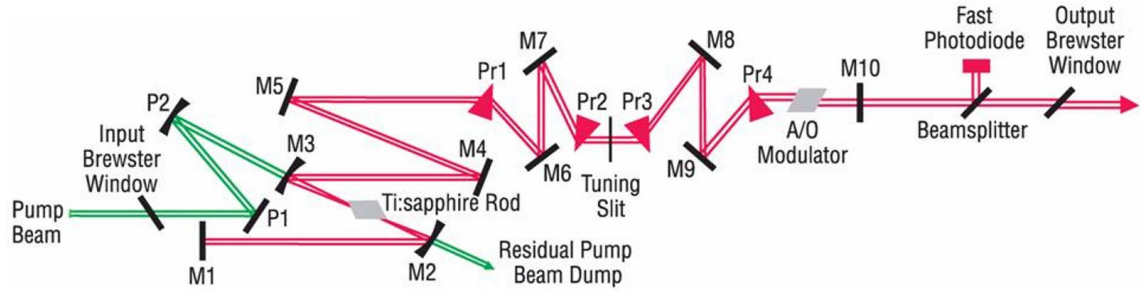


**Figure 2.1: Cavity of Spectra Physics Ti:S mode locked laser [39].**

The gain bandwidth of Ti:S is wide, ranging from 650 nm – 1100 nm, however, the set of optics used in the cavity restricted this bandwidth to 700 nm – 900 nm with a maximum laser efficiency at 800 nm.

The laser operates in a pulsed state by mode locking, i.e., by creating a fixed phase relationship between many thousands of the longitudinal cavity modes within the laser, the phase locked modes sum coherently to generate a temporally short pulse. The Ti:S cavity combines two methods to achieve this mode locking. The first is inherent to the Ti:S crystal, small transient vibrations can cause the oscillating cavity modes to undergo SPM and generate the adjacent cavity mode frequencies. These oscillate and the coherent circulating intensity causes Kerr lensing in the gain medium so that the phase locked modes experience a better overlap with the pump beam, leading to a self-sustaining mode-locked output.

In addition, a standing wave AOM is positioned before the output mirror in order to generate a refractive index variation. By running the AOM at a frequency equal to half the longitudinal cavity mode spacing of the laser it will seed phase matched light into adjacent cavity modes and create a loss for non-phase-locked modes, ensuring the cavity continues to be mode-locked.

The laser cavity has a preferential polarisation and emits a strong linear vertical polarisation.

### **2.1.2 Measurement and Characterisation of Ti:S Laser.**

The output of the Ti:S laser was continually monitored in wavelength by a fibre coupled spectrometer that observed scattered light from the output beam splitter of the laser. This is a useful tool as it allows the measurement of the peak wavelength of the tuneable lasers, as well as the spectral width of the laser line. The degree of mode locking and resultant pulse output width could be estimated from this spectral width.

The spatial profile of the laser pulse was checked and complied with the manufacturer standards of a 2 mm Gaussian beam at  $1/e^2$  with divergence of  $< 0.6$  milliradian [39]. The diameter was confirmed with a scanning slit beam profiler shown in Figure 2.2. Profiles at multiple distances were taken to ensure the laser divergence was within specification.

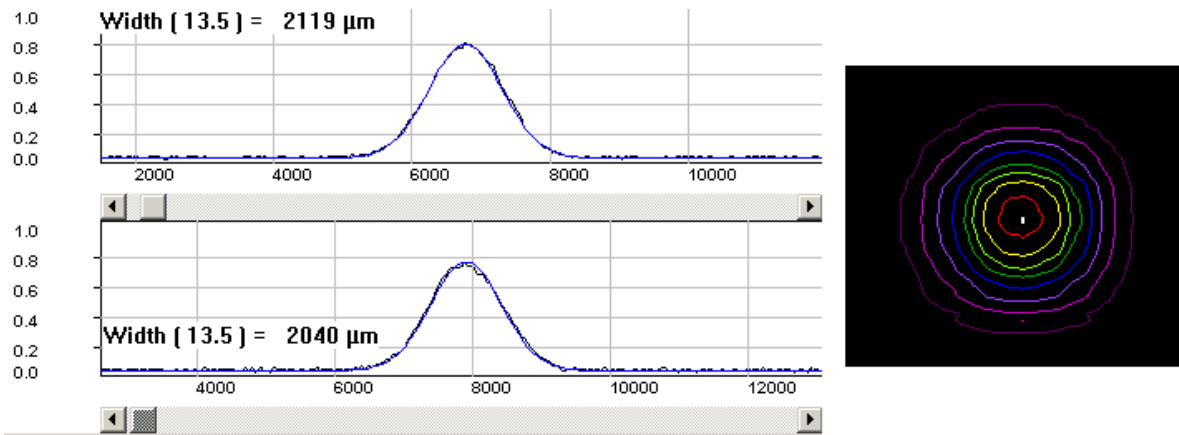


**Figure 2.2: Intensity profile of the Ti:S output matching a 2 mm wide Gaussian beam.**

The laser repetition rate of 82 MHz was confirmed with a reverse biased fast photodiode and a 500 MHz TDS 520D Tektronix oscilloscope.

The temporal width of the laser pulse was confirmed by a Spectra Physics PSCOUT HR optical autocorrelation device with PMT detector and a resolution of 50-3500 fs.

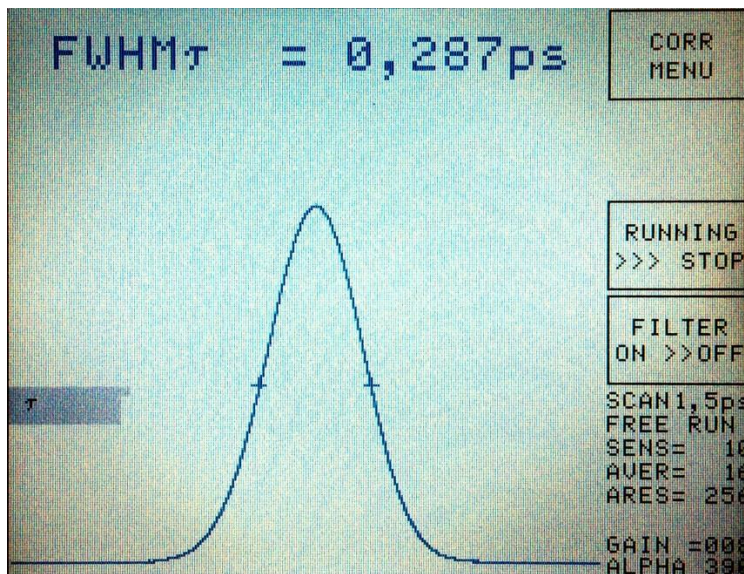


**Figure 2.3: Autocorrelation of Ti:S pulse. This has been broadened by the Faraday isolator.**

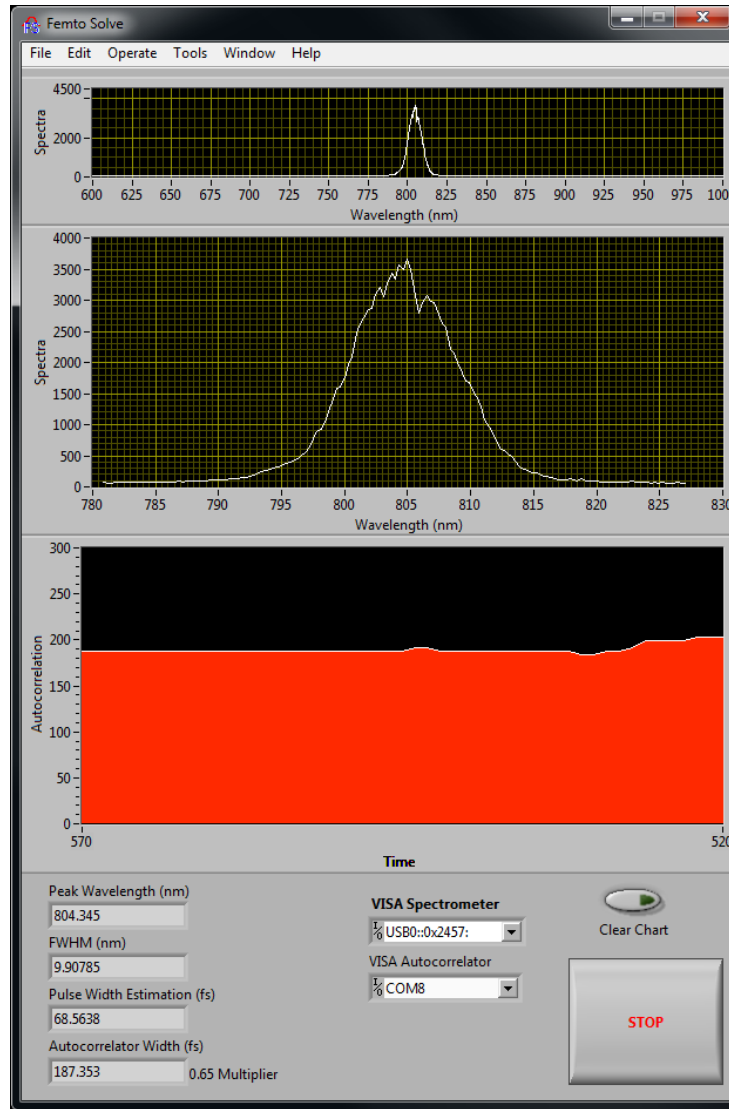


**Figure 2.4: FemtoSolve program written in LabVIEW to display the spectral output of the Ti:S from a spectrometer and the temporal width from the autocorrelator.**

The spectral components of the laser were measured with a repurposed fibre coupled OceanOptics S2000 spectrometer with an OceanOptics ADC1000-USB converter. Laser light was fed to this spectrometer through a multimode measurement fibre placed inside the Ti:S case that collected scattered light from the output coupler. A programme called FemtoSolve was developed in LabVIEW by the author to read both the spectrometer and the Autocorrelator and display the information and is shown in Figure 2.4. The Ti:S could then be easily tuned and optimised with this program.

## ***2.2 Microstructured Optical Fibre***

The nonlinear medium used in the project is pure fused silica. As mentioned in section 1.3.5, light must exist in the anomalous dispersion region to be able to generate solitons. As the zero dispersion point for fused silica is 1300 nm and anomalous dispersion

occurs at higher wavelengths, it is the small core and the symmetry and dimensions of the air hole array in a MOF that dramatically lowers the waveguide dispersion, bringing the zero GVD point to  $\sim 750$  nm and therefore bringing the anomalous region down to the 800 nm range matching the Ti:S laser emission so that the Ti:S laser can pump directly into the anomalous region and generate solitons, as shown in section 1.2.

Four different MOFs are used through these experiments. Three fibres were commercially available with different zero GVD wavelengths and one was drawn specifically for research by the Optical Fibre Technology Centre.

MOF is expensive,  $\sim \$1000$  per meter. Care was taken to minimise waste of the fibre. As the fibre end is a structure with air gaps and struts less than 200 nm wide, sealing the fibre in a connector and polishing the end would only destroy the microstructure and fill the channels with glue. Instead, the fibre was held in free space and cleaved by hand when the end face needed refreshing. This free standing fibre was susceptible to a number of environmental issues including becoming dirty, the structural collapse of the microstructure at the end face and the destruction of the structure and core from melting the end with the input laser beam.

Within the lab, the fibre can be imaged using a fibre splicer to check the cleave angle and quality. An optical microscope with a CCD camera and objective lens were used to observe the core structure of the MOF as shown in Figure 2.5. This aided in checking for damage and finding the orientation of the fibre. An example image is given in Figure 2.6.



**Figure 2.5: Photograph of fibre microscope capable of resolving some of the MOF structure.**

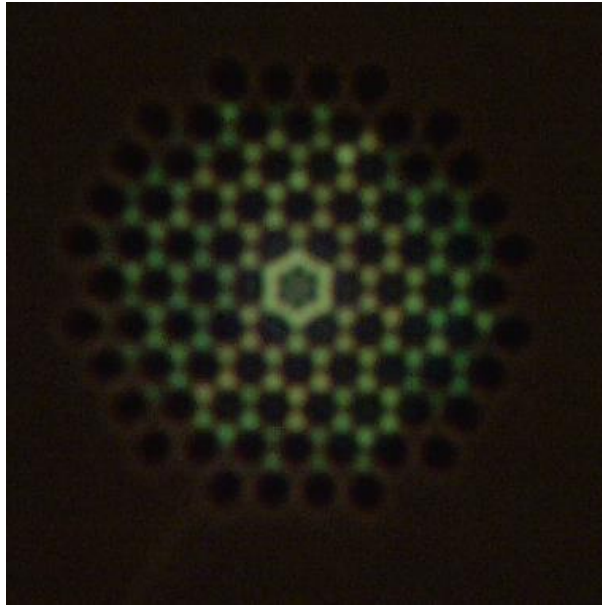


**Figure 2.6:** Image of fibre taken with microscope shown in Figure 2.5. White light has been coupled in to the fibre to show transmission. Note this matches Figure 2.7 but is rotated by 30 degrees.

In addition, detailed images were taken with a scanning electron microscope (SEM) to resolve the finest details of the MOFs (Figures 2.7-2.11 below). These SEM images are useful for seeing the true structure of the MOF and making sure the correct structure is used for simulating the modes and refractive indexes of each fibre.

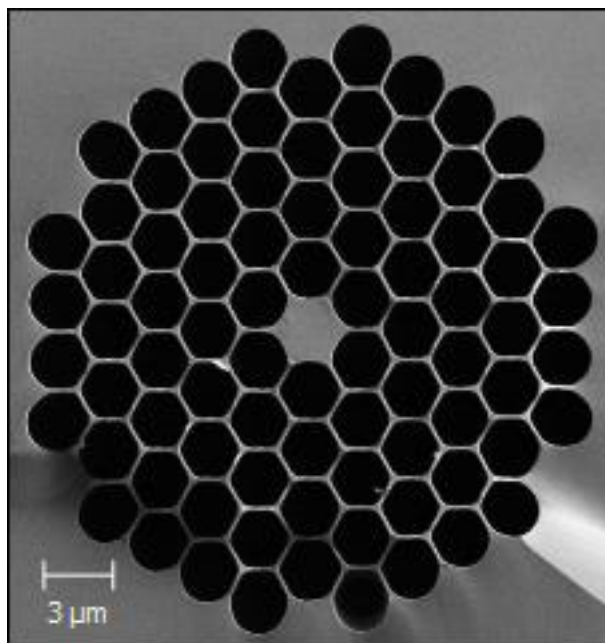


**Figure 2.7:** SEM of the core microstructure for the Thorlabs NL-2.8-850-02. The small ridge in the glass surface is due to the cleave propagation through the microstructure.

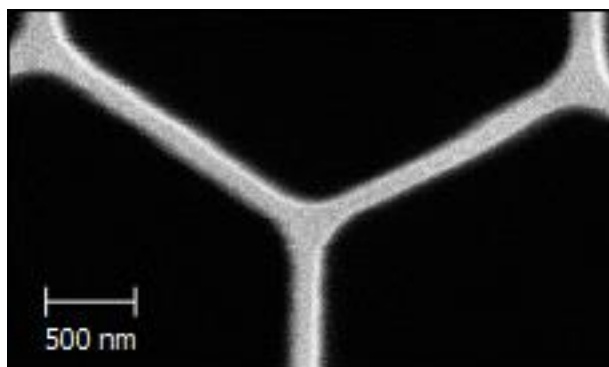


**Figure 2.8:** Magnified section of the supporting structure for the solid core shown in Figure 2.7.

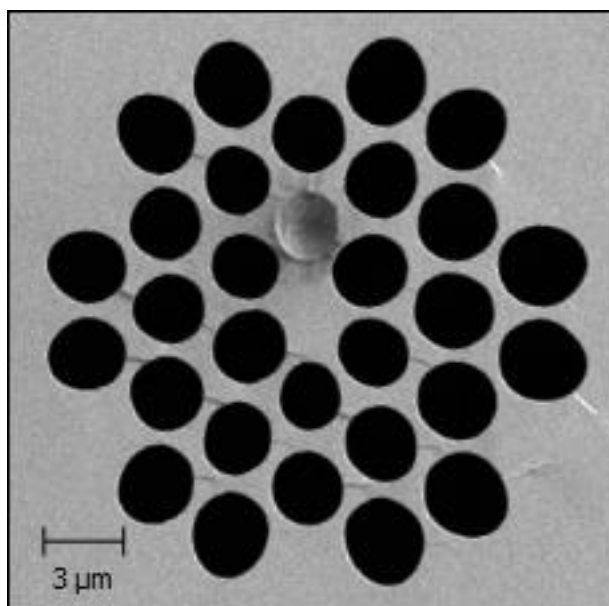


**Figure 2.9:** SEM of the core of the spun high birefringence MOF. Note that one of the holes has been contaminated, most likely with the graphene paste used to prepare the sample for imaging.

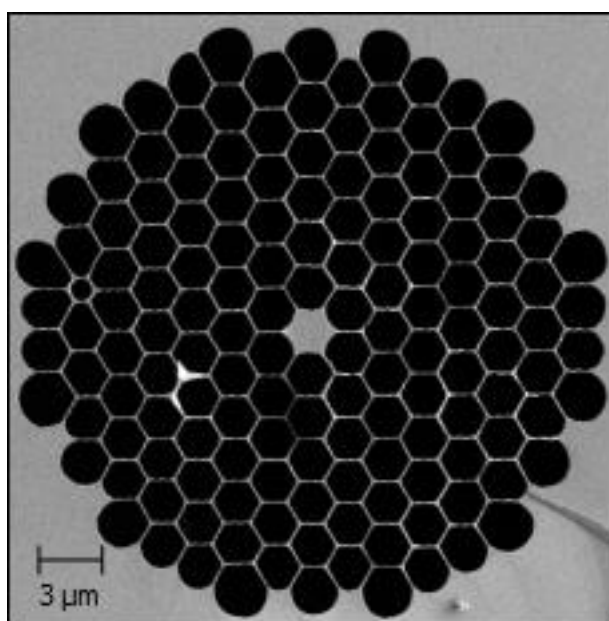


**Figure 2.10:** SEM of Thorlabs NL-2.0-745-02. Note the defective hole at 9 o'clock on the left hand side that is likely due to a failed pressurisation while drawing the fibre.

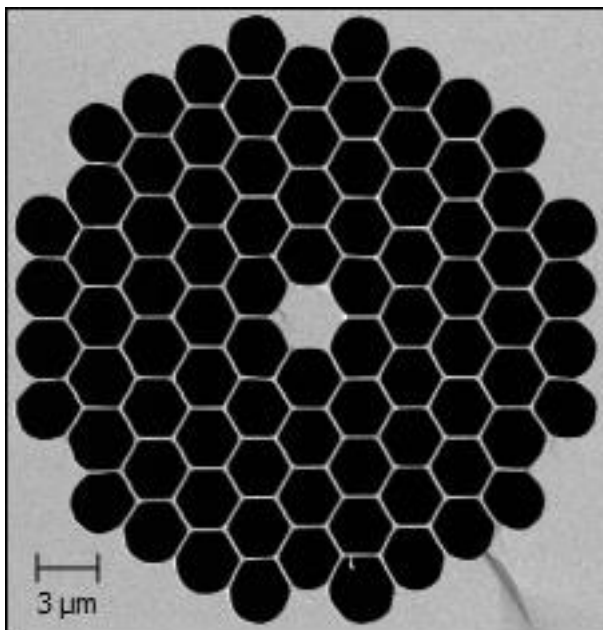


Figure 2.11: SEM of NL-3.0-850.

## 2.3 Optics

The manipulation of light in this experiment used a host of commonly seen optical tools to direct and align and focus the light in a desired way. Most of these optomechanical devices are standard and require no special mention in this thesis. This section will deal with the more complicated parts of the optical setup and stability that are less common.

All directing mirrors are first surface silver mirrors or ultra-fast chirp-free dielectric coated mirrors to minimise loss and dispersion of the pulse.

### 2.3.1 Faraday Isolator

The Faraday isolator is a unidirectional optical device used to prevent feedback into the laser. When coupling to the surface of the MOF, Fresnel reflections will couple back into the laser cavity. This causes seeding of new pulses in the cavity and destabilises the mode locking discussed in 2.1.1. The Faraday isolator overcomes this problem with an initial polarising filter aligned with the vertical laser output polarisation, then waveplates to rotate the polarisation of the light, one of which uses the Faraday effect, and finally passes out through a linear polariser. The rotation of the Faraday element is in the same direction regardless of propagation direction, therefore, any returning beam will be cross polarised and blocked by the polarising filter.

This device is critical for the operation of a Ti:S laser when generating a supercontinuum using a MOF.

### 2.3.2 Beam Steering and Stabilisation

Fine control of the beam coupling into the fibre focusing lens allows for much higher precision on the fibre end-face as larger movements on the input side of the lens only create small changes in the focussed beam position due to the “optical lever” effect of the lens. To achieve this result, the system was actively stabilised using a combination of piezo actuated gimbal mirrors with quadrant detectors providing the control feedback.

Quadrant detectors allow the laser beam to be positioned with high resolution as they have high position sensitivity of a laser beam when illuminated. The detailed structure of the detector is shown in Figure 2.12 and the use in the specific application is outlined below.

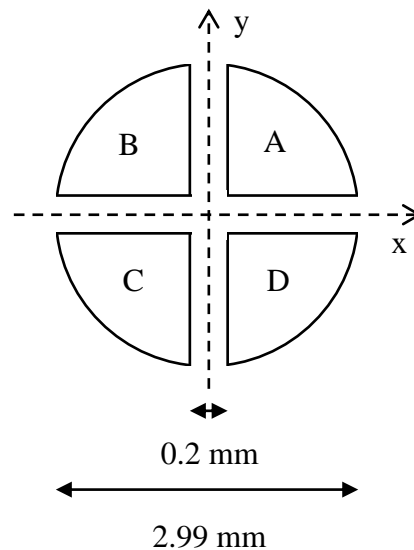


Figure 2.12: Diagram of a four quadrant silicon diode detector (QD7-5T)

The position of the beam can be calculated using the following equations.

$$X = \frac{(A + D) - (B + C)}{A + B + C + D} \quad (2.1)$$

$$Y = \frac{(A + B) - (C + D)}{A + B + C + D} \quad (2.2)$$

where  $A$ ,  $B$ ,  $C$  and  $D$  are the photo-currents generated from each quadrant of the detector in Figure 2.12 and  $X$  and  $Y$  are the contrast between the left, right and up, down. These values are proportional to  $x_0$  and  $y_0$ , where these are the central coordinates of the beam in equation (2.3) and the validity of this can be tested with a simple simulation.

The input laser beam, as detailed in section 2.1.2, can be approximated as a 2-dimensional Gaussian;

$$I(x, y) = Ae^{-\frac{(x-x_0)^2+(y-y_0)^2}{\omega_0^2}} \quad (2.3)$$

where  $\omega_0$  is the beam width of the laser and for the Ti:S laser has a value of  $525 \mu m$ . The Gaussian can be simulated as a 2D array and moved over the detector surface. The sum of the photocurrent from each quadrant detector indicates the total current and is a measure of the overall beam intensity. The calculated values of contrast from equations (2.1) and (2.2) were directly compared to the real position in equation (2.3) as the 2D array was “moved” across the surface with the results for this simulation shown in Figure 2.13. Code can be found in Section 10.3.3. A polynomial fit to the data is shown.

$$\begin{aligned} x_0 = & [3.54 \times 10^{-16} + 5.80X - 1.28 \times 10^{-14}X^2 - 2.62X^3 + 7.12 \\ & \times 10^{-14}X^4 + 22.3X^5 + 7.97 \times 10^{-14}X^6 + 38.5X^7 \\ & - 3.84 \times 10^{-13}X^8 + 25.2X^9 + 2.53 \\ & \times 10^{-13}X^{10}]10^{-4} \end{aligned} \quad (2.4)$$

This expression (2.4) is used in the control program outlined later to convert the output from the detectors into a real offset in metres with precision.

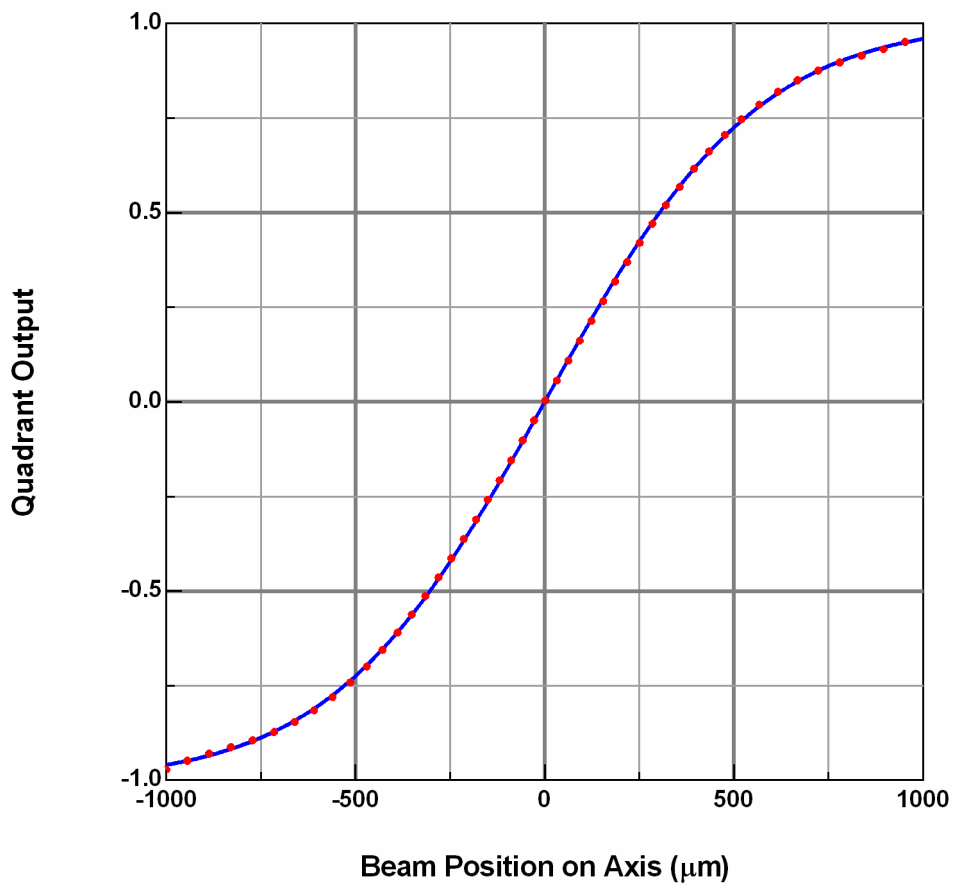


**Figure 2.13: Simulated position of quadrant detectors. The blue line shows the simulated response. Red dots follow the polynomial fit to the data.**

When coupled with actuated mirror deflection, the information from the quadrant detectors can be used to create a feedback loop and control the position of the laser beam. This kind of beam-stabilising control arrangement is well established, and has been shown before in Grafström et al [40], and is usually used to correct for beam pointing wander in laser systems. It works for the control input to the fibre face for identical reasons.

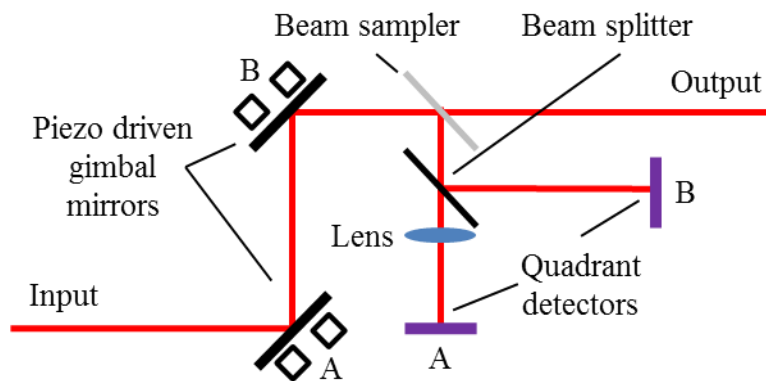


**Figure 2.14: Beam stabilisation and control setup.**

The setup shown in Figure 2.14 controls the beam by sampling at two points with each point having a separate quadrant detector. The detector B measures the position of the output beam which is controlled by mirror B. Detector A uses a lens to image the laser position at a virtual point on the top piezo mirror and controls its position with mirror A. This second point is not affected by adjustment of mirror B and hence decouples the points of control.

In addition to controlling the beam position with high accuracy, this system also runs as a feedback loop to provide stabilisation of the beam from laser drift over long periods. The system is measured through a simple operational amplifier transducer board for both quadrant detectors and an analogue to digital converter to digitise the signal. The signal is processed by a LabVIEW program written by the author that uses equations (2.1), (2.2) and (2.4) to calculate the beam positions and then provide a correcting signal via USB to four high voltage drivers that actuate piezo-electric actuators connected to the two steering gimbal mirrors. The control interface for this program is shown in Figure 2.12.

This control over the input beam position allowed extended experimental observations of stable supercontinua over periods of an hour. The position of the light coupled into the fibre as well as the angle of the light can be controlled by this setup in the following way. The system was aligned such that detector and mirror B controlled the position of the laser on the fibre coupling lens and detector and mirror A controlled the position at mirror A and as such controlled the angle of input into the fibre.

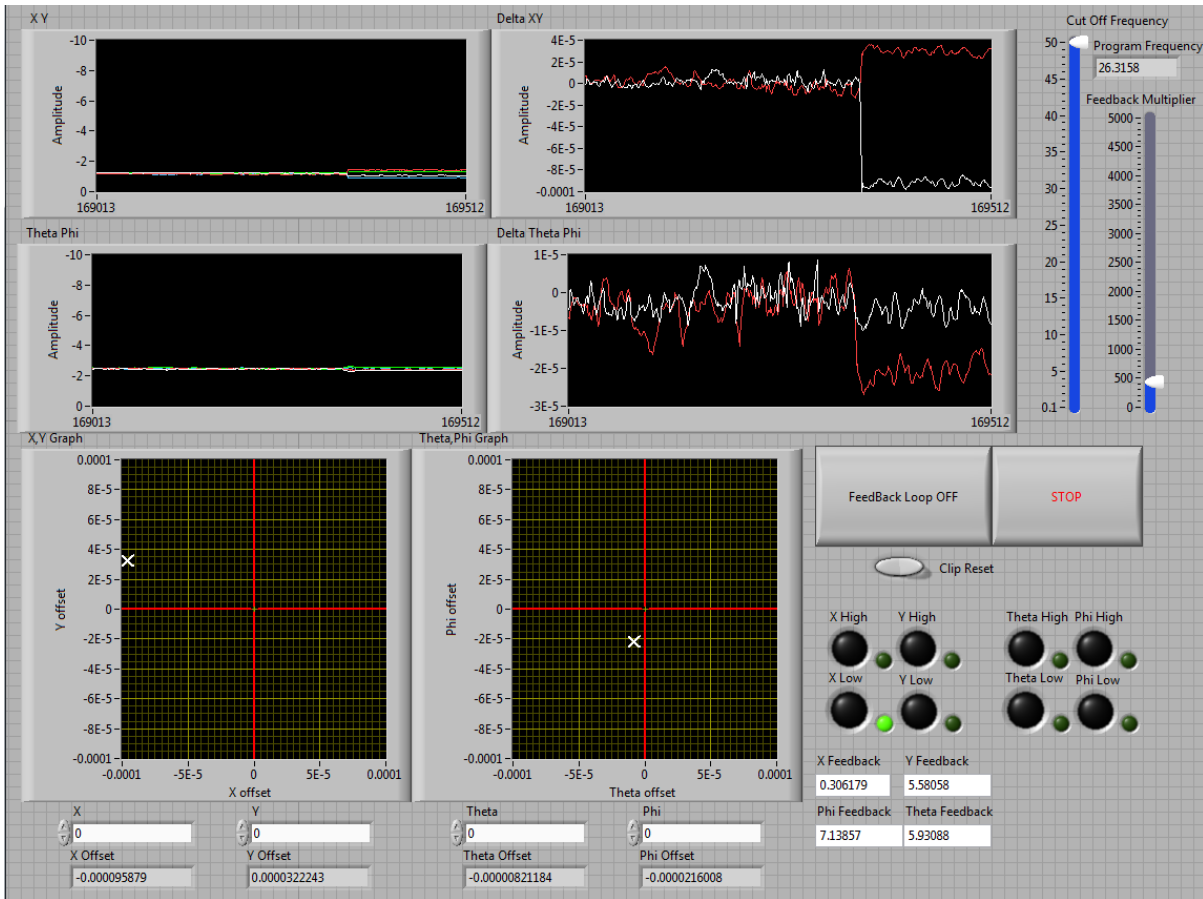


**Figure 2.15: Implementation of computer program used to control and read beam positioning feedback loop. Note that the two graphs at the top right show the variation from the desired position in meters. This display is changing since a recent change has been made to one of the mirrors to affect the beam position.**

### 2.3.3 Fibre Coupling System

The MOF was mounted on a rotation block allowing the laser to enter the fibre at any input angle. This block is held on a three-axis piezo micrometre stage (Thorlabs NanoMax MAX312D/M) that allowed precise positioning of the MOF core relative to the focussed laser beam input. The lens used was a single biconvex lens with a 2 mm focal length and antireflective coatings in the Ti:S output range. Figure 2.16 shows this setup.

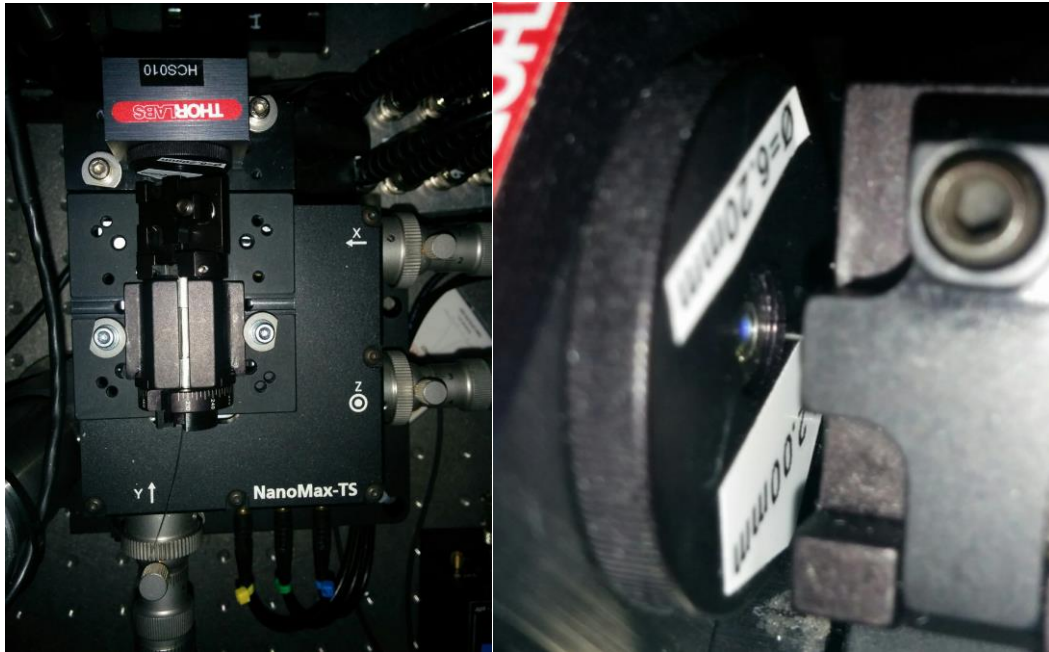


**Figure 2.16: Fibre launch system with lens, rotational holder and micrometre piezo three axis stage (the high voltage control for three axis stage is not shown).**

### 2.3.4 Apparatus Configuration

The following diagram shows the latest variant of the optical arrangement of the supercontinuum source, and detection equipment, with the full piezo positional control.

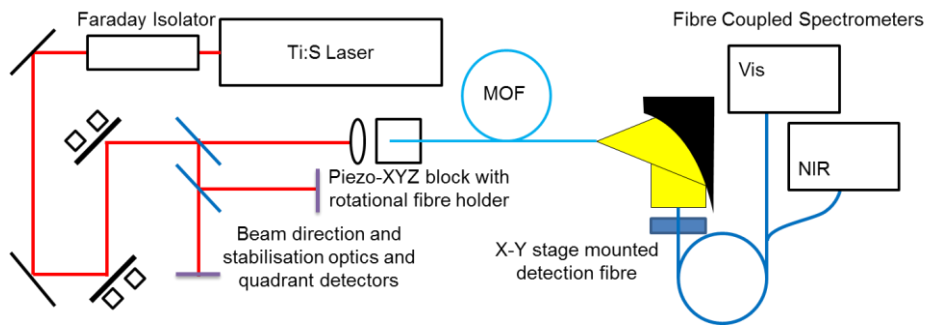


**Figure 2.17: Generalised schematic for Supercontinuum measurement**

This system was advantageous as once the beam steering system before the MOF was set up it required only minimal adjustment to excite the required mode. The output of the MOF could be routed to numerous systems for analysis and measurement. Figure 2.17 shows the setup with the reflective collimator and mode field scanner.

### 2.3.5 Collimator and Mode Scanner

The output from the MOF was collimated using an off axis parabolic mirror as shown in Figure 2.17. The collimated output of the MOF could be scanned over a 32 mm by 32 mm range with a stage resolution of 1  $\mu\text{m}$ , though this limit was rarely used as the raster

scans could take a long time and the finest structure in the far field output is of the order of 2-3 mm. The linear stages were controlled by stepper motors with a highly repeatable motion as shown in Figure 2.18.

Each pixel of the scan was recorded as an average of ~25 shots to reduce noise. The integration time for each spectrometer was set prior to each scan at the brightest point of the output to avoid saturation.

The spectrometers are important and full details of their configuration will be in the following section 2.4. The representation of this data is discussed in section 2.5.2.

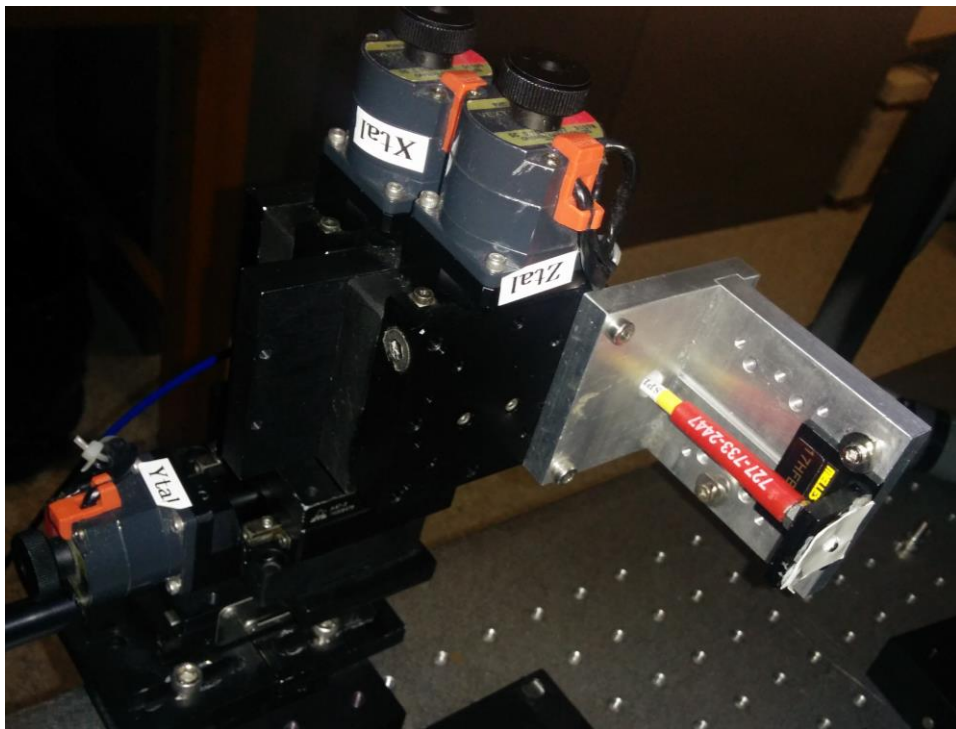


**Figure 2.18: Bifurcated sample fibre affixed to scanning stage. Stepper motor controlled linear stages are doubled to give the required translation in x and y.**

The control of this system is automated through a LabVIEW program. The front panel control of this system can be seen in Figure 2.19. This software controls the position of the stepper motors used to record the spectrum from each spectrometer at each position over a rectangular grid of points.

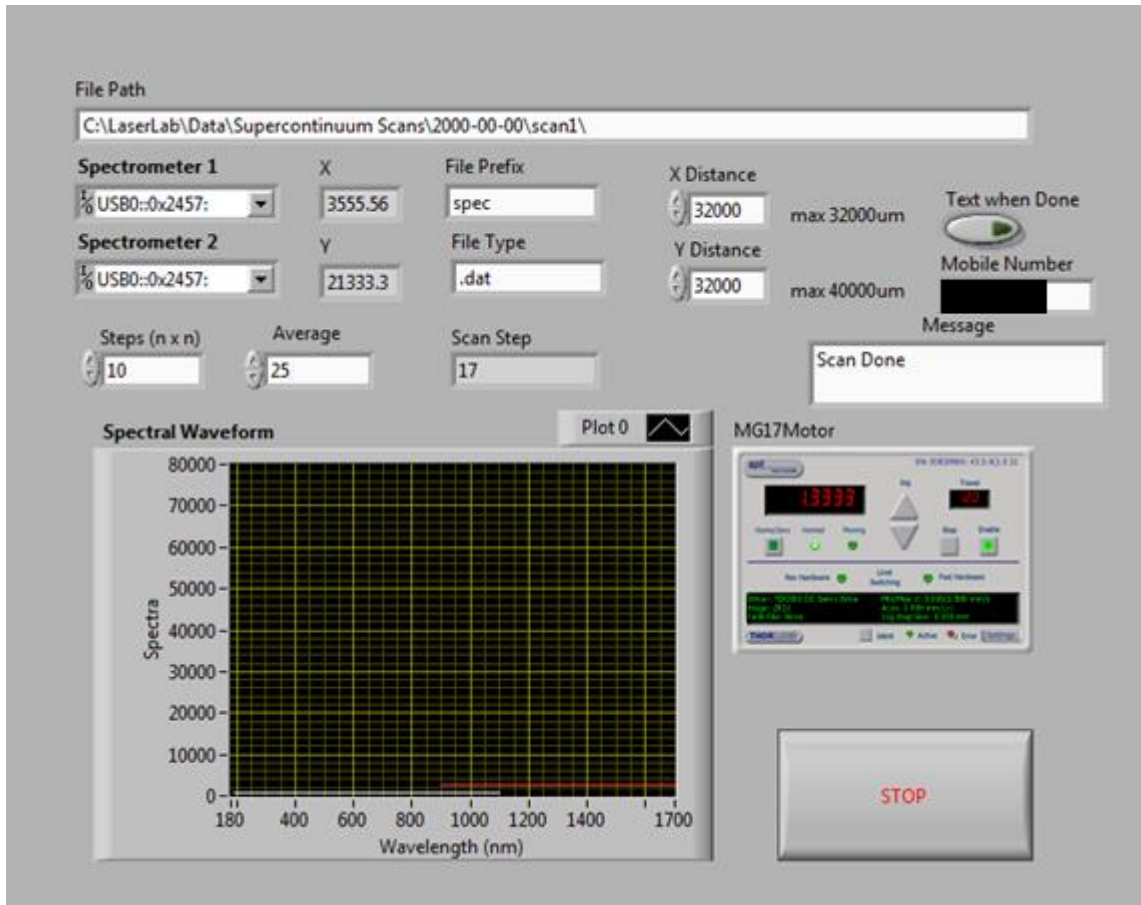


**Figure 2.19: MOF Mode Scanning software created in LabVIEW to control the stepper motors and automatically save the spectral data.**

### **2.3.6 *Polariser and Screen***

The mode output could be observed simply with a screen of graph paper, or a webcam could be used to take photographs of the output. This setup was used to acquire many of the pictures taken using throughout this thesis, and was used to obtain polarisation results discussed in Chapter 6.

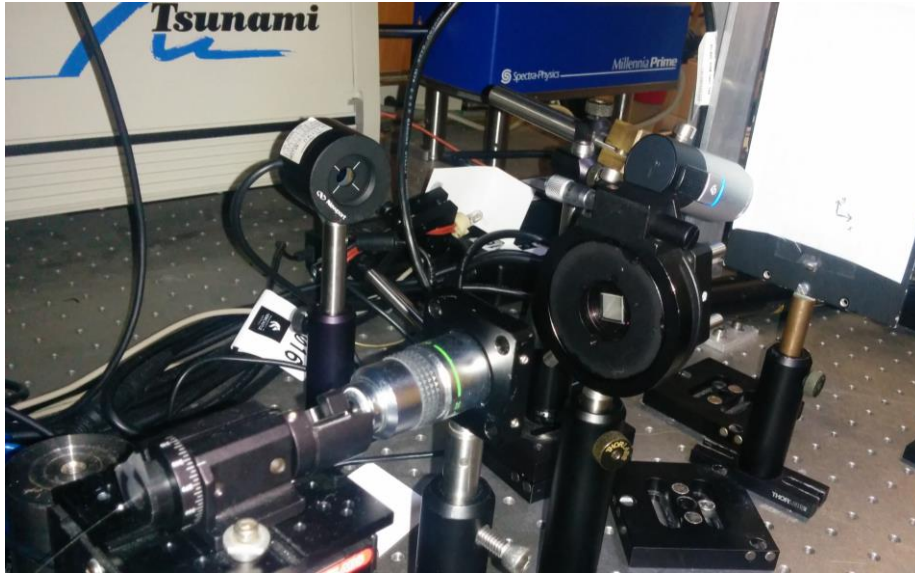


**Figure 2.20: Polarisation investigation setup utilising fibre rotator, microscope objective, Glan–Thompson prism in rotating mount and graph paper screen with a mounted webcam.**

## **2.4 Spectrometers**

The spectrometers used for this experiment were the Ocean Optics HR2000+ and an Ocean Optics NIRQuest. The light was sampled using an Ocean Optics bifurcated fibre, QBIF400-VIS-NIR, which had a 400  $\mu\text{m}$  core and a transmission window from 400 nm – 2100 nm.

The integration time for each spectrometer was set before each experiment to avoid saturation from the brightest part of any scan. Both spectrometers used can be seen setup in Figure 2.22.

### **2.4.1 HR2000+**

This spectrometer uses a 2048 pixel silicon array detector. The wavelength range is 200 nm – 1100 nm with a 0.5 nm resolution. The responsivity of the spectrometer is good in the range of 400 nm – 900 nm, however, the device is not suited to looking at broadband light sources wider than this range, so the device was used in tandem with an infrared spectrometer.

### **2.4.2 NIRQuest**

This spectrometer uses a 512 pixel InGaAs array detector that is chilled to  $-10^\circ$  Celsius by a Peltier cooler. The spectrometer has a range from 900 nm – 1700 nm with a 3 nm resolution.

The spectrometer originally contained no input filter and suffered from second order interference from the shorter wavelength light in the continuum. This was rectified by installing a Semrock long pass filter BLP01-830R that has a cut-off at 845.3 nm as detailed in Figure 2.21. This removes almost all second order interference from the spectrometer with only a small amount of 800 nm – 850 nm light showing up past 1690 nm on the spectrometer detector and far past any important spectral features of the supercontinuum output.

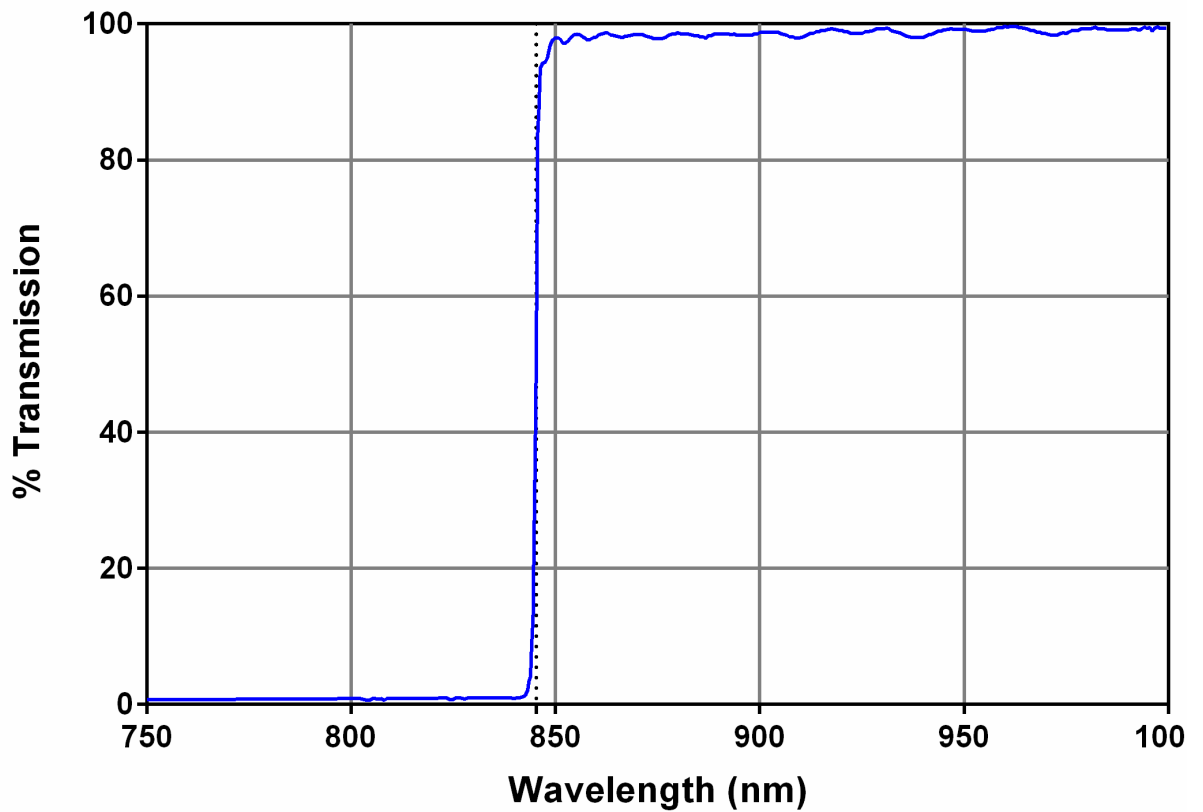


Figure 2.21: Transmission measurement of Semrock BLP01-830R filter used to remove 2<sup>nd</sup> order interference. The 50% transmission wavelength is 845.3 nm.



**Figure 2.22: HR2000+ and NIRQuest Spectrometers connected to bifurcated sampling fibre for spectral mode field scanning measurements detailed in section 2.3.5.**

## 2.5 Processing

The data measured produces an intensity spectrum for a 2D array of data points. This data is sent through a post-processing program that performs the following processes.

### 2.5.1 Radiometric Calibration

The integration time for each spectrometer is saved for every scan. This allows the use of equation (2.5) and a previously measured calibration (see section 10.2) to obtain a radiometric calibration of this data. This is useful as it removes the effect of spectral response from the measurement devices and sampling fibre.

$$I(\lambda_0) = \frac{C_i}{M_i} C(\lambda_0) [M(\lambda_0) - D(\lambda_0)] \quad (2.5)$$

where  $I(\lambda_0)$  is the radiometric intensity,  $C$  is the calibration factor,  $M$  is the measured spectral intensity,  $D$  is the dark current intensity and  $C_i$  and  $M_i$  are the calibration and measurement integration times respectively. The process for generating the calibration factor is detailed in appendix 10.2. The calibration process is integrated into the data visualisation software developed in section 2.5.2.

### 2.5.2 Data Restructure and Visualisation

The data is formatted into a 3 dimensional array with intensity as a function of pixel position in x, y and spectral wavelength,  $I(\lambda_0, x, y)$ . To observe the wide range of data created from each scan, a visualisation program was written by the author in Matlab with a graphical user interface to make it easy to explore the data.

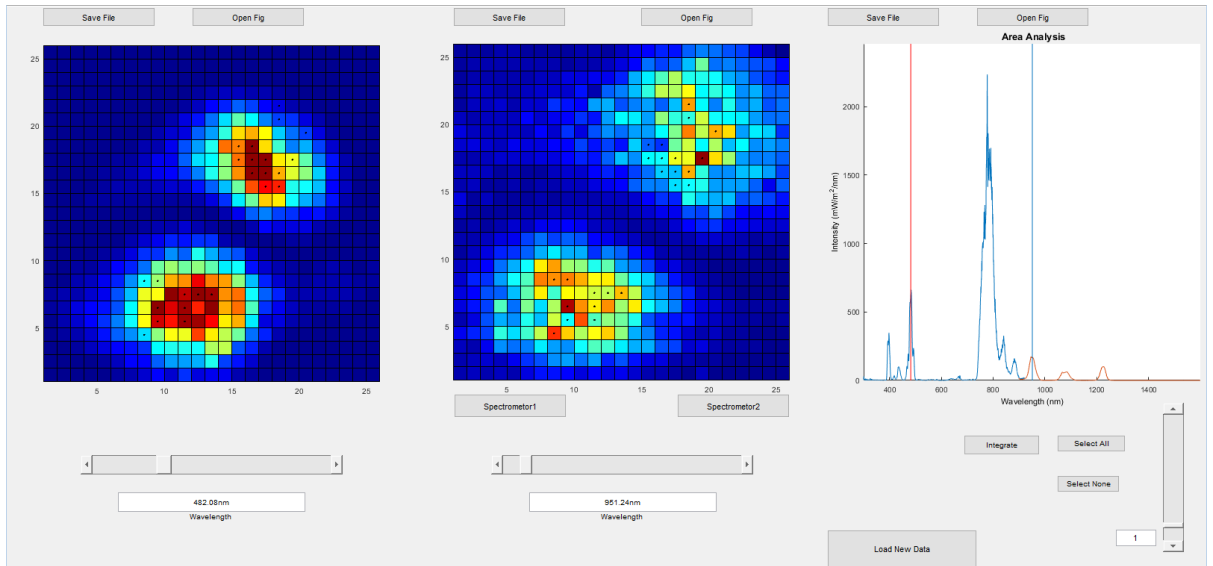


**Figure 2.23: Mode Spectrum software used to explore the data generated in the mode scanning process specified in section 2.3.5.**

The function of the software in Figure 2.23 is as follows. The first graphical panel shows a two dimensional intensity profile for a chosen wavelength of the HR2000+ spectrometer, selected using the slider below it. The second panel is similar to the first, and can be toggled between the HR2000+ and the NIRQuest spectrometer with the buttons below. The third panel shows the spectrum, and is generated by clicking pixels on either of the previous panels. The spectrum is an average of all selected pixels (marked with dots on panels one and two) as well as a line indication of the position of the two dimensional profile in panels one and two. In addition, beneath this panel there is an option to select all pixels and clear all pixels as well as a calibration slider for the second spectrometer. In the rare case where the radiometric calibration fails, this can be used to normalise spectrum two so the overlap matches spectrum one.

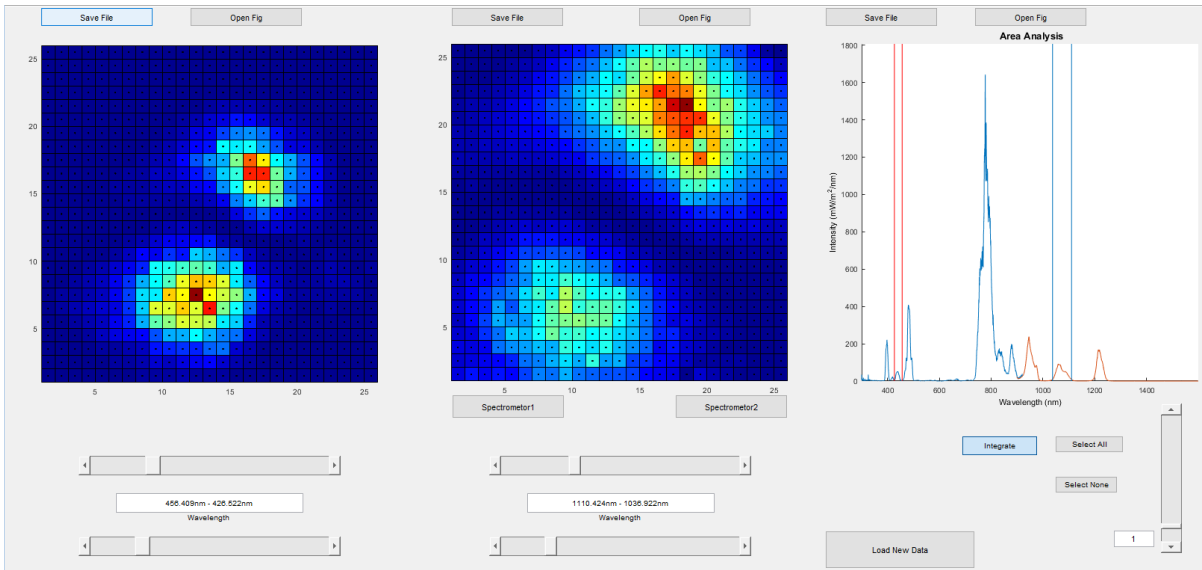


**Figure 2.24:** This shows the spectrum integration feature for the Mode Spectrum software.

Figure 2.23 shows the integration feature that was developed to look at the average mode field profile over a range of wavelengths. A second spectrum slider is added to panels one and two, and the average intensity of each pixel between those panels is calculated, allowing the full mode spectrum of a complete spectral peak to be resolved. Here, a near infrared soliton and a dispersive wave peak have been selected, as indicated by the two lines around each spectral peak in panel three.

An average 25 by 25 pixel scan produces over 10 MB of this three dimensional data, and processing the results would be extremely difficult without this program. This allowed for easy processing of the data and the ability to find trends and matches in the spatial output of the MOF to the spectral output. The program included tools to export the data to an image or back into Matlab for further processing of the data presentation.

### ***3 Modelling of Optical Modes in Microstructured Optical Fibres***

To understand the processes that govern light propagation within an optical fibre it is important to know its refraction and dispersion properties. As discussed in sections 1.1.3 and 1.1.4 both the EM mode and the material properties combined to generate an effective refractive index. There is no simple way to experimentally measure this index over the wide bandwidth utilised in these experiments, instead, simulations are run to find both the allowed modes within the complex waveguide structure and their effective indices over a relevant range of wavelengths

The material of all the MOFs is pure fused silica as no doping is required. The refractive index of this material can be approximated by the Sellmeier equation [41]

$$n(\lambda_0) = \sqrt{1 + \frac{0.6961663\lambda_0^2}{\lambda_0^2 - 0.0684043^2} + \frac{0.4079426\lambda_0^2}{\lambda_0^2 - 0.1162414^2} + \frac{0.8974794\lambda_0^2}{\lambda_0^2 - 9.896161^2}} \quad (3.1)$$

where  $\lambda_0$  is wavelength in microns. The effective index of the waveguide is dependent on a combination of the material dispersion and the waveguide dispersion. Each EM mode propagating within the waveguide has a different waveguide dispersion.

#### ***3.1 Multipole Method***

To solve the allowed modes in the MOF used for this thesis, the multipole method and source model technique were initially used [42]. The multipole method has been used extensively for MOF and the literature indicates that this is both a valid technique and yields accurate results for the MOF simulations [42,43].

Initially the CUDOS MOF Utilities [44,45] were used, however the limitations of this code, namely the inability to simulate noncircular and asymmetrical holes in the MOF, meant that the fibres were remodelled using the Source-Model Technique Package (SMTP) [43] for Matlab that, as the name suggests, incorporates a source model, meaning it can accommodate any refractive index profile and geometry.

### 3.2 *Finite Element Frequency Domain Method*

In addition to the work and approach above, finite element frequency domain analysis was used as it was both; able to calculate refractive indexes over a large range and; much faster than the multipole method.

This method, which solves the Helmholtz Equations in two dimensions using a 2D geometry frequency domain analysis, is appropriate, as the electric field varies sinusoidally throughout the waveguide.

It should be noted that, in most of the MOF simulations, the rings further from the core have a negligible impact on the guiding properties of the fibre, so only the first ring of holes around the core is simulated to reduce complexity and simulation time.

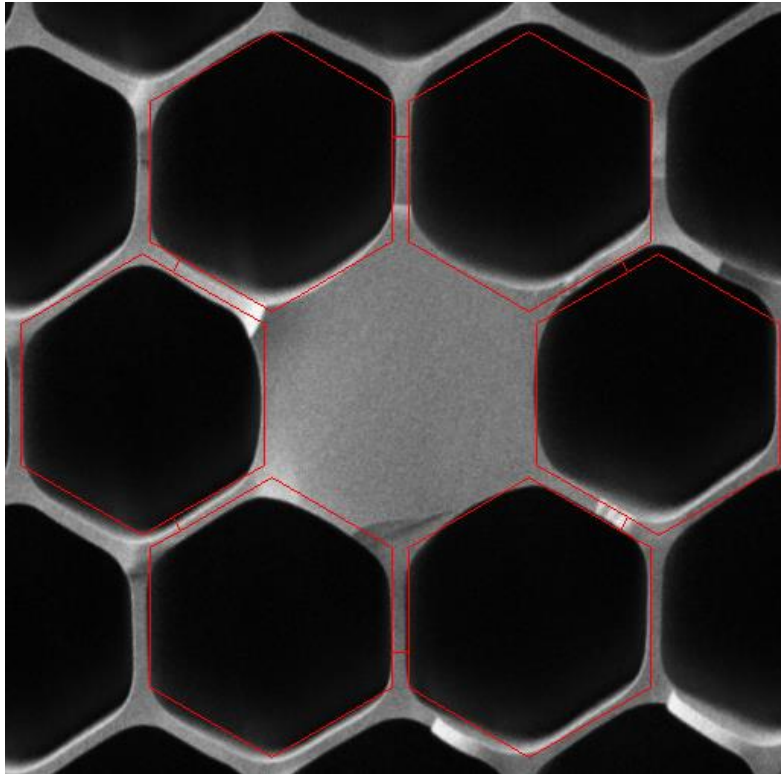


**Figure 3.1: Computational boundaries overlaid on SEM of Thorlabs NL-2.8-850-02 fibre. Other fibres used similar grids based on SEM images.**

### 3.3 *Curve Fitting*

Numerical results were fitted to this variation of the Herzberger and Salzberg equation

$$n(\lambda_0) = A + B\lambda_0^2 + C\lambda_0^4 + D\lambda_0^6 + \frac{E}{(\lambda_0^2 - J)} + \frac{F}{(\lambda_0^2 - K)^2} \quad (3.2)$$

providing a good fit for mode transitions [46]. Of note, the coefficient J is usually kept at a low value, *viz.*  $0.028 \mu\text{m}^2$ , however it can be useful to move K to higher wavelengths to indicate a resonance in the infrared as, for some higher order modes, n falls to an effective index of one as wavelength increases.

The units for the coefficients in equation (3.2) are the reciprocal of the corresponding wavelength measurement in microns. For example, coefficient B has units  $\mu\text{m}^{-2}$ , however C is in  $\mu\text{m}^{-4}$  and coefficient E has units  $\mu\text{m}^2$ .

The fitting process used the GRG-Nonlinear solver package included with Microsoft EXCEL2010. The numerical derivatives were taken while solving to compare to the simulation results and coefficients were matched using a least squares fit weighted between derivatives.

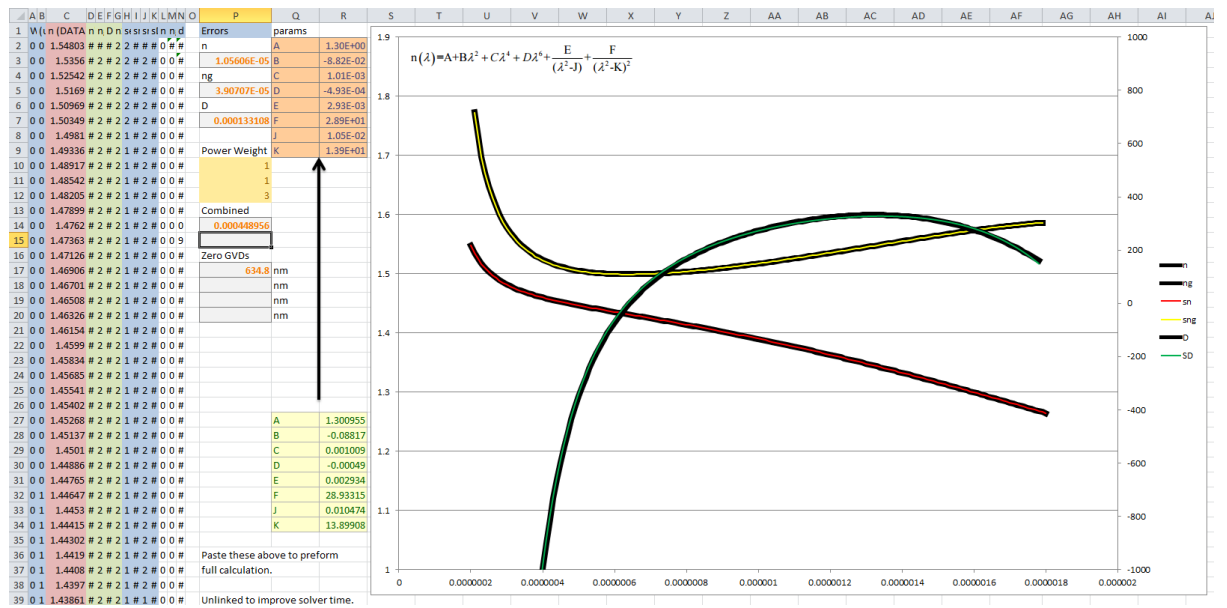


Figure 3.2: EXCEL spreadsheet showing fitted refractive index to numerical simulation.

### 3.4 Results

The following results show the simulated refractive index, group index, dispersion and intensity profile for each mode within a particular fibre structure. Results were obtained with Comsol Multiphysics and verified with SMTP.

#### 3.4.1 Thorlabs NL-2.8-850-02

This is the primary fibre used in most of the experiments as it has a zero GVD wavelength close to the peak efficiency wavelength of the Ti:S laser.

This MOF has a hexagonal grid of silica with a pitch of  $2.5\ \mu\text{m}$  between  $2.35\ \mu\text{m}$  diameter holes and a missing central hole as observed in Figure 2.7.

Figure 3.3 shows the typical x and y (transverse) cross sections of the electric fields associated with propagating modes within this fibre. Figure 3.4 and Figure 3.5 show the x-y cross section of the  $\text{HE}_{11}$  and  $\text{TM}_{01}$  modes. More complicated vector fields are harder to visualise on paper but are similar to those shown in Section 1.1.4.

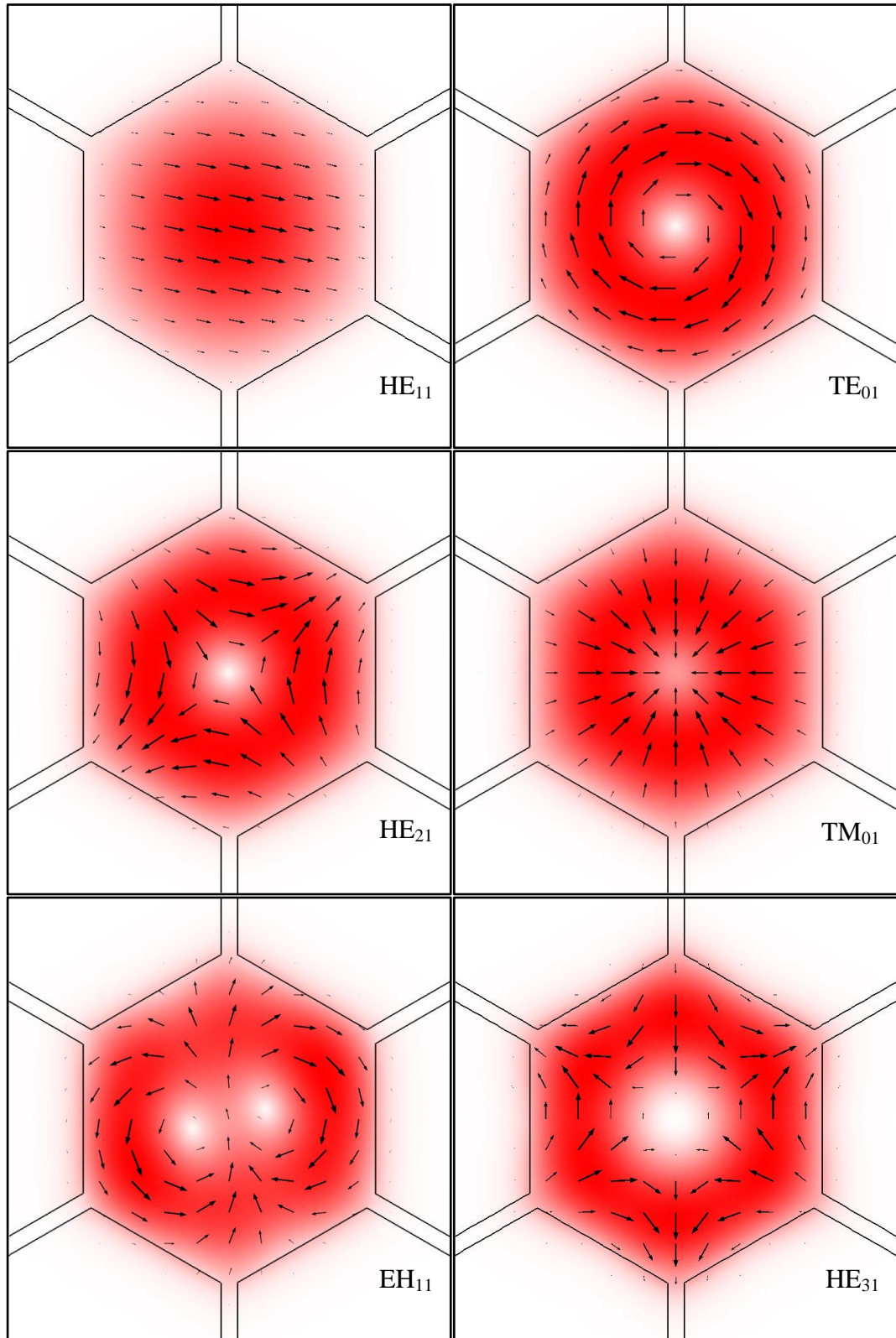


**Figure 3.3:** Normalised electric field intensities  $\sqrt{E_x^2 + E_y^2 + E_z^2}$  (red), in Thorlabs NL-2.8-850-02 MOF calculated at 800 nm. Mode labels are included in the bottom right of each image. Each image is  $2\ \mu\text{m}$  by  $2\ \mu\text{m}$  square with the interfaces between the silica and air holes shown as black lines. The direction of the electric field in the x-y plane is shown by the black arrows.

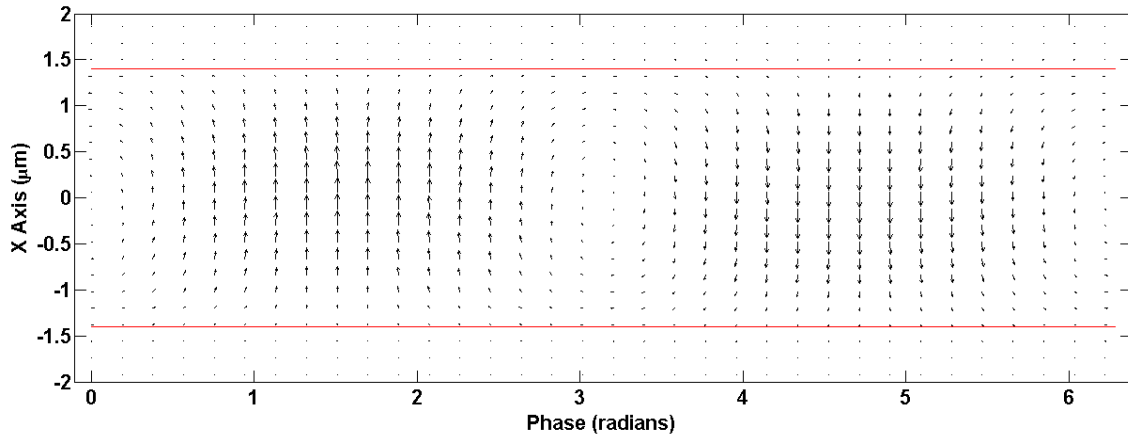


Figure 3.4:  $HE_{11}$  mode showing the electric field in the x-z plane. Red lines indicate the edge of the core.

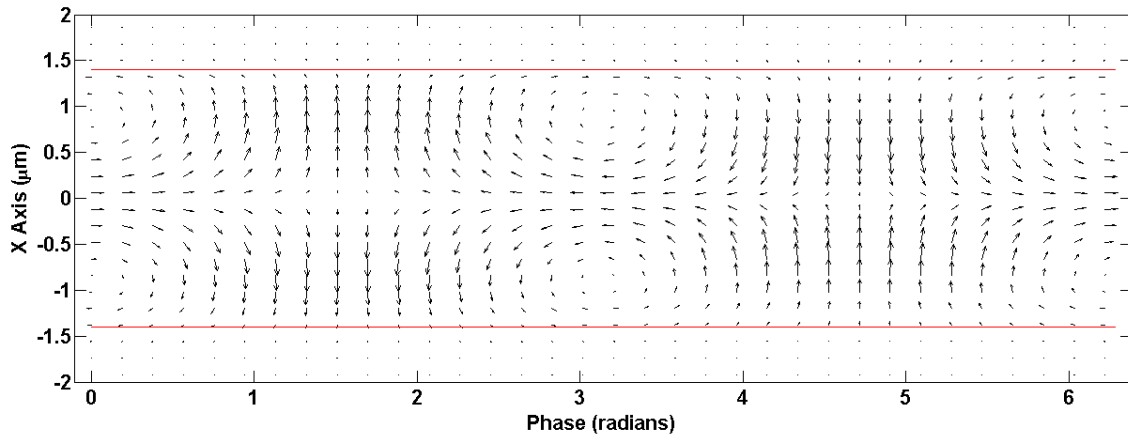


Figure 3.5:  $TM_{01}$  mode showing the electric field in the x-z plane. Red lines indicate the edge of the core.

Table 3.1: Fitting coefficients for the modes shown in Figure 3.3 to equation (3.2). The column labelled N is used to indicate the degeneracy number of each mode.

N	Mode	A	B	C	D	E	F	J	K
2	$HE_{11}$	$1.34 \times 10^0$	$-3.52 \times 10^{-2}$	$-1.02 \times 10^{-4}$	$-3.18 \times 10^{-4}$	$2.93 \times 10^{-3}$	$2.83 \times 10^{+1}$	$1.05 \times 10^{-2}$	$1.57 \times 10^1$
1	$TE_{01}$	$1.14 \times 10^0$	$-8.30 \times 10^{-2}$	$-8.01 \times 10^{-5}$	$-7.36 \times 10^{-4}$	$2.93 \times 10^{-3}$	$8.49 \times 10^{+1}$	$1.05 \times 10^{-2}$	$1.65 \times 10^1$
2	$HE_{21}$	$1.31 \times 10^0$	$-6.60 \times 10^{-2}$	$4.05 \times 10^{-4}$	$-5.19 \times 10^{-4}$	$2.93 \times 10^{-3}$	$3.09 \times 10^{+1}$	$1.05 \times 10^{-2}$	$1.46 \times 10^1$
1	$TM_{01}$	$1.31 \times 10^0$	$-6.59 \times 10^{-2}$	$2.84 \times 10^{-4}$	$-4.00 \times 10^{-4}$	$2.93 \times 10^{-3}$	$3.18 \times 10^{+1}$	$1.05 \times 10^{-2}$	$1.51 \times 10^1$
2	$EH_{11}$	$1.26 \times 10^0$	$-1.08 \times 10^{-1}$	$1.84 \times 10^{-3}$	$-8.97 \times 10^{-4}$	$2.94 \times 10^{-3}$	$3.46 \times 10^{+1}$	$1.05 \times 10^{-2}$	$1.35 \times 10^1$
1	$HE_{31}$	$1.05 \times 10^0$	$-1.33 \times 10^{-1}$	$-1.35 \times 10^{-3}$	$-1.09 \times 10^{-3}$	$2.94 \times 10^{-3}$	$9.07 \times 10^{+1}$	$1.04 \times 10^{-2}$	$1.50 \times 10^1$

**Table 3.2: Zero Group Velocity Dispersion points. These are visible graphically in Figure 3.7.**

Mode	HE <sub>11</sub>	TE <sub>01</sub>	HE <sub>21</sub>	TM <sub>01</sub>	EH <sub>11</sub>	HE <sub>31</sub>
Zero	809.8	659.3	641.4	634.8	563.0	564.2
GVD(nm)					1738.4	1666.7

Each of these modes can be compared to the standard circular waveguide fibre modes shown in section 1.1.4. The primary differences include the splitting of previously degenerate modes due to the sharp dielectric interface.

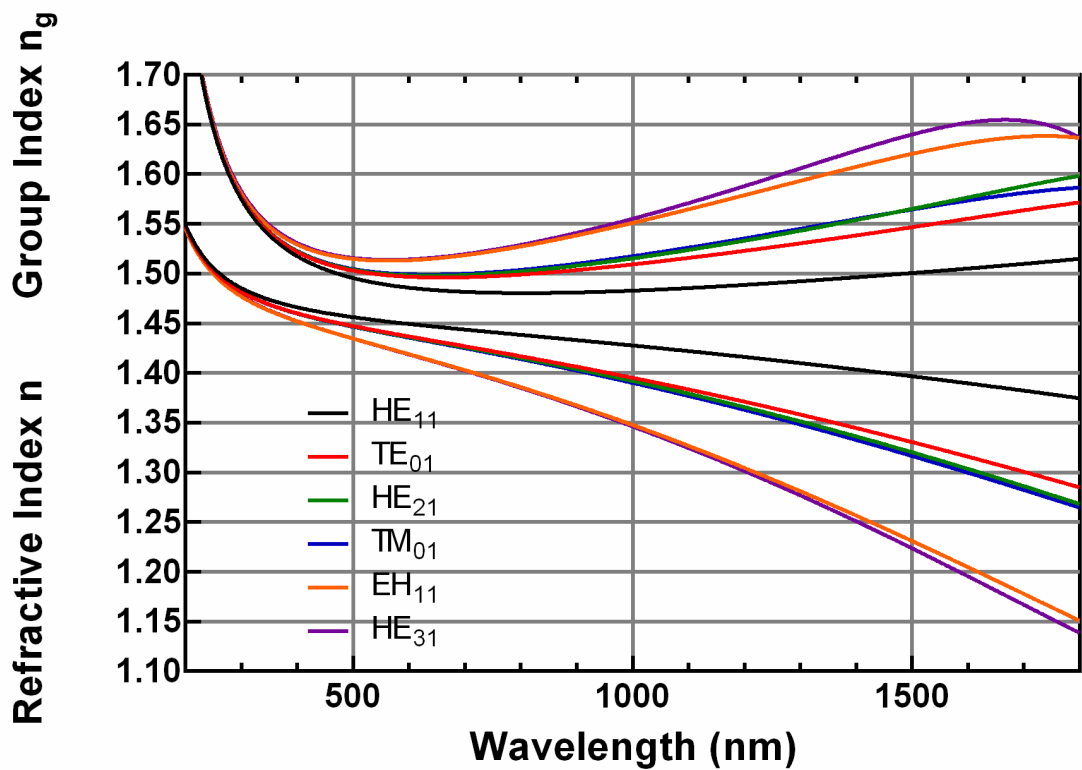


**Figure 3.6: Graphed fits for the first six Thorlabs NL-2.8-850-02 modes. The refractive index is the lower group of curves; the group index is the higher group. Note that even though some of the degenerate modes look to have very similar refractive and group indices, the slight variations significantly affect the dispersion as shown in Figure 3.7.**

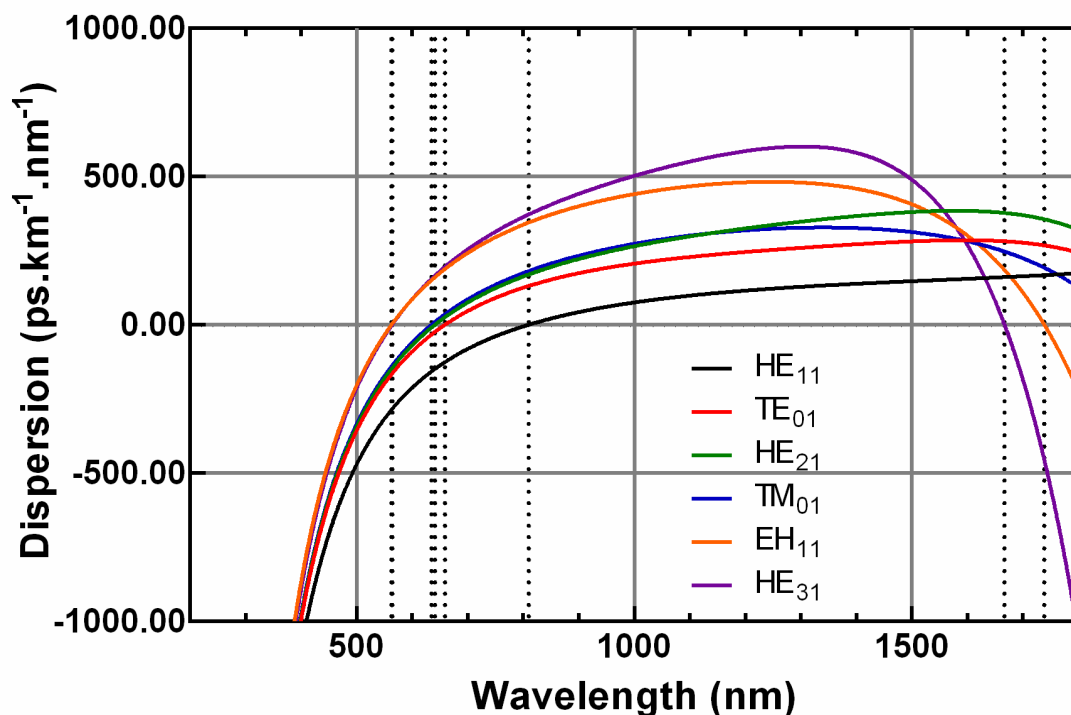


Figure 3.7: Dispersion of each mode in Thorlabs NL-2.8-850-02. The zero GVD points for each mode are shown in Table 3.2.

### 3.4.2 Thorlabs NL-2.0-745-02

Physical parameters of this MOF are a hexagonal grid of silica with a pitch of 2.1  $\mu\text{m}$  between 2  $\mu\text{m}$  diameter holes and a missing central hole as observed in Figure 2.10.

The electromagnetic mode structure is very similar to the previous fibre discussed in section 3.4.1 and as such the vector field diagrams there should give sufficient illustration to these modes. The refractive index of these modes, however, do vary, as seen in the following tables and graphs.

**Table 3.3: Fitting coefficients for the modes to equation (3.2). The column labelled N is used to indicate the degeneracy number of each mode.**

N	Mode	A	B	C	D	E	F	J	K
2	HE <sub>11</sub>	$9.86 \times 10^{-1}$	$-8.93 \times 10^{-2}$	$-1.21 \times 10^{-3}$	$-7.39 \times 10^{-4}$	$2.93 \times 10^{-3}$	$1.52 \times 10^2$	$1.05 \times 10^{-2}$	$1.81 \times 10^1$
1	TE <sub>01</sub>	$1.22 \times 10^0$	$-1.20 \times 10^{-1}$	$4.13 \times 10^{-3}$	$-1.31 \times 10^{-3}$	$2.94 \times 10^{-3}$	$4.18 \times 10^1$	$1.04 \times 10^{-2}$	$1.34 \times 10^1$
2	HE <sub>21</sub>	$1.23 \times 10^0$	$-1.25 \times 10^{-1}$	$1.49 \times 10^{-3}$	$-1.12 \times 10^{-3}$	$2.95 \times 10^{-3}$	$3.34 \times 10^1$	$1.04 \times 10^{-2}$	$1.25 \times 10^1$
1	TM <sub>01</sub>	$1.17 \times 10^0$	$-1.31 \times 10^{-1}$	$1.07 \times 10^{-3}$	$-4.43 \times 10^{-4}$	$2.94 \times 10^{-3}$	$6.00 \times 10^1$	$1.04 \times 10^{-2}$	$1.47 \times 10^1$
2	EH <sub>11</sub>	$1.10 \times 10^0$	$-2.41 \times 10^{-1}$	$4.41 \times 10^{-3}$	$-4.79 \times 10^{-3}$	$2.95 \times 10^{-3}$	$2.84 \times 10^1$	$1.04 \times 10^{-2}$	$9.01 \times 10^0$
1	HE <sub>31</sub>	$2.93 \times 10^{-1}$	$-4.07 \times 10^{-1}$	$-2.16 \times 10^{-2}$	$-1.05 \times 10^{-2}$	$2.96 \times 10^{-3}$	$1.05 \times 10^2$	$1.04 \times 10^{-2}$	$9.51 \times 10^0$

**Table 3.4: Zero Group Velocity Dispersion points. These are visible graphically in Figure 3.9.**

Mode	HE <sub>11</sub>	TE <sub>01</sub>	HE <sub>21</sub>	TM <sub>01</sub>	EH <sub>11</sub>	HE <sub>31</sub>
Zero	750.6	610.4	591.4	585.1	520.4	516.9
GVD(nm)				1633.3	1478.8	1423.5

The calculated zero GVD point for the fundamental HE<sub>11</sub> mode is 750.6 nm, close to the manufacturer estimation of 745 nm.

It should also be noted that the EH<sub>11</sub> and HE<sub>31</sub> modes reach their cut-off wavelength before 1800 nm in Figure 3.8. This is shown as the point where the effective index falls to 1.1. Index values below 1.1 are insufficiently different from the air gap cladding around the solid core, so the mode does not propagate.

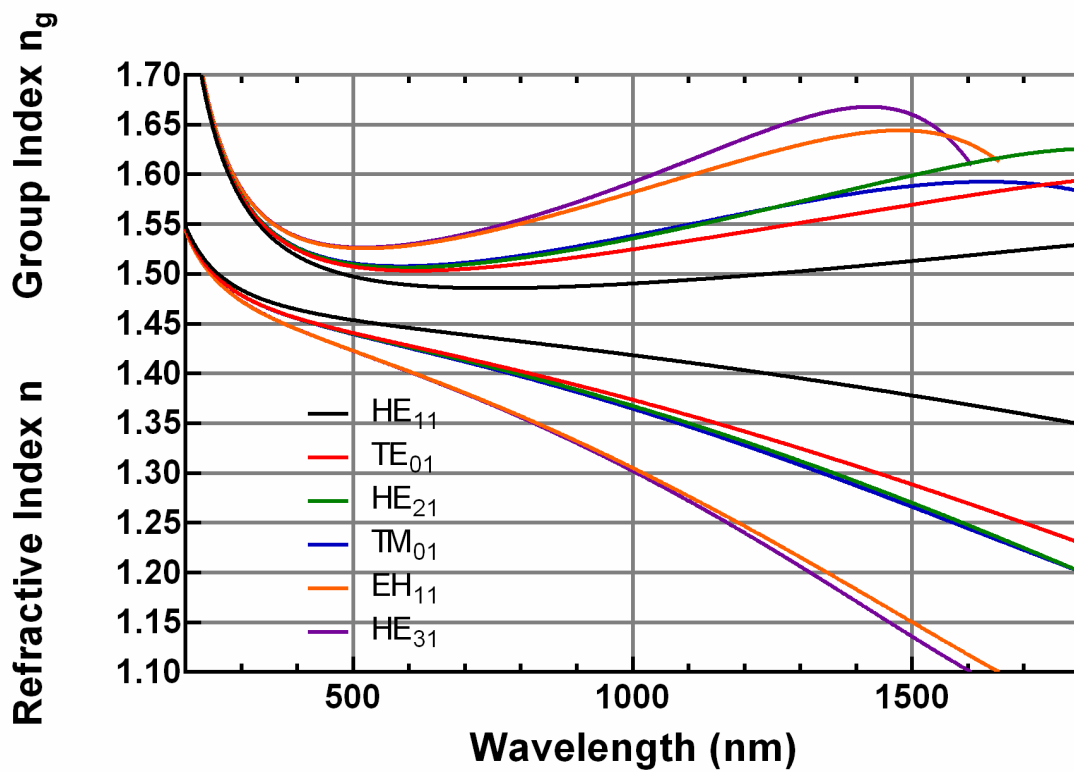


Figure 3.8: Graphed fits for the first six Thorlabs NL-2.0-745-02 modes. The refractive index is the lower group of curves; the group index is the higher group.

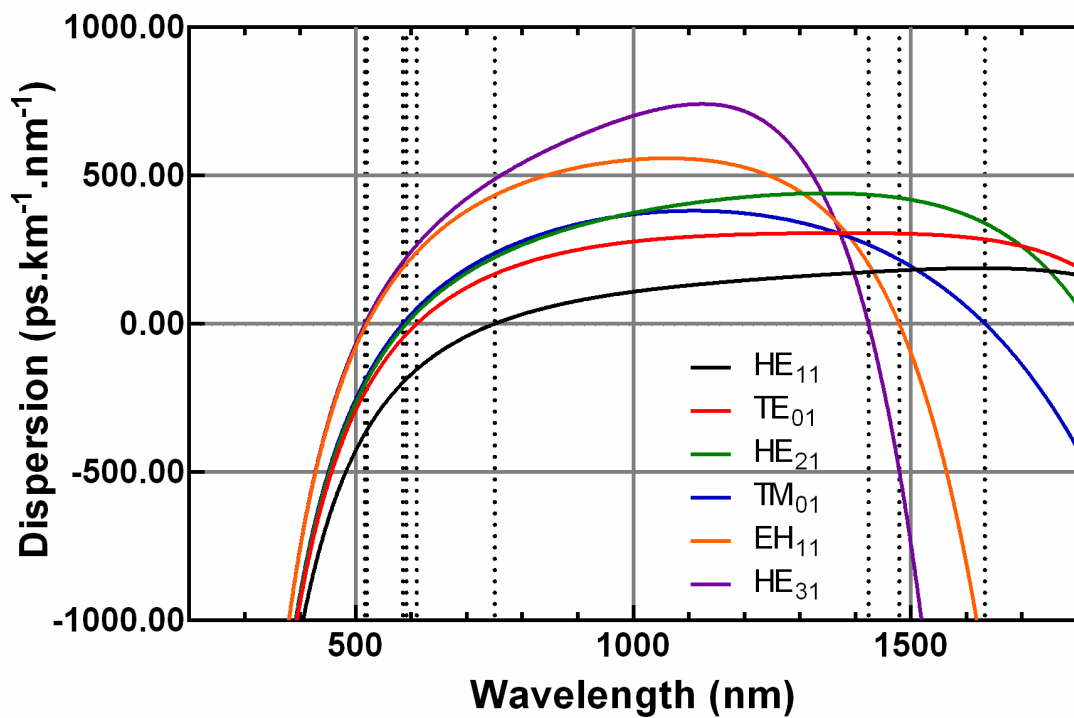


Figure 3.9: Dispersion of each mode in Thorlabs NL-2.0-745-02. The zero GVD points for each mode are listed in Table 3.4.

### 3.4.3 Thorlabs NL-3.0-850

Physical parameters of this MOF are a hexagonal grid of silica with a pitch of 3  $\mu\text{m}$  between 2.8  $\mu\text{m}$  diameter holes and a missing central hole as observed in Figure 2.11.

The electromagnetic mode structure is very similar to the previous fibre discussed in section 3.4.1 and, as such, the vector filled diagrams there should give sufficient illustration to these modes. The refractive index of these modes, however, do vary, as seen in the following tables and graphs.

**Table 3.5: Fitting coefficients for the modes to equation (3.2). The column labelled N is used to indicate the degeneracy number of each mode.**

N	Mode	A	B	C	D	E	F	J	K
2	HE <sub>11</sub>	$1.34 \times 10^0$	$-3.52 \times 10^{-2}$	$-1.02 \times 10^{-4}$	$-3.18 \times 10^{-4}$	$2.93 \times 10^{-3}$	$2.83 \times 10^1$	$1.05 \times 10^{-2}$	$1.57 \times 10^1$
1	TE <sub>01</sub>	$1.14 \times 10^0$	$-8.30 \times 10^{-2}$	$-8.01 \times 10^{-5}$	$-7.36 \times 10^{-4}$	$2.93 \times 10^{-3}$	$8.49 \times 10^1$	$1.05 \times 10^{-2}$	$1.65 \times 10^1$
2	HE <sub>21</sub>	$1.31 \times 10^0$	$-6.60 \times 10^{-2}$	$4.05 \times 10^{-4}$	$-5.19 \times 10^{-4}$	$2.93 \times 10^{-3}$	$3.09 \times 10^1$	$1.05 \times 10^{-2}$	$1.46 \times 10^1$
1	TM <sub>01</sub>	$1.31 \times 10^0$	$-6.59 \times 10^{-2}$	$2.84 \times 10^{-4}$	$-4.00 \times 10^{-4}$	$2.93 \times 10^{-3}$	$3.18 \times 10^1$	$1.05 \times 10^{-2}$	$1.51 \times 10^1$
2	EH <sub>11</sub>	$1.26 \times 10^0$	$-1.08 \times 10^{-1}$	$1.84 \times 10^{-3}$	$-8.97 \times 10^{-4}$	$2.94 \times 10^{-3}$	$3.46 \times 10^1$	$1.05 \times 10^{-2}$	$1.35 \times 10^1$
1	HE <sub>31</sub>	$1.05 \times 10^0$	$-1.33 \times 10^{-1}$	$-1.35 \times 10^{-3}$	$-1.09 \times 10^{-3}$	$2.94 \times 10^{-3}$	$9.07 \times 10^1$	$1.04 \times 10^{-2}$	$1.50 \times 10^1$

**Table 3.6: Zero Group Velocity Dispersion points. These are visible graphically in Figure 3.11**

Mode	HE <sub>11</sub>	TE <sub>01</sub>	HE <sub>21</sub>	TM <sub>01</sub>	EH <sub>11</sub>	HE <sub>31</sub>
Zero GVD(nm)	868.0	712.5	695.7	688.7	609.9	607.8

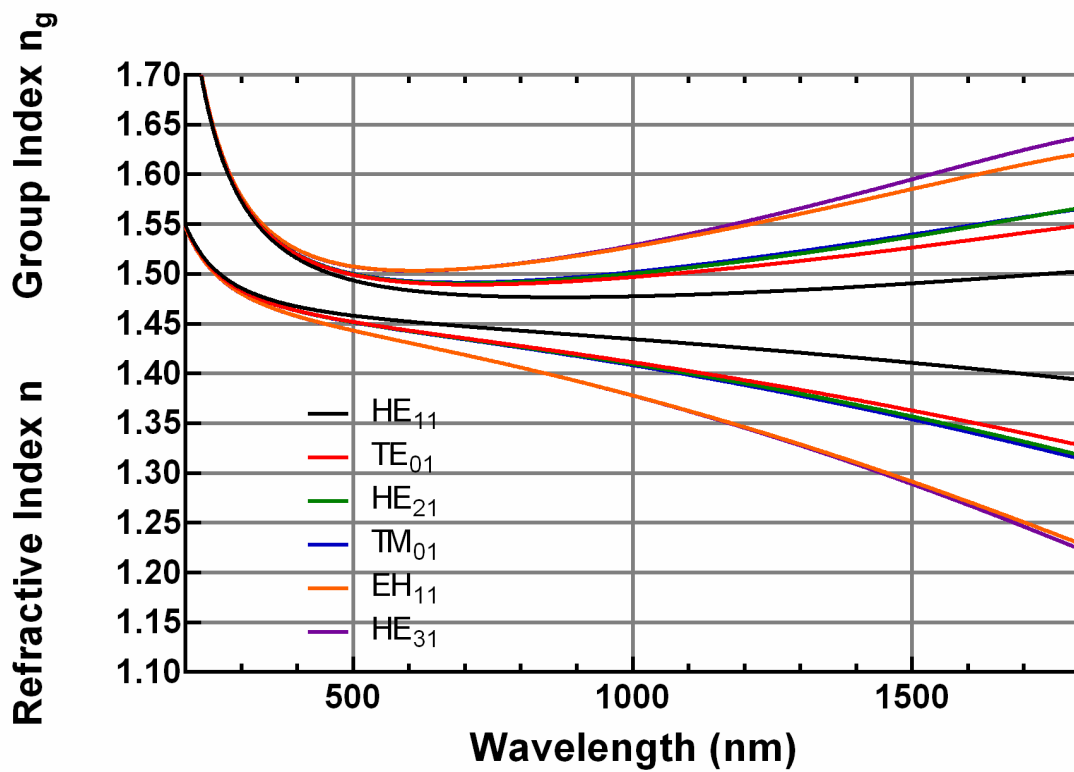


Figure 3.10: Graphed fits for the first six Thorlabs NL-3.0-850 modes. The refractive index is the lower group of curves; the group index is the higher group.

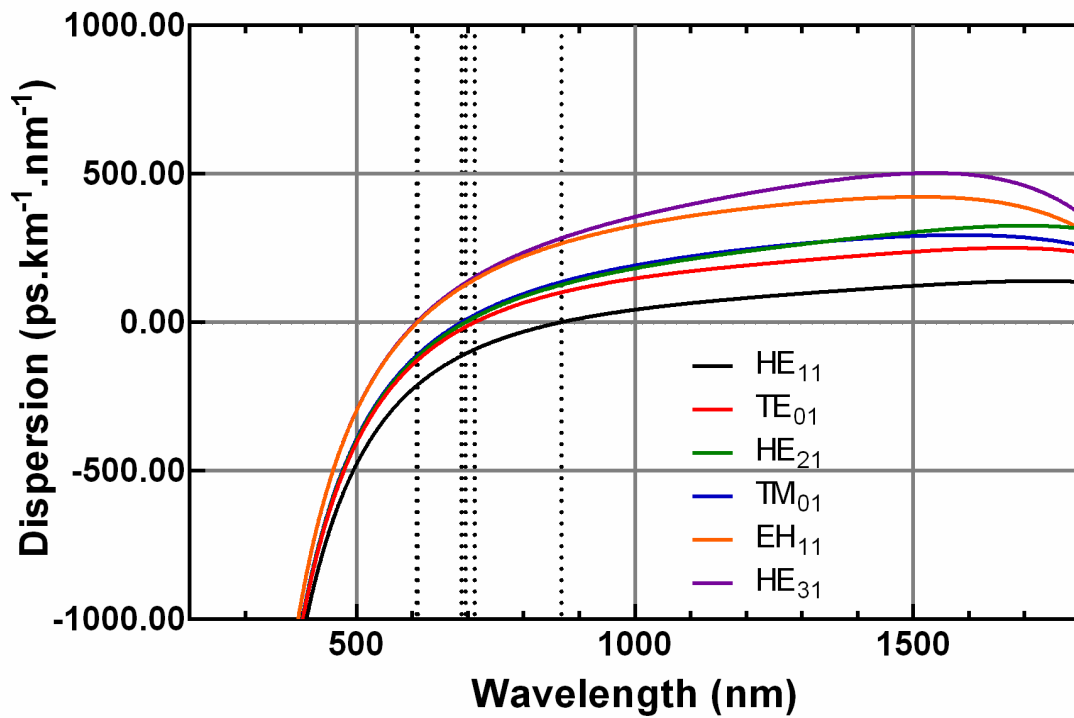


Figure 3.11: Dispersion of each mode in Thorlabs NL-3.0-850. The zero GVD points for each mode are listed in Table 3.6.

### 3.4.4 OFTC Spun High Birefringence Fibre

The structure of this fibre breaks the pattern of the previous MOF investigated in this chapter. The structure can be seen in Figure 2.9. This was simulated by an elliptical ring of six circular air holes with varying radii positioned elliptically around a solid core.

The birefringence of this fibre is useful, as it splits the degeneracy of all of the modes. The double  $HE_{11}$  mode degeneracy of the previous fibres can be seen as a split effective index curve in the long and short axis of the elliptical core. As such, the full vector mode notation (HE, EH, TE and TM) used in the previous fibre can be replaced with the LP notation as all propagating modes in this strongly birefringent fibre are linearly polarised.

Each LP mode has two numbers indicating the azimuthal mode order  $l$  and the radial mode order  $m$ . Modes with an azimuthal order have a double degeneracy as the azimuthal intensity is dependent on  $\cos(l\phi)$  and  $\sin(l\phi)$ , these are described as odd and even modes. In addition, each mode has a polarisation direction. These modes are notated as follows  $LP_{lm,v}^*$  where  $v$  is the polarisation direction and the  $*$  indicates an odd mode. For example the first six modes of the following fibre are  $LP_{01,y}$ ,  $LP_{01,x}$ ,  $LP_{11,y}$ ,  $LP_{11,x}$ ,  $LP_{11,y}^*$ ,  $LP_{11,x}^*$ .

These modes can be split into fast and slow variants as should be clear in Figure 3.13 as the group index of all similar modes is lower for the modes with the electric field polarisation in the direction of the long axis. Here  $y$  is the longer vertical axis and  $x$  is the shorter horizontal axis, i.e.  $LP_{01,x}$  and  $LP_{01,y}$  are the fast and slow fundamental modes respectively.

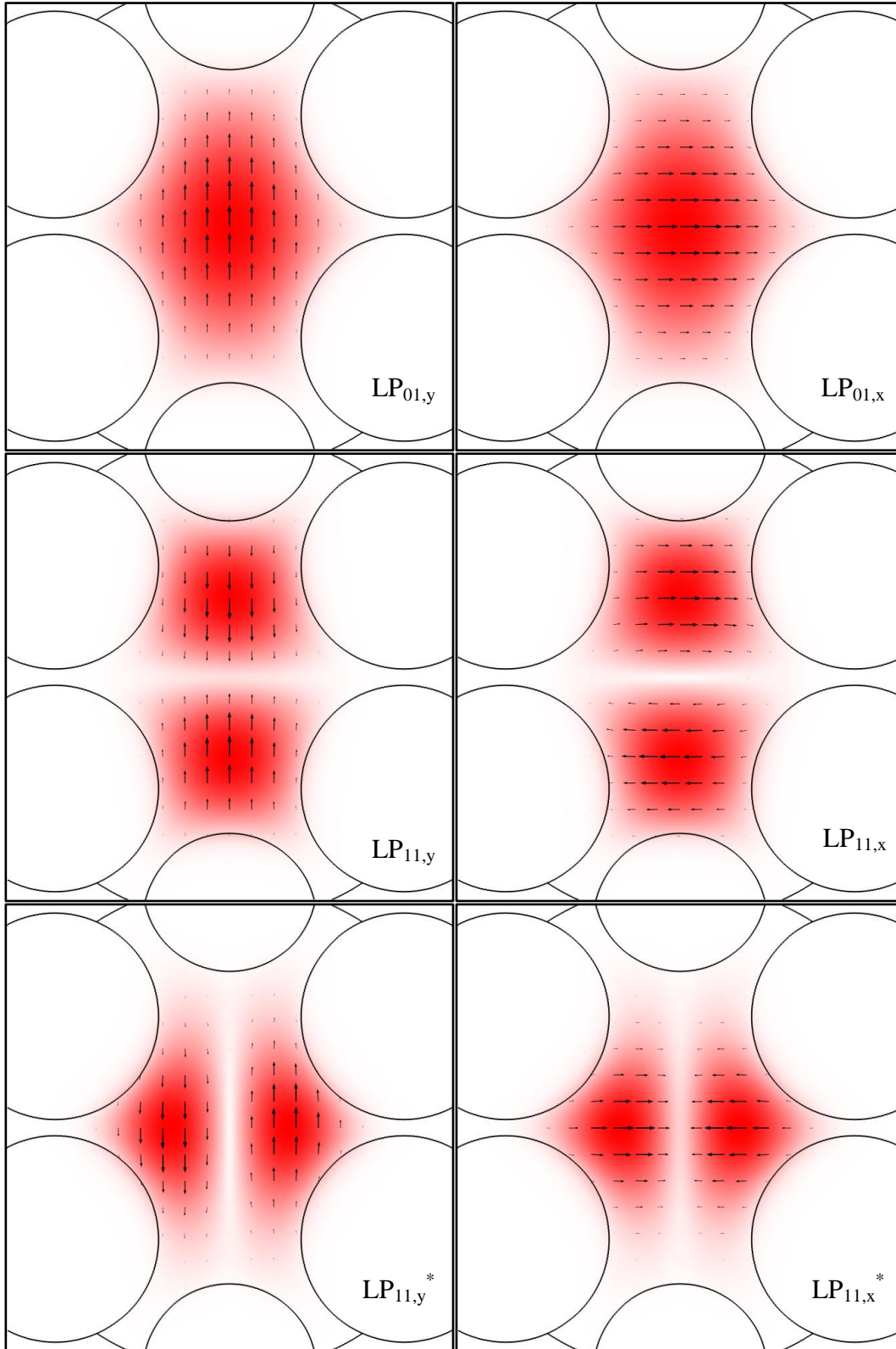


Figure 3.12: Normalised electric field intensities  $\sqrt{E_x^2 + E_y^2 + E_z^2}$  (red), in the spun Hi-Bi MOF calculated at 800 nm. Mode labels are included in the bottom right of each image. Each image is  $3 \mu\text{m}$  by  $3 \mu\text{m}$  square with the interfaces between the silica and air holes show as black lines. The direction of the electric field in the x-y plane is shown by the black arrows.

**Table 3.7: Fitting coefficients for the modes to equation (3.2). The column labelled N is used to indicate the degeneracy number of each mode.**

N	Mode	A	B	C	D	E	F	J	K
1	LP <sub>01,y</sub>	1.29×10 <sup>0</sup>	-4.05×10 <sup>-2</sup>	-1.82×10 <sup>-4</sup>	-4.03×10 <sup>-4</sup>	2.93×10 <sup>-3</sup>	4.22×10 <sup>1</sup>	1.05×10 <sup>-2</sup>	1.62×10 <sup>1</sup>
1	LP <sub>01,x</sub>	1.30×10 <sup>0</sup>	-3.94×10 <sup>-2</sup>	-2.49×10 <sup>-4</sup>	-3.49×10 <sup>-4</sup>	2.93×10 <sup>-3</sup>	4.01×10 <sup>1</sup>	1.05×10 <sup>-2</sup>	1.64×10 <sup>1</sup>
1	LP <sub>11,y</sub>	1.29×10 <sup>0</sup>	-5.91×10 <sup>-2</sup>	5.77×10 <sup>-4</sup>	-5.68×10 <sup>-4</sup>	2.93×10 <sup>-3</sup>	3.38×10 <sup>1</sup>	1.05×10 <sup>-2</sup>	1.47×10 <sup>1</sup>
1	LP <sub>11,x</sub>	1.31×10 <sup>0</sup>	-5.81×10 <sup>-2</sup>	5.13×10 <sup>-4</sup>	-4.84×10 <sup>-4</sup>	2.93×10 <sup>-3</sup>	3.30×10 <sup>1</sup>	1.05×10 <sup>-2</sup>	1.51×10 <sup>1</sup>
1	LP <sub>11,y</sub> *	1.25×10 <sup>0</sup>	-8.04×10 <sup>-2</sup>	1.08×10 <sup>-3</sup>	-7.55×10 <sup>-4</sup>	2.94×10 <sup>-3</sup>	4.14×10 <sup>1</sup>	1.05×10 <sup>-2</sup>	1.45×10 <sup>1</sup>
1	LP <sub>11,x</sub> *	1.12×10 <sup>0</sup>	-9.48×10 <sup>-2</sup>	-1.25×10 <sup>-4</sup>	-7.27×10 <sup>-4</sup>	2.93×10 <sup>-3</sup>	9.04×10 <sup>1</sup>	1.05×10 <sup>-2</sup>	1.65×10 <sup>1</sup>

**Table 3.8: Zero Group Velocity Dispersion points. These are visible graphically in Figure 3.14.**

Mode	LP <sub>01,y</sub>	LP <sub>01,x</sub>	LP <sub>11,y</sub>	LP <sub>11,x</sub>	LP <sub>11,y</sub> *	LP <sub>11,x</sub> *
Zero GVD(nm)	886.5	865.6	745.2	734.7	681.7	675.1

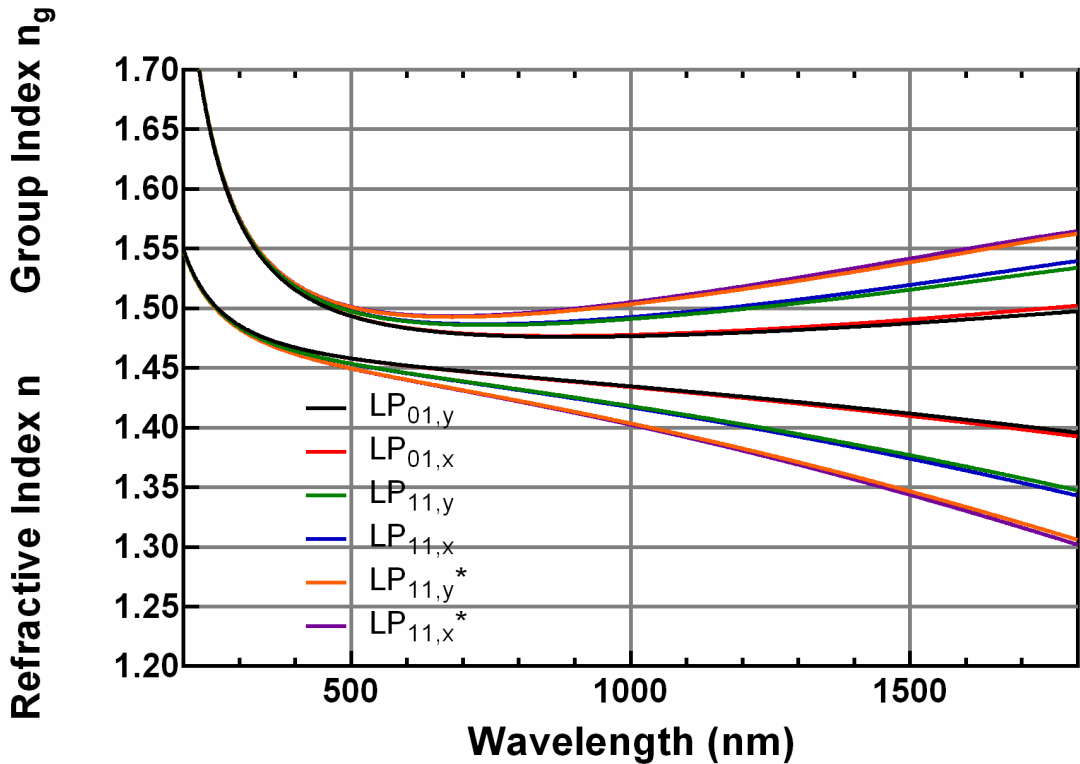


**Figure 3.13: Graphed fits for the first six spun Hi-Bi fibre modes. The refractive index is the lower group of curves; the group index is the higher group.**

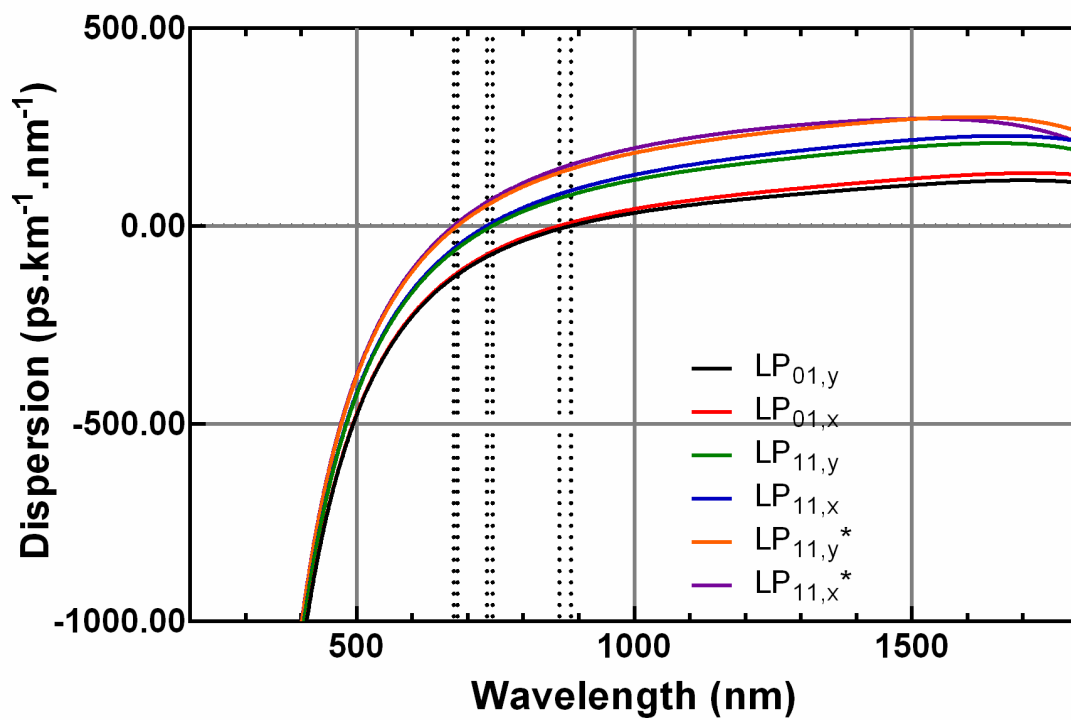


Figure 3.14: Dispersion of each mode in the spun Hi-Bi fibre. The zero GVD points for each mode are listed in Table 3.8.

## ***4 Observation of Supercontinuum Generation in Higher Order Modes of Microstructured Optical Fibre.***

This chapter details the results of observation of supercontinua in HOMs of MOF for the purpose of understanding the underlying physics of the wavelength shift of the dispersive wave. This was inspired by work done previously by Duck et al [27] discussed in section 1.5.1.

### ***4.1 Overview***

A suitably intense light source, when focussed onto a MOF and coupled into the fundamental mode of the MOF waveguide, will generate a supercontinuum if there is some component of the initial input radiation or nonlinearly broadened radiation in the anomalous dispersion regime of the MOF allowing solitons to form [2].

This section of the thesis shows novel measurements on the spatial output of supercontinuum generated in MOF. The apparatus used and the measurements taken are the first of this kind and give insight into the complex electromagnetic mode dynamics that can exist in MOF as shown in Figure 4.1, where multimode nonlinear effects can be seen visibly when aligning a MOF for continuum generation. Sections 1.4 and 1.5 provide the background theoretical explanation for this experimental chapter.

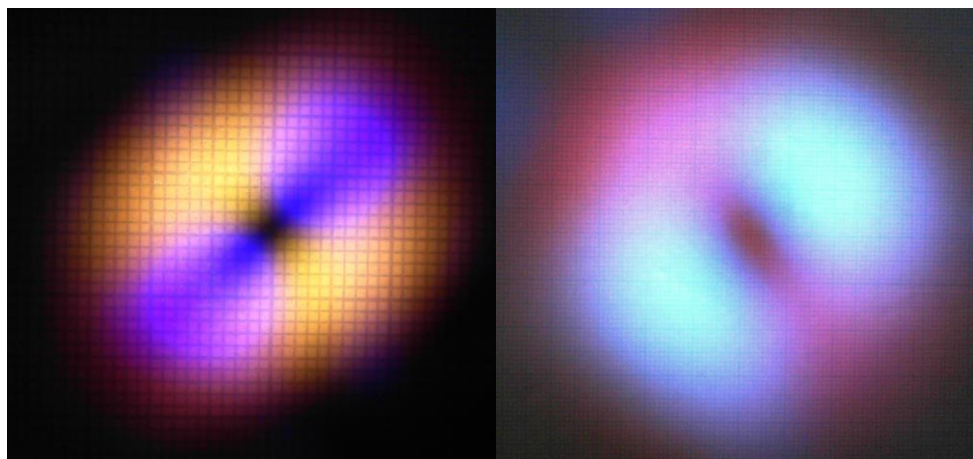


**Figure 4.1: Images of interesting supercontinuum generated in MOF showing the various colours generated in different fibre modes from ~800 nm light.**

Often the broadest continuum will occur when the maximum amount of power is coupled into the waveguide; hence, the fundamental mode is often used as it has the highest coupling efficiency. However, as shown in Chapter 3, the waveguide dispersion of MOF changes for each allowable mode, and for certain wavelength ranges the

fundamental mode will often have normal dispersion whereas the higher order modes may have anomalous dispersion. In these cases, it is often possible to generate a continuum by coupling into the higher order modes where solitons can form. For example in Figure 3.7 it can be seen that the fundamental  $HE_{11}$  mode is anomalous for wavelengths above 810 nm whereas the next  $TM_{01}$  mode is anomalous for wavelengths above 659 nm. As solitons can only form in anomalous dispersion, it was expected that pumping into this fibre in the 700 nm – 800 nm range would excite solitons in higher order modes and not in the fundamental mode as they would be unable to form under normal dispersion.

In reality, when using a lens to couple to the MOF such in the setup described in 2.3.3, it is difficult not to couple into multiple EM modes of the MOF. The focussed beam waist of the laser on the fibre core will usually overlap the mode field area of numerous EM modes.

These higher-order mode continua have been studied in the past [28–31], however, the measurement of the continuum output was limited to basic spectral measurements and colour photographs. In the experiments outlined in this chapter, using the system described in 2.3.5, it is possible to observe all EM modes and measure the wavelengths generated. Every MOF is different, with some having complicated mode structures or degenerate modes. Some are elliptical and some are hexagonally symmetrical.

Coupling between EM modes within the MOF seemed to be relatively minor except for when modes were closely degenerate in energy. Simulations shown in Chapter 3 indicate that most MOF had no effective index matching between non-degenerate modes at any wavelength and hence there should be no allowed coupling between them as the EM field propagates in the waveguide. This becomes more complicated with the degenerate modes in the hexagonal core of the MOF as will be discussed.

## ***4.2 Results and Discussion***

Investigation of supercontinuum generation in the higher order EM modes within MOF has revealed unique spectral and spatial features [28,29] not observed for supercontinua in the fundamental EM mode. Continuing work examined the temporal variation between modes [47], the spectral variation between supercontinua generated in different EM modes [31,33], and EM mode variation within a single supercontinuum [34]. A

paper [48] investigated the inter-conversion between modes in a few-moded solid core step index fibre excited at 1045 nm and the possibility of energy interchange between these modes at 1120 nm.

The Koronov and Cherif papers [29,31] detail the existence of a region between the zero group velocity dispersion (GVD) wavelengths for the fundamental mode and for the higher modes that will support soliton generation in only the higher order EM modes.

This work investigates this 700 nm – 850 nm region with a technique that allows spatial and spectral characterisation of the supercontinuum light emitted at the output of the MOF. The ability to offset pump the higher order EM modes by precise direction of the input laser into the MOF is central to this work as detailed in Figure 4.2. The 700 nm – 850 nm region allows for solitonic behaviour purely in higher modes while the group index differences will dictate the spectral characteristics of the resultant continuum [49].

This unique setup excites different EM modes by shifting the position and angle of the focussed beam across the fibre core with nanometre precision as detailed in sections 2.3.2 and 2.3.3. This is shown schematically in Figure 4.2(a-c), where pumping in the centre of the core excites the fundamental mode shown in Figure 4.2(d) and pumping off axis excites higher order modes shown in Figure 4.2(e,f). There is evidence in Figure 4.2(e) of both the fundamental mode and the higher mode being excited by the laser at the input position shown in Figure 4.2(b) where the red dot is representative of the beam diameter. The data set recorded allows the spatial EM mode at each wavelength to be extracted and viewed.

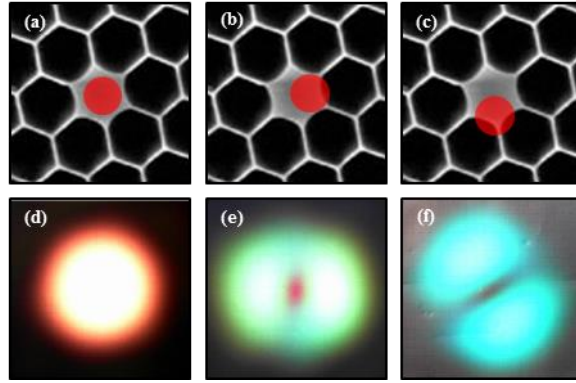


**Figure 4.2: Variation of integrated supercontinuum electromagnetic mode structures imaged with schematic of estimated laser beam position on MOF core face. Higher order modes (e) and (f) result from offset fibre inputs (b) and (c). (d-f) are CCD recorded images of the integrated supercontinuum at the output of the MOF.**

Very different supercontinuum spectra emerge from the MOF as the input beam position on the MOF core is altered. Figure 4.3 displays four measured spectra with the only difference being the position at which the laser beam strikes the input face of the MOF core. All other input parameters, the 200 fs pulse duration, the centre wavelength of 785 nm, and the 15 nJ pulse energy were fixed. The insets of each plot show the visible light output of the MOF for each case integrated by the CCD array over all responsive wavelengths.

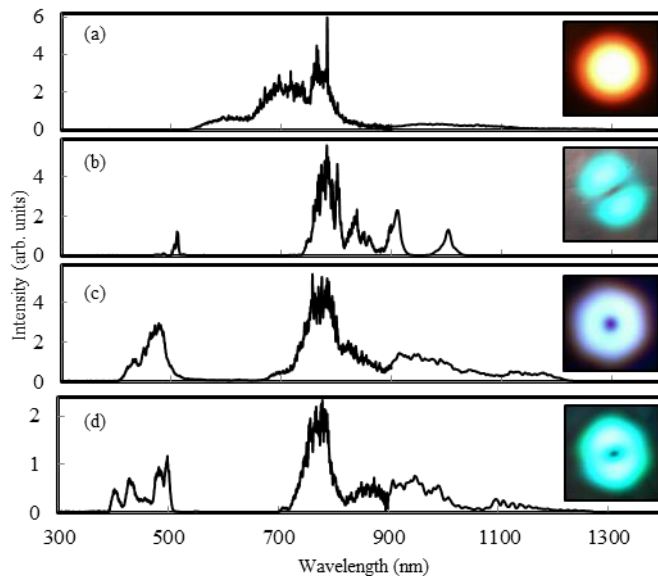


**Figure 4.3: Spectral variation of output supercontinuum and electromagnetic mode structures with position for identical input pulse duration, power and wavelength.**

The striking differences between the spectra in Figure 4.3 indicate that different processes dominate in the fibre. Supercontinua generated through solitons propagating in higher order EM modes, as in Figure 4.3(b-d), exhibit evidence that the input energy

is coupling into lower order solitons, to produce dispersive waves and Raman self-frequency shifted solitons [2] upon fission, resulting in discrete spectral features across the broadened spectrum and retaining the spatial mode properties. In contrast, the continuum generated by coupling into the fundamental EM mode, below the zero GVD wavelength, as shown in Figure 4.3(a), yields a spectrum broadened by non-solitonic third-order nonlinear processes, where all wavelengths of light produced occupy the fundamental EM mode. Generating a supercontinuum in the fundamental EM mode above the zero GVD wavelength, Figure 4.4 matches the expected, well documented [2,50], solitonic and third-order nonlinear process broadened output, with all wavelengths propagating in the fundamental EM mode.

Figure 4.4 and Figure 4.5 display the emission spectrum in blue for the UV-Vis spectrometer and in green for the NIR spectrometer, with the spatial mode as measured at each of the wavelengths identified. The rich data set available from the experiment has a spatial result recorded for each pixel of the two spectrometer arrays between 300 nm – 1600 nm. The spectrum recorded at each raster point was an average of at least 656 million individual laser, and therefore supercontinuum, pulses.

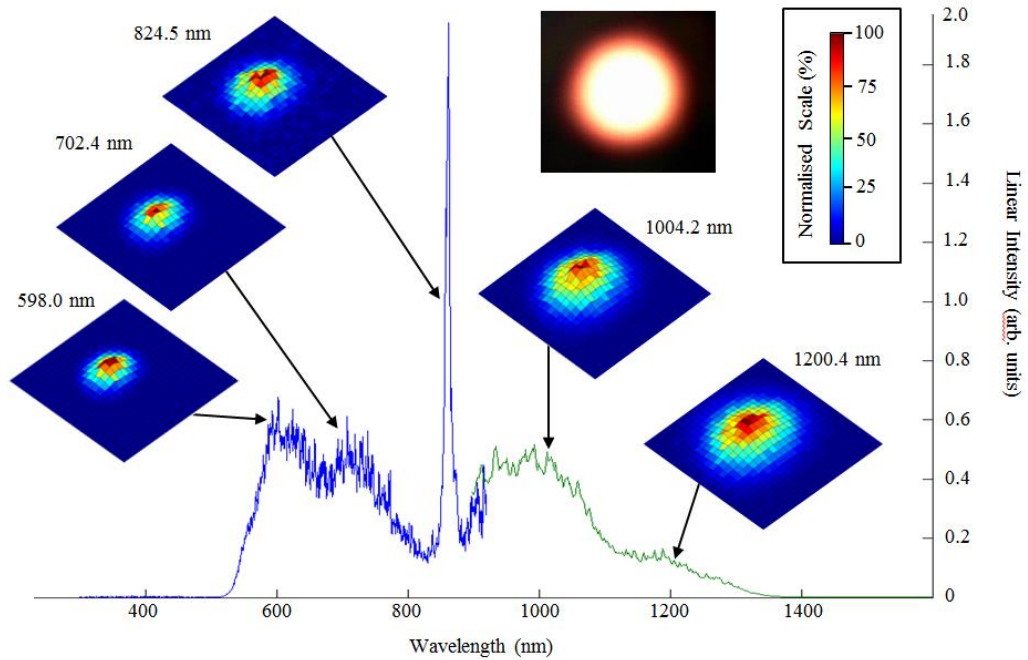


**Figure 4.4: Measured spectrum and spatial mode properties of a SC generated in the fundamental mode of Thorlabs NL-2.8-850-02 MOF using a 15 nJ, 210 fs input pulse at 860 nm, 10 nm above the zero GVD wavelength. Inset is a visible camera image. The spectrum is representative of the broad continuous spectra characteristic of a fundamental EM mode generated SC in MOF.**

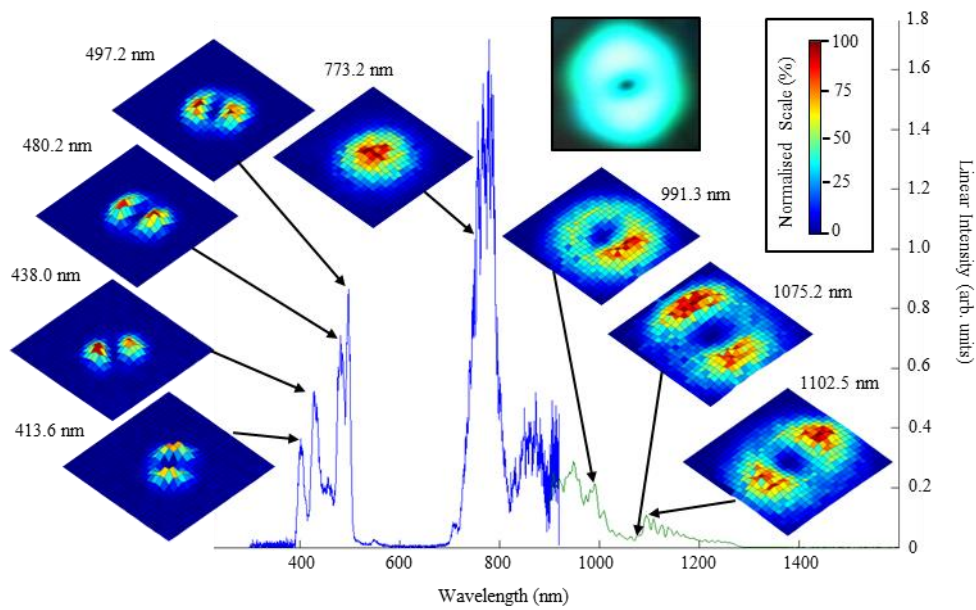


**Figure 4.5: Measured spectrum and spatial mode properties of a SC generated in the higher EM modes of Thorlabs NL-2.8-850-02 MOF using a 15 nJ, 210 fs input pulse at 784 nm, 66 nm below the fundamental EM mode zero GVD wavelength. Inset is a visible camera image.**

The spatial mode structure of higher order EM mode supercontinua in Figure 4.5 reveals a previously undocumented spectral complexity with six distinct dispersive wave peaks ranging from 400 nm – 550 nm generated using an input pulse wavelength of 784 nm. Cristiani et al. [51] proposed that each dispersive wave peak present in a supercontinuum output corresponds to a different fission event of a higher order soliton excited by the input pulse. With this interpretation, the spectrum presented in Figure 4.5 reveals that the multiple peak features are characteristic of dispersive waves emanating from fission of lower order, possibly  $n=2$  solitons, occupying higher order EM modes. Furthermore, it was found that light in each spectral peak occupies a different, closely degenerate, higher order EM mode of the MOF as shown in Figure 4.6.

Figure 4.4 and Figure 4.5 correlate well with the group index matching as shown in Figure 3.6, where the broadening of the fundamental and the higher order mode spread to equivalent points on the group index for the corresponding mode [49]. Further investigation into this is discussed in Chapter 5.

The different relative rotational position of the mode intensity lobes are a measure of the alignment of those modes relative to the structure of the fibre. As the fibre has hexagonal symmetry, or near to it, the expectation is that the fibre should support modes exhibiting this underlying symmetry. A detailed investigation of the spatial mode of

identifiable peaks in the dispersive wave region matched the expected symmetry as shown in Figure 4.6.

The discrete mode effective refractive indices are not expected to cross over in the 800 nm – 1300 nm region so the coupling of light into the fundamental mode differs from Cheng [48] and is ascribed to the coupling coefficient for that mode based on the overlap between the input pump beam and the mode cross-section at launch.

The two lobe nature of these modes indicates a linear polarisation form of either the  $TM_{01}$ ,  $TE_{01}$  or  $HE_{21}$  modes shown in Figure 3.3, or some combination of these modes. As both  $TM_{01}$  and  $TE_{01}$  modes are rotationally symmetric it is unlikely they will deviate significantly from the simulation due to fibre imperfections and will continue to be nondegenerate. However, the  $HE_{21}$  modes are not rotationally symmetric, and are affected by alignment with the hexagonal core and the perturbations of that hexagonal core shape arising from manufacturing imperfections and external bending of the fibre. These imperfections have most likely caused the light coupled into the  $HE_{21}$  mode to split into six variations of  $HE_{21}$  and  $HE_{21}^*$  that are sufficiently degenerate to loosely couple between each other and yet propagate with slightly different propagation constants and optical power. This has caused the magnitude of the dispersive wave spectra, labelled (a) – (e) in Figure 4.6, to vary.

The slightly larger mode dimensions in Figure 4.6(d-f) are the basis of the major axis postulate for these modes, while the slightly smaller dimensions of modes in Figure 4.6(a-c) are consistent with the minor axis postulate.

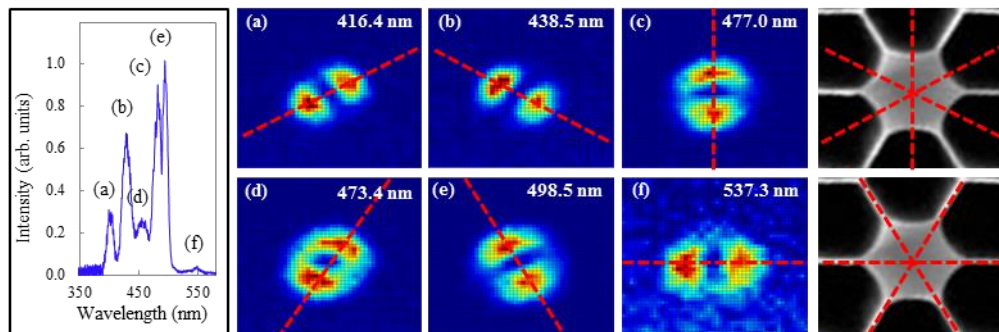


**Figure 4.6: Measured dispersive wave spectrum with peaks (a)-(e), measured spatial mode of each identified peak and postulated orientation of mode within the MOF core.**

Note that these modes are not energetically degenerate. The higher order mode solitons are excited in discrete spatial orientations and, when undergoing fission, produce

dispersive waves spatially aligned to their initial mode. The author postulates that due to the imperfect fibre core geometry, that is, loss of hexagonal symmetry, the electromagnetic modes are not degenerate and thus the dispersive waves should appear at different energies.

However, it would also be possible to explain the different shifts as due to variations in the power of the corresponding infrared solitons, as higher power solitons will shift to a longer wavelength in the infrared more rapidly, creating a greater shift in the trapped blue light as discussed in section 1.4.6. The two sets of three major and minor axis oriented modes overlap in wavelength, possibly due to the power in the individual modes. Further investigation into the polarisation of the EM modes in MOF is discussed in Chapter 6.

### ***4.3 Conclusions***

The figures included above graphically convey new details of spatial mode features in supercontinua generated in higher order EM modes in MOF that have not been measured before. Discrete spectral features are associated with symmetrical spatial patterns arising from the host fibre geometry, and suggest the electromagnetic mode pairing between the longer wavelength solitons and associated visible dispersive waves. These data should inform theoretical studies and modelling of soliton fission and dispersive wave generation.

## ***5 The Sparse Supercontinuum.***

### ***5.1 Overview***

As a full multiple-octave broad band supercontinuum results from the action of a number of frequency mixing and frequency generating  $\chi^3$  nonlinear effects, it is often difficult to observe and experimentally validate any individual process, because the associated spectral detail is lost to the wave mixing and frequency broadening that are occurring simultaneously. Gorbach and Skryabin [22,23], Chen et al [25], Stone et al [52], and even as far back as Beaud et al and their work in telecoms fibre [24] have inferred the shift in the blue wavelength, or dispersive wave, side of the supercontinuum to shorter wavelengths by measuring the limiting spectral width of the continuum (section 1.4.6). These observations, however, necessarily include broadened and wave-mixed components of the continuum.

While in simulation it is possible to analyse the propagation of a pulse in detail, experientially this is not achievable. Observations are usually limited to a detailed measurement of the average of millions of input pulses of laser light and the resulting output pulses. However, what occurs within the fibre is somewhat hidden. By far the most common analysis of supercontinuum generation uses the variation of input parameters (often pulse power) on the same length of fibre. The supercontinuum produced is usually compared to a simulated split step Fourier propagation of a pulse through the fibre using the Taylor series expansion of the fibre propagation constant (see section 10.1) and the resulting simulated spectral envelope is shown to match roughly with the experimental data [2]. While this is a validation of the theoretical model, the model itself must combine all known theoretical processes that contribute to supercontinuum generation and it is difficult to test a single process, as any individual event is lost to the broadening and smoothing that gives that desired continuum.

In this chapter, the confusing, competing effects have been avoided, and direct observation of changes to discrete features in the blue spectral region, associated with the Raman shift of solitons in the red side of the supercontinuum, has been recorded. This surprising and unique observation is of blue light, once generated, shifting in its wavelength and is the required experimental validation of the theoretical explanation for

the formation of, and limits to, the short wavelength side of a supercontinuum [22,23,53].

This section of the thesis shows experimental work with both hexagonal and elliptical core MOF that resolves the individual effects of soliton to visible nonlinear interactions within a supercontinuum generation by exciting a limited number of solitons. This novel approach is compared to recent theories [23] and is the first of its kind to directly observe these effects in a typical supercontinuum generation setup as opposed to indirectly looking at the bounding edges of the continuum or seeding visible light behind a single soliton. These results can hence be taken as experimental validation of the theory in isolation of competing, or occluding, effects.

These results are achieved by spatial and spectral characterisation of the supercontinuum generated by the MOF through the generation and observation of spectrally sparse supercontinua. While this description may be at odds with the usual and stated definition of a supercontinuum, the ability to pump energy into and excite solitons in higher order electromagnetic modes (EMMs) within a micro-structured optical fibre allows the generation of low order solitons. When these solitons fission and self-Raman shift to longer wavelengths, they demonstrate the characteristic extreme broadening of the input pump light over multiple frequency octaves, but with a sparse and dispersed spectrum displaying a small number of discrete peaks [38,54], rather than a filled-in continuous supercontinuum.

## ***5.2 Method and Reasoning***

A supercontinuum was generated by a mode-locked titanium-doped sapphire femtosecond laser (Spectra Physics Tsunami) coupled into highly nonlinear MOF (Thorlabs NL-2.8-850-02 MOF and OFTC Spun Hi-Bi MOF).

While a normal supercontinuum is a continuous spectral emitter over more than an octave in frequency, in order to observe interactions between the red-shifting solitons and the blue-shifting short wavelength side of the generated light, the continuum was deliberately tuned to be spectrally sparse, while still being strongly nonlinear. With this approach, the individual index matching effects may be observed, and are not lost in the general broadening effects that obscure the individual nonlinear processes in a standard supercontinuum. The desired approach to this discrete observation is to lower the

soliton order  $N$ , where the functional determination of  $N$  as a function of experimental parameters is described in Equation (5.1) [2,10].

$$N^2 = \frac{T_0^2 P_0 \omega_0 n_2(\omega_0)}{|\beta_2| c A_{eff}(\omega_0)} \quad (5.1)$$

Experimentally, most parameters are held relatively constant by the laser, in that the pulse temporal width  $T_0$ , power  $P_0$ , and angular frequency  $\omega_0$  are stable within a few percent over time. The MOF's nonlinear refractive index,  $n_2(\omega_0)$ , and the effective mode area,  $A_{eff}(\omega_0)$  are constant for a fixed input wavelength. The dispersion,  $\beta_2$ , varies significantly with mode, however, and shifting to higher order modes will usually increase the overall dispersion of the fibre in the anomalous region as may be seen in Figure 3.7 and Figure 3.14. With fine-tuning of the coupling afforded by the piezo-electric controls and the correct laser power, the soliton order can be easily reduced to 2 or 3 in a higher order EMM where the increased dispersion gives a lower  $N$  while keeping the high intensity  $P_0$  required for other nonlinear effects.

### 5.3 Results and Discussion

The group index of the propagating modes within the fibre was calculated using SMTP [43] and used to match the interaction between the blue light and the solitons.

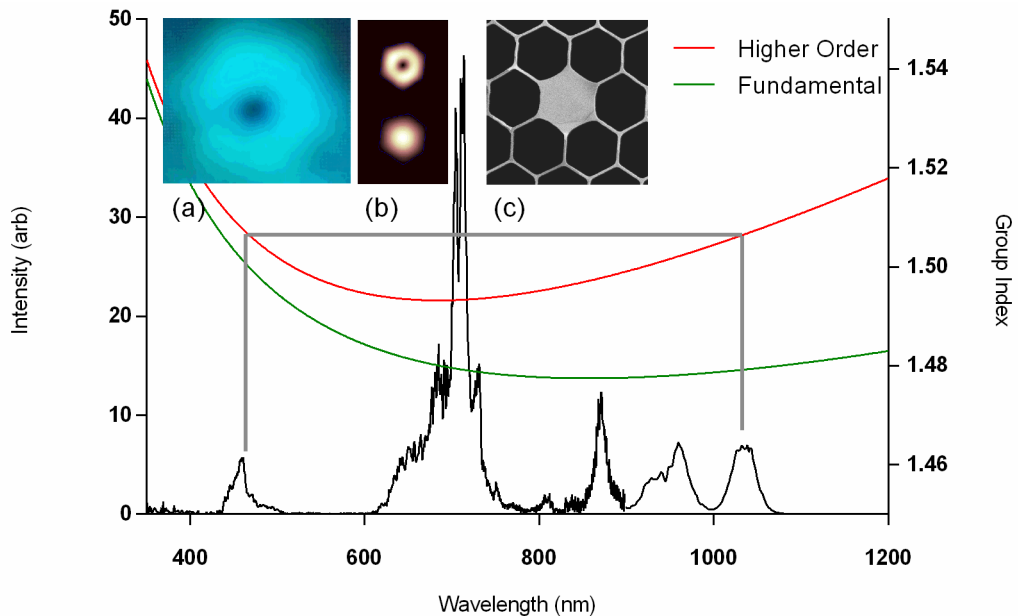


**Figure 5.1:** Sparse supercontinuum generated in 0.6 m of Thorlabs NL-2.8-850-02 MOF from the averaged propagation of 100 kW 180 fs Ti:S pulses at 780 nm. Inserts show (a) visible camera image of supercontinuum, (b) modelled mode intensity profiles at 800 nm for the fundamental and the 2<sup>nd</sup> order mode and (c) an electron micrograph of the 2.8 micron average diameter MOF core.

Figure 5.1 shows a continuum for one of the industry-standard MOFs (NKT Photonics, Denmark, sourced through ThorLabs) used for nonlinear effects and creating a broad continuum when energy is coupled into the fundamental EM mode. When coupling light into this fibre it is very easy to couple into multiple EMMs and often the more extreme wavelengths on the blue side of the continuum are observed to occupy these higher order modes [54]. The measured spectral changes of a MOF with length of fibre shows that the blue light evident in Figure 5.2(a) at ~480 nm shifts in wavelength to shorter values shown at ~400 nm in Figure 5.2(b) as it progresses through an additional 900 mm of fibre. This is an 80 nm shift in wavelength over less than 1 m of propagation through silica. Confirmation of this light being in a higher order EM mode is obtained from observation of the far field mode output at the corresponding wavelengths using the experimental apparatus in section 2.3.5.

Interpreting the theories for this shift in the blue light [22,53] requires that both the blue and the soliton spectral peaks stay at the same group velocity even as the solitons self-Raman shift to longer wavelengths. The group refractive indices plotted and the guiding lines shown in

Figure 5.1 clearly show the values of the group indices match for the blue light (480 nm) and the solitonic radiation in the NIR (1100 nm) for the higher order EM mode (red curve) and not for the fundamental EM modes (green curve).

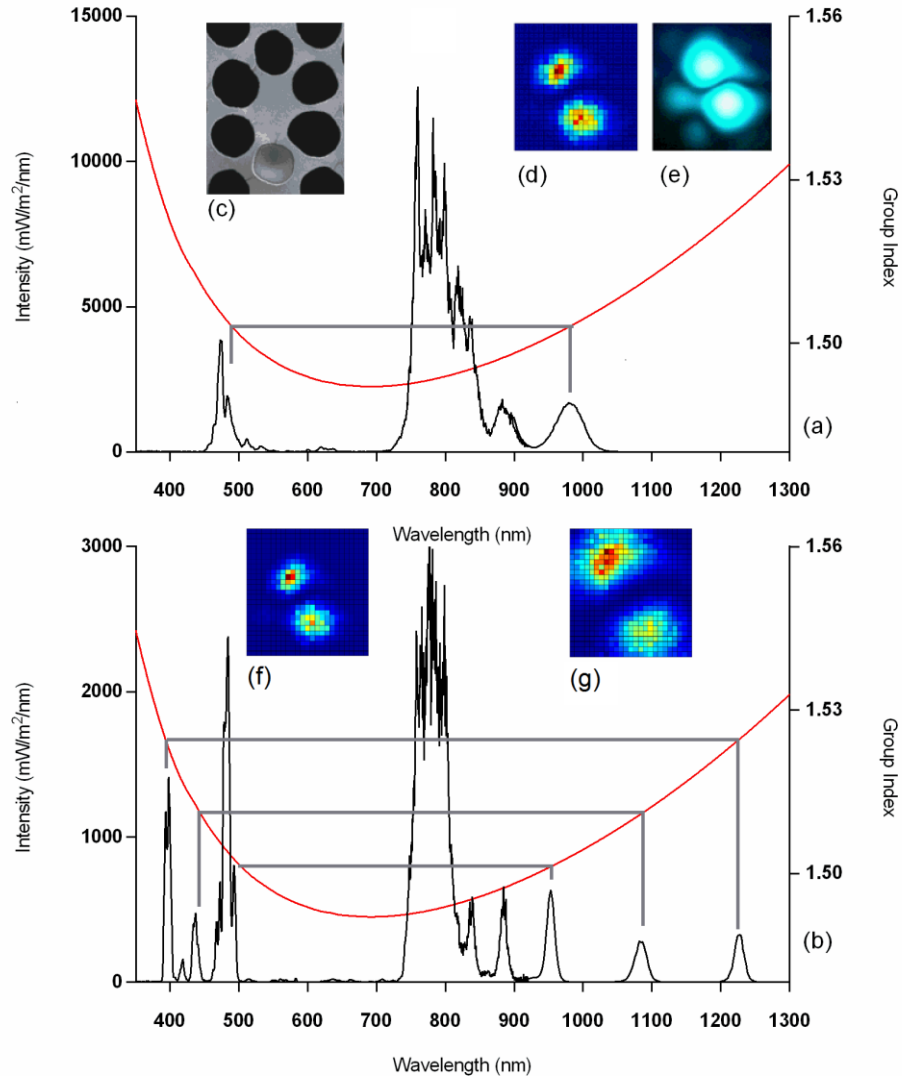


**Figure 5.2: Spectrum of a sparse continuum generated in the Spun High Birefringent MOF from the averaged propagation of 100 kW 180 fs Ti:S pulses at 780 nm through 0.1 m (a) and 1 m (b) of fibre in the 2nd order EMM (group index shown in red) with a low coupling efficiency. The reduced length shortens the interaction time and reduces the redshift and blueshift of the solitons and the blue light. Inserts show (c) an electron micrograph of the MOF core; (d) the measured far field mode intensity of the MOF output of (a) at 480 nm; (e) visible camera image of supercontinuum and; (f) and; (g) show the far field output of the long fibre at 395 nm and 1085 nm respectively, where the different spatial size is as a result of the fibre numerical aperture at each wavelength.**

It was found that moving from the Thorlabs MOF in Figure 5.1 to the OFTC MOF in Figure 5.2 with a slightly larger core, and hence lower nonlinear index, removed the contribution of some nonlinear effects, most importantly four wave mixing, and helped reduce the soliton order. This is clearly observable in the long wavelength side of the

spectrum shown in Figure 5.2(b). Here a series of solitonic shaped spectral peaks are clearly defined. All of these solitons occupy the same EMM in this birefringent fibre.

The blue side of the continua in Figure 5.2(b) shows a seemingly complex series of strong peaks, all of which are propagating in the same EMM as the solitons. Most of these peaks can be shown to be matched in their group velocities to respective solitons in the near infrared as can be seen by the indicating lines on the spectrum and the overlaid group index for that mode. For the first time the direct interaction of a soliton and corresponding trapped blue light has been observed in MOF from a femtosecond pulsed laser typically used in supercontinuum generation with no pre-generation of solitons or lagging blue light [22,23].

As these interactions take time, the longer the fibre, the further both the wavelengths of the solitons and the blue light will be able to shift from the pump wavelength. However, the group index matching should be observable at all points in the fibre. This was tested by cutting back the fibre shown in Figure 5.2(b) to only 0.1 m, as shown in Figure 5.2(a), resulting in the simpler continuum seen. Due to the length, and associated ~500 ps transit time along the fibre, there has not been sufficient time for the different solitons to separate spectrally from each other, however, they do appear to be nearly half way along the shift to the longer wavelengths seen in Figure 5.2(b). In Figure 5.2(a) the discrete blue light peaks appear at longer wavelengths closer to the pump as well as in a clustered group compared to the shorter dispersed peaks in Figure 5.2(b). Checking the group index of this mode and the observable solitons again shows a correlation, as can be seen by the overlaid lines. The wavelengths are not as short on the blue side as in the longer length of fibre, as the NIR solitons are yet to Raman shift to longer wavelengths.

The shifting of the blue light to shorter wavelengths can be attributed to intra-pulse four-wave mixing [21,23] as the fibre dispersion alters due to the nonlinear interaction of the soliton and media, creating an efficient phase matching process within the pulse. As the blue light is pushed to shorter wavelengths, the limit of the waveguide material begins to dominate and the group index increases dramatically as the 380 nm absorption band of silica is approached. Thus, it becomes very difficult to shift the blue light to wavelengths below 400 nm, as the steepening group index curve causes the bands of blue light to cluster to this limit. Most published supercontinua generated in uniform

fibres have this edge evident in the spectrum. There has to be a much greater increase in the NIR Raman shifted soliton wavelength to effectively index match to a much smaller wavelength shift to blue, unless the waveguide is manipulated by tapering.

#### ***5.4 Conclusions***

The clear experimental results presented in this chapter demonstrably support the theoretical framework of Gorbach and Skyrabin [22,23] with the clear group index match of the Raman shifted NIR soliton peak wavelength and the shifting blue wavelengths in uniform fibre. By utilising the dispersion properties of higher order electro-magnetic modes in micro-structured optical fibre, these very low order solitons generated in a spectrally sparse continuum allow the definitive correlation of the soliton with its index matched, and shifting, blue light without the obscuration of nonlinear wave-mixing effects. This is the first discrete measurement of this effect in the femtosecond pulsed regime as opposed to an inferred result from the limiting spectral boundaries of the continuum.

## **6 Polarisation Study**

### **6.1 Overview**

The polarisation state of the light output from the MOF can be measured to yield information on the efficiency with which light is coupled to a particular mode within the fibre. The discussion in section 1.1.4 on the allowed waveguide modes of the fibre, as well as the MOF mode simulation in Chapter 3, are essential background for this section, as the linearly polarised input pump light has to couple to a set of the allowed waveguide modes. The output polarisation state must be interpreted following analysis of what the measurement tool used actually does to the state.

### **6.2 Experimental and method**

Based on the knowledge of the EM modes propagating in the fibre, an understanding of the likely polarisation of the output emerges as the far field emission is generated by the mode oscillations on the end surface of the fibre. In fact, with a tool as simple as a linear polariser, it becomes possible to identify various EM modes based on their field shape with respect to the polarisation angle and the direction of rotation.

To visualise this, the modes shown in Figure 3.3 can be imagined to propagate out in a conical shape matching the numerical aperture of the fibre. The polarisation of this output is considered linear with some spatial electrical field pattern.

From the Thorlabs hexagonal type MOF, the four degenerate modes can be identified with a linear polariser. The HE modes will rotate against the rotation of the polariser and the TM and TE modes go with the rotation of the polariser. To distinguish between the two HE and TM TE modes the orientation of the dark null is either with or against the direction of polarisation.

When observing the vector mode solutions such as  $TE_{01}$ ,  $TM_{01}$ ,  $HE_{21}$  and  $HE_{21}^*$  through a linear polariser, they appear as the  $LP_{11}$  mode as expected. Even though all these modes have similar spatial intensities, they can be differentiated as shown in Figure 6.1.

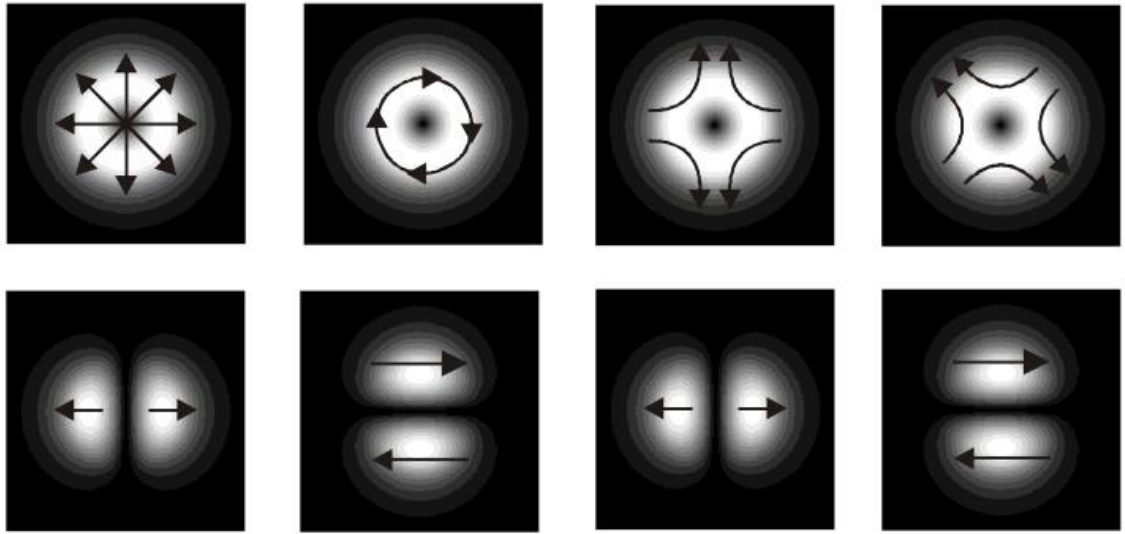


**Figure 6.1:** Top row shows  $TM_{01}$ ,  $TE_{01}$ ,  $HE_{21}$  and  $HE_{21}^*$  from left to right. Arrows indicate the direction of the electric field polarisation. The bottom row shows the result of placing a linear polariser in the horizontal direction on each of these modes. If the polariser is rotated the resulting fields from the TE and TM modes will rotate with the polariser while the HE fields will rotate in the opposite direction. In this manner, all four modes can be identified.

This effect applies equally when these modes are split degenerately and is applicable to the hexagonal MOF used in this thesis. Figure 6.2 shows the effect of linearly polarising modes within one of these hexagonal MOF. As expected the results mimic the LP mode structure observed in birefringent optical fibres and as shown in Figure 6.1 and can be used to distinguish modes that in their non-polarised states have near identical mode field profile intensities.

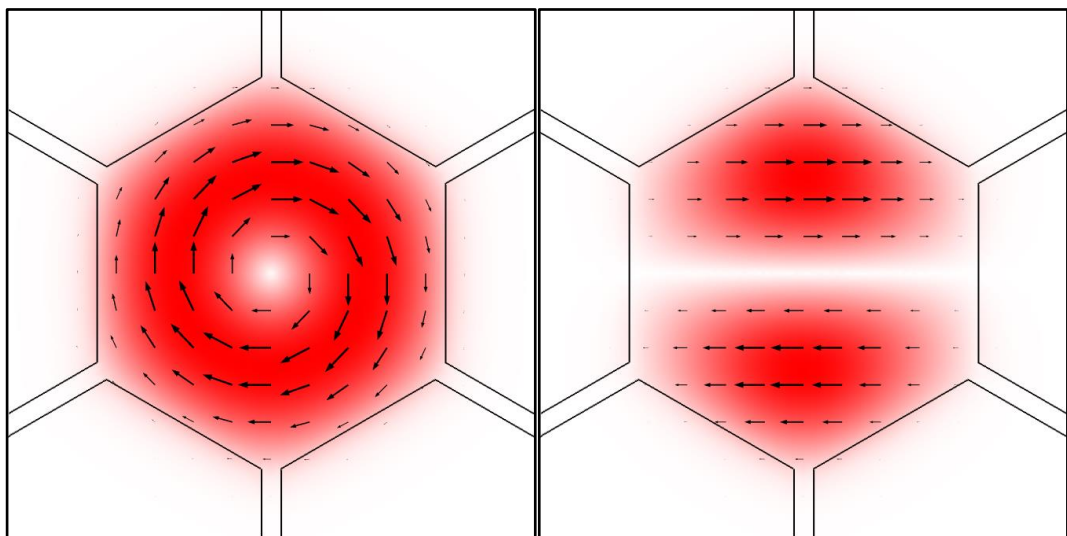


**Figure 6.2:** This is the  $TE_{01}$  mode from Figure 3.3 on the left and the same mode with a horizontal linear polariser applied on the right.

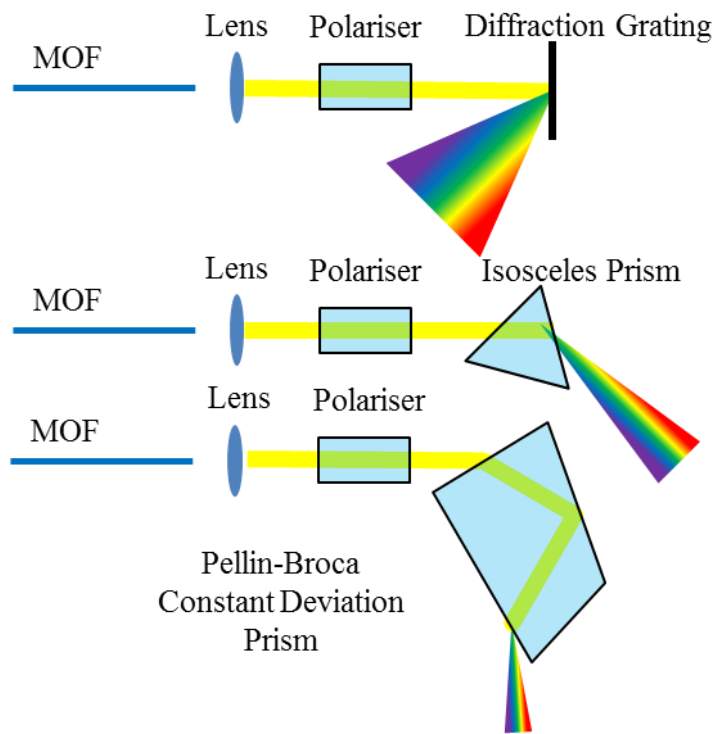


**Figure 6.3: Experimental arrangements used to investigate the polarised supercontinuum output from the MOF. The diffraction grating and the prisms were used in an attempt to spectrally resolve the continuum, however, they were found to inevitably tamper with the polarisation state.**

Experimental setups shown in Figure 6.3 were used to observe the polarised supercontinuum output. One disadvantage of using a prism or grating to observe the output of the supercontinuum is that each device will modify the polarisation of the resultant light. Gratings, in particular, have varying reflection coefficients in the parallel and perpendicular plane as seen in Figure 6.4 as well as a sine dependent dispersion.

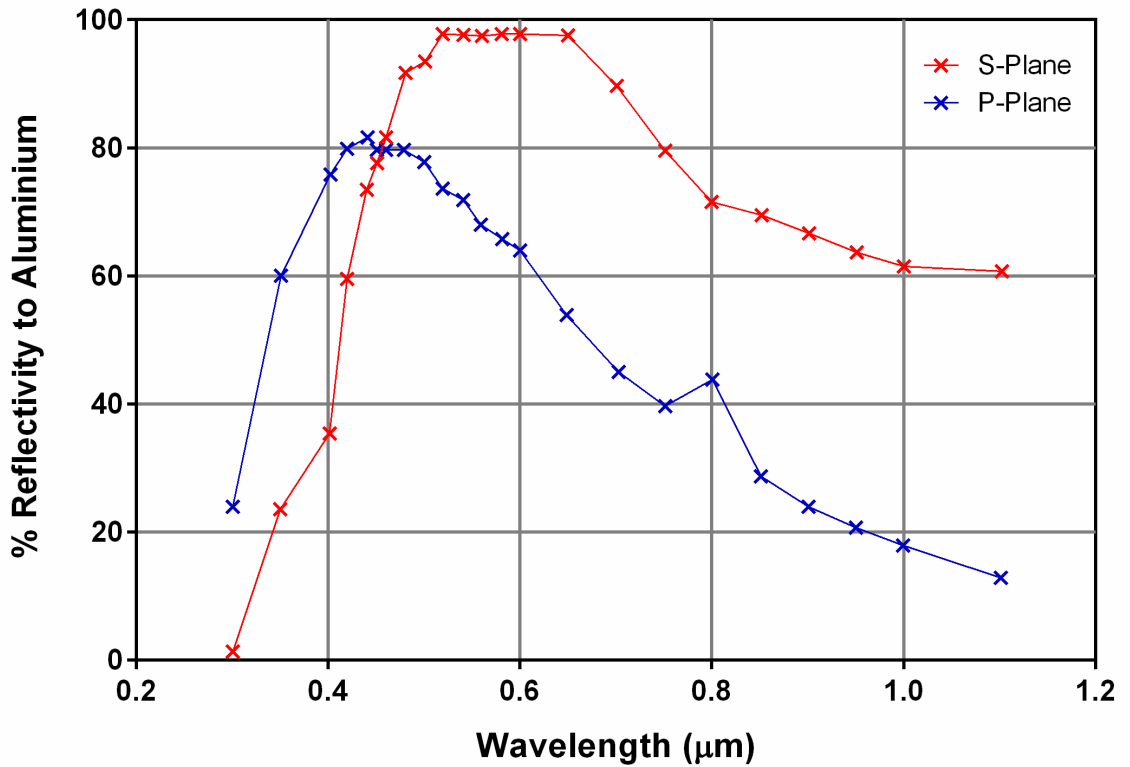


Figure 6.4: An example of the P and S plane polarisation reflections from a Richardson Gratings ruled reflection grating [55].

As prisms are usually used with angles of incidence of more than 60 degrees, the first surface external reflection is different in the parallel and perpendicular planes, as is the internal reflection for the constant deviation prism and also the exit face transmission for both prisms used. Of course, the prism dispersion comes from the prism material refractive index. In addition to these methods, the polarisation state was also investigated using a quarter wave plate polarimeter, however, these devices do not work well with broad light sources as the quarter wave plate is only useful over a limited bandwidth and they are not well suited to rapidly changing polarisation states. The results shown in this chapter are all taken with the setup in Figure 6.5, using a Glan-Thompson polariser and not pursuing the detailed spectral information.

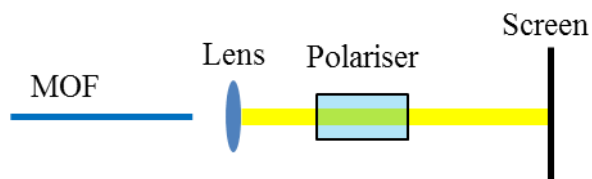
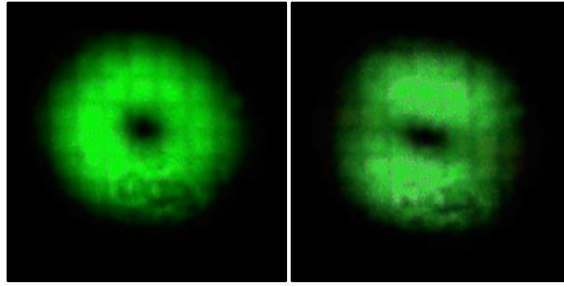


Figure 6.5: Simple polarisation state measurement.

### 6.3 Results and discussion



**Figure 6.6: Image of MOF supercontinuum output in higher order mode without a linear polariser (left) and with a horizontal linear polariser (right).**

In Figure 6.6 a typical supercontinuum is generated in a second order mode of NL-2.8-850-02 MOF and collimated using a microscope objective onto a screen. A variation in the intensity of this mode structure when a linear polariser was placed before the screen can be seen with stronger lobes at the top and bottom of the previously evenly distributed circular mode. This matches the effect shown in Figure 6.2. As discussed in Chapter 4, it is difficult to excite a single pure higher order mode and, as such, the resultant output is usually a combination of degenerate or closely degenerate modes.

The propagation of multiple modes creates a problem when using this method to identify them. For example if  $TM_{01}$  and  $TE_{01}$  were simultaneously propagating within the fibre, then the linear polariser would still display the original circular pattern, assuming a similar intensity and colour.

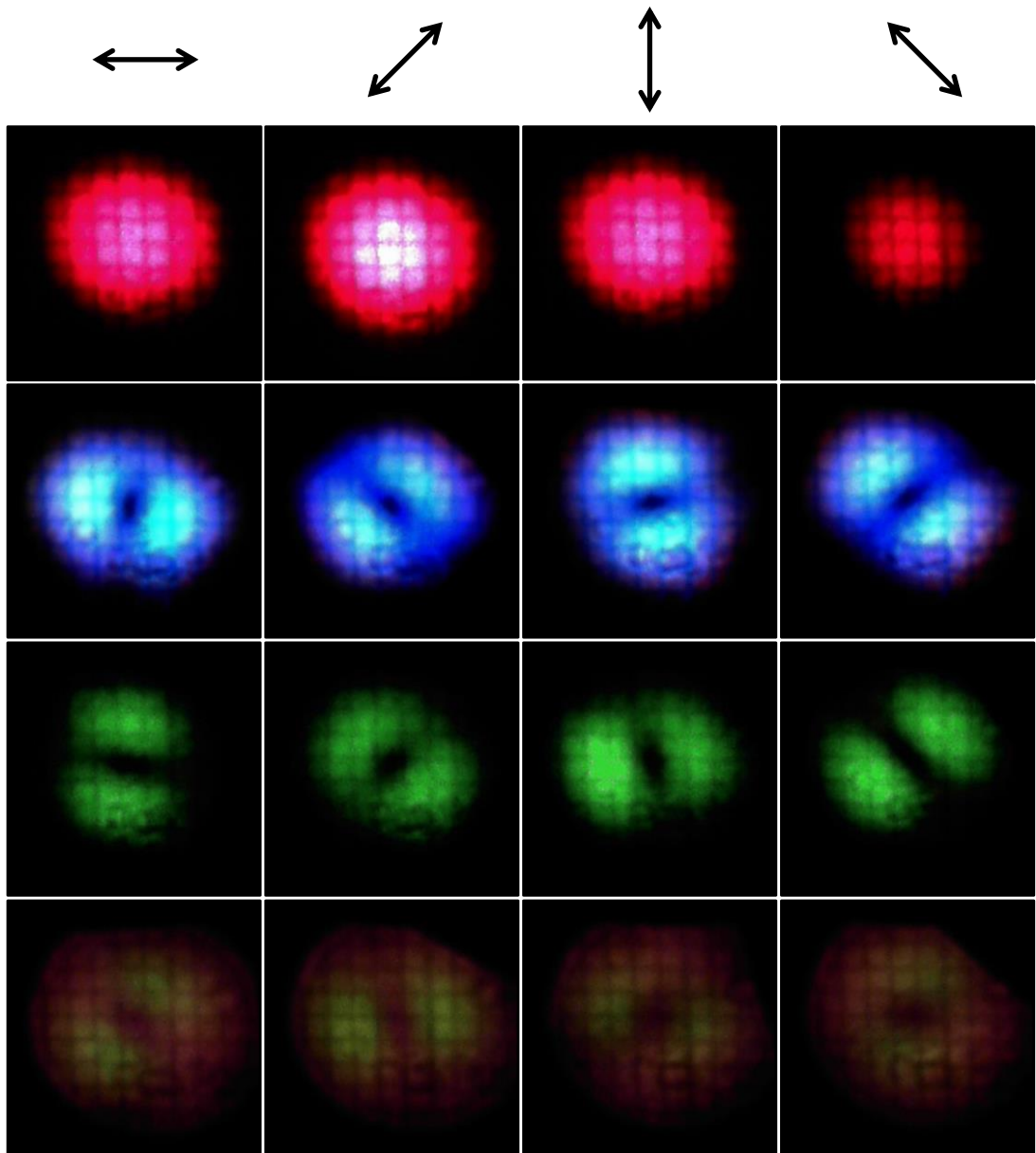


**Figure 6.7: Images of  $HE_{11}$ ,  $TM_{01}$ ,  $TE_{01}$  and  $HE_{21}$  modes through a linear polariser. Polarisation direction is indicated by arrows on top row. Each image is on 1 mm graph paper with a 700 nm short pass filter to remove the pump wavelength.**

Figure 6.7 shows experimental measurements of the fundamental and the various second order EM modes in Thorlabs NL-2.8-850-02 fibre. The  $HE_{11}$ ,  $TM_{01}$ ,  $TE_{01}$  and  $HE_{21}$  modes can be clearly identified using the method discussed in section 6.2. It will be helpful to the reader to refer back to section 3.4.1, specifically Figure 3.3 to understand how these images are analysed.

The first row in Figure 6.7 clearly corresponds to a  $HE_{11}$  fundamental mode. The supercontinuum is generating a dispersive wave at visible red wavelengths. It can be

seen that this mode is polarised as is expected from the linear polarisation input from the laser.

The second row shows a supercontinuum generating blue wavelengths in a higher order mode. The two lobes of this mode when polarised are in the same axis of the linear polariser and rotate in the same direction as the linear polariser is rotated. This corresponds to a  $TM_{01}$  mode.

The third row shows a supercontinuum generating green wavelengths in a higher order mode. Similar to the previous mode, the linear polarisation of this mode generates two lobes, however, these lobes are perpendicular to the linear polariser axis. Again, these lobes rotate in the same direction as rotation of the linear polariser is rotated. This corresponds to a  $TE_{01}$  mode in agreement with Figure 6.2

The fourth row shows a much weaker signal with wavelengths generated in the yellow-green in a higher order mode. This mode, while still a two lobe mode like the  $TE_{01}$  and  $TM_{01}$  modes, does not follow the same clear pattern with lobes aligned with the polarisation direction. Instead, the lobes rotate in the opposite direction as the linear polariser is rotated. This is characteristic of a  $HE_{21}$  mode.

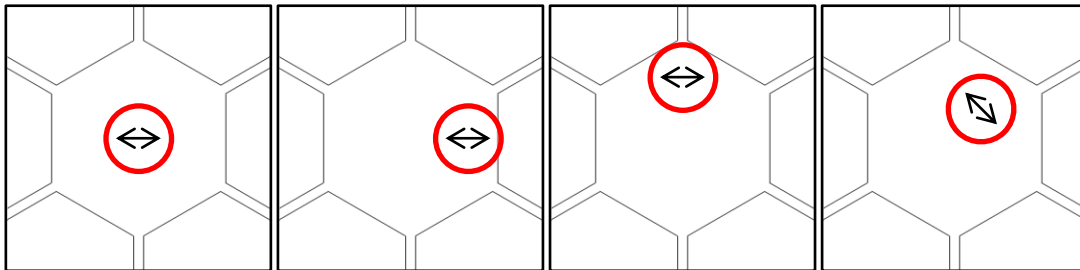


**Figure 6.8:** Laser coupling position used to excite  $HE_{11}$ ,  $TM_{01}$ ,  $TE_{01}$ , and  $HE_{21}$  modes, respectively, on the core of the Thorlabs NL-2.8-850-02 MOF. Each diagram is  $2\ \mu\text{m}$  by  $2\ \mu\text{m}$ .

Each mode excited here was achieved by positioning of the laser focal waist onto the surface of the MOF and rotating the polarisation direction of the laser relative to the fibre, as indicated in Figure 6.8. It was found when generating these results that the  $HE_{21}$  modes were much harder to excite than the  $TM_{01}$  and  $TE_{01}$  modes even though they are of similar profiles.

The work done here is complementary to the observations seen in Chapter 4, specifically the work on the mode variation in the spectral output of the MOF shown in Figure 4.6. This work begins to unveil the shroud of the exact modes seen here and their

degeneracy. It is hypothesised based on the behaviour of the  $HE_{21}$  mode that the peaks seen are indeed travelling within this mode and that, contrary to the simplified simulation, the fibre itself has numerous degenerate modes here based on the symmetry of the fibre and the imperfections to the hexagonal core.

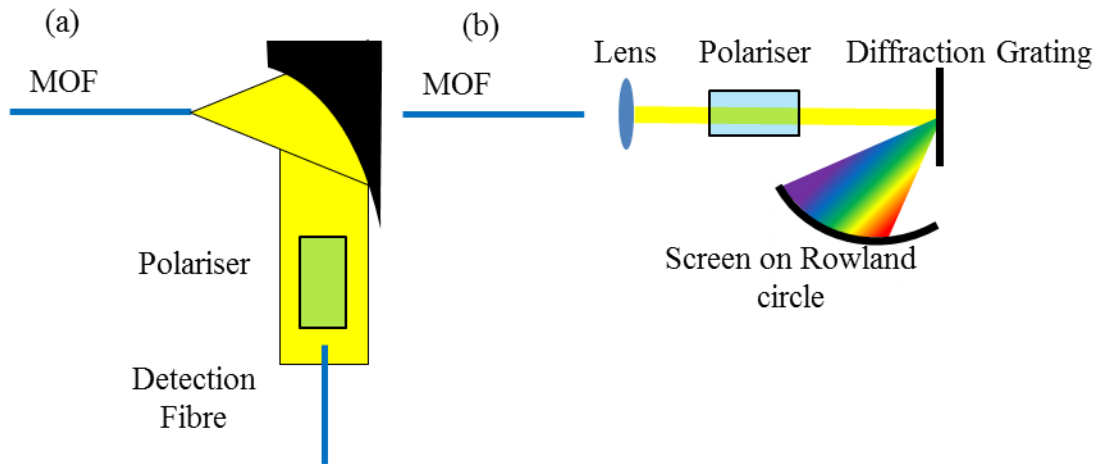


**Figure 6.9: Schematic of two mode field scanner arrangements with polariser. (a) Both the polariser and fibre are mounted on the x-y translation stage and multiple scans can be taken with varying polarisation angles while acquiring spectral information. (b) This arrangement will allow coarse spectrally resolved mode visualisation on a screen placed at the Rowland circle of the grating.**

Figure 6.9(a) shows a modification of the mode field scanner from section 2.3.5 that could be used to further investigate these polarisation effects. Each scan can be done without the polariser and then with the linear polariser at different angles. This setup is free from the problems with the previous spectrally resolved methods discussed in section 6.2 as, although there is a phase shift in the reflection off the metal surface, this poses no real change to the output of the linear polariser. In addition, the multimode detection fibre significantly scrambles the sampled light, removing any polarisation dependence of the spectrometers themselves.

Figure 6.9(b) shows an alternative option where the diffraction grating is used with a polariser, however, in this case, the polarisation is static in the p plane of reflection and the MOF is rotated to generate the varying field patterns that will be spectrally dispersed on the Rowland circle. This method has issues, as the spectrally close modes will overlap whereas the mode field scanner avoids this issue.

In addition to this, ideal coupling into select modes could be achieved using a phase mask or spatial light modulator. This would remove the cross coupling limitations that are inherent to the focussed beam excitation shown in Figure 6.8.

## **6.4 Conclusions**

In this chapter, a method for distinguishing between EM modes with similar spatial profiles with a linear polariser was proposed and experimentally validated by observing the first four experimental modes in hexagonal MOF. The results show a validation of the mode simulations performed in Chapter 3. In addition, they give insight into this as a further technique for exploring the output of supercontinuum in higher order modes of MOF.

The results also inform that the likely mode of propagation for the dispersive wave discussed in Chapter 4 is indeed the  $HE_{21}$  mode. A method is described that could further illuminate the polarisation states and electromagnetic modes of these previous results.

The experimental setup used in Chapters 4 and 5 could not resolve information on the polarisation of the input modes, however, the experimental methods and analysis techniques described in this chapter could be used to improve previous experiments.

## ***7 Conclusions and Further Work***

This thesis primarily observed and characterised supercontinuum generation within multimode MOF. Numerous novel experimental techniques have been developed and utilised through this work to both create and measure the generated supercontinua. The MOF used has been extensively characterised in all EM modes through simulation and explored experimentally.

A complex experimental setup evolved over the duration of this project with the Ti:S laser and numerous MOFs subjected to numerous iterations and improvements in similar experiments until adequate detail could be resolved. The system involved the operation of complex lasers, optical and mechanical components, electrical hardware systems and significant software control design and implementation to achieve the final results presented here.

The data generated has illuminated new experimental observations in the form of higher order mode structure in the dispersive wave of a supercontinuum. In hexagonal MOF it was found that discrete spectral peaks in the dispersive wave of the supercontinuum were associated with electromagnetic modes aligned to the six axes of the fibre core. The small wavelength difference between these modes was attributed to degeneracy splitting of the  $HE_{21}$  and  $HE_{21}^*$  modes due to imperfections in the hexagonal core structure.

In addition, the generation of supercontinuum in these fibre modes with altered dispersion and mode field area lead to the generation of supercontinua with a small number of solitons compared to that generated in the fundamental with the same light intensity. The generated spectra were named the sparse supercontinua and gave insight into the inner workings behind one of the newer nonlinear effects to gain significant interest since the discovery of supercontinuum generation, the blue light trapping from NIR solitons. This effect, responsible for the extreme spectral broadening and continued shift of the blue side of the continuum as proposed by the theoretical framework of Gorbach and Skyrabin [22,23] is for the first time directly observed between individual solitons and shorter wavelength pulses in a supercontinuum. This experimental observation adds significant weight to these theories that have previously only been confirmed in supercontinuum generation by indirect observation of the spectral limits.

The MOF themselves have been fully explored in their waveguide capabilities with simulation results showing the full vector mode analysis of the fibre modes and the resulting refractive index, group index and dispersion for each of these modes. These results were confirmed both with finite element frequency analysis and source-model numerical techniques.

By using a unique technique of observing the rotation of linearly polarised EM mode far field outputs, it was found that full vector modes could be identified in fibre. These modes were observed through analysis of the output of the MOF and the identification of the expected  $HE_{11}$ ,  $TE_{01}$ ,  $TM_{01}$  and  $HE_{21}$  propagating modes are readily observed in hexagonal core fibre. These preliminary results show the potential of further enhancements to the measurement of the mode scanner as the addition of polarisation information allows the closely degenerate EM modes with similar mode field profiles to be resolved experimentally.

This thesis adds novel scientific knowledge in the fields of supercontinuum generation, nonlinear optics and higher order electromagnetic modes in microstructured optical fibres. Numerous experimental measurements, calibrations, numerical simulations and data analysis have been performed in the pursuit of further and deeper insight into the reasons for, and the physics behind, the spectral content of supercontinua emerging from MOF. Some of the results have been published and are now in literature, presentations have been made at international conferences as detailed in Chapter 9. It is anticipated one further publication on the polarisation study will be forthcoming.

## 8 References

1. J. K. Ranka, R. S. Windeler and A. J. Stentz, “Visible continuum generation in air-silica microstructure optical fibers with anomalous dispersion at 800 nm,” **Optics Letters**, **25**, 25–27, (2000).
2. J. M. Dudley, G. Genty and S. Coen, “Supercontinuum generation in photonic crystal fiber,” **Reviews of Modern Physics**, **78**, 1135, (2006).
3. User\_A1, “Optic fibre-numerical aperture diagram,” [https://en.wikipedia.org/wiki/File:Optic\\_fibre-numerical\\_aperture\\_diagram.svg](https://en.wikipedia.org/wiki/File:Optic_fibre-numerical_aperture_diagram.svg), (2007).
4. Thorlabs, “FG05LGA Multimode Fiber Attenuation,” [https://www.thorlabs.com/images/TabImages/FG050LGA\\_Attenuation\\_800.gif](https://www.thorlabs.com/images/TabImages/FG050LGA_Attenuation_800.gif), (2013).
5. T. Okoshi, “Optical Fibers,” (1982).
6. R. Paschotta, “LP Modes,” [https://www.rp-photonics.com/lp\\_modes.html](https://www.rp-photonics.com/lp_modes.html), (2016).
7. T. A. Birks, J. C. Knight and P. S. J. Russell, “Endlessly single-mode photonic crystal fiber,” **Optics Letters**, **22**, 961–963, (1997).
8. J. Knight, T. Birks, P. S. J. Russell and D. Atkin, “All-silica single-mode optical fiber with photonic crystal cladding,” **Optics Letters**, **21**, 1547–1549, (1996).
9. R. Guobin, W. Zhi, L. Shuqin and J. Shuisheng, “Mode classification and degeneracy in photonic crystal fibers,” **Optics Express**, **11**, 1310–1321, (2003).
10. G. P. Agrawal, “Nonlinear Fiber Optics,” (2012).
11. L. F. Mollenauer and J. P. Gordon, “Solitons in optical fibers: fundamentals and applications,” (2006).
12. D. Hollenbeck and C. D. Cantrell, “Multiple-vibrational-mode model for fiber-optic Raman gain spectrum and response function,” **JOSA B**, **19**, 2886–2892, (2002).
13. J. P. Gordon, “Theory of the soliton self-frequency shift,” **Optics Letters**, **11**, 662–664, (1986).
14. F. M. Mitschke and L. F. Mollenauer, “Discovery of the soliton self-frequency shift,” **Optics Letters**, **11**, 659–661, (1986).
15. R. Alfano and S. Shapiro, “Emission in the region 4000 to 7000 Å via four-photon coupling in glass,” **Physical Review Letters**, **24**, 584, (1970).
16. C. Lin and R. Stolen, “New nanosecond continuum for excited-state spectroscopy,” **Applied Physics Letters**, **28**, 216–218, (1976).
17. R. Holzwarth, J. Reichert, T. Udem and T. Hänsch, “Optical frequency metrology and its contribution to the determination of fundamental constants,” **ATOMIC PHYSICS 17: XVII International Conference on Atomic Physics; ICAP 2000**, **551**, 58–72, (2001).
18. D. J. Jones, S. A. Diddams, J. K. Ranka, A. Stentz, R. S. Windeler, et al., “Carrier-envelope phase control of femtosecond mode-locked lasers and direct optical frequency synthesis,” **Science**, **288**, 635–639, (2000).
19. T. Udem, R. Holzwarth and T. W. Hänsch, “Optical frequency metrology,” **Nature**, **416**, 233–237, (2002).
20. N. Akhmediev and M. Karlsson, “Cherenkov radiation emitted by solitons in optical fibers,” **Physical Review A**, **51**, 2602, (1995).
21. A. Gorbach, D. Skryabin, J. M. Stone and J. Knight, “Four-wave mixing of solitons with radiation and quasi-nondispersive wave packets at the short-wavelength edge of a supercontinuum,” **Optics Express**, **14**, 9854–9863, (2006).

22. A. V. Gorbach and D. V. Skryabin, “*Light trapping in gravity-like potentials and expansion of supercontinuum spectra in photonic-crystal fibres*,” **Nature Photonics**, **1**, 653–657, (2007).
23. D. V. Skryabin and A. V. Gorbach, “*Colloquium: Looking at a soliton through the prism of optical supercontinuum*,” **Reviews of Modern Physics**, **82**, 1287, (2010).
24. P. Beaud, W. Hodel, B. Zysset and H. Weber, “*Ultrashort pulse propagation, pulse breakup, and fundamental soliton formation in a single-mode optical fiber*,” **Quantum Electronics, IEEE Journal of**, **23**, 1938–1946, (1987).
25. Y. Chen, Z. Chen, W. Wadsworth and T. Birks, “*Nonlinear optics in the LP 02 higher-order mode of a fiber*,” **Optics Express**, **21**, 17786–17799, (2013).
26. J. M. Dudley and J. R. Taylor, “*Supercontinuum generation in optical fibers*,” (2010).
27. B. Duck, B. Dean, J. Holdsworth and P. Dastoor, “*Mode structure in continuum generation*,” **ACOFT/AOS 2006-Australian Conference on Optical Fibre Technology/Australian Optical Society**, (2006).
28. A. Efimov, A. Taylor, F. Omenetto, J. Knight, W. Wadsworth, et al., “*Nonlinear generation of very high-order UV modes in microstructured fibers*,” **Optics Express**, **11**, 910–918, (2003).
29. S. Konorov, E. Serebryannikov, A. Zheltikov, P. Zhou, A. Tarasevitch, et al., “*Mode-controlled colors from microstructure fibers*,” **Optics Express**, **12**, 730–735, (2004).
30. R. Cherif, M. Zghal, I. Nikolov and M. Danailov, “*High energy femtosecond supercontinuum light generation in large mode area photonic crystal fiber*,” **Optics Communications**, **283**, 4378–4382, (2010).
31. R. Cherif, M. Zghal, L. Tartara and V. Degiorgio, “*Supercontinuum generation by higher-order mode excitation in a photonic crystal fiber*,” **Optics Express**, **16**, 2147–2152, (2008).
32. F. Poletti and P. Horak, “*Dynamics of femtosecond supercontinuum generation in multimode fibers*,” **Optics Express**, **17**, 6134–6147, (2009).
33. N. Karasawa and K. Tada, “*The generation of dispersive waves from a photonic crystal fiber by higher-order mode excitation*,” **Optics Express**, **18**, 5338–5343, (2010).
34. S. Legge, J. Holdsworth and B. Zwan, “*Supercontinuum generation in higher order modes of photonic crystal fibre*,” **International Commission for Optics (ICO 22)**, 801146–801146, (2011).
35. S. Legge, B. Zwan and J. Holdsworth, “*Spatio-spectral Identification of Solitons Occupying Higher Order Electromagnetic Modes in Photonic Crystal Fibre*,” **Australian Conference on Optical Fibre Technology (ACOFT 2012)**, (2012).
36. J. Holdsworth, S. Legge and B. Zwan, “*Higher-order electromagnetic mode solitons illuminate theory*,” **International Commission for Optics (ICO 23)**, (2014).
37. S. Legge and J. Holdsworth, “*Sparse supercontinuum with low order solitons in higher order electromagnetic modes*,” **Journal of Optics**, **17**, 105502, (2015).
38. S. Legge, J. Holdsworth, B. Zwan, L. Collins, J. Martin, et al., “*Low order solitons in higher order electromagnetic modes of photonic crystal fibre*,” **Australian and New Zealand Conference on Optics and Photonics (ANZCOP 2013)**, 7–9, (2013).
39. Spectra-Physics, “*Tsunami Mode-Locked Ti:sapphire Laser User’s Manual*,” (1995).

40. S. Grafström, U. Harbarth, J. Kowalski, R. Neumann and S. Noehte, “Fast laser beam position control with submicroradian precision,” **Optics Communications**, **65**, 121–126, (1988).
41. I. Malitson, “Interspecimen comparison of the refractive index of fused silica,” **JOSA**, **55**, 1205–1208, (1965).
42. M. Szpulak, W. Urbanczyk, E. Serebryannikov, A. Zheltikov, A. Hochman, et al., “Comparison of different methods for rigorous modeling of photonic crystal fibers,” **Optics Express**, **14**, 5699–5714, (2006).
43. A. Hochman and Y. Leviatan, “Efficient and spurious-free integral-equation-based optical waveguide mode solver,” **Optics Express**, **15**, 14431–14453, (2007).
44. B. T. Kuhlmey, T. P. White, G. Renversez, D. Maystre, L. C. Botten, et al., “Multipole method for microstructured optical fibers. II. Implementation and results,” **JOSA B**, **19**, 2331–2340, (2002).
45. T. White, B. Kuhlmey, R. McPhedran, D. Maystre, G. Renversez, et al., “Multipole method for microstructured optical fibers. I. Formulation,” **JOSA B**, **19**, 2322–2330, (2002).
46. M. Herzberger and C. D. Salzberg, “Refractive Indices of Infrared Optical Materials and Color Correction of Infrared Lenses\*,” **JOSA**, **52**, 420–427, (1962).
47. Y. Vidne and M. Rosenbluh, “Spatial modes in a PCF fiber generated continuum,” **Optics Express**, **13**, 9721–9728, (2005).
48. J. Cheng, M. E. Pedersen, K. Charan, K. Wang, C. Xu, et al., “Intermodal Cerenkov radiation in a higher-order-mode fiber,” **Optics Letters**, **37**, 4410–4412, (2012).
49. J. Stone and J. Knight, “From zero dispersion to group index matching: How tapering fibers offers the best of both worlds for visible supercontinuum generation,” **Optical Fiber Technology**, **18**, 315–321, (2012).
50. G. P. Agrawal, “Nonlinear fiber optics: its history and recent progress [Invited],” **JOSA B**, **28**, A1–A10, (2011).
51. I. Cristiani, R. Tediosi, L. Tartara and V. Degiorgio, “Dispersive wave generation by solitons in microstructured optical fibers,” **Optics Express**, **12**, 124–135, (2004).
52. J. M. Stone and J. C. Knight, “Visibly ‘white’ light generation in uniform photonic crystal fiber using a microchip laser,” **Optics Express**, **16**, 2670–2675, (2008).
53. K. E. Webb, M. Erkintalo, Y. Xu, N. G. Broderick, J. M. Dudley, et al., “Nonlinear optics of fibre event horizons,” **Nature Communications**, **5**, (2014).
54. B. Zwan, S. Legge, J. Holdsworth and B. King, “Spatio-spectral analysis of supercontinuum generation in higher order electromagnetic modes of photonic crystal fiber,” **Optics Express**, **21**, 834–839, (2013).
55. Newport-Corporation, “53-\*280R DIFFRACTION GRATING SPECIFICATION SHEET,” [http://www.gratinglab.com/Products/Product\\_Tables/Efficiency/Efficiency.aspx?catalog=53-\\*280R](http://www.gratinglab.com/Products/Product_Tables/Efficiency/Efficiency.aspx?catalog=53-*280R), (2016).
56. Newport-Corporation, “Spectral Irradiance,” [http://assets.newport.com/webdocuments-en/images/light\\_sources.pdf](http://assets.newport.com/webdocuments-en/images/light_sources.pdf), (2016).

## **9 Papers**

The following pages are copies of scientific papers published in relation to this thesis.

Each paper is self-contained with its own references and figure numbers.

### **List of papers and details:**

#### 9.1 Supercontinuum Generation in Higher Order Modes of Photonic Crystal Fibre [34]

Refereed conference paper for ICO22.

Published by SPIE in ICO22 conference proceedings.

#### 9.2 Spatio-spectral Identification of Solitons Occupying Higher Order Electromagnetic Modes in Photonic Crystal Fibre [35]

Refereed conference paper for AIP/ACOFT 2012

#### 9.3 Spatio-spectral Analysis of Supercontinuum Generation in Higher Order Electromagnetic Modes of Photonic Crystal Fiber [54]

Refereed journal article in Optics Express.

Published by OSA (2013).

#### 9.4 Low Order Solitons in Higher Order Electromagnetic Modes of Photonic Crystal Fibre [38]

Refereed conference paper for ANZCOP 2013

Published by Engineers Australia in ANZCOP 2013 conference proceedings.

#### 9.5 Higher-Order Electromagnetic Mode Solitons Illuminate Theory [36]

Invited keynote conference paper for ICO23.

#### 9.6 Sparse Supercontinuum with Low Order Solitons in Higher Order Electromagnetic Modes [37]

Refereed journal article in Journal of Optics.

Published by IOP (2015).

# Supercontinuum generation in higher order modes of photonic crystal fibre

Samuel Legge, John Holdsworth, Benjamin Zwan.  
SMAPS, University of Newcastle, University Drive, Callaghan, NSW, Australia 2308

## ABSTRACT

Soliton behaviour in higher order electromagnetic (EM) modes in commercial highly nonlinear photonic crystal fibre (PCF) was investigated by mapping spatial and spectral emission. A femtosecond mode-locked Titanium:Sapphire laser was used to generate supercontinua within a set of higher-order electromagnetic modes by piezoelectric control of the spatial field input to the PCF. Coupling pump wavelengths within the normal dispersion regime for the fundamental EM mode into higher EM modes resulted in the emission of blue light, characteristic of higher order soliton fission, in higher order EM modes. Detailed spectral measurements across the spatial mode field output from the PCF, showed different spectral components of the generated continua occupying different spatial electromagnetic modes. In particular, the blue emission was found to be structured with spectral wavelengths at 440 nm and 450 nm associated with different spatial EM modes.

These new measurements are the first to detail high order solitonic interactions in higher order electromagnetic modes and to record different spectral emission wavelengths associated with different higher order spatial modes. These results are not well matched to current theoretical models for supercontinuum generation developed for the fundamental EM mode. The lower zero dispersion wavelengths associated with higher EM modes in PCF enable previously undetected engagement of these modes in supercontinuum generation and propagation.

Supercontinuum Generation Higher Order Modes PCF Spatial Spectral Measurements

## 1. INTRODUCTION

Soliton propagation and behaviour in highly nonlinear PCF is now a well researched area and the processes have been modelled and discussed in detail.<sup>[1]</sup> With few exceptions, this body of work has concentrated on the fundamental electromagnetic mode in the fibre waveguide.<sup>[2,3]</sup> Additionally, the usual approach to supercontinuum generation is to tune the incoming pump radiation to be well above the zero dispersion wavelength of the fibre so that the full range of solitonic and other non-linear broadening processes are engaged with maximum effect.

In this work, the wavelength region below the zero Group Velocity Dispersion (GVD) point for the fundamental EM mode supported by the fibre has been explored. Higher order EM modes were selectively excited in PCF in order to spatially and spectrally map the supercontinuum generated from pump wavelengths below the fundamental GVD zero.

## 2. MODELING

The spatial mode fields and dispersion of different EM modes in the PCF were calculated using a multipole method.<sup>[4,5]</sup> This method solves for allowed modes within a structured waveguide using a determinate minimisation procedure to find modes and their effective indexes. This method is limited as there is always the possibility that modes may be missed.

The dispersion of separate modes is determined by recalculating the effective mode index in small wavelength steps over the wavelength range desired and numerically taking the second derivative of index against wavelength using equation 1.

$$D = -\frac{\lambda d^2 n}{c d\lambda^2} \quad (1)$$

Figure 1 shows the simulated fibre structure used in this method (representing Thorlabs NL-2.8-850-02 fibre). The resultant dispersion curves and their respective spatial mode profiles are shown in Figure 2.

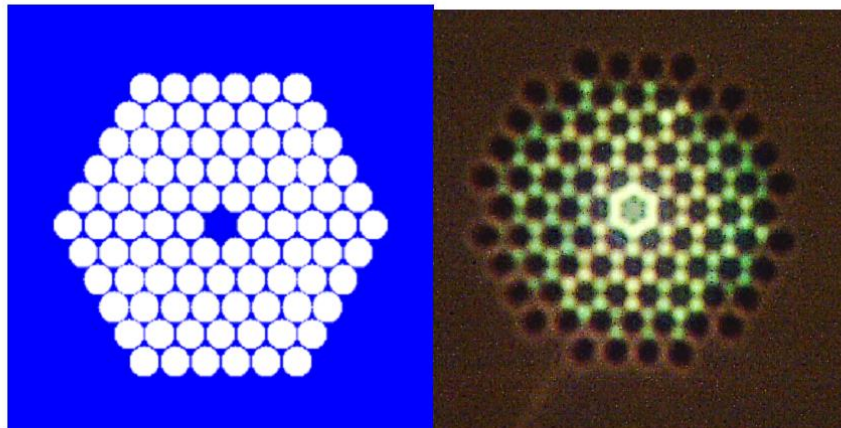


Figure 1. Simulated PCF structure (left) closely matching an optical image of illuminated experimental PCF (right) taken through a fibre microscope. This fibre has a pitch of 2.7  $\mu\text{m}$  with the holes having a radius of 1.26  $\mu\text{m}$ . The simulation uses circles to approximate the rough hexagonal shape of the holes in the real fibre.

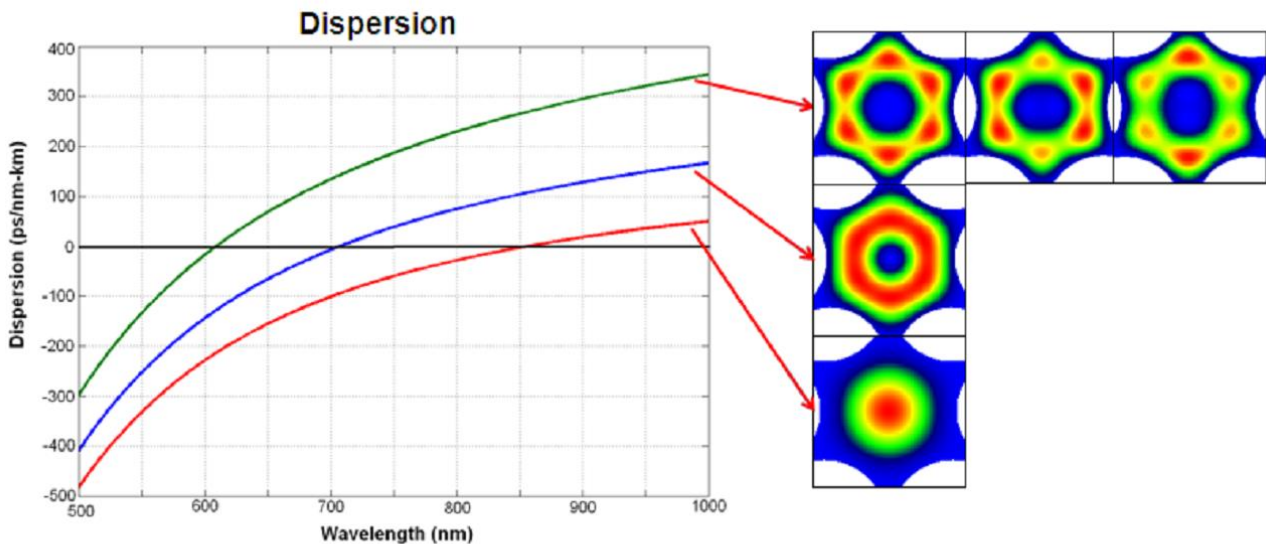


Figure 2. Calculated dispersion of the first three modes of the PCF. The images in the right show the mode field intensities for each of the calculated modes at 800 nm. Both the mode field profiles and the dispersion curves were calculated using CUDOS MOF Utilities.<sup>[4,5]</sup> The calculated fundamental dispersion matched well with the supplier's specifications and experimentally observed modes follow the calculated intensity profiles. Top three modes have similar effective indices and the dispersion curves are nearly degenerate.

### 3. EXPERIMENTAL

The experimental setup as shown in Figure 3 details a femtosecond mode-locked Ti:S laser generating supercontinua within a set of higher-order electromagnetic modes by control of the PCF input spatial field. The direction of the incoming laser beam was stabilised and controlled via a piezoelectrically deflected mirror and a quadrant detector forming a feedback loop. The spatial output of the PCF was scanned using a motorised theta, phi mirror to direct the light towards a fibre coupled spectrometer. The input was sampled and recorded at each spatial grid point addressed by the theta, phi mirror scan.

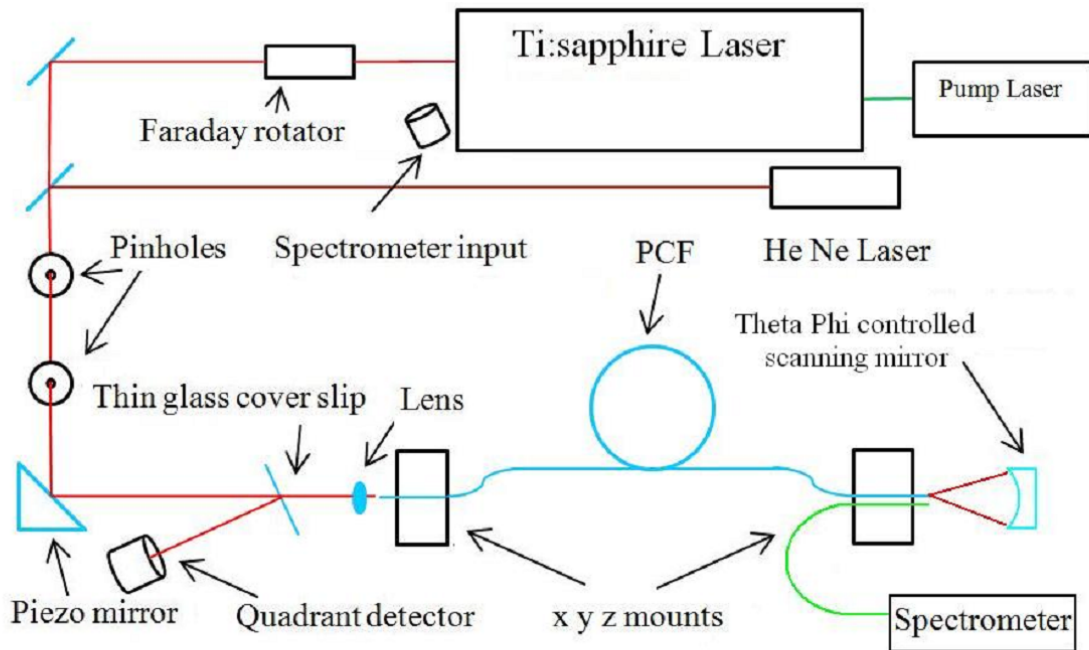


Figure 3. Experimental setup used to generate and scan the mode field output of the supercontinuum.

The experimental setup and equipment used has certain limitations that affect the quality of the results. The piezo mirror feedback loop only has two axis of control and as such adjustment of laser input position on the fibre face resulted in a different angle of incidence into the fibre. The spectrometer used was also easily saturated by the intensity of the generated continuum making it difficult to take scans of the spatial outputs of the brighter wavelengths in the continuum. The latter is an annoyance and the former will be corrected with ongoing work in the laboratory.

### 4. RESULTS AND DISCUSSION

When the input wavelengths are in the range of 750 nm to 850 nm, a wide variety of continua outputs can be generated with varying spectral components in different EM modes by the initial coupling of the input light into different EM modes of the fibre. Results in Figure 4 are indicative of the complexity of the mode field generated with multiple wavelengths evident in a variety of modes simultaneously. These modes are of the correct spatial pattern to agree with the simulated modes in Figure 2.

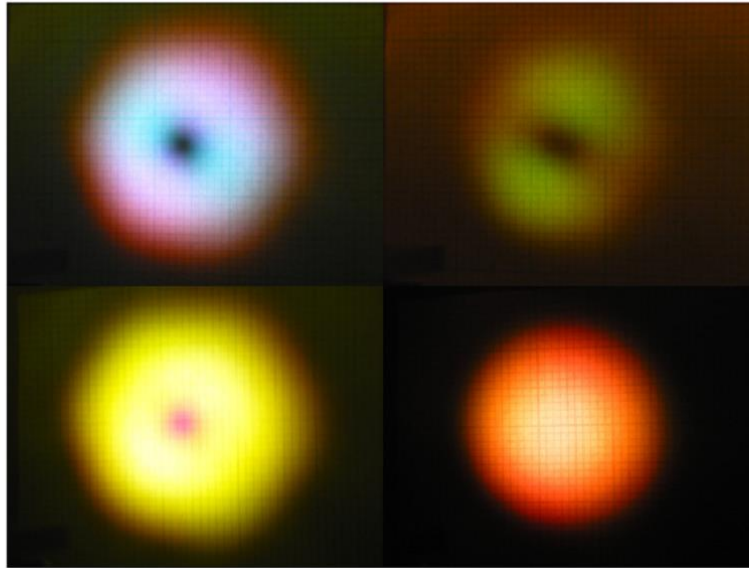


Figure 4. Supercontinua generated with a  $\sim 50$  fs pulse at 782 nm showing spectral structure in higher order modes. The fundamental is shown at the bottom right. Residual pump light is removed with a 420 nm – 750 nm pass filter to avoid camera saturation.

Blue light, the characteristic emission of higher order soliton fission, is seen in Figure 5 and, was observed to be in higher order EM spatial modes when input wavelengths within the normal dispersion regime for the fundamental EM mode were coupled off axis into higher EM modes. In particular, the blue emission was found to be structured with spectral components at 440 nm and 455 nm associated with different spatial EM modes as shown in Figure 6.

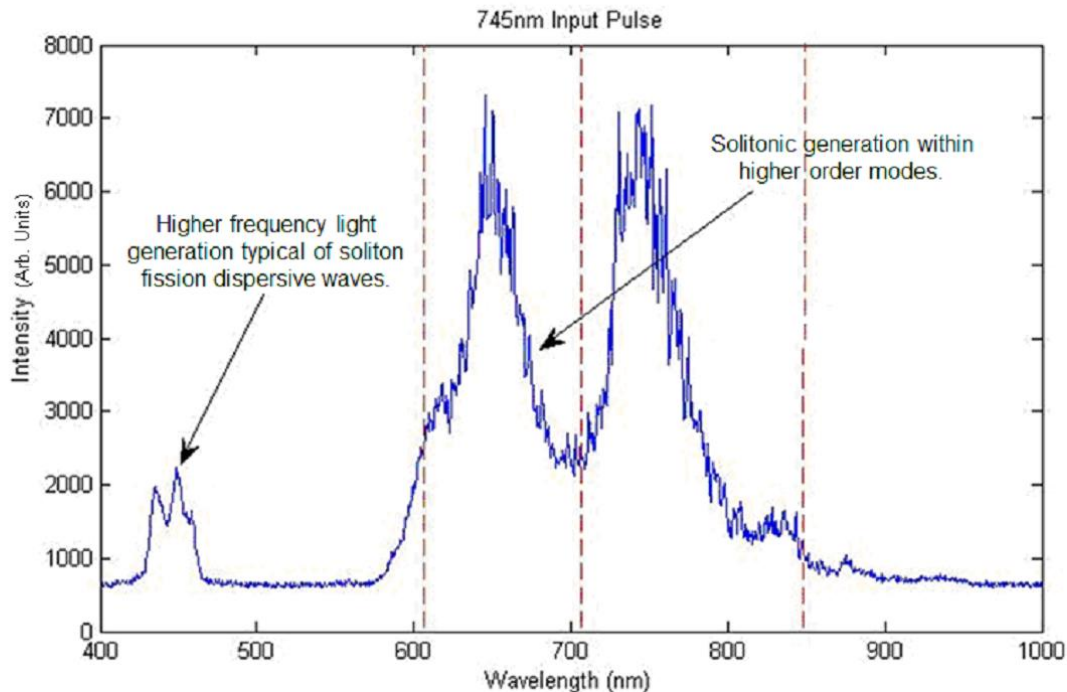


Figure 5. Spectrum of supercontinuum generated with a 50 ps input pulse of 745 nm. Dashed red lines indicate the zero group velocity dispersion points of the fundamental and two higher order modes shown in Figure 2.

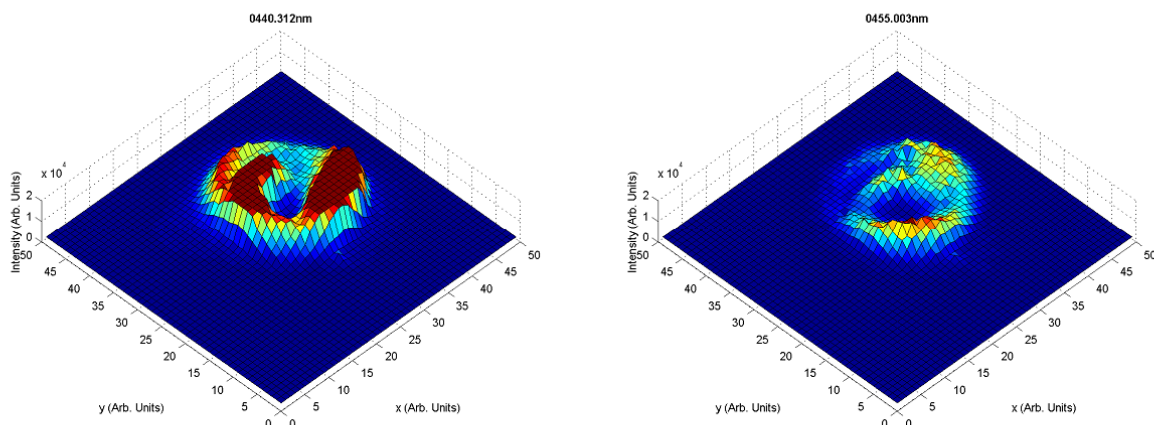


Figure 6. Spatial mode field scans at 440 nm and 455 nm. These correspond to peaks seen in Figure 5 and higher order modes calculated in Figure 2.

These new measurements are the first to detail high order solitonic interactions in higher order electromagnetic modes and to record different emission wavelengths associated with different higher order modes. The current models for supercontinuum generation do not match these results well, as the focus of theoretical calculations and modelling has been almost entirely on the fundamental EM mode.

Figure 5 also shows a strong peak at 650 nm. While wave mixing processes are known to be common in continuum generation, the characteristic lower frequency peak that would be generated in a three wave mixing process is not apparent in this case. A hypothesis is that this light is part of the solitonic light that is generating the dispersive wave peaks seen at 440 nm and 455 nm. This hypothesis explains the lack of solitonic light seen in frequencies below the input wavelength, however the spectral range of this experiment only detected wavelengths up to 1100 nm allowing the possibility that the soliton has self frequency shifted past this wavelength.

It should be noted that if the peak seen at 650 nm is solitonic, it must exist in the 3rd order closely degenerate EM modes simulated in Figure 2 as the lower order EM modes have normal dispersion at this wavelength. This supports the hypothesis that the characteristic dispersive wave seen at lower wavelengths is in fact generated by solitons within the 3rd order EM mode as they show a clear higher order mode structure. The rotation of the 440 nm to the 455 nm peak can be explained by each wavelength propagating in the different but closely degenerate higher order EM modes. While this is a good explanation of the generation of the dispersive wave peaks, it leaves the process that generated light at 650 nm from the input wavelength of 745nm unexplained.

Further investigation is underway. A computational model that can incorporate interactions between EM modes within PCF is needed to begin to properly understand the experimental results that have been seen thus far.

## 5. CONCLUSION

This investigation into the supercontinuum generation in higher order modes has clearly shown that the nonlinear effects of PCF can be significantly altered by the coupling of light into the higher order modes in the fibre. It is clear that, as in the fundamental mode, the zero GVD point of these higher order modes plays a critical role in the generation of the blue light. These higher order modes allow soliton generation in regions of normal dispersion in the fundamental mode. This process allows for blue light generation mechanics of a supercontinuum to be observed while pumping in the normal

dispersion regime of the fundamental mode and highlights that regular fundamental mode supercontinua may couple into the higher spatial modes within a PCF fibre and undergo further solitonic processes within these modes.

## REFERENCES

- [1] Dudley J. M., Genty G. and Coen S., “Supercontinuum generation in photonic crystal fiber” *Rev. Mod. Phys.* 78, 1135–1184, (2006)
- [2] Cherif R., Zghal M., Tartara L. and Degiorgio V., “Supercontinuum generation by higher-order mode excitation in a photonic crystal fiber” *Optics Express*, Vol. 16(3), 2147-2152, (2008)
- [3] Vidne Y. and Rosenbluh M., “Spatial modes in a PCF fiber generated continuum” *Optics Express*, Vol. 13(24), 9721-9728, (2005)
- [4] White T. P., Kuhlmeier B. T., McPhedran R. C., Maystre D., Renversez G., Martijn De Sterke C. and Botten L. C., “Multipole method for microstructured optical fibers. I. Formulation” *JOSA B*, Vol. 19(10), 2322-2330, (2002)
- [5] Kuhlmeier B. T., White T. P., Renversez G., Maystre D., Botten L. C., Martijn de Sterke C. and McPhedran R. C., “Multipole method for microstructured optical fibers. II. Implementation and results” *JOSA B*, Vol. 19(10), 2331-2340, (2002)

# Spatio-spectral Identification of Solitons Occupying Higher Order Electromagnetic Modes in Photonic Crystal Fibre

Samuel Legge<sup>1</sup>, Benjamin Zwan<sup>1</sup> and John Holdsworth<sup>1</sup>.

<sup>1</sup>School of Mathematical and Physical Sciences  
University of Newcastle, Callaghan NSW 2308, Australia

## Abstract Summary

*Solitons occupying higher order electromagnetic modes in photonic crystal fibre have been generated. The unique spatial and spectral measurement of a supercontinuum output field details characteristic signature wavelengths and mode structure not previously observed.*

**Nonlinear Optics; Supercontinuum; Higher-order EM Modes; Solitons.**

## I. INTRODUCTION

Supercontinuum generation using ultra-short pulse duration femtosecond lasers focussed into Photonic Crystal Fibre (PCF) is a well-documented experimental process [1]. The majority of work published to date uses only the fundamental Electro-Magnetic (EM) mode supported within the PCF and details the non-linear and soliton interactions as this Gaussian-like mode propagates along the PCF. The experimental approach used in these cases is to couple as much input light into the fundamental EM mode with a wavelength longer than the zero Group Velocity Dispersion (GVD) wavelength of the fibre and within the anomalous dispersion region.

When broad wavelength supercontinua are generated, the spectral components at the extremities arise from input energy propagating in soliton form. Wavelengths in the blue region of the spectrum arise from the fission of a higher-order ( $n>3$ ) soliton into two, a lower-order ( $n>2$ ) soliton plus a fundamental ( $n=1$ ) soliton. Wavelengths longer than the input arise from the Raman self-frequency shifting of the soliton itself [1].

All intermediate wavelengths are generated by  $\chi_3$  processes which serve to change, combine and broaden propagating wavelengths through Raman shifting, three and four wave mixing and self-phase modulation. These optical Kerr processes fill in and broaden the 400-1600 nm supercontinuum observed by Ranka et al [2].

The solitonic pathways require that the energy is propagating in the anomalous dispersion region of the waveguide. The dispersion characteristics of the PCF therefore determine the soliton behaviour [3]. Higher order EM modes in Thorlabs NL-2.8-850-02 PCF have different calculated dispersion characteristics from the fundamental [4], as shown in Fig. 1. In agreement with the manufacturer's specifications, the zero GVD of the fundamental EM mode was at 850nm. The higher order EM modes calculated were in circular ring

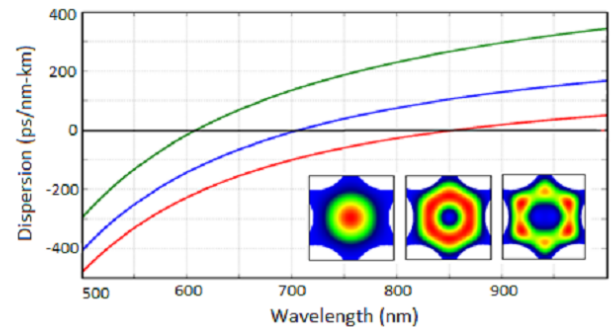


Figure 1. Dispersion of modes in Thorlabs NL-2.8-850-02 PCF calculated using CUDOS MOF[6][7]. The red curve is the fundamental EM mode depicted to the left and shown experimentally in Fig. 2, (e). The blue curve is the next highest EM mode depicted in the center and shown experimentally in Fig. 2, (g). The green curve is the next highest EM mode depicted on the right and is not clearly observed experimentally.

type modes as evidenced in the inserts and have calculated zero GVD points at 707 nm and 609 nm. The different dispersion values allow solitonic interactions for light coupled into higher EM modes at wavelengths below the zero GVD point of the fundamental mode. This opens areas of opportunity that have been explored with groups observing shorter wavelengths in the generated supercontinua [3] and different temporal propagation of each propagating EM mode [5].

This work further explores this phenomenon with an attempt to couple selectively into the higher order EM modes of PCF. As the excited mode within the PCF is highly dependent on the position and angle of the light entering the fibre core, precise control of the focussed laser on the surface of the PCF core is required.

## II. EXPERIMENTAL METHOD

A Spectra Physics Tsunami mode locked titanium sapphire laser is used to generate pulses of light in the temporal range of 140 fs – 300 fs and a spectral range of 700 nm - 850 nm. The output from this laser is coupled into the PCF through a piezo controlled stabilisation mirror system following the design of Grafström [8]. This feedback loop system, shown in Fig. 3 uses two quadrant detectors and two piezo-electrically actuated gimbal mounted mirrors to correct for beam wander of the exciting laser, and enable super-fine control of position and

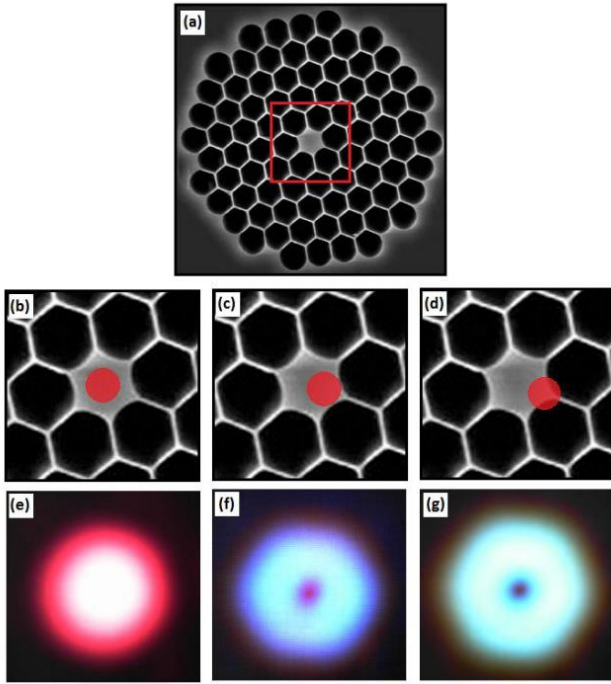


Figure 2. Offset pumping technique. Image (a) is an AFM scan of the Thorlabs NL-2.8-850-02 PCF used in this experiment with a core diameter of  $2.8\mu\text{m}$ , pitch of  $2.7\mu\text{m}$  and hole diameter of  $2.5\mu\text{m}$ . Images (b), (c) and (d) represent schematically the fine positioning of the input beam focal spot (red circle) on the PCF core to generate the continuum shown in the far field output images from a filtered digital camera, (e), (f) and (g). Image (e) is the fundamental mode, image (g) is the next highest order mode with image (f) been a combination of both.

angle of the focussed input beam on the PCF face. This degree of control allows coupling of the input energy into the discrete allowed modes of the PCF, as shown in Fig. 2, for extended ( $\sim 45$  min) periods of time.

The output of the PCF is measured both spectrally and spatially. The generated continuum is collimated using an off-axis parabolic mirror. The far field output of the continuum is imaged by scanning a 400 micron diameter fibre in a 2 dimensional raster grid perpendicular to the collimated output as shown in Fig. 3. At each point across the field, the fibre coupled sampled supercontinuum is split in two and coupled equally into two Ocean Optics spectrometers, one with UV-Vis response and the other with NIR response. This effectively creates a spectral camera over the range  $300\text{ nm} - 1600\text{ nm}$ .

The  $82\text{ MHz}$  repetition rate of the laser generates a supercontinuum signal at each field point which is integrated by the UV-Vis spectrometer for  $15\text{ ms}$  and the NIR spectrometer for  $400\text{ ms}$ . Each scan is repeated five times yielding an average acquisition time of  $2.075$  seconds per point on the raster scan to gain an acceptable signal to noise ratio.

Once the scan is completed, each spectrum is processed in Matlab to remove dark noise and apply a photoradiometric correction factor for the response of each spectrometer to the data. A two-dimensional image is generated for each wavelength recorded by the spectrometers as shown in Fig. 4.

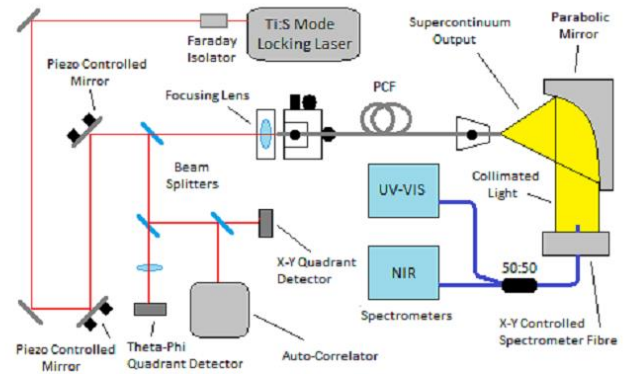


Figure 3. Experimental setup used to generate and measure the spectral far field output of any fibre generated continuum. Output from the PCF is sampled by fibre coupled spectrometers. The spectrum fibre is rastered in an XY grid to collect the mode field data.

This data analysis allows the different spectral components occupying different spatial electromagnetic modes to be observed and recorded.

### III. RESULTS AND DISCUSSION

The experimental parameters of input pulse wavelength and input position into the PCF are observed to be critical to the supercontinuum generated. The temporal variation of the input pulse is observed to be less critical, with a shorter input pulse resulting in more stable output supercontinua.

The stability of the experimental arrangement allows for generation of a constant supercontinuum and measurement of the spatial mode field output. The results, when compiled into a representative figure, Fig. 5, detail previously unobserved complexity in mode structure associated with the spectral output signature of a generated supercontinuum.

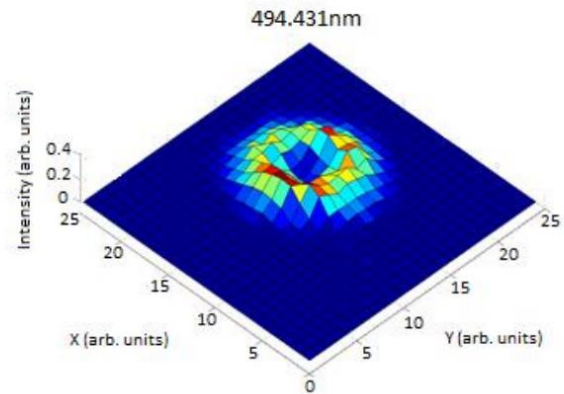


Figure 4. Supercontinuum generated light in a higher order mode imaged by the spectral camera

Fig. 4 clearly shows that light at this wavelength has been generated in a higher order EM mode within the PCF. Furthermore, this mode occurs at a wavelength of 494.431 nm, indicating that it has resulted from a dispersive wave generated by the fission of a higher order solitons. The spatial mode field measurement implies that solitons are being guided exclusively in higher order EM modes rather than in the fundamental mode, as observed in previous studies.

The continuum shown in Fig. 5 exhibits characteristic solitonic behaviour at the extreme ends of the generated spectrum, as expected, but these outputs occur within EM modes clearly of higher order than the fundamental. This is a logical outcome as the input wavelength of the exciting laser (799 nm) is in the anomalous dispersion regime for higher order EM modes but in the normal regime for the fundamental mode, as indicated in the calculations displayed in Fig. 1. Therefore, for an input wavelength in this region it is expected that all spectral features associated with solitonic behaviour should occur in higher order EM modes, as observed in Fig. 4 and Fig. 5. This is the first experimental observation of this phenomenon which displays soliton generation at wavelengths well into the normal dispersion regime of the fundamental mode.

The spectrum shown in Fig. 5 displays three main peaks at longer wavelengths (915 nm, 1000 nm and 1120 nm) and three

peaks at shorter wavelengths (430 nm, 495 nm and 513 nm). Many of these peaks correspond to different higher order spatial mode structures and, in fact, it was observed that the modal structure of the output light was highly dependent on wavelength, with each peak itself containing multiple spatial modes. Another fascinating result emerging from Fig. 5 is the spatial mode field rotation observed between the peaks at 1000 nm and 1120 nm. This is the first recorded observation of orthogonal mode fields in adjacent spectral features. This orthogonal structure should be evident in the dispersive waves generated from fission of the original  $n > 2$  order soliton into fundamental solitons, though we have yet to identify unequivocal associations between these outputs.

Of note, the peak at 915 nm is characteristic of a Raman shifted soliton and this is occupying the fundamental EM mode. This indicates that solitons are formed from the optical Kerr broadening and wave mixing processes spreading the input pump light to reach past the fundamental zero GVD wavelength, approximately 50 nm away from the pump central wavelength. The light in this EM mode has then propagated in the anomalous dispersion regime and can form a soliton. It is unclear if a higher EM order soliton will populate the fundamental EM mode in PCF following a fission event.

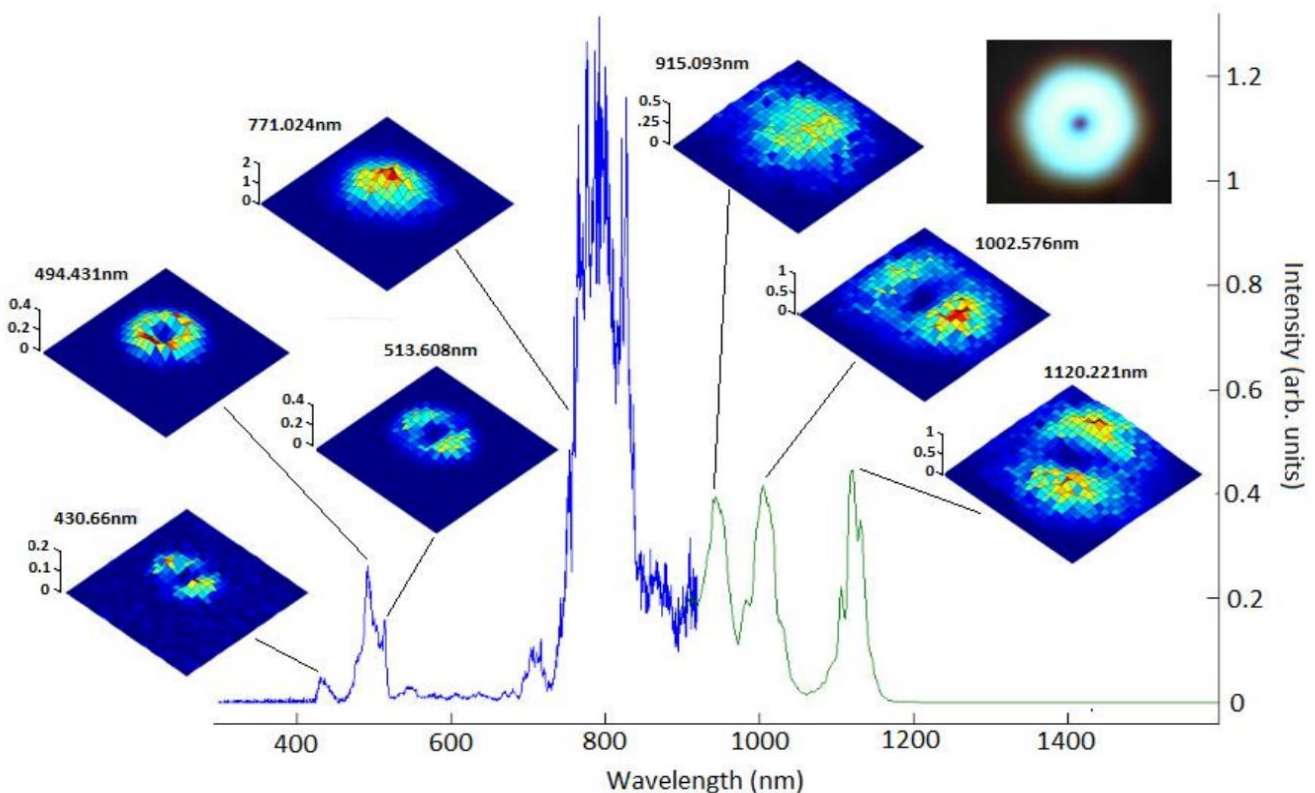


Figure 5. Continuum generated using 799 nm mode locked input with a 250 fs pulse with the far field output of different spectral components displayed. This spectrum photograph is displayed in the top right.

The results clearly indicate that different wavelength components of the generated supercontinuum spectrum occupy both the fundamental and higher order EM modes. One explanation for this is that the input beam is simply being coupled into solitons propagating in multiple EM modes and each of these modes undergoes both solitonic and  $\chi_3$  broadening process to give the observed spatial mode structure. This case, however, does not explain the existence of three dispersive wave peaks at different wavelengths at the blue end of the spectrum. It is perhaps the case that majority of the input light is coupled into a single higher order EM mode and an unknown mode conversion process is the cause of the spatial mode variation across the continuum. More experimental data is required to differentiate between the possible and plausible explanations of these previously unobserved results.

#### IV. CONCLUSIONS

A unique experimental setup, incorporating a piezo-electric actuated and stabilised mirror system under computer control, enables super-fine control of the input beam position and angle incident upon the core region of PCF, allowing the selective generation of stable supercontinua and solitonic behaviour in higher order EM modes. The light at the output of the PCF is spectrally and spatially analysed in order to observe and record the spatial mode field structure of each wavelength component generated. The results reveal that spectral features of the supercontinuum spectrum have spatial mode structure, and that light at wavelengths associated with solitonic propagation is exclusively in higher order EM modes.

This spatial mode field analysis reveals a previously unobserved complexity in the supercontinuum spectrum. As such, the possibility of further measurements of this phenomenon is attractive for future research. The output spectrum of a supercontinuum is highly dependent on the input beam parameters and the properties of the PCF and future work

will seek to study the effect of varying these parameters, with a focus on varying the properties of the PCF used.

#### ACKNOWLEDGEMENTS

The authors acknowledge the University of Newcastle for RHD Stipend support and for financial support of the Ultra-short pulse laser facility within the Priority Research Centre for Organic Electronics. Prof. John Canning and Dr Kevin Cook are acknowledged for helpful discussions and supply of speciality PCF fibres for ongoing work.

#### REFERENCES

- [1] J. Dudley, G. Genty and S. Coen, "Supercontinuum generation in photonic crystal fiber", *Rev. Mod. Phys.* 78, 1135–1184 (2006)
- [2] J. K. Ranka, R. S. Windeler, and A. J. Stentz, "Visible continuum generation in air-silica microstructure optical fibers with anomalous dispersion at 800 nm" *Opt. Lett.* 25, 25-27 (2000)
- [3] R. Cherif, M. Zghal, L. Tartara, and V. Degiorgio, "Supercontinuum generation by higher-order mode excitation in a photonic crystal fiber" *Opt. Express* 16, 2147-2152 (2008)
- [4] S. Legge, J. Holdsworth and B. Zwan, "Supercontinuum generation in higher order modes of photonic crystal fibre", *Proc. SPIE* 8011, 801146 (2011)
- [5] Y. Vidne and M. Rosenbluh, "Spatial modes in a PCF fiber generated continuum" *Opt. Express* 13, 9721-9728 (2005)
- [6] T. P. White, B. T. Kuhlmeier, R. C. McPhedran, D. Maystre, G. Renversez, C. Martijn de Sterke, and L. C. Botten, "Multipole method for microstructured optical fibers. I. Formulation," *J. Opt. Soc. Am. B* 19, 2322-2330 (2002)
- [7] B T. Kuhlmeier, T P. White, G Renversez, D Maystre, L C. Botten, C. Martijn de Sterke, and R C. McPhedran, "Multipole method for microstructured optical fibers. II. Implementation and results," *J. Opt. Soc. Am. B* 19, 2331-2340 (2002)
- [8] S. Grafström, U. Harbarth, J. Kowalski, R. Neumann, S. Noehte, "Fast laser beam position control with submicroradian precision", *Optics Communications*, Volume 65, Issue 2, 15 January 1988, Pages 121-126

## Spatio-spectral analysis of supercontinuum generation in higher order electromagnetic modes of photonic crystal fiber

Benjamin Zwan,<sup>1</sup> Samuel Legge,<sup>1</sup> John Holdsworth,<sup>1,\*</sup> and Bruce King<sup>1</sup>

<sup>1</sup>*School of Mathematical and Physical Sciences, University of Newcastle, University Drive, Callaghan 2308 NSW, Australia*

\*[john.holdsworth@newcastle.edu.au](mailto:john.holdsworth@newcastle.edu.au)

**Abstract:** The far-field spatial distributions of higher order electromagnetic mode supercontinua were resolved spectrally and recorded. The supercontinua were created by precise control and direction of input pump energy offset axially from the photonic crystal fiber core. By processing the measured spectra, the spatial mode shape at each wavelength was determined. Discrete spectral features are associated with symmetrical spatial patterns arising from the host fiber geometry and suggest the electromagnetic mode pairing between the longer wavelength solitons and associated visible dispersive waves. Clear differences between supercontinua generated in fundamental and higher order electromagnetic modes exist. These data should inform theoretical studies as the solitons and the dispersive wave generated by fission may be matched by spatial orientation of the electromagnetic mode that both occupy.

©2013 Optical Society of America

**OCIS codes:** (190.3270) Kerr effect; (190.4420) Nonlinear optics, transverse effects in; (320.6629) Supercontinuum generation; (320.7140) Ultrafast processes in fibers; (190.4370) Nonlinear optics, fibers; (060.4005) Microstructured fibers; (190.5530) Pulse propagation and temporal solitons.

---

### References and links

1. J. Dudley, G. Genty, and S. Coen, "Supercontinuum generation in photonic crystal fiber," *Rev. Mod. Phys.* **78**(4), 1135–1184 (2006).
2. G. P. Agrawal, "Nonlinear fiber optics: its history and recent progress (invited)," *J. Opt. Soc. Am. B* **28**(12), A1–A10 (2011).
3. S. Konorov, E. Serebryannikov, A. Zheltikov, P. Zhou, A. Tarasevitch, and D. von der Linde, "Mode-controlled colors from microstructure fibers," *Opt. Express* **12**(5), 730–735 (2004).
4. A. Efimov, A. Taylor, F. Omenetto, J. Knight, W. Wadsworth, and P. Russell, "Nonlinear generation of very high-order UV modes in microstructured fibers," *Opt. Express* **11**(8), 910–918 (2003).
5. Y. Vidne and M. Rosenbluh, "Spatial modes in a PCF fiber generated continuum," *Opt. Express* **13**(24), 9721–9728 (2005).
6. R. Cherif, M. Zghal, L. Tartara, and V. Degiorgio, "Supercontinuum generation by higher-order mode excitation in a photonic crystal fiber," *Opt. Express* **16**(3), 2147–2152 (2008).
7. N. Karasawa and K. Tada, "The generation of dispersive waves from a photonic crystal fiber by higher-order mode excitation," *Opt. Express* **18**(5), 5338–5343 (2010).
8. S. Legge, J. Holdsworth, and B. Zwan, "Supercontinuum generation in higher order modes of photonic crystal fibre," *Proc. SPIE* **8011**, 801146, 801146-6 (2011).
9. J. Cheng, M. E. Pedersen, K. Charan, K. Wang, C. Xu, L. Grüner-Nielsen, and D. Jakobsen, "Intermodal Čerenkov radiation in a higher-order-mode fiber," *Opt. Lett.* **37**(21), 4410–4412 (2012).
10. B. Kulmey, "CUDOS MOF Utilities," (2012). <http://sydney.edu.au/science/physics/cudos/research/mofsoftware.shtml>
11. J. M. Stone and J. C. Knight, "From zero dispersion to group index matching: How tapering fibers offers the best of both worlds for visible supercontinuum generation," *Opt. Fiber Technol.* **18**(5), 315–321 (2012).
12. S. Grafstrom, U. Harbarth, J. Kowalski, R. Neumann, and S. Nohte, "Fast laser beam position control with submicroradian precision," *Opt. Comms.* **65**(2), 121–126 (1988).
13. I. Cristiani, R. Tediosi, L. Tartara, and V. Degiorgio, "Dispersive wave generation by solitons in microstructured optical fibers," *Opt. Express* **12**(1), 124–135 (2004).

## 1. Introduction

Much of the experimental and numerical work in the field of supercontinuum (SC) generation within photonic crystal fiber (PCF) focusses on the spectral and temporal properties of light from non-linear processes occurring during propagation of the fundamental electromagnetic (EM) mode in PCF [1,2]. Modeling based on a sound theoretical understanding of the underlying processes has successfully predicted the spectral properties of experimental supercontinuum generation in the fundamental EM mode ([1,2] and references therein).

Investigation of supercontinuum generation in the higher order EM modes within PCF, has revealed unique spectral and spatial features [3,4] not observed for supercontinua in the fundamental EM mode. Continuing work examined the temporal variation between modes [5], the spectral variation between supercontinua generated in different EM modes [6,7] and EM mode variation within a single supercontinuum [8]. A very recent paper [9] investigated the inter-conversion between modes in a few-moded solid core step index fiber excited at 1045nm and the possibility of energy interchange between these modes at 1120nm.

The Koronov and Cherif papers [3,6] detail the existence of a region between the zero group velocity dispersion (GVD) wavelengths for the fundamental mode and for the higher modes that will support soliton generation in only the higher order EM modes.

This work investigates this 700-850nm region with a technique that allows spatial and spectral characterization of the supercontinuum light emitted at the output of the PCF. The ability to offset pump the higher order EM modes by precise direction of the input laser into the PCF is central to this work as detailed below.

## 2. Experiment

The PCF (Thorlabs NL-850-2.8-02) was modeled to calculate dispersion and the group index of the fundamental and higher order modes using the CUDOS-MOF facility [10] as shown in Fig. 1. The 700-850nm region allows for solitonic behavior purely in higher modes while the group index differences will dictate the spectral characteristics of the resultant continuum [11]. The inset mode field representations show the limitations of the hexagonal close packed geometry of the model.

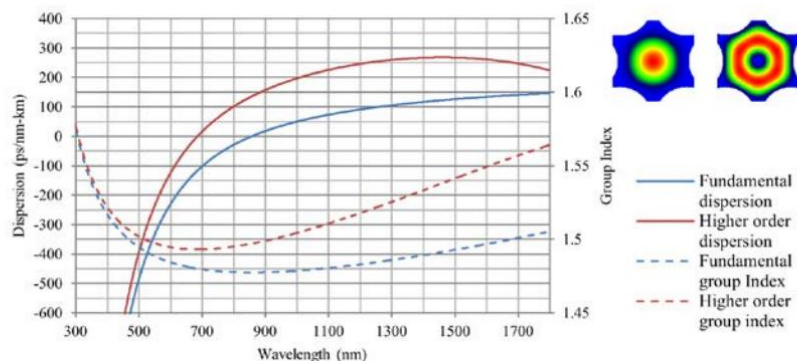


Fig. 1. Modeled PCF dispersion and group index.

Generating stable supercontinua in higher order EM modes requires the input laser beam be focused (*via* 2.00mm f.l. Thorlabs C150TME-B) onto the face of the PCF offset from the central axis of the fiber core and be held in position for extended periods of time. All results are generated in 0.75m of PCF. Two piezo-electrically controlled gimbal mounted mirrors are employed to control and stabilize beam position and angle, with quadrant detectors forming a feedback loop following the principles of Grafström et al. [12]. This gives sub-micron control

of the location at which the horizontally polarized laser beam is focused onto the face of the PCF. Figure 2 details the experimental arrangement.

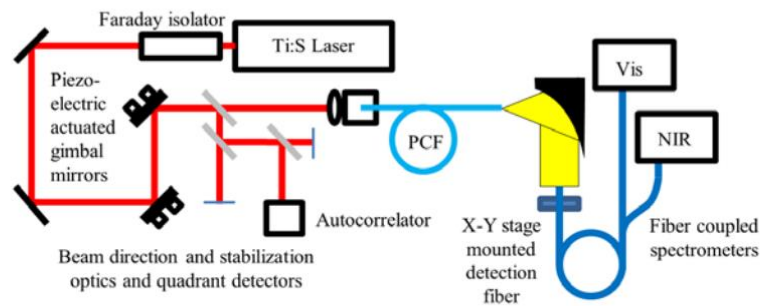


Fig. 2. Experimental arrangement for spatio-spectral measurement of supercontinuum.

This unique setup excites different EM modes by shifting the position and angle of the focused beam across the fiber core with nanometer precision. This is shown schematically in Fig. 3(a)-3(c), where pumping in the center of the core excites the fundamental mode Fig. 2(d) and pumping off axis excites higher order modes Fig. 2(e), 2(f). Figure 2(d)-2(f) are ccd recorded images of the integrated supercontinuum at the output of the PCF. There is evidence in Fig. 2(e) of both the fundamental mode and the higher mode being excited by the laser at input position Fig. 2(b) where the red dot is representative of the beam diameter. The data set recorded allows the spatial EM mode at each wavelength to be extracted and viewed.

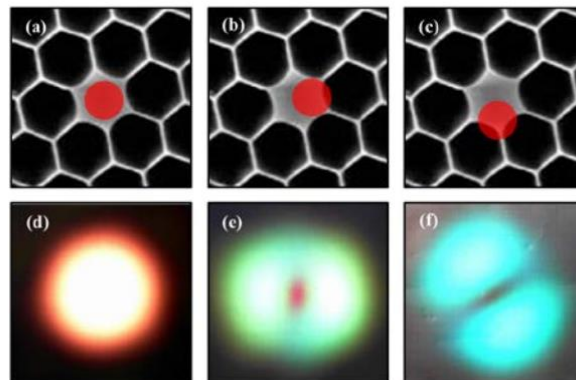


Fig. 3. Variation of integrated supercontinuum electromagnetic mode structures imaged with schematic of laser beam position on photonic crystal fiber core face. Higher order modes (e) and (f) result from offset fiber inputs (b) and (c).

Three axis differential screw microblocks served as coarse position adjusters at both ends of the PCF. The PCF output was achromatically expanded and collimated by reflection from an off-axis parabolic mirror (Fig. 2). A 400  $\mu\text{m}$  diameter low OH silica core multimode fiber was raster scanned across the collimated supercontinuum far field over a 25 x 25 grid of spatial locations. The bifurcated output from the probe fiber was coupled to UV-Vis and NIR Ocean Optics spectrometers. A calibrated combined spectrum from 300 - 1600 nm was obtained at each of the 625 points on the raster grid.

### 3. Results and discussion

Very different supercontinuum spectra emerge from the PCF as the input beam position on the PCF core is altered. Figure 4 displays four measured spectra with the only difference being the position at which the laser beam strikes the input face of the PCF core. All other input parameters; the 200fs pulse duration; the center wavelength of 785nm and the 15nJ

pulse energy were fixed. The insets of each plot show the visible light output of the PCF for each case integrated by the CCD array over all responsive wavelengths.

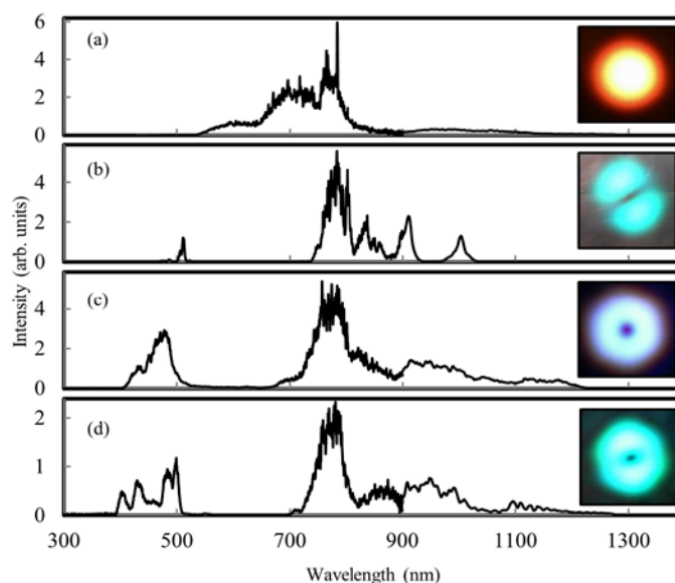


Fig. 4. Spectral variation of output supercontinuum and electromagnetic mode structures with position for identical input pulse duration, power and wavelength.

The striking differences between the spectra in Fig. 4 indicate that different processes dominate in the fiber. Supercontinua generated through solitons propagating in higher order EM modes, as in Fig. 4(b)-4(d), exhibit evidence that the input energy is coupling into lower order solitons, to produce dispersive waves and Raman self-frequency shifted solitons [1] upon fission resulting in discrete spectral features across the broadened spectrum and retaining the spatial mode properties. In contrast, the continuum generated by coupling into the fundamental EM mode, below the zero GVD wavelength Fig. 4(a), yields a spectrum broadened by non-solitonic third-order non-linear processes, where all wavelengths of light produced occupy the fundamental EM mode. Generating a supercontinuum in the fundamental EM mode above the zero GVD wavelength, Fig. 5 matches the expected, well documented [1,2], solitonic *and* third-order non-linear process broadened output, with all wavelengths propagating in the fundamental EM mode.

Figures 5 and 6 display the emission spectrum in blue for the UV-Vis spectrometer and in green for the NIR spectrometer with the spatial mode as measured at each of the wavelengths identified. The rich data set available from the experiment has a spatial result recorded for each pixel of the two spectrometer arrays between 300nm and 1600nm. The spectrum recorded at each raster point was an average of at least 6.56 million individual laser, and therefore supercontinuum, pulses.

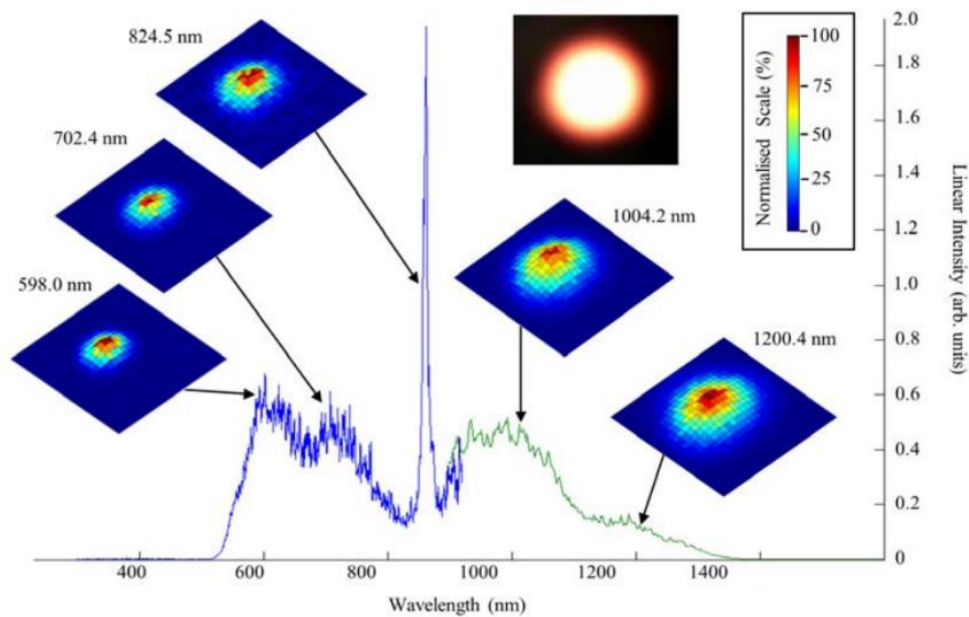


Fig. 5. Measured spectrum and spatial mode properties of a SC generated in the fundamental mode of Thorlabs NL-2.8-850-02 PCF using a 15nJ, 210 fs input pulse at 860nm, 10nm above the zero GVD wavelength. Inset is a visible camera image. The spectrum is representative of the broad continuous spectra characteristic of a fundamental EM mode generated SC in PCF.

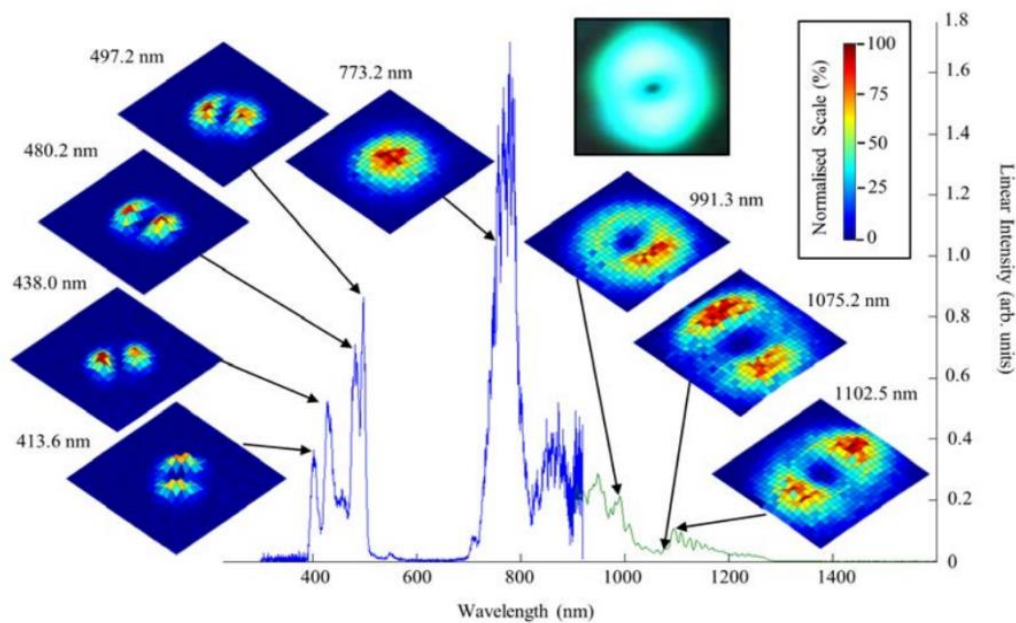


Fig. 6. Measured spectrum and spatial mode properties of a SC generated in the higher EM modes of Thorlabs NL-2.8-850-02 PCF using a 15nJ, 210 fs input pulse at 784nm, 66 nm below the fundamental EM mode zero GVD wavelength. Inset is a visible camera image.

The spatial mode structure of higher order EM mode supercontinua in Fig. 6 reveals a previously undocumented spectral complexity with six distinct dispersive wave peaks ranging from 400 – 550 nm generated using an input pulse wavelength of 784 nm. Cristiani et al. [13] proposed that each dispersive wave peak present in a supercontinuum output corresponds to a

different fission event of a higher order soliton excited by the input pulse. With this interpretation, the spectrum in Fig. 6 reveals that the multiple peak features are characteristic of dispersive waves emanating from fission of lower order, possibly  $n = 2$ , solitons occupying higher order EM modes. Furthermore, it was found that light in each spectral peak in the 400-550nm region occupies a different, closely degenerate, higher order EM mode of the PCF as shown in Fig. 7. The dispersive wave may be matched to a parent soliton by EM mode.

Figures 5 and 6 correlate well with the group index matching as shown in Fig. 1 where the broadening of the fundamental and the higher order mode spread to equivalent points on the group index for the corresponding mode [11].

The different relative rotational position of the mode intensity lobes are a measure of the alignment of those modes relative to the structure of the fiber. As the fiber has hexagonal symmetry, or near to it, the expectation is that the fiber should support modes exhibiting this underlying symmetry. A detailed investigation of the spatial mode of identifiable peaks in the dispersive wave region matched the expected symmetry as shown in Fig. 7.

The discrete mode effective refractive indices are not expected to cross over in the 800-1300 nm region so the coupling of light into the fundamental mode differs from Cheng [9] and is ascribed to the coupling coefficient for that mode based on the overlap between the input pump beam and the mode cross-section at launch.

The slightly larger mode dimensions in Fig. 7(d)-7(f) is the basis of the major axis postulate for these modes while the slightly smaller dimension of modes in Fig. 7 (a)-7(c) is consistent with the minor axis postulate.

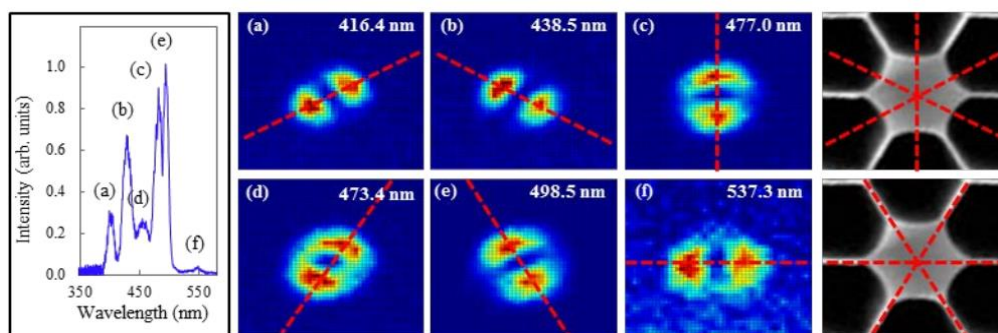


Fig. 7. Measured dispersive wave spectrum with peaks (a)-(e), measured spatial mode of each identified peak and postulated orientation of mode within the PCF core.

Note that these modes are not energetically degenerate. The higher order mode solitons are excited in discrete spatial orientations and, when undergoing fission, produce dispersive waves spatially aligned to their initial mode. Our postulate is that due to the imperfect fiber core geometry, that is, loss of hexagonal symmetry, the electromagnetic modes are not degenerate and thus the dispersive waves should appear at different energies.

#### 4. Conclusion

The figures included above graphically convey new details of spatial mode features in supercontinua generated in higher order EM modes in PCF. Discrete spectral features are associated with symmetrical spatial patterns arising from the host fiber geometry and suggest the electromagnetic mode pairing between the longer wavelength solitons and associated visible dispersive waves. These data should inform theoretical studies and modeling of soliton fission and dispersive wave generation.

#### Acknowledgments

Sam Legge acknowledges the University of Newcastle for research higher degree support.

# Low Order Solitons in Higher Order Electromagnetic Modes of Photonic Crystal Fibre

Samuel Legge<sup>1</sup>, John Holdsworth<sup>1\*</sup>, Benjamin Zwan<sup>1</sup>, Lyle Collins<sup>1</sup>, James Martin<sup>1</sup>, Kevin Cook<sup>2</sup> and John Canning<sup>2</sup>

<sup>1</sup>School of Mathematics and Physical Sciences, University of Newcastle, Callaghan, NSW 2308, Australia

<sup>2</sup>interdisciplinary Photonics Laboratories, School of Chemistry, The University of Sydney, NSW 2006, Australia.

[John.Holdsworth@newcastle.edu.au](mailto:John.Holdsworth@newcastle.edu.au)

## Abstract Summary

*Comparative measurements of supercontinua generated in various photonic crystal fibres (PCFs) reveal unique low-order solitons occupying higher-order electromagnetic modes in each PCF. Matching modes allows correlation of soliton and associated dispersive wave, informing energy transfer processes.*

**Photonic crystal fibre; Microstructured fibre; Structured fibre; Supercontinuum; Solitons; Spatio-spectral Measurements.**

## I. INTRODUCTION

The use of PCF to generate a supercontinuum is a well-known phenomenon [1]. However, optimising the role of the electromagnetic (EM) mode within the PCF waveguide and identifying all nonlinear contributions remains an active area of research [2-4].

Supercontinua generated with lower order solitons provide a unique view into the continuum generation process because the spectrum becomes more discrete for wavelengths above 850 nm, as is evident in Figure 2. This desirable state is more easily observed in higher order EM modes of PCF where the altered dispersion of the mode allows for increased spectral broadening with an inherently lower soliton order.

One of the more recent theoretical explanations of the observed spectral shift of the blue wavelengths occupying the normal dispersion region is outlined by Gorbach and Skryabin [5]. The postulate of gravity-like trapping of the dispersive wave is a convenient way to explain this effect and has been observed in supercontinuum modeling [5,6], however, the experimental observation of this is difficult and has not been thoroughly investigated. Usually the limits of a smooth continuum are observed [7] and the individual soliton-dispersive wave interaction is lost in the spectrum that arises from the various non-linear frequency mixing and generating processes active in the fibre. This work with low order solitons allows the observation of direct group index matching between discrete solitons and their dispersive waves.

## II. METHOD

The supercontinua studied were generated by focusing a 750 nm - 850 nm tuneable, mode-locked Ti:S laser with ~200 fs pulses and 82MHz pulse repetition frequency, into highly nonlinear PCF [2,3]. Peak powers were of the order of 100 kW. The precise input position of the incident beam at the fibre

surface was determined and stabilised by piezo-electric actuators on the beam direction optics and a feedback loop. This allows selection of and also dictates the coupling efficiency into each EM mode. The generated continuum emerging from the cleaved fibre end was collimated by an off axis parabola and then sampled over its spatial area with a multimode fibre coupled into spectrometers as shown in Figure 1. The spatial resolution of this measurement was limited by the step size of the 200 micron diameter sampling fibre mount in its X-Y stage. The fibres used in this experiment were solid core microstructured fibres (Thorlabs NL-2.8-850-02 and spun high birefringent [8] PCF).

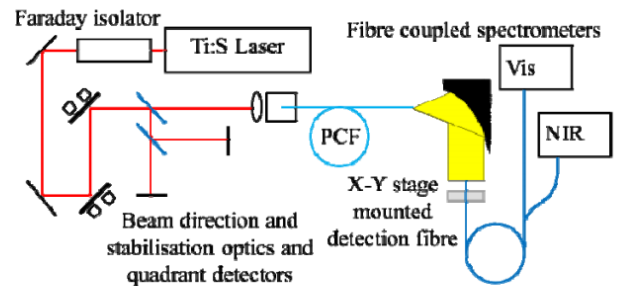


Figure 1: Experimental arrangement for spatio-spectral measurement of supercontinuum [9]

The effective index of each mode within the PCFs was calculated using the source-model technique based optical waveguide mode solver by Hochman and Leviatan [10].

## III. RESULTS AND DISCUSSION

Discrete continuum spectra were obtained by varying input wavelength and coupling position on the fibre end face. Light in each EM mode moved out of phase relative to other coupled modes due to variations in dispersion. This allowed observation of solitons in higher order EM modes without interference from the light that was strongly coupled into the fundamental mode of the PCF. A dispersive trapped wave was generated for each Raman shifted soliton in a discrete EM mode, as shown in Figure 2.

Each dispersive wave can be matched to a soliton based on the wavelength shift of each peak. Note that as the group index rises quickly at lower wavelengths the blue peaks tend to cluster as the near infrared solitons Raman shift to longer wavelengths.

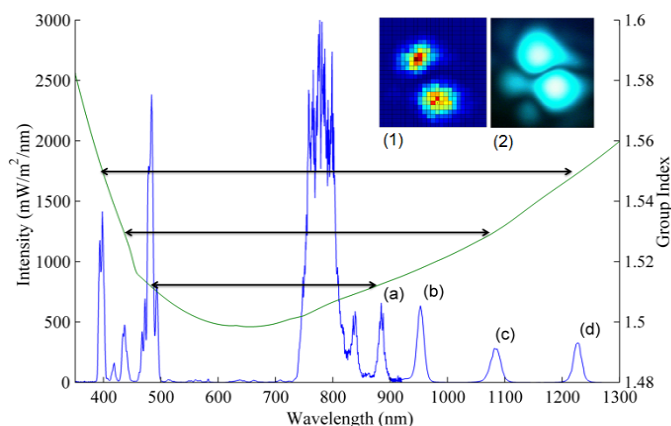


Figure 2: Discrete solitons (a-d) obtained in a higher order EM mode in 2 m of the spun high birefringent PCF. Recorded blue light (1) shifts from group index matching with the curve shown (y axis 2). Panel (2) is a visual emission image.

The clearest experimental observation of the trapping of dispersive waves by solitons is the group index matching between the two pulses of light. This can be seen in Figure 2 as the group index of solitons at peaks labelled (a), (c) and (d) clearly correspond to pulses of light within the normal dispersion regime at equal values of the group index.

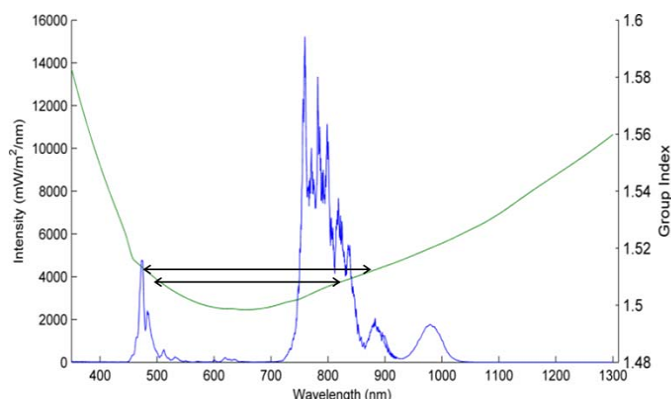


Figure 3: Solitons generated with the same experimental parameters as Fig. 2 but with the fibre cut back to 0.1 m.

By cutting back the fibre, a compression of the continuum was observed, in line with expectations, as the solitons have not had sufficient time to undergo self Raman shifting and, by extension, have not had sufficient time to shift the dispersive wave blue light to shorter wavelengths. Figure 3 shows this compressed continuum with many of the discrete spectral components seen in Figure 2 still overlapping. It was apparent that the discrete solitons separate spectrally as they Raman shifted to longer wavelengths at different rates. It is also possible that some of the generated blue light, associated with the fissioning event spawning each separate fundamental soliton, has not yet caught up with the Raman-shifting near IR soliton it will be trapped behind.

One disadvantage of only having spectral information is that the temporal position of these pulses is unknown in this experiment. Pulses that are separated temporally may be overlapping spectrally.

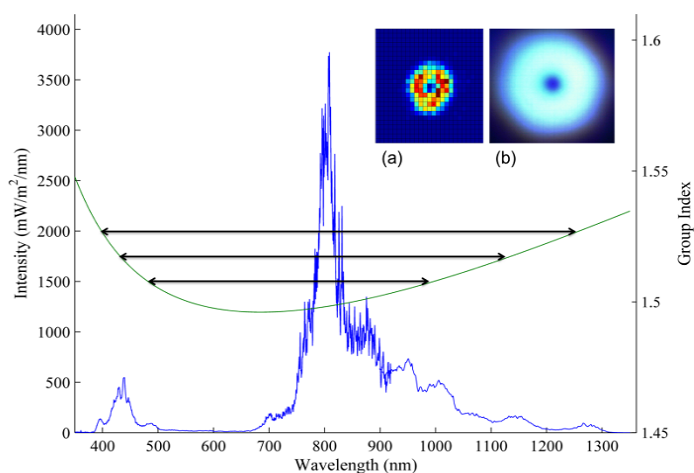


Figure 4. Solitons generated in a higher order EM mode in 1m of the Thorlabs NL-2.8-850-02 PCF. Recorded blue light in a higher EM mode, insert panel (a), shifts from group index matching with the curve shown in green (y axis 2). Note that the solitons have dispersed in wavelength and are less discrete in this continuum. Insert panel (b) is a visual emission image.

The supercontinuum generated in the Thorlabs fibre is shown in Figure 4. This continuum does not clearly show the spectrally separated shifted solitons as seen in Figures 2 and 3, however, peaks likely belonging to solitons are still discernable above the broadband spectrum. Although the peaks are not as clear, it is still possible to roughly observe the matching in group index between the dispersive wave and the long wavelength side of the spectrum [7]. Figure 4 shows that the discrete effects seen in the previous fibre can still be observed in a more typical continuum output. Further increase in pump power and changes in the dispersion or mode would yield a typical smooth continuum, and while the effect of soliton trapping would still shift the blue light, the effect would not be discernable on its own.

#### IV. FUTURE WORK

The polarisation of the output light has not been investigated. The spun high birefringent PCF is elliptically polarised and the possible effect of this on the continuum output is unknown.

Further checking of the simulated group index should be performed as well as experimental measurement to validate the group index of each mode within the PCFs.

The temporal information of the continuum output is not observable. The implementation of a modified multiband FROG would allow the observation of each soliton and dispersive wave couple and should observe them leaving the fibre at the same time.

#### V. CONCLUSION

The experimental results recorded agree well with the theory, in particular, showing a strong support of the theory that solitons can trap light behind them [5,6]. These results should help in validating newer multi-mode pulse propagation models [4] that have recently been published.

## VI. REFERENCES

1. Dudley, John M., Goery Genty, and Stéphane Coen. "Supercontinuum generation in photonic crystal fiber." *Reviews of Modern Physics* 78.4 (2006): 1135.
2. B. Zwan, S. Legge, J. Holdsworth, and B. King, "Spatio-spectral analysis of supercontinuum generation in higher order electromagnetic modes of photonic crystal fiber," *Optics Express* 21, 834-839 (2013).
3. Zwan, Benjamin, Samuel Legge, John Holdsworth, and Bruce King. "Spatio-spectral analysis of supercontinuum generation in higher order electromagnetic modes of photonic crystal fiber." *Optics Express* 21.1 (2013): 834-839.
4. Khakimov, Roman, Igor Shavrin, Steffen Novotny, Matti Kaivola, and Hanne Ludvigsen. "Numerical solver for supercontinuum generation in multimode optical fibers." *Optics Express* 21.12 (2013): 14388-14398.
5. Gorbach, Andriy V., and Dmitry V. Skryabin. "Light trapping in gravity-like potentials and expansion of supercontinuum spectra in photonic-crystal fibres." *Nature Photonics* 1.11 (2007): 653-657.
6. Travers, J. C. "Blue extension of optical fibre supercontinuum generation." *J. Opt.* 12.11 (2010): 113001.
7. Stone, James M., Jonathan C. Knight, and John Clowes. "Visibly "white" light generation in uniform photonic crystal fiber using a microchip laser." *Conference on Lasers and Electro-Optics*. Optical Society of America, 2008.
8. Michie, Andrew, John Canning, Ian Bassett, John Haywood, Katja Digweed, Brian Ashton, Michael Stevenson, Justin Digweed, Alfred Lau, and Daniel Scandurra. "Spun elliptically birefringent photonic crystal fibre for current sensing." *Measurement Science and Technology* 18.10 (2007): 3070.
9. Grafström, S., Harbarth, U., Kowalski, J., Neumann, R., & Noehte, S. "Fast laser beam position control with submicroradian precision." *Optics Communications* 65.2 (1988): 121-126.
10. Hochman, Amit, and Yehuda Leviatan. "Efficient and spurious-free integral-equation-based optical waveguide mode solver." *Optics Express* 15.22 (2007): 14431-14453.

# Higher-order electromagnetic mode solitons illuminate theory

John Holdsworth<sup>1\*</sup>, Samuel Legge<sup>1</sup> and Benjamin Zwan<sup>1</sup>

<sup>1</sup>*School of Mathematical and Physical Sciences, FSCIT, University of Newcastle, Callaghan, NSW 2038, Australia*

\*E-mail: [john.holdsworth@newcastle.edu.au](mailto:john.holdsworth@newcastle.edu.au)

## 1. Introduction

Generation of a supercontinuum in a photonic crystal fibre (PCF) [1] is now a well-known phenomenon with commercial suppliers of supercontinuum sources now available and the light used in a variety of applications. The supercontinuum light generated in commercial sources and in the bulk of literature is almost exclusively confined to the fundamental electro-magnetic (EM) mode of the fibre. The many and definitive non-linear processes engaged in the generation of a supercontinuum are integrated within this fundamental EM mode making the identification of the process associated with particular frequencies within the supercontinuum difficult to isolate and identify.

Coupling energy into a higher-order EM mode results in increased dispersion within a given fibre due to the larger EM mode area. When soliton generation is factored in, a lower-order soliton is produced [1] in the mode by the input pulse than one would achieve in the fundamental EM mode and this has the experimental benefit that less soliton fission, where the  $N^{\text{th}}$  order soliton generated by the input pulse fissions to a fundamental ( $N=1$ ) soliton and a  $(N-1)^{\text{th}}$  order soliton, occurs as the input energy propagates down the fibre. Additionally, the zero dispersion wavelength of the higher EM mode in the fibre is at a shorter wavelength than the fundamental EM mode [2] allowing the choice of a laser pump wavelength that is in the normal dispersion regime and so does not create solitons in the fundamental EM mode, but is in the anomalous dispersion regime and does generate solitons in the higher-order EM modes.

The net result of this approach is to generate a sparse continuum spectrum, particularly above 850nm, and this facilitates the identification of the nonlinear contributions to the spectrum. This approach has been used by us and others [2-4] to research the source of blue light with a view to understanding the processes and the apparent limit to the wavelengths generated at the blue end of the supercontinuum. While UV emission has been reported [5-7], the generation of these wavelengths has been ascribed to non-supercontinuum processes or has resulted from tapered fibres with the zero dispersion wavelength varying along the length of the fibre.

Gorbach and Skryabin [8] have postulated gravity-like trapping of the dispersive wave as an explanation for the spectral shift of the blue light observed in supercontinua. The categorical experimental observation of this is difficult in the fundamental EM mode, where the limits of a smooth continuum are observed [9] and the dispersive wave interaction arising from an individual soliton is lost in the spectrum that arises from the whole variety of non-linear frequency mixing and frequency generating processes active in the fibre.

This work with low-order solitons in the higher EM modes allows the observation of direct group index matching between discrete solitons and their dispersive waves.

## 2. Experimental

The supercontinua studied were generated by focusing a 750 nm - 850 nm tuneable, mode-locked Ti:S laser (SP Tsunami) with ~200 fs pulse duration, ~ 80 kW pulse energy and 82MHz pulse repetition frequency, into an 80 cm length of highly nonlinear PCF (Thorlabs NL-2.8-850-02) with a measured zero dispersion wavelength of 850nm for the fundamental EM mode. The precise input position of the incident beam onto the cleaved fibre end face was controlled by feedback-loop stabilized piezo-electric actuators on the beam delivery optics, as well as a piezo-controlled xyz microblock with rotational fibre holder attached. This provides 6 degrees of freedom and the required precision in the coupling of light to each EM mode. The continuum generated emerged from the other cleaved fibre end and was collimated by an off axis parabola and then sampled over its spatial area with a raster scanned multimode fibre coupled into dual spectrometers as shown in Figure 1. The spatial resolution of this measurement was limited by the step size of the 200 micron diameter sampling fibre mount in its X-Y mount. Alternately, a spectrum can be taken at a point of interest by positioning the spectral analysis fibre manually within a far-field mode pattern.

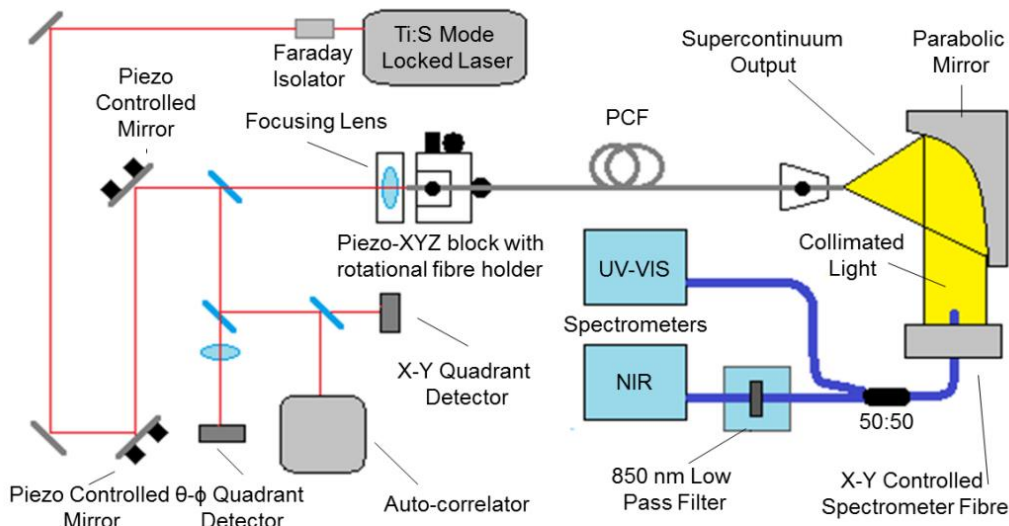


**Figure 1** Experimental arrangement with Piezo-electric beam pointing stabilization and fibre positioning.

Dispersion curves for the NL-2.8-850-02 fibre were calculated using the multipole method on a fused silica hexagon sized to match scanning electron micrographs recorded of the PCF. These silica cores are shown in blue on the inserts (a) and (b) in Figure 2.

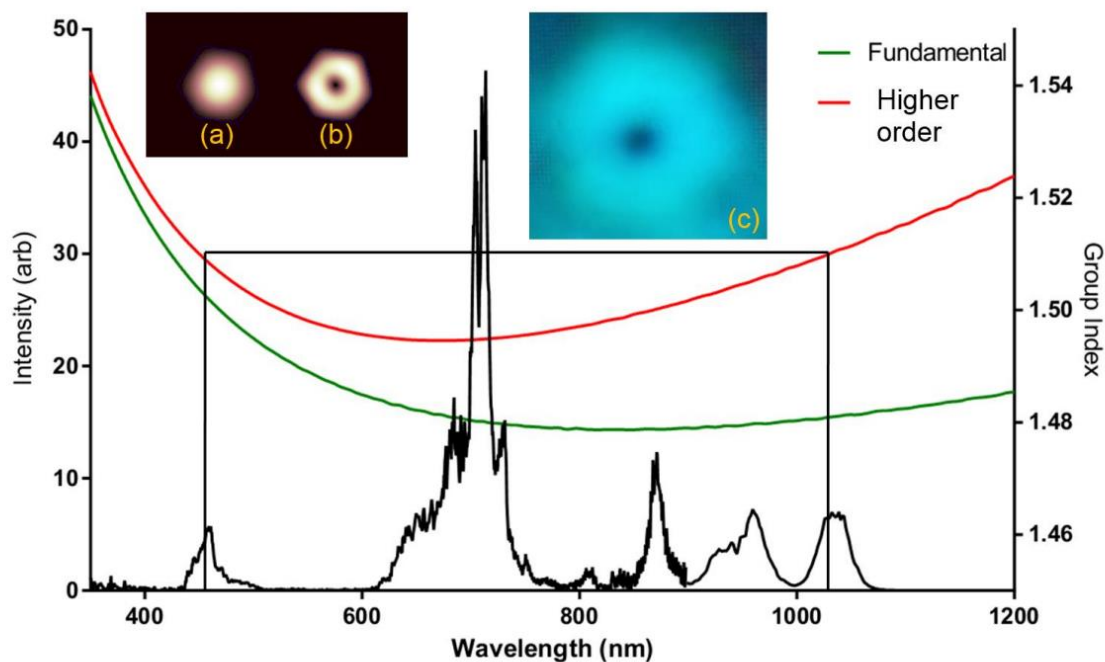


**Figure 2** A sparse supercontinuum recorded by coupling an 82MHz stream of  $\sim 80$  kW,  $\sim 200$  fs, pulses at 775 nm into a higher order ring mode of Thorlabs NL850-2.3-02 PCF. The group index for the fundamental and higher order mode is shown with guiding lines overlaid. Inserts (a) and (b) show calculated spatial intensities at 800 nm for the fundamental and higher order modes respectively while (c) is a photograph of the continuum far field output.

We observe matching through the group refractive index between the emission at 450 nm in the blue and a Raman shifted soliton in the near infra-red at 1050 nm. The guiding lines in Figure 2 show the correlation between the blue light generated from the fibre and the NIR Raman shifted solitonic peak. These wavelengths are not coupled by wave-mixing phenomena or frequency splitting parametric oscillation as the wavelengths do not match those required for those processes.

In other results we observe the separation between the blue and matched NIR soliton varying with the length of fibre. The steeply rising section of the group refractive index in the UV causes the individual peaks within the blue spectral region to cluster [3]. It is clear the group refractive indices of these peaks

are matched as an analysis of the spatial mode has both blue and NIR in the identical spatial EM mode.

### 3. Conclusions

Our analysis of data allow us to strongly support the work of Gorbach and Skryabin [8] where in particular we are able to definitively match the individual soliton in the near IR with the blue dispersive wave generated during the fission event. These are matched via the group refractive index of the fibre and not by 2, 3 or 4 wave mixing processes.

### Acknowledgments

Sam Legge acknowledges the University of Newcastle for scholarship support. We thank Mourad Zghal and Amine Ben Salem, of the Universite de Carthage for helpful discussions.

### References

- [1] J. Dudley, G. Genty and S. Coen, "Supercontinuum generation in photonic crystal fiber", *Rev. Mod. Phys.* **78**, 1135–1184 (2006)
- [2] Cherif R., Zghal M., Tartara L. and Degiorgio V., "Supercontinuum generation by higher-order mode excitation in a photonic crystal fiber" *Opt. Express*, **16**(3), p. 2147-2152, (2008)
- [3] B. Zwan, S. Legge, J. Holdsworth, and B. King, "Spatio-spectral analysis of supercontinuum generation in higher order electromagnetic modes of photonic crystal fiber," *Opt. Express* **21**, 834-839 (2013).
- [4] S. Legge, B. Zwan and J. Holdsworth, "Spatio-spectral Identification of Solitons Occupying Higher Order Electromagnetic Modes in Photonic Crystal Fibre" *Proc. 37th ACOFT*, ISBN 9780858259911 (2012)
- [5] Y. Chen, W. J. Wadsworth, and T. A. Birks, "Ultraviolet four-wave mixing in the LP<sub>02</sub> fiber mode," *Opt. Lett.* **38** p3747-50, 2013
- [6] A. Efimov et. al., "Nonlinear generation of very high-order UV modes in microstructured fibers" *Opt. Exp.* **11** p910-918 (2003)
- [7] A. Kudlinski, et.al., "Zero-dispersion wavelength decreasing photonic crystal fibers for ultraviolet-extended supercontinuum generation," *Opt. Exp.* **14** p5715-22 (2006)
- [8] A. Gorbach and D. Skryabin, "Light trapping in gravity-like potentials and expansion of supercontinuum spectra in photonic-crystal fibres." *Nature Phot.* **1** p653-657 (2007).
- [9] J. Stone, J. Knight and J. Clowes, "Visibly "white" light generation in uniform photonic crystal fiber using a microchip laser." *Conference on Lasers and Electro-Optics*, OSA, 2008

# Sparse supercontinuum with low order solitons in higher order electromagnetic modes

Samuel Legge and John Holdsworth

School of Mathematical and Physical Sciences, University of Newcastle, University Drive, Callaghan 2308 NSW, Australia

E-mail: [john.holdsworth@newcastle.edu.au](mailto:john.holdsworth@newcastle.edu.au)

Received 14 May 2015, revised 16 July 2015

Accepted for publication 17 July 2015

Published 25 August 2015



CrossMark

## Abstract

By fine control of initial launch conditions and utilizing the dispersion properties of micro-structured optical fibre for the transmission of higher order electro-magnetic modes, very low order solitons have been generated in a spectrally sparse continuum. The few Raman self-frequency shifted solitons in the near IR demonstrably match with the change in wavelength of the blue emission through group refractive index matching. These experimental spectral results agree with recent theory on the wavelength shift of blue supercontinuum light.

Keywords: microstructured optical fibre, supercontinuum, solitons

## 1. Introduction

The understanding of the nonlinear processes behind supercontinuum generation in micro-structured optical fibre (MOF) has been an area of fascination for scientists over the last 15 years and the understanding of these phenomena, expressed within the body of literature, provides a model of the physical effects [1, 2]. As a full four-octave broad band supercontinuum results from the action of a number of frequency mixing and frequency generating  $\chi_3$  nonlinear effects, it is often difficult to observe and experimentally validate any individual process as the associated spectral detail is lost to the wave mixing and frequency broadening effects occurring simultaneously. Gorbach and Skryabin [2, 3], Chen *et al* [4], Stone and Knight [5] and even as far back as Beaud *et al* and their work in telecoms fibre [6], have inferred the shift in the blue wavelength, or dispersive wave, side of the supercontinuum to shorter wavelengths by measuring the limiting spectral width of the continuum, however, this outcome necessarily includes broadened and wave-mixed components of the continuum when observed experimentally. A significant body of work exists [7–9] where both the blue wavelength limit and the conversion efficiency has been deliberately engineered by tapering the fibre. This gives an axial position-dependent group velocity which, for the blue and near-IR, results in mismatched soliton and dispersive

wave group velocities. The different rate of change in the blue and near-IR group velocities due to the taper, can be thought of as a group acceleration mismatch and defines the conversion efficiency of the dispersive wave into shorter wavelengths.

In the case of uniform fibres, the theoretical understanding of the blue light altering in its wavelength is limited to gravity like potential wells and cross-phase modulation as the fibre uniformity does not give rise to a significant group acceleration mismatch between the dispersive wave and the Raman-shifting near-IR soliton.

In this work, the confusing, competing effects have been avoided and direct observation of changes to discrete features in the blue spectral region associated with the Raman shift of solitons in the red side of the supercontinuum, have been recorded. This surprising and unique observation is of blue light, once generated, shifting in its wavelength and is the required experimental validation of the theoretical explanation for the formation of, and limits to, the short wavelength side of a supercontinuum [2, 3, 10].

These results are achieved by spatial and spectral characterization of the supercontinuum generated by the MOF through the generation and observation of spectrally sparse supercontinua. While this description may be at odds with the usual and stated definition of a supercontinuum, the ability to pump energy into and excite solitons in higher order

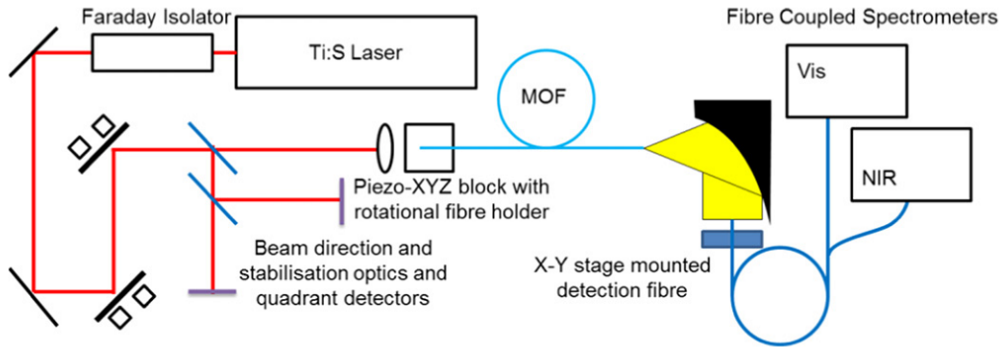


**Figure 1.** Experimental setup to efficiently couple linearly polarized fs pulses into higher order modes within MOF cores.

electro-magnetic modes (EMMs) within a MOF, allows the generation of low order solitons. When these solitons fission and undergo self-Raman shifting to longer wavelengths, they demonstrate the characteristic extreme broadening of the input pump light over multiple frequency octaves, but with a sparse and dispersed spectrum displaying a small number of discrete peaks [11, 12], rather than the filled-in continuous supercontinuum now available as a commercial product. Supercontinuum generation has reliably been seen in multiple EMMs and has been noted for the change in the continuum and the unique changes it adds to the spectrum [13, 14] as a result of significant changes to the waveguide dispersion.

## 2. Method and reasoning

A supercontinuum was generated by a mode-locked titanium-doped sapphire femtosecond laser (Spectra Physics Tsunami) coupled into highly nonlinear photonic crystal fibre (PCF) (Thorlabs NL-2.8-850-02 PCF and OFTC Spun Hi-Bi PCF). The beam direction and spatial location of the focused laser on the fibre end face is piezo-electrically controlled to give varied coupling efficiencies into allowed EEMs of the fibre as shown in figure 1. The supercontinuum output from the fibre is collimated with an off-axis parabolic mirror and then measured through a bifurcated sampling fibre coupled into dual spectrometers (Ocean Optics 2000+ and NIRQuest) recording the spectral content of the continuum over a 300–1700 nm range. This sampling fibre can be positioned across the collimated far field output from the nonlinear fibre to record the spectrum associated with the various EM modes excited. The experimental setup is similar to that shown in Zwan *et al* [12]. However, significant improvements have been made to the experimental apparatus, specifically in the use of a piezo-electrically adjustable fibre launch platform and rotational control on the fibre input mount. These enhancements allow the symmetry of the MOF core structure to be aligned at different rotational angles to the linearly polarized input laser and to provide the enhanced precision necessary to couple efficiently into specific higher-order EEMs with high enough efficiency to generate a supercontinuum in those modes.

By definition, a supercontinuum is a continuous band of emitted light over more than an octave in frequency, however,

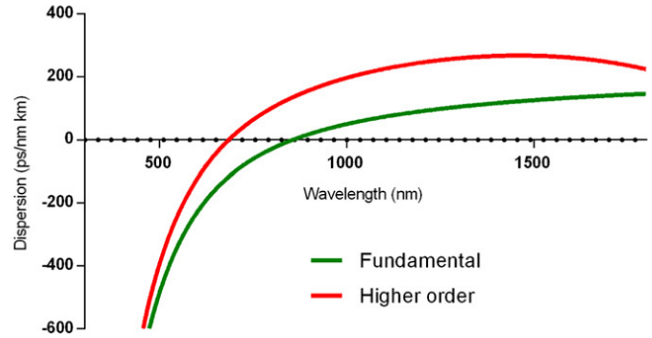


**Figure 2.** Dispersion of the fundamental and higher order mode in Thorlabs NL-2.8-850-02 MOF. This trend of a zero group velocity dispersion points to lower wavelengths and an increase in anomalous dispersion is common for many variations of MOF.

in order to observe interactions between the red-shifting solitons and the blue-shifting short wavelength side of the generated light, the continuum was deliberately tuned to be spectrally sparse, while still being strongly nonlinear. With this approach, the individual index matching effects may be observed and are not lost in the general broadening effects that obscure the individual nonlinear processes in a standard supercontinuum. The desired approach to this discrete observation is to lower the soliton order  $N$ , where the functional determination of  $N$  within experimental parameters is described in equation (1) [1]

$$N^2 = \frac{T_0^2 P_0 \omega_0 n_2(\omega_0)}{|\beta_2| c A_{\text{eff}}(\omega_0)}. \quad (1)$$

Experimentally, most parameters are held relatively constant by the laser, in that the pulse temporal width  $T_0$ , power  $P_0$ , and angular frequency  $\omega_0$  are stable within a few percent over time. The MOF's nonlinear refractive index,  $n_2(\omega_0)$ , and the effective mode area,  $A_{\text{eff}}(\omega_0)$  are constant for a fixed input wavelength. The dispersion,  $\beta_2$ , varies significantly by mode, and shifting to higher order modes will usually increase the overall dispersion of the fibre in the anomalous region as may be seen in figure 2. With fine tuning of the coupling afforded by the piezo-electric controls and the correct laser power, the soliton order can be easily reduced to two or three in a higher order EEM where the increased

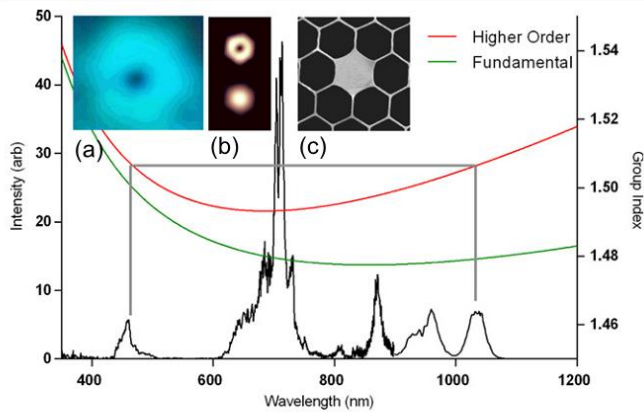


**Figure 3.** Sparse supercontinuum generated in 0.6 m of Thorlabs NL-2.8-850-02 MOF. Inserts show (a) visible camera image of supercontinuum, (b) modelled mode intensity profiles at 800 nm for the fundamental and the second order mode and (c) an electron micrograph of the 2.8  $\mu\text{m}$  average diameter MOF core.

dispersion gives a lower  $N$  while keeping the high intensity  $P_0$  for other nonlinear effects.

### 3. Results

The group index of the propagating modes within the fibre was calculated using SMTP [15] and used to match the interaction between the blue light and the solitons. Figure 4 is a further analysis of results already published in Legge *et al* [11]. Notably, the group index calculations have been significantly improved.

### 4. Discussion

Figure 3 shows a continuum for one of the industry-standard MOFs (NKT Photonics, Denmark sourced through ThorLabs) used for nonlinear effects and creating a broad continuum when energy is coupled into the fundamental EM mode. When coupling light into this fibre it is very easy to couple into multiple EMMs and often the more extreme wavelengths on the blue side of the continuum are observed to occupy these higher order modes [12]. The measured spectral changes in the sparse supercontinuum as length of fibre is varied show that the blue light evident in figure 4(a) at  $\sim 480$  nm shifts by 80 nm to the shorter  $\sim 400$  nm wavelength, as shown in figure 4(b), by progressing through an additional 900 nm of silica fibre. Confirmation of this light being in a higher order EM mode is obtained from observation of the far field mode output at the corresponding wavelengths.

Interpreting the theories for this shift in the blue light [3, 10], requires that both the blue and the soliton spectral peaks stay at the same group velocity even as the solitons self-Raman shift to longer wavelengths. The group refractive indices plotted and the guiding lines shown in figure 3 clearly show the values of the group indices match for the blue light and the solitonic radiation in the NIR for the higher order EM

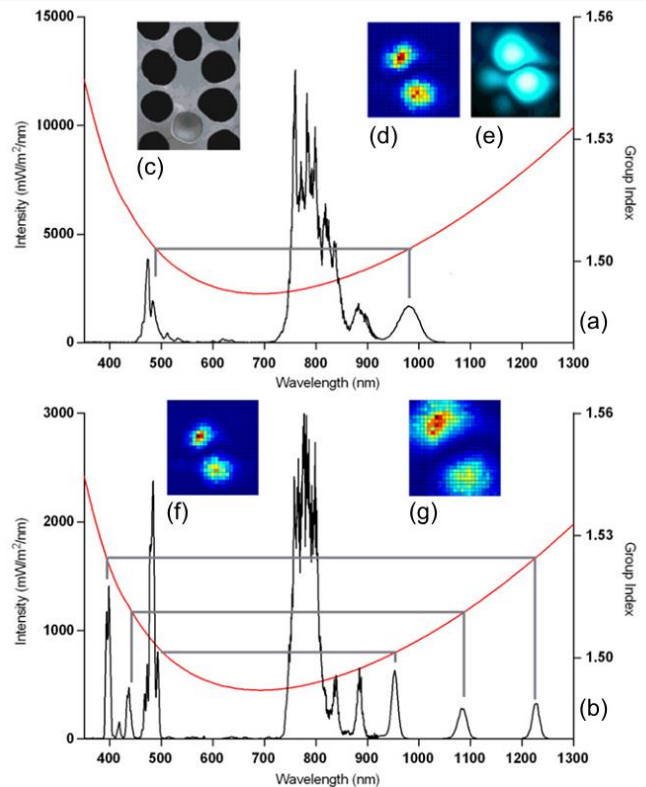


**Figure 4.** Spectrum of a sparse continuum generated in the Spun High Birefringent MOF from the averaged propagation of Ti: S pulse at 780 nm and approximately 100 kW 180 fs through 0.1 m (a) and 1 m (b) of fibre in the second order EMM (group index shown in red) with a low coupling efficiency. The reduced length shortens the interaction time and reduces the redshift and blueshift of the solitons and the blue light. Inserts show; (c) an electron micrograph of the MOF core; (d) the measured far field mode intensity of the MOF output of (a) at 480 nm; (e) visible camera image of supercontinuum and; (f) and; (g) show the far field output of the long fibre at 395 and 1085 nm respectively, where the different spatial size is as a result of the fibre numerical aperture at each wavelength.

mode (red curve) and not for the fundamental EM modes, (green curve).

It was found that moving to a fibre with a slightly larger core, and hence lower nonlinear index, removed the contribution of some nonlinear effects, most importantly four wave mixing, and helped reduce the soliton order. This is clearly observable in the long wavelength side of the spectrum shown in figure 4(b). Here a series of solitonic shaped spectral peaks are clearly defined. All of these solitons appear to occupy the same EMM in this birefringent fibre.

The blue side of the continua in figure 4(b) shows a seemingly complex series of strong peaks, all of which are propagating in the same EMM as the solitons. Most of these peaks can be shown to be matched in their group velocities to respective solitons in the near infrared as can be seen by the indicating lines on the spectrum and the overlaid group index for that mode. For the first time to our knowledge the direct interaction of a soliton and corresponding trapped blue light has been observed in MOF from a femtosecond pulsed laser

typically used in supercontinuum generation with no pre-generation of solitons or lagging blue light.

As these interactions take time, the longer the fibre, the further both solitons and blue light will be able to shift from the pump wavelength. However, the group index matching should be kept at all times. This was tested by cutting back the fibre shown in figure 4(b) to only 0.1 m, as shown in figure 4(a), resulting in the simpler continuum seen. Due to the length, and associated  $\sim 500$  ps transit time along the fibre, there has not been sufficient time for the different solitons to fission and separate spectrally from each other, however, they do appear to be nearly half way along the shift to the longer wavelengths seen in figure 4(b). In figure 4(a) the discrete blue light peaks appear at wavelengths closer to the pump as well as in a clustered group. Checking the group index of this light and the observable solitons again shows a correlation as can be seen by the overlaid lines. The wavelengths are not as short on the blue side, as the NIR solitons are yet to Raman shift to longer wavelengths.

The shifting of the blue light to shorter wavelengths can be attributed to intra-pulse four-wave mixing [2, 16] as the fibre dispersion alters due to the nonlinear interaction of the soliton and media, creating an efficient phase matching process within the pulse. As the blue light is pushed to shorter wavelengths, the limit of the waveguide material begins to dominate and the group index increases dramatically as the 380 nm absorption band of silica is approached. Thus, it becomes very difficult to shift the blue light to wavelengths below 400 nm, as the steepening group index curve causes the bands of blue light to cluster to this limit. Most published supercontinua generated in uniform fibres have this edge evident in the spectrum. There has to be a much greater increase in the NIR Raman shifted soliton wavelength to effectively index match to a much smaller wavelength shift to blue, unless the waveguide is manipulated by tapering.

## 5. Conclusion

The clear experimental results presented above demonstrably support the theoretical framework of Gorbach and Skryabin [2, 3] with the clear index match of Raman shifted NIR soliton peak wavelength and shifting blue wavelengths in uniform fibre. By utilizing the dispersion properties of higher order EMMs in MOF, these very low order solitons generated in a spectrally sparse continuum allow the definitive correlation of the soliton with its index matched, and shifting, blue light without the obscuration of nonlinear wave-mixing effects. This is the first discrete measurement of this effect in the femtosecond pulsed regime as opposed to an inferred result from the limiting spectral boundaries of the continuum.

## Acknowledgements

Samuel Legge acknowledges the University of Newcastle for research higher degree support. We are grateful to John Canning iPL University of Sydney for the spun hi-bi MOF.

## References

- [1] Dudley J M, Genty G and Coen S 2006 Supercontinuum generation in photonic crystal fiber *Rev. Mod. Phys.* **78** 1135
- [2] Skryabin D V and Gorbach A V 2010 Colloquium: looking at a soliton through the prism of optical supercontinuum *Rev. Mod. Phys.* **82** 1287
- [3] Gorbach A V and Skryabin D V 2007 Light trapping in gravity-like potentials and expansion of supercontinuum spectra in photonic-crystal fibres *Nat. Photonics* **1** 653–7
- [4] Chen Y, Chen Z, Wadsworth W and Birks T 2013 Nonlinear optics in the LP 02 higher-order mode of a fiber *Opt. Express* **21** 17786–99
- [5] Stone J M and Knight J C 2008 Visibly ‘white’ light generation in uniform photonic crystal fiber using a microchip laser *Opt. Express* **16** 2670–5
- [6] Beaud P, Hodel W, Zysset B and Weber H 1987 Ultrashort pulse propagation, pulse breakup, and fundamental soliton formation in a single-mode optical fiber *IEEE J. Quantum Electron.* **23** 1938–46
- [7] Birks T, Wadsworth W and Russell P S J 2000 Supercontinuum generation in tapered fibers *Opt. Lett.* **25** 1415–7
- [8] Sørensen S T, Judge A, Thomsen C L and Bang O 2011 Optimum fiber tapers for increasing the power in the blue edge of a supercontinuum—group-acceleration matching *Opt. Lett.* **36** 816–8
- [9] Sørensen S T, Møller U, Larsen C, Moselund P, Jakobsen C, Johansen J, Andersen T, Thomsen C and Bang O 2012 Deep-blue supercontinuum sources with optimum taper profiles—verification of GAM *Opt. Express* **20** 10635–45
- [10] Webb K E, Erkintalo M, Xu Y, Broderick N G R, Dudley J M, Genty G and Murdoch S G 2014 Nonlinear optics of fibre event horizons *Nat. Commun.* **5** 4969
- [11] Legge S, Holdsworth J, Zwan B, Collins L, Martin J, Cook K and Canning J 2013 Low order solitons in higher order electromagnetic modes of photonic crystal fibre 2013 *Australian and New Zealand Conf. on Optics and Photonics* pp 7–9
- [12] Zwan B, Legge S, Holdsworth J and King B 2013 Spatio-spectral analysis of supercontinuum generation in higher order electromagnetic modes of photonic crystal fiber *Opt. Express* **21** 834–9
- [13] Cherif R, Zghal M, Nikolov I and Danailov M 2010 High energy femtosecond supercontinuum light generation in large mode area photonic crystal fiber *Opt. Commun.* **283** 4378–82
- [14] Duck B, Dean B, Holdsworth J and Dastoor P 2006 Mode structure in continuum generation, *Australian Conf. on Optical Fibre Technology/Australian Optical Society, 2006 ACOFT/AOS (Piscataway, NJ) (IEEE)*
- [15] Hochman A and Leviatan Y 2007 Efficient and spurious-free integral-equation-based optical waveguide mode solver *Opt. Express* **15** 14431–53
- [16] Gorbach A, Skryabin D, Stone J M and Knight J 2006 Four-wave mixing of solitons with radiation and quasi-nondispersive wave packets at the short-wavelength edge of a supercontinuum *Optics Express* **14** 9854–63

## 10 Appendices

### 10.1 Taylor Series Expansion of Phase Constant.

The following variable related to the propagation of guided modes has many names: wavenumber, phase constant, propagation constant; and many symbols, most often  $\beta$  or  $k$ .

$$\beta(\omega) = \frac{2\pi}{\lambda(\omega)} = n(\omega) \frac{\omega}{c} \quad (10.1)$$

Mathematically it is often useful to approximate  $\beta(\omega)$  as a Taylor series around some important central frequency  $\omega_0$ . This approximation is often used in nonlinear optics.

$$\beta(\omega) = \beta_0 + \beta_1(\omega - \omega_0) + \frac{1}{2}\beta_2(\omega - \omega_0)^2 + \frac{1}{6}\beta_3(\omega - \omega_0)^3 + \dots \quad (10.2)$$

i.e.

$$\beta(\omega) = \sum_{m=0}^N \frac{\beta_m}{m!} (\omega - \omega_0)^m \quad (10.3)$$

Each coefficient can be found by evaluating the  $m^{\text{th}}$  derivative at  $\omega_0$

$$\beta_m = \left( \frac{d^m \beta}{d\omega^m} \right)_{\omega=\omega_0} \quad (10.4)$$

It is often helpful to calculate these coefficients in terms of the refractive index.

$$\beta_0 = \beta(\omega_0) = n(\omega_0) \frac{\omega_0}{c} \quad (10.5)$$

$$\beta_1 = \frac{1}{v_g} = \frac{n_g}{c} = \frac{1}{c} \left( n(\omega) + \omega \frac{dn(\omega)}{d\omega} \right)_{\omega=\omega_0} \quad (10.6)$$

$$\beta_2 = \frac{1}{c} \left( 2 \frac{dn(\omega)}{d\omega} + \omega \frac{d^2 n(\omega)}{d\omega^2} \right)_{\omega=\omega_0} \quad (10.7)$$

$$\beta_m = \frac{1}{c} \left( m \frac{d^{m-1}n(\omega)}{d\omega^{m-1}} + \omega \frac{d^m n(\omega)}{d\omega^m} \right)_{\omega=\omega_0} \quad (10.8)$$

It should be noted that  $\beta_0$ ,  $\beta_1$  and  $\beta_2$  can also be related to the physical properties of phase velocity, group velocity and dispersion as discussed in section 1.1.3.

## 10.2 Radiometric Calibration

To have a NIST standard radiometric calibration a certified NIST source is required. With this source it is possible to generate a radiometric calibration for the apparatus that is considered known.

As the actual power measurement of the supercontinuum in this thesis was not critical it was not necessary to calibrate to such a source. Instead, a standard OSRAM 20W tungsten halogen lamp as shown in Figure 10.1 was used to generate the calibration of the mode field scanner in section 2.3.5. This is adequate as removing the response curve of the apparatus will provide the true relative spectrum of the broadband supercontinuum source.

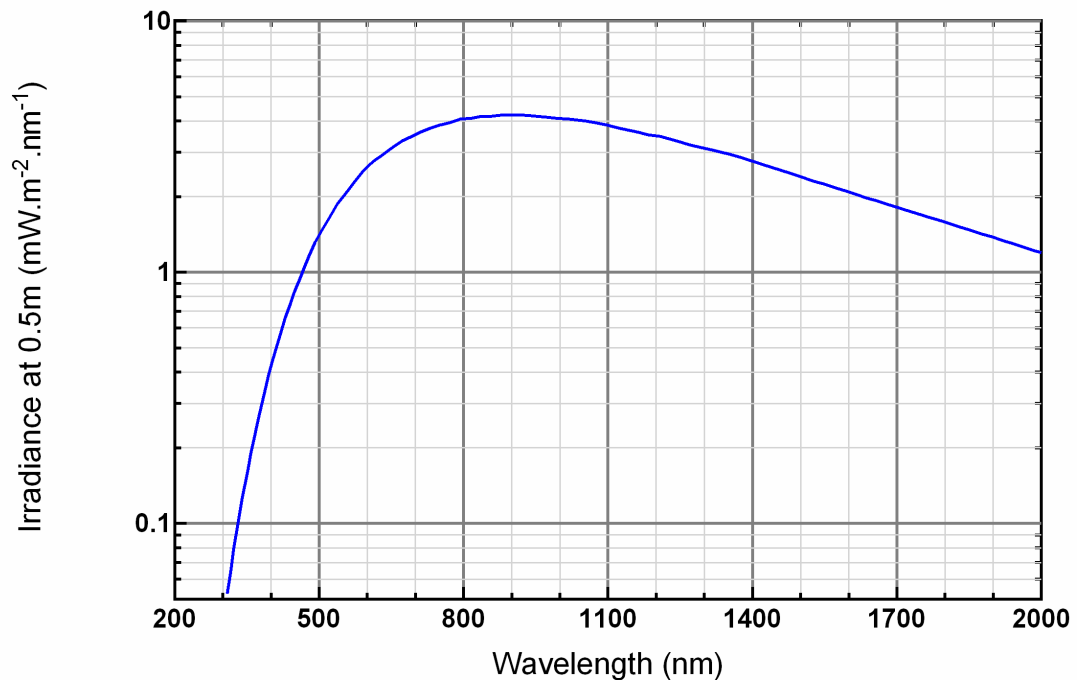


Figure 10.1: Spectral Irradiance of 20 W Quartz Tungsten Halogen lamp [56].

The spectrometers and bifurcated fibre from section 2.4 in accordance with the method detailed in the Newport Spectral Irradiance manual [56] and the equations detailed in section 2.5.1. This process was automated with a LabVIEW program written by the author and repeated as needed. This removed all detector spectral response from the measured data in this thesis.

### ***10.3 Source Code for Programs***

Not all programs are included as most are too long to print. Please email the author at samuel.legge@gmail.com if you desire a copy or find them uploaded here: <https://goo.gl/YSqfXa>

#### ***10.3.1 List of other programs written***

##### **Robot PCF scan:**

LabVIEW program used to control the stepper motors and record the spectrometer data in the mode field scans.

##### **FemtoSolve:**

LabVIEW program used to display data from the laser spectrometer and autocorrelator.

##### **Beam Stabiliser:**

LabVIEW program used to control the beam steering system and feedback loop.

##### **Calibrated Spectrum:**

LabVIEW program used to record and test radiometric calibrations of spectrometer data.

##### **Integration Changer:**

LabVIEW program used to adjust the integration time of the spectrometers before each measurement.

##### **PCF Profiler:**

LabVIEW program used to observe the MOF profile through a scan of the piezo electric fibre launch stage.

##### **Mode Spectrum:**

Matlab program detailed in section 2.5.2.

### 10.3.2 Refraction of Fused Silica

```
%Sellmeier equation
B1 = 0.6961663;
B2 = 0.4079426;
B3 = 0.8974794;
C1 = 0.0684043^2;
C2 = 0.1162414^2;
C3 = 9.896161^2;

L=0.2:0.001:3.5;    %Wavelength in um
n = (1+(B1.*L.^2)./(L.^2-C1)+(B2.*L.^2)./(L.^2-C2)+(B3.*L.^2)./(L.^2-
C3)).^0.5; %refractive Index
L=200e-9:1e-9:3.5e-6;    %Wavelength in nm

ng = n-L.*gradient(n,1e-9); %Group Index

D=(-L.*gradient(gradient(n,1e-9),1e-9)./3e8).*1e6; %Dispersion
%1e6 makes it in ps.nm-1.km-1
```

### 10.3.3 Self-Phase Modulation Simulation

```
%Self Phase Modulation
clear
clc
t=-300e-15:0.1e-15:300e-15;    % Time grid

FWHM = 200e-15;                %Pulse FWHM in Seconds
Energy=1e-8;                   %Pulse Energy in Joules
lambda=800e-9;                 %Wavelength in free space in meters

L=0.1;                         %Fibre Length in meters
r=5e-6;                        %Core radius in meters (assume top hat
intensity)
n=1.45;                        %Core Refractive index (silica)
n2=6.16e-23;                   %nonliner parameter V^-2 (silica)

c=FWHM/(2*log(2)^0.5);        %1/e^2 value
P0=((2/pi)^0.5)*Energy/c;     %Peak Intensity in Watts
w0=2*pi*(3e8/lambda);        %Angular frequency
A=pi*r^2;                     %Core area

P=P0*exp(-2*(t.^2./c^2));     %Gaussian Power profile in watts
I=P/A;                        %Intensity profile in W.m^-2
E=(2*I/(3e8*8.854E-12*n)).^0.5; %Electric Field envelope in Volts

w=w0-2*pi/lambda*L*n2*gradient(E.^2,0.1e-15); %Instantaneous frequency
shift
```

### 10.3.4 Quadrant Detection Simulation

```
clear
clc
%Set parameters
grid_dist=5e-3; %meters
n=100;
%FWHM=1235.9e-6;
FWHM=1235.9e-6;
sigma = FWHM/2.35482;
r = 2.99e-3/2;      %quadrant radius (m)
r2 = r^2;
sep = 0.2e-3/2;    %diode seperation (m)
step = grid_dist/n;

%Build 2D Grid
[X,Y] = ndgrid(-1:2/n:1,-1:2/n:1);
X = X*grid_dist/2;
Y = Y*grid_dist/2;

X_OUT_M=[];
Y_OUT_M=[];
for m=-1e-3:1e-6:1e-3
    %central point in meters
    x0=m;
    y0=0e-3;

    %Create Guassian Function
    G2 = 1.* exp(-(((X-x0).^2.+(Y-y0).^2)./(2*sigma^2)));
    %Plot it if we want

%Surf(X(:,1),Y(1,:),G2,'EdgeColor','none','LineStyle','none','FaceLighting','phong'); %contour plot
    %plot(X(:,1),G2(:,n/2+1)); % use to check 2d profile across center

%Now we do some quadrant calculations
Q1=0;
Q2=0;
Q3=0;
Q4=0;

%lets do this
for i=0:n
    for j=0:n
        x=(i-n/2)*step;
        y=(j-n/2)*step;

        if ((x>sep) && (y>sep) && (x^2+y^2<r2))
            Q1 = Q1+ G2 (i+1,j+1);
        end

        if ((x<-sep) && (y>sep) && (x^2+y^2<r2))
            Q2 = Q2+ G2 (i+1,j+1);
        end

        if ((x<-sep) && (y<-sep) && (x^2+y^2<r2))
            Q3 = Q3+ G2 (i+1,j+1);
        end
    end
end
```

```

        if ((x>sep) && (y<-sep) && (x^2+y^3<r2))
            Q4 = Q4+ G2(i+1,j+1);
        end

    end

end

SUM=Q1+Q2+Q3+Q4;

X_OUT = ((Q1+Q4)-(Q2+Q3))/SUM;
Y_OUT = ((Q1+Q2)-(Q3+Q4))/SUM;

X_OUT_M=[X_OUT_M,X_OUT];
Y_OUT_M=[Y_OUT_M,Y_OUT];
end

plot(-1e-3:1e-6:1e-3,X_OUT_M);

```